



AVERTISSEMENT

Ce document est le fruit d'un long travail approuvé par le jury de soutenance et mis à disposition de l'ensemble de la communauté universitaire élargie.

Il est soumis à la propriété intellectuelle de l'auteur. Ceci implique une obligation de citation et de référencement lors de l'utilisation de ce document.

D'autre part, toute contrefaçon, plagiat, reproduction illicite encourt une poursuite pénale.

Contact : ddoc-theses-contact@univ-lorraine.fr

LIENS

Code de la Propriété Intellectuelle. articles L 122. 4

Code de la Propriété Intellectuelle. articles L 335.2- L 335.10

http://www.cfcopies.com/V2/leg/leg_droi.php

<http://www.culture.gouv.fr/culture/infos-pratiques/droits/protection.htm>



UNIVERSITÉ DE METZ



NORTHEASTERN UNIVERSITY

DISSERTATION

Presented at

University of Metz and Northeastern University

CONG Daoyong 从道永

To obtain the doctor's degree of
University of Metz and Northeastern University

SPECIAL FIELD: Engineering Sciences
OPTION: Materials Science

Crystallographic Study on Ni-Mn-Ga Ferromagnetic Shape Memory Alloys

Defended on the 16th of July 2008 in front of the jury:

R. PENELLE	Professor:	Université Paris-Sud XI, France	Reviewer
W. SKROTZKI	Professor:	TU Dresden, Germany	Reviewer
Z. Q. HU	Professor Academician:	Institute of Materials Research Chinese Academy of Sciences	Reviewer
C. ESLING	Professor:	Université de Metz, France	Supervisor
L. ZUO	Professor:	Northeastern University, PR China	Supervisor
Y. D. WANG	Professor:	Northeastern University, PR China	Co-Supervisor
Y. D. ZHANG	Doctor:	Université de Metz, France	Co-Supervisor
I. MORELON	Doctor:	Science and Technology Attachée French Embassy in China, Beijing	Jury member
X. ZHAO	Professor:	Northeastern University, PR China	Jury member

Laboratoire d'Etude des Textures et Application aux Matériaux CNRS UMR 7078
Ile du Saulcy 57012 Metz Cedex 01

Contents

Abstract.....	I
Résumé.....	II
摘 要.....	III
Acknowledgements.....	IV

Introduction 1

1. Background.....	1
2. Ni-Mn-Ga ferromagnetic shape memory alloys.....	3
2.1 Crystal structure of Ni-Mn-Ga alloys.....	3
2.1.1 Crystal structure of parent phase.....	3
2.1.2 Crystal structure of martensite.....	5
2.2 Phase transformation in Ni-Mn-Ga alloys.....	8
2.2.1 Transformation sequence.....	8
2.2.2 Solidification and disorder-order transition.....	10
2.2.3 Premartensitic transformation.....	10
2.2.4 Martensitic transformation.....	11
2.2.5 Intermartensitic transformation.....	13
2.3 Magnetic properties of Ni-Mn-Ga alloys.....	15
2.3.1 Curie temperature.....	15
2.3.2 Magnetic moment.....	15
2.3.3 Magnetization.....	16
2.3.4 Magnetic anisotropy.....	17
2.3.5 Magnetic domain structure.....	18
2.4 Magnetic shape memory effect in Ni-Mn-Ga alloys.....	20
2.4.1 Prerequisite.....	20
2.4.2 Mechanism.....	20
2.4.3 Theoretical and observed values of MFIS.....	22
2.5 Microstructure of Ni-Mn-Ga alloys.....	24
2.6 Crystallography of Ni-Mn-Ga alloys.....	27
2.6.1 Crystallographic texture.....	27
2.6.2 Orientation relationships.....	28

2.7 Mechanical properties of Ni-Mn-Ga alloys.....	29
2.8 Alloying of Ni-Mn-Ga alloys	32
3. Significance and contents of the present work.....	34

Chapter 1

Investigation on crystal structure and phase transformation in Ni-Mn-Ga alloys by in situ neutron diffraction technique 53

Introduction.....	53
Crystal structure and phase transformation in Ni ₅₃ Mn ₂₅ Ga ₂₂ shape memory alloy from 20 K to 473 K	54
Neutron diffraction study on crystal structure and phase transformation in Ni-Mn-Ga ferromagnetic shape memory alloys.....	63

Chapter 2

Microstructure and martensitic transformation crystallography of Ni-Mn-Ga alloys ... 75

Introduction.....	75
Determination of microstructure and twinning relationship between martensitic variants in 53 at.%Ni–25 at.%Mn–22 at.%Ga ferromagnetic shape memory alloy	76
Experiment and theoretical prediction of martensitic transformation crystallography in a Ni–Mn–Ga ferromagnetic shape memory alloy	89
Multiples twinned nanostructure in novel ferromagnetic shape-memory alloys	112

Chapter 3

Crystallographic texture in Ni-Mn-Ga alloys 132

Introduction.....	132
Crystal Structures and Textures in the Hot-Forged Ni-Mn-Ga Shape Memory Alloys.....	133

Chapter 4

Alloying of Ni-Mn-Ga alloys with Co element..... 146

Introduction.....	146
Martensitic and magnetic transformation in Ni–Mn–Ga–Co ferromagnetic shape memory alloys....	146

Conclusions 161

Publication List..... 166

Abstract

Ni-Mn-Ga ferromagnetic shape memory alloys (FSMAs) with chemical composition close to Ni_2MnGa have received great attention due to their giant magnetic shape memory effect and fast dynamic response. In this work, the crystal structure, martensitic transformation crystallography, texture and alloying in Ni-Mn-Ga FSMAs are systematically investigated.

In situ neutron diffraction experiments show that $\text{Ni}_{53}\text{Mn}_{25}\text{Ga}_{22}$ has a tetragonal $I4/mmm$ structure from 20K to 403K, with a pretransformation occurring in the martensitic phase around room temperature. $\text{Ni}_{48}\text{Mn}_{30}\text{Ga}_{22}$ has a cubic, $L2_1$ Heusler structure from 373K to 293K. Its crystal structure changes into a seven-layered orthorhombic martensitic structure when cooled to 243K. There is no intermartensitic transformation upon further cooling to 19K.

Electron backscatter diffraction (EBSD) analyses show that the neighboring martensitic variants in the $\text{Ni}_{53}\text{Mn}_{25}\text{Ga}_{22}$ alloy have a compound twinning relationship with the twinning elements $\mathbf{K}_1 = \{112\}$, $\mathbf{K}_2 = \{11\bar{2}\}$, $\boldsymbol{\eta}_1 = \langle 111 \rangle$, $\boldsymbol{\eta}_2 = \langle 111 \rangle$, $\mathbf{P} = \{1\bar{1}0\}$ and $s = 0.379$. The twin interface plane coincides with the twinning plane. The ratio of the relative amounts of twins within the same initial austenite grain is ~ 1.70 . The main orientation relationship between austenite (A) and martensite (M) is Kurdjumov-Sachs (K-S) relationship with $(111)_A // (101)_M$, $[1\bar{1}0]_A // [11\bar{1}]_M$. Based on the crystallographic phenomenological theory, the calculated habit plane is $\{0.690 \ -0.102 \ 0.716\}_A$ (5.95° from $\{101\}_A$), and the magnitude, direction and shear angle of the macroscopic transformation shear are 0.121 , $\langle -0.709 \ 0.105 \ 0.698 \rangle_A$ (6.04° from $\langle -101 \rangle_A$) and 6.88° , respectively. Nanoscale twins inside the martensitic lamellae are found in the $\text{Ni}_{53}\text{Mn}_{25}\text{Ga}_{22}$ alloy annealed at 1173K for 4h followed by furnace cooling. Two kinds of interfaces, i.e. interpenetrated inter-lamellar interface and stepped intra-lamellar interface, are observed. The orientation relationships between the nanotwins connected by different interface configurations are determined.

Texture in Ni-Mn-Ga FSMAs is developed by hot forging. The texture evolution in the hot-forged $\text{Ni}_{48}\text{Mn}_{25}\text{Ga}_{22}\text{Co}_5$ alloy after room temperature deformation and subsequent annealing is found to be closely related to its thermally activated shape memory effect. The texture changes significantly during deformation and it recovers to its initial state after subsequent annealing. An excellent shape memory effect with a recovery ratio of 74% is observed.

The substitution of Co for Ni in $\text{Ni}_{53-x}\text{Mn}_{25}\text{Ga}_{22}\text{Co}_x$ ($x=0-14$) alloys proves very efficient in increasing the Curie temperature. It only slightly decreases the martensitic transformation temperature when the Co content is less than 6%. In contrast, an abrupt decrease of martensitic transformation temperature is observed when the Co content exceeds 6%, due to the atomic disorder as a result of the addition of a large amount of Co. It is suggested that the substitution of a small amount of Co for Ni is helpful to the development of FSMAs with high martensitic transformation temperature and high Curie temperature.

Insights into the fundamental aspects such as microstructure, crystallography and phase transformation in Ni-Mn-Ga FSMAs are of great significance to the improvement of the functional performances of the present Ni-Mn-Ga alloys and to the design of new promising FSMAs.

Keywords: Ferromagnetic shape memory alloys (FSMAs); Martensitic transformation; Crystal structure; Texture; Orientation relationship; Neutron diffraction

Résumé

Les alliages ferromagnétiques à mémoire de forme (FSMAs: Ferromagnetic shape memory alloys) avec des compositions proches de Ni_2MnGa ont attiré beaucoup d'attention en raison de leur effet de mémoire de forme gigantesque et de leur réponse rapide et dynamique. Dans ce travail, la structure cristalline, la cristallographie de transformation marténitique, la texture et l'effet de l'addition de Co à l'alliage Ni-Mn-Ga sont examinés systématiquement.

Les mesures de diffraction aux neutrons montrent que la structure de $\text{Ni}_{53}\text{Mn}_{25}\text{Ga}_{22}$ est caractérisée par un réseau tétragonal du groupe $I4/mmm$ de 20K jusqu'à 403K avec une prétransformation ayant lieu dans la phase martensitique autour de la température ambiante alors que la structure de l'alliage $\text{Ni}_{48}\text{Mn}_{30}\text{Ga}_{22}$ est caractérisée par un réseau de Heusler cubique $L2_1$ de 373K à 293K. La structure cristalline de ce dernier alliage se transforme en structure martensitique orthorhombique à 7 couches s'il est refroidi à 243K. Il n'y a plus la transformation intermartensitique lorsqu'il est refroidi jusqu'à 19K.

Les résultats d'EBSD (Electron Backscattered Diffraction) nous permettent de déterminer que les variants martensitiques voisins possèdent une relation de maclage composée, avec les éléments de $\mathbf{K}_1 = \{112\}$, $\mathbf{K}_2 = \{11\bar{2}\}$, $\boldsymbol{\eta}_1 = \langle 11\bar{1} \rangle$, $\boldsymbol{\eta}_2 = \langle 111 \rangle$, $\mathbf{P} = \{1\bar{1}0\}$ et $s = 0.379$. Le plan d'interface entre les macles coïncide avec le plan de maclage. Le rapport de quantités relatives de paires de macles au sein d'un même grain d'austénite initiale est d'environ 1.70. La relation d'orientation dominante entre l'austénite et la martensite est la relation de Kurdjumov-Sachs (K-S) avec $(111)_A // (101)_M$, $[\bar{1}10]_A // [11\bar{1}]_M$. Le plan d'habitat calculé par la théorie cristallographique phénoménologique est $\{0.690 \ -0.102 \ 0.716\}_A$, qui est proche de $\{1 \ 0 \ 1\}_A$. L'amplitude et l'angle du cisaillement sont 0.121 et 6.88°C. La direction du cisaillement est $\langle -0.709 \ 0.105 \ 0.698 \rangle_A$ qui est proche de $\langle -1 \ 0 \ 1 \rangle_A$ dans ce même plan. Les macles à l'échelle nanométrique au sein des lamelles martensitiques sont observées dans l'alliage $\text{Ni}_{53}\text{Mn}_{25}\text{Ga}_{22}$ recuit à 1173K pendant 4 heures et suivi d'un refroidissement à l'intérieur du four. Deux types d'interfaces sont trouvées, qui sont d'une part l'interface marquée par l'interpenetration des nano-macles entre les lamelles et d'autre part l'interface avec des marches au sein même des lamelles. Les relations d'orientations entre les nano-macles séparées par les deux types d'interfaces ont été déterminées.

La texture de l'alliage Ni-Mn-Ga est développée par forgeage à chaud. L'évolution de la texture dans l'alliage forgé à chaud lors de la déformation ultérieure à température ambiante et suivie de recuit est trouvée associée à l'effet de mémoire de forme activé thermiquement. La texture évolue de manière significative lors de la déformation et reprend l'état initial après le recuit qui suit. Un excellent effet de mémoire de forme avec le rapport de recouvrement de 74% est observé.

La substitution de Co pour Ni dans les alliages $\text{Ni}_{53-x}\text{Mn}_{25}\text{Ga}_{22}\text{Co}_x$ ($x=0-14$ at.%) s'avère très efficace pour élever la température de Curie. La température de transformation martensitique décroît un peu si la teneur en Co est inférieure à 6%. Au contraire, une chute brusque de la température de transformation martensitique s'opère quand la teneur en Co dépasse 6% du fait du désordre atomique par l'addition de Co en grande quantité. Cela suggère que la substitution de Co pour Ni en petite quantité est utile pour développer des alliages ferromagnétique à mémoire de forme avec température de transformation martensitique et température de Curie élevées.

L'étude des aspects fondamentaux tels que la microstructure, la cristallographie et la transformation de phase des alliages ferromagnétique à mémoire de forme est importante pour améliorer les performances fonctionnelles des alliages Ni-Mn-Ga actuels et pour concevoir de nouveaux alliages à mémoire de forme prometteurs.

Mots clés: Alliages ferromagnétique à mémoire de forme (FSMAs); transformation martensitique; structure cristalline; texture; relations d'orientation; diffraction de neutrons

摘 要

化学成分接近 Ni_2MnGa 的Ni-Mn-Ga磁致形状记忆合金由于具有磁致输出应变大、响应速度快等优点而备受关注。本文对Ni-Mn-Ga磁致形状记忆合金的晶体学结构、马氏体转变晶体学、织构以及合金化进行了系统研究。

原位中子衍射实验表明 $\text{Ni}_{53}\text{Mn}_{25}\text{Ga}_{22}$ 合金在 20K到 403K温度区间内具有四方 $I4/mmm$ 马氏体结构；该合金室温附近在马氏体相区存在一个预转变。 $\text{Ni}_{48}\text{Mn}_{30}\text{Ga}_{22}$ 合金在 373K到 293K温度区间内具有立方 $L2_1$ Heusler奥氏体结构，当冷却到 243K时该合金的晶体结构已经转变成七层正交马氏体结构，继续冷却到 19K的过程中没有发生中间马氏体转变。

电子背散射（EBSD）取向分析表明 $\text{Ni}_{53}\text{Mn}_{25}\text{Ga}_{22}$ 合金中相邻的马氏体变体具有复合孪晶关系，孪生元素为 $\mathbf{K}_1 = \{112\}$ ， $\mathbf{K}_2 = \{11\bar{2}\}$ ， $\boldsymbol{\eta}_1 = \langle 11\bar{1} \rangle$ ， $\boldsymbol{\eta}_2 = \langle 111 \rangle$ ， $\mathbf{P} = \{1\bar{1}0\}$ ， $s = 0.379$ 。孪生面即为孪晶界面。相同原始奥氏体晶粒内部孪晶变体的相对量之比约为 1.70。马氏体转变过程中奥氏体（A）与马氏体（M）之间的主要取向关系为Kurdjumov-Sachs (K-S)关系： $(111)_A // (101)_M$ ， $[1\bar{1}0]_A // [11\bar{1}]_M$ 。根据晶体学唯象理论计算得出，马氏体转变过程中的惯析面为 $\{0.690 \ -0.102 \ 0.716\}_A$ ，宏观切变量、切变方向和切变角分别为 0.121， $\langle -0.709 \ 0.105 \ 0.698 \rangle_A$ 和 6.88° 。在经过 1173K退火 4 小时、随炉冷却的 $\text{Ni}_{53}\text{Mn}_{25}\text{Ga}_{22}$ 合金中发现了存在于马氏体片层内部的纳米尺度孪晶，观测到了两种不同的界面：相互穿插的片层间界面和台阶状的片层内界面，并确定了通过这两种界面连接的纳米孪晶之间的取向关系。

等温锻后Ni-Mn-Ga磁致形状记忆合金中产生了织构。研究表明 $\text{Ni}_{48}\text{Mn}_{25}\text{Ga}_{22}\text{Co}_5$ 合金室温变形和随后退火过程中的织构演变与其温控形状记忆效应密切相关。该合金的织构在变形过程中发生了显著变化，并在退火以后恢复到了原始状态。在该合金中发现了恢复比为 74%的形状记忆效应。

在 $\text{Ni}_{53-x}\text{Mn}_{25}\text{Ga}_{22}\text{Co}_x$ ($x=0-14$)合金中用Co取代Ni能有效提高合金的居里温度。当Co含量小于 6%时用Co取代Ni仅稍微降低合金的马氏体转变温度，但是当Co含量超过 6%时由于大量Co 元素的添加引起原子占位混乱合金的马氏体转变温度突然下降。这意味着用少量的Co取代Ni有助于开发具有高马氏体转变温度、高居里温度的磁致形状记忆合金。

对 Ni-Mn-Ga 磁致形状记忆合金诸如微观组织、晶体学、相变等基础问题进行研究对提高现有 Ni-Mn-Ga 磁致形状记忆合金的功能行为和开发新型先进磁致形状记忆合金具有重要的指导意义。

关键词: 磁致形状记忆合金；马氏体转变；晶体结构；织构；取向关系；中子衍射

Acknowledgements

This work is financially supported by National Natural Science Foundation of China (NSFC) (Grant Nos. 50531020, 50528102, 50325102 and 50471026), the National Ministry of Education of China (with the New-Century Outstanding Scholars Fund NCET-04-0282), the Chinese-French Cooperative Research Project PRA MX04-02, and the Swedish Research Council in the frame of the SIDA project (Grant No. 348-2004-3475). It is also partially funded by the Ph.D fund of Northeastern University, China. I would like to give my sincere thanks to these institutions.

This work is completed at LETAM, University of Metz, France, the Key Laboratory for Anisotropy and Texture of Materials, Northeastern University, China, and the Studsvik Neutron Research Laboratory, Uppsala University, Sweden. I would like to give my hearted thanks to all the members for their kind help.

I would like to sincerely thank the reviewers, Prof. R. Penelle at Université Paris-Sud XI, France, Prof. W. Skrotzki at TU Dresden, Germany, and Prof. Z. Q. Hu at Institute of Metal Research, Chinese Academy of Sciences, China, for taking time to review my dissertation and give a lot of valuable suggestions and comments.

I would like to give my special thanks to my supervisors, Prof. Claude Esling, Dr. Yudong Zhang at University of Metz, and Prof. Liang Zuo, and Prof. Yandong Wang at Northeastern University for guiding me into this research field and for their constant help and support on my research work. Every progress in this work coagulated their care and enlightenment. They are learnt, modest, serious and kind supervisors. From them, I have learnt not only knowledge but also precise scientific attitude towards work and persistence to overcome difficulty. I also sincerely thank Prof. Claude Esling for helping me to apply for the scholarship to support my PhD study in France.

I am deeply indebted to Prof. Xiang Zhao for his care and help on both my scientific work and daily life. I would like to sincerely thank Dr. Per Zetterström and Dr. Ru Lin Peng for their kind help during the period when I was doing experiments in Sweden. Special thanks should be given to Prof. Tadao Watanabe for his kind help and for his care for my future career. I would like to acknowledge Prof. M. Humbert, Prof. J. Z. Xu, Dr. Z. F. Zhang, Dr. H. F. Zhang, Prof. P. K. Liaw, Dr. Y. Ren, Dr. G. Wang, Dr. Y. D. Liu, Prof. Y. H. Sha, Dr. C. S. He, Dr. N. Gey, Dr. J. S. Lecomte, Mr. J. N. Deng and other related scientists for their kind help on my research work and for their fruitful discussions.

During my study, I always received direct help from the Ph. D students and master degree

students from LETAM, University of Metz, France, and the Key Laboratory for Anisotropy and Texture of Materials, Northeastern University, China. Their kind care, selfless help and the deep friendship between us have made up of large part of the support and enjoyment of my study. I will cherish all of these deep in my mind.

Last but not least, I would like to give my heartfelt thanks to my parents, my fiancée Miss Xiaoxia Jiang, and my sisters. Their deep love and understanding, and their constant support, help and encouragement over the years are the great impetus to my study.

I apologize in advance to those whose important contributions have been overlooked here because of my inability to fully appreciate their significance or my own unfamiliarity with them, but thanks for their help.

Introduction

1. Background

With the rapid development of science and technology, the demand for high-performance materials with multi-functional properties has been increasing. Modern technologies need transducing materials, also referred to as smart materials that undergo a substantial change in one or more properties in response to a change in external conditions. Distinctly from structural materials, smart materials possess physical and chemical properties that are sensitive to a change in the environment such as temperature, pressure, electric field, magnetic field, optical wavelength, humidity, and pH. All of the smart materials are transducer materials as they transform one form of energy into another, and hence they have wide applications as both actuators and sensors in various fields such as medical, defense, aerospace, and marine industries.

Smart materials can be categorized according to the type of response and type of activation. Among the large numbers of smart materials, the electrically driven piezoelectric materials, magnetically controlled magnetostrictive materials and thermally activated shape memory alloys are most widely explored because of their numerous potential applications [1]. However, each of these materials has its own advantages and drawbacks. Piezoelectric materials can be deformed under the application of an electric field because of the electro-mechanical coupling in these materials. Likewise, these materials can generate an electric field in response to an external strain field. Piezoelectric devices are known for their high frequency capability, on the order of tens of kHz. Nevertheless, the induced strain in these materials is relatively small; the best piezoelectric ceramics only exhibit a strain of about 0.19% [2]. Magnetostrictive materials, such as Terfenol-D, can generate induced strain under magnetic fields. They can operate at high frequencies up to 10 kHz, but they also have the same drawbacks of small output strain. The maximum observed strain in single crystals is about 0.2% [3]. Moreover, the magnetostrictive materials are relatively expensive to produce and highly brittle. Shape memory alloys, like NiTi, have the ability to recover large plastic

strain up to 8% [4] as a result of a thermally activated reversible martensitic transformation. However, the working frequency for these alloys is quite low (less than 1 Hz) because of the slow process of heating and cooling that control the martensitic transformation and the reverse transformation. The respective drawbacks of the above-mentioned smart materials have greatly limited their practical applications in certain fields. The development of high-performance smart materials with both large output strain and fast response has become imperative.

Recently, a new class of smart materials called ferromagnetic shape memory alloys (FSMAs), also referred to as magnetic shape memory alloys (MSMAs), was developed. These FSMAs combine the properties of ferromagnetism with those of a diffusionless, reversible martensitic transformation. The field-induced strain in these materials results from the rearrangement of martensitic variants under applied magnetic fields. Thus they integrate the advantages of both thermally controlled shape memory alloys and magnetostrictive materials, showing giant magnetic shape memory effect and fast dynamic response. The reported magnetic-field-induced strain is as high as 9.5% [5], which is an order of magnitude higher than the strains generated in piezoelectric and magnetostrictive materials. Meanwhile, the working frequency of the FSMAs is very high, on the order of kHz [6, 7]. Inspired by the merits of these materials, considerable efforts have been devoted to the investigation on various aspects of these FSMAs in the past few decades [5-26].

Up to now, several alloy systems have been confirmed to exhibit the characteristics of FSMAs, including Ni-Mn-Ga [5-11], Co-Ni-Ga [12], Co-Ni-Al [13, 14], Ni-Fe-Ga [15, 16], Ni-Mn-Al [17], Fe-Pd [18-20] and Fe-Pt [21]. Among these alloys, Ni-Mn-Ga alloys with chemical compositions close to the stoichiometric compound Ni_2MnGa are the most promising FSMAs. There are several key characteristics that make Ni-Mn-Ga alloys unique and remarkable, attracting a high degree of research interest. First, they are the only known ferromagnetic intermetallic compounds that undergo a thermoelastic martensitic transformation from a cubic $L2_1$ -ordered Heusler structure to a complex martensitic structure [22, 23]. Second, the martensitic transformation in these alloys exhibits several active properties that are of great interest to the smart materials society, including the two-way shape memory effect [24, 25], superelasticity [26] and magnetic-field-induced strain [8, 9]. Finally,

and the most importantly, the largest magnetic-field-induced strain is only observed in Ni-Mn-Ga alloys [5]. Consequently, Ni-Mn-Ga alloys, which are the focus of this thesis, become the most extensively studied FSMAs in the past ten years.

2. Ni-Mn-Ga ferromagnetic shape memory alloys

Ni-Mn-Ga alloys have already been investigated for more than 40 years. At the very beginning, Ni₂MnGa together with other alloys were demonstrated as Heusler alloys having the formula X₂YZ [27-32]. Soltys was the first to concentrate only on the Ni-Mn-Ga alloy system [33, 34]. The martensitic transformation and magnetic order were later investigated in detail by Webster *et al.* [22] in 1984. More systematic studies by Kokorin *et al.* [35] and Chernenko *et al.* [36] were initiated in the early 1990s when Ni-Mn-Ga alloys were studied as potential shape memory alloys. The novel idea of rearranging martensitic variants by a magnetic field and thus generating a field-induced strain was relatively newly developed and received attention only in recent years. In 1996, Ullakko *et al.* [8] firstly demonstrated a magnetic-field-induced strain of 0.2% in a Ni₂MnGa single crystal with a magnetic field of 8kOe applied at 265K. After that, a totally new era of investigations started. Extensive researches were carried out both experimentally and theoretically on various properties of Ni-Mn-Ga FSMAs. Theoretical models on the field-induced rearrangement of martensitic variants were established by O'Handley *et al.* [37] and James *et al.* [18] in 1998. In 2000, Murray *et al.* have succeeded in the observation of a large magnetic-field-induced strain of 6% in the five-layered martensitic phase [9, 38]. More recently, a much larger strain close to 10% was observed by Sozinov *et al.* [5] in the seven-layered martensite, which is, heretofore, the largest magnetic-field-induced strain obtained in FSMAs. Up to now, numerous studies have been performed on many aspects of Ni-Mn-Ga alloys, including crystal structure, phase transformation, magnetic properties, magnetic shape memory effect, mechanical behavior, martensite stabilization and alloying, and a lot of interesting phenomena have been revealed.

2.1 Crystal structure of Ni-Mn-Ga alloys

2.1.1 Crystal structure of parent phase

The crystal structure of Ni-Mn-Ga alloys with chemical compositions close to the

stoichiometric compound Ni_2MnGa have been extensively studied mostly by means of X-ray or electron diffraction and, less commonly, by means of neutron diffraction. However, it is worth noting that it is very difficult to accurately determine the crystal structure of Ni-Mn-Ga alloys by X-ray diffraction technique, as the X-ray scattering factors of Ni, Mn and Ga atoms are similar to each other. In contrast, neutron diffraction is a more powerful tool to precisely characterize the detailed crystal structure of Ni-Mn-Ga alloys due to the significantly different neutron scattering factors of the constituent atoms.

Webster *et al.* [22] were the first to study the crystal structure of the stoichiometric Ni_2MnGa by neutron diffraction technique. They revealed that Ni_2MnGa has a cubic, $L2_1$ Heusler structure above martensitic transformation temperature. The lattice parameter was reported to be around 5.82\AA . A more systematic neutron diffraction study was recently carried out by Brown *et al.* [39]. It was shown that the crystal structure of the parent phase in Ni_2MnGa belongs to the space group $Fm\bar{3}m$ (No. 225). Ni atoms occupy 8c (0.25, 0.25, 0.25) Wyckoff sites, while Mn and Ga atoms occupy 4a (0, 0, 0) and 4b (0.5, 0.5, 0.5) sites, respectively. It was demonstrated that the lattice parameter of the parent phase is temperature dependent [39]. In addition to the temperature dependency, the lattice parameters of the Ni-Mn-Ga alloys also depend on the chemical composition and heat treatment.

Although the crystal structure of the austenitic parent phase in the stoichiometric Ni_2MnGa has been precisely determined by neutron diffraction [22, 39], the off-stoichiometric compounds have only been studied by X-ray or electron diffraction and, due to the similar atomic scattering factors of the constituent atoms, the reflections indicating the second neighbour ordering (characteristic of the $L2_1$ structure) have never been found. In spite of this, the crystal structure of the parent phase has been conventionally treated to be $L2_1$ ordered [40]. As a matter of fact, the unambiguous determination of the crystal structure of the parent phase in off-stoichiometric Ni-Mn-Ga alloys is quite essential, as the magnetic shape memory effect is usually observed in the off-stoichiometric compounds.

2.1.2 Crystal structure of martensite

The crystal structure of martensite in Ni-Mn-Ga alloys is an important factor because it affects their magnetic anisotropy [41-43], mechanical properties [42, 44] and chemical behavior [45, 46] that ultimately determine the functional performances of these alloys. The Ni-Mn-Ga alloys show different martensitic structures. Depending on composition and temperature, three types of martensitic structures are commonly observed, i.e. five-layered tetragonal martensite (5M), seven-layered near-orthorhombic martensite (7M) and non-modulated tetragonal martensite (NM or T). Among the three types of martensites, the NM martensite is the most stable one while 5M martensite is the most unstable one [42, 47-49], as shown in Fig. 1-1 (a). Therefore, if the 5M structure is to be observed it is transformed directly from the parent phase while the NM martensite can be a final transformation product of intermartensitic transformations from 7M or 5M martensites [50]. The first martensite transformed directly from parent phase depends on composition and there exists an empirical correlation between the martensitic transformation temperature and the first martensitic structure [49], as shown in Fig. 1-1 (b). The alloys transforming directly to the NM martensite typically have martensitic transformation temperatures that can be higher than their Curie temperatures [51, 52] and the 7M martensite appears first only in a narrow temperature range [49]. Thus, NM martensite is the only martensite that can exist both at very low temperatures as an intermartensitic transformation product and at elevated temperatures above Curie temperature as a first martensite transformed directly from parent phase.

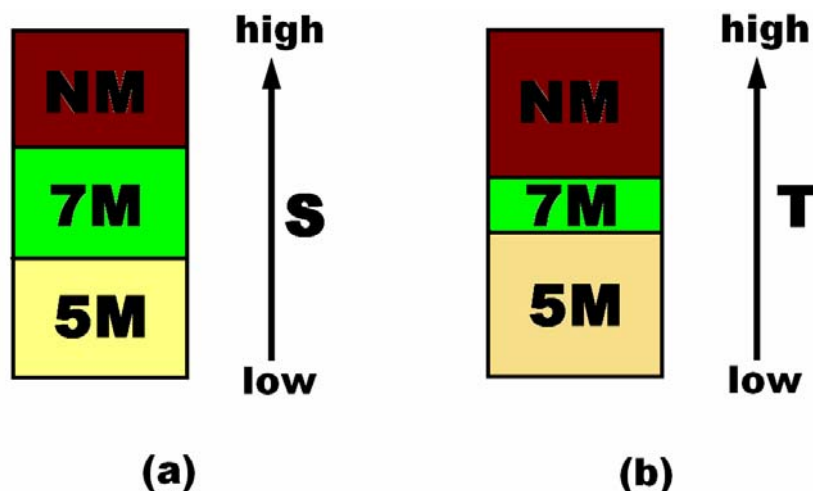


Fig. 1-1 (a) The stability (S) of the three types of martensites; (b) Relation between the first martensitic structure and the martensitic transformation temperature (T).

Prior to the detailed description of the above-mentioned crystal structures of martensites in Ni-Mn-Ga alloys, it is necessary to clarify the different coordinates with respect to which the martensitic structures are expressed. There are two different cases in which the martensitic structure are expressed with respect to (i) the orthorhombic martensite coordinate system constructed from the martensitic principal axes and (ii) the cubic parent phase coordinate system constructed from the cubic axes of the parent phase, respectively. The choice of (i) is crystallographically reasonable as it involves a smaller unit cell volume and it is also convenient to use this coordinate system to describe the crystal lattice modulation in the layered structure as a long-period superstructure. However, for a simple description of the strain values induced by stress or magnetic field, the choice of (ii) is more practical [32], as it is directly related to the change of lattice parameters, in the cubic coordinate system, after martensitic transformation. Since the cubic coordinate system is commonly accepted in the literature, for consistency the description of the literature work (unless specified) will also use this coordinate system in this chapter. A subscript “C” will be added to the lattice parameters and crystallographic planes and directions, denoting that they are expressed in the cubic parent phase coordinate system. However, in the other chapters of this thesis, the orthorhombic martensite coordinate system that is more crystallographically reasonable to analyze the crystallographic features of these FSMA will be used. One should bear in mind that the lattice parameters expressed with respect to the two coordinates are different from each other.

(1) Five-layered martensite (5M)

The 5M martensite of the low-temperature phase was observed by means of electron diffraction and X-ray diffraction in single crystals of $\text{Ni}_{51.5}\text{Mn}_{23.6}\text{Ga}_{24.9}$ ($M_s=293\text{K}$) [47, 53, 54], $\text{Ni}_{49.2}\text{Mn}_{26.6}\text{Ga}_{24.2}$ ($M_s\sim 180\text{K}$) [55, 56], $\text{Ni}_{52.6}\text{Mn}_{23.5}\text{Ga}_{23.9}$ ($M_s=283\text{K}$) [55], $\text{Ni}_{52}\text{Mn}_{23}\text{Ga}_{25}$ ($M_s=227\text{K}$) [57], etc. The crystal structure is modulated by a transverse displacive wave along the $[110]_C$ direction [53, 56] and it may be presented as a periodic shuffling along $(110)_C[110]_C$ system or a long-period stacking of $\{110\}_C$ close-packed planes [40, 47]. Modulation occurs in such a way that each fifth $(110)_C$ plane does not undergo displacements,

while the other four are displaced from their regular positions. The modulation can be observed in electron or X-ray diffraction as four additional spots between the main diffraction reflections [58, 59]. The average lattice is approximately tetragonal or slightly monoclinic with a short c_C axis, i.e. $c_C/a_C < 1$ (in the cubic coordinates). The tetragonality of the 5M martensite was found to increase with decreasing temperature and saturate at very low temperatures [58].

(2) Seven-layered martensite (7M)

The 7M martensite was observed in single crystals of $\text{Ni}_{52}\text{Mn}_{25}\text{Ga}_{23}$ ($M_s=333\text{K}$) [53], $\text{Ni}_{48.8}\text{Mn}_{29.7}\text{Ga}_{21.5}$ ($M_s=337\text{K}$) [5] and so on. Having a modulation mechanism similar to the case of 5M martensite, modulation in 7M martensite occurs in such a way that each seventh $(110)_C$ plane does not undergo displacements, while the other six are displaced from their regular positions. X-ray and electron diffractions show that, in the diffraction pattern, the distance between the main reflection along the $[110]^*_C$ direction in reciprocal space is divided into seven parts by six additional spots [56, 60, 61]. The average lattice is approximately orthorhombic with $c_C/a_C < 1$ and a monoclinic distortion of less than 0.4° was observed by Sozinov *et al.* [62]. Martynov [53] interpreted the crystal structure of $\text{Ni}_{52}\text{Mn}_{25}\text{Ga}_{23}$ as monoclinic with the lattice parameters $a_C=6.14\text{\AA}$, $b_C=5.78\text{\AA}$ and $c_C=5.51\text{\AA}$ and with $\gamma=90.5^\circ$, while Sozinov *et al.* [5] reported that the crystal structure of the 7M martensite in $\text{Ni}_{48.8}\text{Mn}_{29.7}\text{Ga}_{21.5}$ is nearly orthorhombic and has lattice parameters of $a_C=6.19\text{\AA}$, $b_C=5.80\text{\AA}$ and $c_C=5.53\text{\AA}$.

(3) Non-modulated martensite (NM)

The NM martensite was found in single crystal samples and thin films of the alloys such as $\text{Ni}_{53.1}\text{Mn}_{26.6}\text{Ga}_{20.3}$ ($M_s=380\text{K}$) [63, 64] and $\text{Ni}_{52.8}\text{Mn}_{25.7}\text{Ga}_{21.5}$ ($M_s=390\text{K}$) [65]. No modulation occurs in this type of martensite. The crystal structure of the NM martensite was confirmed to be tetragonal with a long c_C axis. The NM martensite is the only type of martensite with $c_C/a_C > 1$. Liu *et al.* [66] reported that the lattice parameters of $\text{Ni}_{46.4}\text{Mn}_{32.3}\text{Ga}_{21.3}$ are $a_C=b_C=5.517\text{\AA}$, $c_C=6.562\text{\AA}$ and $c_C/a_C=1.189$ while those of $\text{Ni}_{51.7}\text{Mn}_{27.7}\text{Ga}_{20.6}$ are $a_C=b_C=5.476\text{\AA}$, $c_C=6.568\text{\AA}$ and $c_C/a_C=1.199$. Lanska *et al.* [67]

systematically studied the composition and temperature dependence of the crystal structure and lattice parameters of Ni-Mn-Ga alloys with different types of martensite; a correlation between the martensitic crystal structure, martensitic transformation temperature and electron concentration was established [67].

Although the general configuration of the martensitic structure in Ni-Mn-Ga alloys has been established by electron and X-ray diffractions, the details of crystal structure of the martensites, such as space group and atomic positions, are still far from being understood. Moreover, some controversial results [23, 40, 68] have been obtained due to the inability of electron and X-ray diffractions in characterizing the detailed crystal structures of the Ni-Mn-Ga alloys consisting of nearby constituent elements in the periodic table. The precise determination of the fine crystal structure of martensites in Ni-Mn-Ga alloys by neutron diffraction technique is greatly needed and is of vital importance to the understanding of the mechanism of martensitic transformation and the improvement of the magnetic shape memory effect in these FSMAs.

2.2 Phase transformation in Ni-Mn-Ga alloys

2.2.1 Transformation sequence

As the magnetic shape memory effect due to the rearrangement of martensitic variants occurs only in the ferromagnetic martensitic state in Ni-Mn-Ga FSMAs, the phase transformation sequence and transformation temperature determine the service temperature range of these alloys. Hence, it is important to study the details of phase transformation process in these alloys in order to get a good understanding of the materials behavior. The phase transformation in Ni-Mn-Ga alloys is actually quite complex and different transformation behaviors can occur, depending on the chemical composition and thermal history of the alloys. A schematic illustration of the phase transformation sequence in Ni-Mn-Ga alloys is given in Fig. 1-2. At high temperatures, the melt of these alloys undergoes a solidification process leading to a partially disordered B2' phase, followed by the occurrence of a disorder-order transition from B2' phase to L2₁ ordered Heusler phase upon cooling. After cooled to lower temperatures, some Ni-Mn-Ga alloys undergo firstly a

premartensitic transformation and then a martensitic transformation, while the other alloys directly transform from the Heusler parent phase into martensite. Subsequently, the martensites in some alloys remain stable upon further cooling to very low temperatures whereas those in the other alloys undergo one or more intermartensitic transformations which produce more stable martensites existing at low temperatures. The detailed description of the different phase transformations in Ni-Mn-Ga alloys is presented in the following subsections.

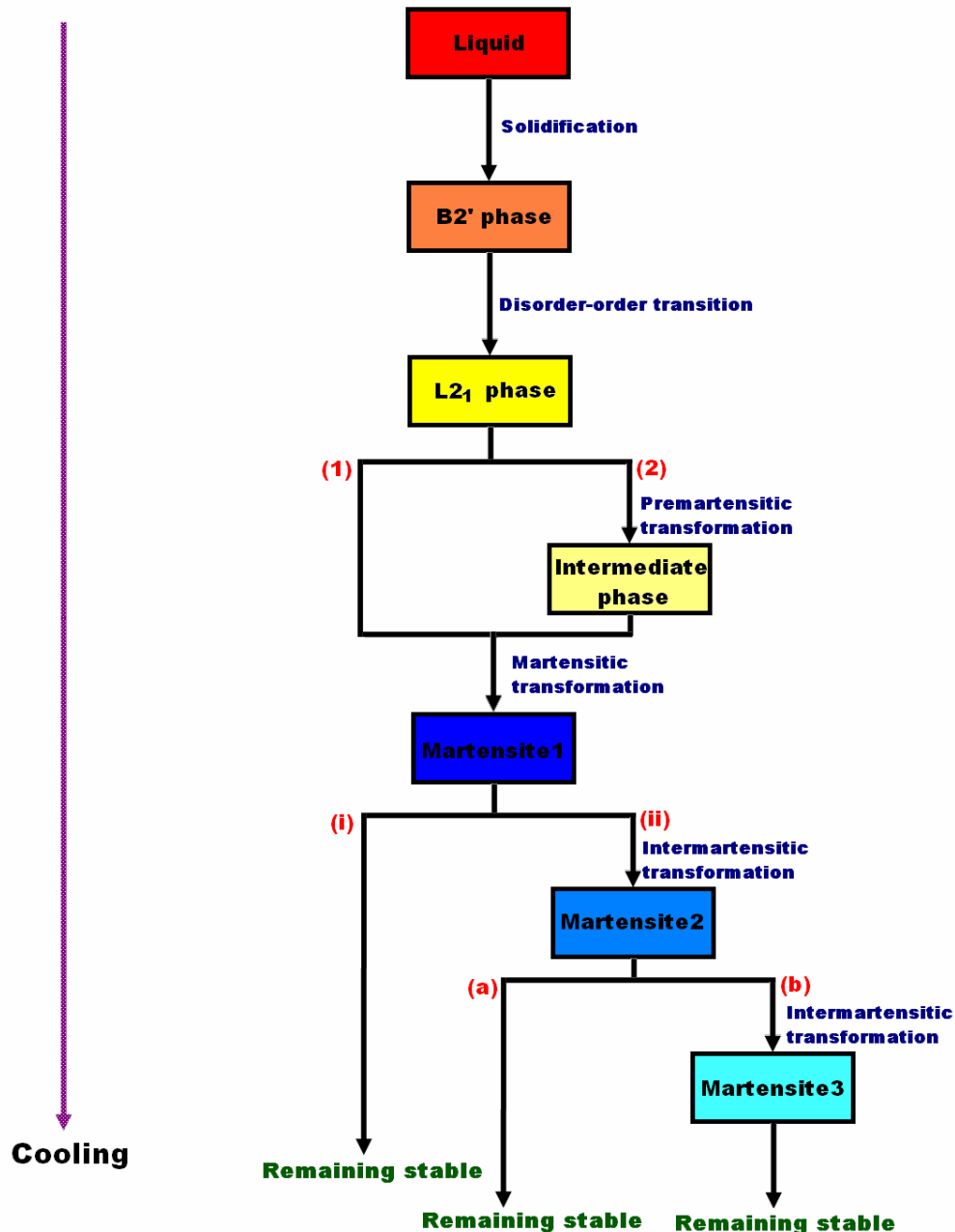


Fig. 1-2 Schematic illustration of phase transformation sequence in Ni-Mn-Ga alloys. The numbers (1) and (2), (I) and (II), and (a) and (b) in the scheme denote that in each case there are two possible transformation paths from high-temperature phase to low-temperature phase.

2.2.2 Solidification and disorder-order transition

The Ni-Mn-Ga alloys solidify into a partially disordered intermediate B2' phase at a certain composition-dependent temperature. Overhosler *et al.* [69] reported that the solidification temperatures of the $\text{Ni}_{50}\text{Mn}_x\text{Ga}_{50-x}$ ($x=15-35$) alloys are in the range of 1340-1400K and Söderberg *et al.* [70] confirmed that the $\text{Ni}_{50.5}\text{Mn}_{30.4}\text{Ga}_{19.1}$ and $\text{Ni}_{53.7}\text{Mn}_{26.4}\text{Ga}_{19.9}$ alloys solidify at 1386K and 1392K, respectively. The B2' phase experiences a disorder-order transition into the L2_1 ordered Heusler phase upon further cooling. The B2'- L2_1 transition was confirmed to be a second order transition [71] and the transition temperature is between 800-1100K, depending on the chemical composition of the alloys [69, 70]. The difference between the B2' and L2_1 structures is that in B2' structure the Ni atoms form the frame of the lattice while Mn and Ga atoms occupy arbitrary positions, whereas in L2_1 structure Mn and Ga atoms are strictly ordered as well as Ni atoms.

2.2.3 Premartensitic transformation

Prior to the martensitic transformation at low temperatures, premartensitic transformation can occur in some Ni-Mn-Ga alloys. The premartensitic transformation in Ni-Mn-Ga system is not directly related to the magnetic shape memory effect of these alloys, but, scientifically, it offers various opportunities to investigate the coexisting interactions of electro-phonon, magnetoelastic and Jahn-Teller mechanisms. The physical nature of the premartensitic transformation in Ni-Mn-Ga alloys has been the topic of both theoretical [72, 73] and experimental work by means of neutron diffraction [39, 74-76], transport [77], magnetic [78, 79], mechanical [80], acoustic [81] and ultrasonic [82] measurements, and electron microscopy [80, 83, 84].

Premartensitic transformation has been observed in $\text{Ni}_{2+x+y}\text{Mn}_{1-x}\text{Ga}_{1-y}$ alloys with relatively small deviations from stoichiometry and martensitic transformation temperature (T_m) lower than 270K [85]. The premartensitic transformation of Ni-Mn-Ga alloys was confirmed to be a weakly first order transformation [72] and it occurs in the stoichiometric Ni_2MnGa ($T_m \sim 220\text{K}$) at around 260K [74]. Khovailo *et al.* [77] found from the anomalies in the temperature dependence of electrical resistivity that the premartensitic transformation

temperature of $\text{Ni}_{2+x}\text{Mn}_{1-x}\text{Ga}$ alloys is only weakly dependent on the substitution of Mn for Ni. By means of neutron diffraction experiments, Brown *et al.* [39] reported that the premartensitic phase in Ni_2MnGa has an orthorhombic (with space group of $Pnmm$, No.58) three-layered structure. In this structure, the modulation mechanism is similar to the cases of 5M and 7M martensites [39].

It should be noted that the premartensitic transformation only occurs in Ni-Mn-Ga alloys with relatively low T_m . Zheludev *et al.* [74] suggested that the premartensitic transformation emerges because of nesting singularities in the Fermi surface. Since the premartensitic transformation temperature is weakly dependent on deviations from stoichiometry and such a transformation is observed only in $\text{Ni}_{2+x+y}\text{Mn}_{1-x}\text{Ga}_{1-y}$ alloys with $T_m < 270\text{K}$ [80], variations in valence electron concentration probably only have a slight effect on the nesting section of the Fermi surface [85]. In the alloys with $T_m > 270\text{K}$, martensitic transformations, accompanied by a radical transformation of the Fermi surface, occur even before the nesting singularities in the parent phase have time to manifest themselves and thus no premartensitic transformation is observed in these alloys [85].

Landau models for the premartensitic transformation have been proposed [73] and successfully explain that (i) the electron-phonon coupling results in a first order premartensitic transformation from the parent phase to a micromodulated intermediate phase in Ni-Mn-Ga alloys and (ii) the magnetoelastic coupling enables the existence of a commensurate premartensitic phase prior to martensitic transformations. The in-depth investigation to understand the intrinsic nature of premartensitic transformation in Ni-Mn-Ga alloys is still needed.

2.2.4 Martensitic transformation

The martensitic transformation is a diffusionless, displacive solid state phase transformation of the first order type, in which the atoms shift within a short range in an organized manner relative to their neighbors [1, 85]. It occurs in a certain temperature region usually showing hysteresis between the forward and reverse transformations. The chemical composition of the alloys does not change after transformation and there usually exists a clear correspondence between the crystal structures of the parent austenitic phase and the product

martensitic phase [32]. The kinetics and morphology are dictated by the strain energy arising from shear displacements. The characteristic transformation temperatures are defined by the martensitic transformation start temperature M_s , the martensitic transformation finish temperature M_f , the austenitic transformation start temperature A_s and the austenitic transformation finish temperature A_f .

As mentioned earlier in Section 2.1, the martensitic transformation in Ni-Mn-Ga alloys may result in three different types of martensites, i.e. 5M, 7M and NM martensites. The NM martensite, if emerging as a first martensite, usually occurs in the alloys with a higher M_s , while the 7M martensite occurs only in the alloys with an M_s within a narrow temperature region (Fig. 1-1 (b)). In contrast, the 5M martensite usually occurs in the alloys with a lower M_s . The M_s of the example alloys showing different martensitic structures is also given in Section 2.1.

The martensitic transformation temperatures in Ni-Mn-Ga alloys are highly dependent on the chemical composition of the alloys [86-89]. It is generally recognized that the martensitic transformation temperatures in Ni-Mn-Ga alloys increase with the increasing of the average number of valence electrons per atom (also called electron concentration) e/a , which is defined as follows:

$$e/a = \frac{10Ni_{at\%} + 7Mn_{at\%} + 3Ga_{at\%}}{Ni_{at\%} + Mn_{at\%} + Ga_{at\%}} \quad (1-1)$$

where $X_{at\%}$ ($X=Ni, Mn, Ga$) denotes the atomic percentage of X . In the equation, the value of 10 is applied for Ni, in which the outer electron shells are occupied as $3d^84s^2$, while for Mn the value becomes 7 from $3d^54s^2$ and for Ga 3 from $4s^24p^1$ [86].

Chernenko *et al.* [87] investigated the composition dependence of martensitic transformation temperatures of Ni-Mn-Ga alloys and concluded that (i) at a constant Mn content, Ga addition lowers M_s , (ii) Mn addition (instead of Ga) at a constant Ni content increases M_s , and (iii) substitution of Ni by Mn at a constant Ga content lowers M_s . Wu *et al.* [88] further quantified the relation between M_s and chemical composition, and derived the following equation:

$$M_s (K) = 25.44Ni_{at\%} - 4.86Mn_{at\%} - 38.83Ga_{at\%} \quad (1-2)$$

which can be used to empirically determine the M_s of the alloys from their chemical composition. The empirical relation between the martensitic transformation temperature T_m and e/a was established by Jin *et al.* [89] as follows:

$$T_m(\text{K}) = 702.5(e/a) - 5067 \quad (1-3)$$

It should be noted that T_m can be generally defined as $(M_s + M_f + A_s + A_f)/4$ [32], but the definition of the T_m in Eq. (1-3) is not given in Ref. [89]. The investigations on the composition dependence of martensitic transformation temperatures can serve as the guides for the development of high-temperature Ni-Mn-Ga FSMAs for practical applications by composition design.

In addition to chemical composition, the atomic order of the parent phase also has a great influence on the martensitic transformation temperatures. Kreissl *et al.* [90] found that the disorder existing between Mn and Ga atoms in Ni_2MnGa alloy substantially suppresses the martensitic transformation by about 100K. Tsuchiya *et al.* [91] and Besseghini *et al.* [92] confirmed that with the ordered $L2_1$ structure obtained from the correct annealing procedure the martensitic transformation temperature region is narrower. Thus, proper thermal treatments are necessary for obtaining high-performance FSMAs with good stability.

2.2.5 Intermartensitic transformation

Aside from premartensitic and martensitic transformations, first order intermartensitic transformation from one martensite to another may occur in certain Ni-Mn-Ga alloys [93-105], due to the different stability of the three types of martensites as shown in Fig. 1-1 (a). A typical transformation path is 5M-7M-NM or 7M-NM, depending on the chemical composition and thermal history of the alloys. As well as being an interesting issue from a fundamental point of view, the occurrence of intermartensitic transformation has a certain influence on the applicability of the FSMAs. In this regard, it means that the working range of the utilization of FSMAs could be restricted to a temperature range where intermartensitic transformation are not observed, i.e. the intermartensitic transformation may set the lower limit for the service temperature of the magnetic shape memory effect [93].

The intermartensitic transformation is usually accompanied by anomalies in the

calorimetric [63, 94, 95], mechanical [95-97], magnetic [95, 98-104] and electrical resistivity [95, 99-103] measurements, both on cooling and heating. Fig. 1-3 displays the typical temperature dependence of low field ac susceptibility in a Ni-Mn-Ga alloy showing Heusler-7M martensitic and 7M-NM intermartensitic transformations. The abrupt change in the value of the susceptibility at $\sim 355\text{K}$ is attributed to the paramagnetic-ferromagnetic transformation of the Heusler parent phase, while the abrupt change during cooling at $\sim 275\text{K}$ indicates the start of the martensitic transformation from Heusler phase to 7M martensite. Upon further cooling to $\sim 100\text{K}$, another abrupt change of the susceptibility occurs, indicating the start of the 7M-NM intermartensitic transformation. During heating both structural phase transformations occur in reverse order and show some temperature hysteresis. The intermartensitic transformation in Ni-Mn-Ga alloys was also confirmed by transmission electron microscopy (TEM) observations [63, 95, 105].

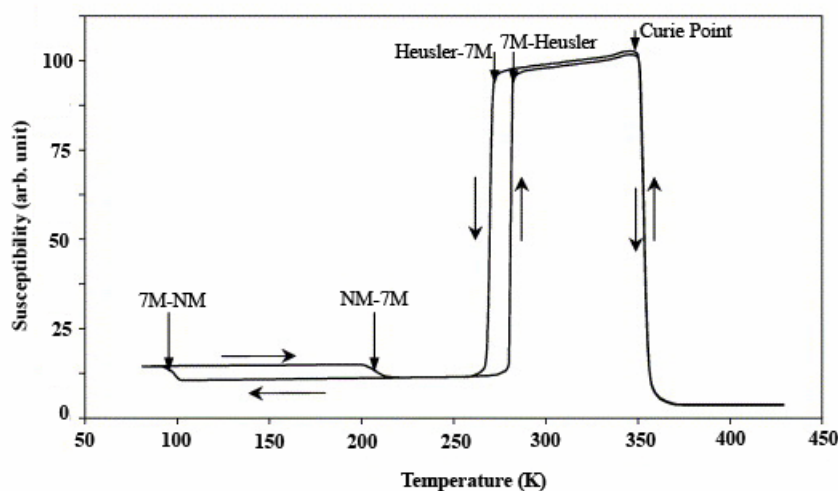


Fig. 1-3 Temperature dependence of low field ac magnetic susceptibility measured during cooling and heating in a Ni-Mn-Ga alloy showing Heusler-7M martensitic and 7M-NM intermartensitic transformations.

It is suggested that the intermartensitic transformation in Ni-Mn-Ga alloys is very sensitive to the internal stress in the samples [98]. According to Wang *et al.* [98], an average internal stress of about 14MPa stored in the distorted lattice may change the transformation sequence and entirely suppress the intermartensitic transformation in $\text{Ni}_{52}\text{Mn}_{24}\text{Ga}_{24}$ single crystals. Chernenko *et al.* [80] also confirmed that the intermartensitic transformation is indeed strongly influenced by the non-chemical terms of the free energy balance (mainly the

elastic energy term), which can be even more important than the martensitic lattice instabilities. This interpretation is supported by the results obtained in rapidly solidified polycrystalline, fine grained alloys which do not show any intermartensitic transformation [64], as these alloys involve much higher accommodation stresses than single crystals during the transformation, due to the large amount of grain boundaries [80].

In spite of extensive studies on the phase transformation behaviors in Ni-Mn-Ga alloys, the in situ observations on the phase transformation behavior are still lacking. Moreover, the intrinsic nature of the phase transformations, especially martensitic and intermartensitic transformations, is still not well understood. In situ neutron diffraction investigations on phase transformation, which directly reveal the detailed crystal structure of the alloys at different temperatures, will enrich the martensitic transformation theory and further be helpful to the design of new FSMA with optimal performances.

2.3 Magnetic properties of Ni-Mn-Ga alloys

2.3.1 Curie temperature

The Curie temperature (T_C), or Curie point, is defined as the temperature at which a ferromagnetic material becomes paramagnetic by losing the long-range magnetic order. This magnetic transition is one of the main limits when considering the service temperatures of the magnetic shape memory effect. The T_C can be clearly observed from the magnetic susceptibility measurement as the susceptibility changes abruptly in the ferromagnetic to paramagnetic transition, as shown in Fig. 1-3. The T_C of the stoichiometric Ni_2MnGa was reported to be 376K [10, 22]. In contrast to the martensitic transformation temperatures, the T_C of Ni-Mn-Ga alloys is less sensitive to the chemical composition [87], having a value of around 370K for a wide range of compositions [67, 87]. Interestingly, it is possible to develop alloys with a magnetostructural transformation, i. e. $T_C=T_m$, by composition adjustment [51, 52, 106], in which some specific effects may occur due to the magnetoelastic coupling.

2.3.2 Magnetic moment

The magnetic moment in Ni-Mn-Ga alloys is mainly localized on the Mn sites, as

confirmed by both experiments [22, 107, 108] and theoretical calculations [109]. From magnetization measurements, Webster *et al.* [22] reported that the total magnetic moment of the cubic Heusler phase of Ni₂MnGa is 4.17 μ_B per formula unit, and it is primarily carried by Mn atoms while Ni atoms only carry a small magnetic moment. On the other hand, from polarized neutron scattering and magnetization studies, Brown *et al.* [107] reported 0.36 μ_B for Ni, 2.80 μ_B for Mn and -0.06 μ_B for Ga at 100K in the martensitic phase of Ni₂MnGa. By means of *ab initio* calculations, Ayuela *et al.* [109] reported that the magnetic moments for Ni, Mn and Ga are 0.36 μ_B , 3.43 μ_B and -0.04 μ_B , respectively, in the parent Heusler phase and 0.40 μ_B , 3.43 μ_B and -0.04 μ_B in the martensite of Ni₂MnGa. For the off-stoichiometric Ni-Mn-Ga alloys, the localization of the magnetic moments on the constituent atoms becomes more complex, due to the substitutive occupation of the extra atoms. Quite recently, Ahuja *et al.* [108] investigated in great detail the magnetic moments of off-stoichiometric Ni-Mn-Ga alloys by using magnetic Compton scattering technique. It was found that the total magnetic moment of Ni-rich Ni_{2.25}Mn_{0.75}Ga (3.38 μ_B) is much smaller than that of the stoichiometric Ni₂MnGa (4.13 μ_B in their study), which is thought to be attributed to the substitution of Ni with a small moment (0.25 μ_B) for Mn with a large moment (3.26 μ_B) [108].

2.3.3 Magnetization

In Ni-Mn-Ga FSMAs, the magnetization in weak fields shows a sharp decline at the martensitic transformation temperatures [22], indicating the transformation from parent phase to martensite. In contrast, the measurements in strong fields have shown that the saturation magnetization in the martensitic phase is higher than that in the parent phase. The saturation magnetization of Ni-Mn-Ga alloys depends on chemical composition and temperature. Heczko *et al.* [110] reported that the saturation magnetization has a maximum value in the stoichiometric Ni₂MnGa and decreases in both the Mn-rich off-stoichiometric alloys due to the local antiferromagnetic ordering of excess Mn atoms [111] and the Mn-deficient off-stoichiometric alloys due to the reduced number of Mn atoms. Khovailo *et al.* [51] and Aliev *et al.* [112] found that the saturation magnetization of Ni-Mn-Ga alloys decreases as temperature increases. Pakhomov *et al.* [113] showed that the saturation magnetization of the parent phase of Ni₅₂Mn_{24.4}Ga_{23.6} at 290K is ~50emu/g and that of the martensitic phase at

160K is ~ 75 emu/g. Interestingly, the difference in magnetizations of parent phase and martensite gives rise to a large change in entropy during the transformation process and offers Ni-Mn-Ga alloys another unique feature, i.e. the so-called *giant magnetocaloric effect*: heating of the sample by adiabatic magnetization and cooling by adiabatic demagnetization, or vice versa [106, 112-114].

The easy axis of magnetization of the parent phase in Ni-Mn-Ga alloys is reported to be $\langle 100 \rangle_C$ axis [115]. According to Heczko *et al.* [116], the easy axis of magnetization of the 5M martensite is the short crystallographic c_C axis, i.e. $[001]_C$, while the hard axis of magnetization is the long crystallographic a_C axis, i.e. $[100]_C$ or $[010]_C$. In 7M martensite, the easy axis of magnetization is the shortest c_C axis (i.e. $[001]_C$) while the longest a_C axis (i.e. $[100]_C$) is the hard axis and the b_C axis (i.e. $[010]_C$) is the mid-hard axis [117]. On the other hand, the NM martensite has an easy plane of magnetization, i.e. $(001)_C$ plane and a hard axis of magnetization, i.e. c_C axis ($[001]_C$) [117].

2.3.4 Magnetic anisotropy

Magnetic anisotropy can be considered as the determining parameter for the achievement of giant magnetic-field-induced strain in FSMAs and it is also a key property to understand the magnetic shape memory effect in Ni-Mn-Ga martensites. The magnetic anisotropy energy is defined as the work required to rotate the magnetization from the easy axis to the hard axis with an applied magnetic field. The magnetic anisotropy energy density of an orthorhombic crystal is expressed with directional cosines α_i of the magnetization along the crystal coordinate axes as

$$E = K_1 \alpha_1^2 + K_2 \alpha_2^2 + K_3 \alpha_3^2 + K_4 \alpha_1^2 \alpha_2^2 + K_5 \alpha_2^4 \quad (1-4)$$

and for a tetragonal crystal in polar coordinates θ, φ with \mathbf{z} axis parallel to $[001]_C$ as

$$E = K_1 \sin^2 \theta + K_2 \sin^4 \theta + K_3 \sin^4 \theta \cos 4\varphi \quad (1-5)$$

where K_i are the magnetic anisotropy constants [117]. For the uniaxial anisotropy, if K_1 in Eq. (1-5) is positive, the crystal has an easy axis of magnetization along the c_C axis, which is the case for 5M martensite. If K_1 in Eq. (1-5) is negative and $K_1 < -2 K_2$, the crystal has an easy

plane of magnetization, in which the ac_b -plane is the easy plane and the c_c axis is the hard axis, which is the case for NM martensite. The magnetic anisotropy constant can be obtained by measuring the magnetization curves for different directions of the magnetic field with respect to the crystallographic axes of the sample. For 7M martensite, experimental results show that K_1 and K_2 are the predominant terms in Eq. (1-4), and two axes $[100]_C$ and $[010]_C$ can be described as hard and mid-hard axes [117].

The magnetic anisotropy constant of the parent austenite phase is relatively moderate, of the order 10^3 J/m^3 . After the transformation to martensite, the anisotropy constant increases two orders of magnitude [115]. The anisotropy constants for different types of martensites differ significantly. According to Straka *et al.* [117], the magnetic anisotropy constants at room temperature for $\text{Ni}_{49.7}\text{Mn}_{29.1}\text{Ga}_{21.2}$ 5M martensite are $K_1=1.65\times 10^5 \text{ J/m}^3$ (K_2 negligible), for $\text{Ni}_{50.5}\text{Mn}_{29.4}\text{Ga}_{20.1}$ 7M martensite are $K_1=1.7\times 10^5 \text{ J/m}^3$ and $K_2=0.9\times 10^5 \text{ J/m}^3$ referring to the hard and mid-hard axes, and for $\text{Ni}_{50.5}\text{Mn}_{30.4}\text{Ga}_{19.1}$ NM martensite are $K_1=-2.3\times 10^5 \text{ J/m}^3$ and $K_2=0.55\times 10^5 \text{ J/m}^3$. It should be noted that the magnetic anisotropy constant varies as a function of temperature. The anisotropy constant K_1 for $\text{Ni}_{48.8}\text{Mn}_{28.6}\text{Ga}_{22.6}$ 5M martensite increases from $2.0\times 10^5 \text{ J/m}^3$ at 283K to $2.65\times 10^5 \text{ J/m}^3$ at 130K [116]. In addition to the temperature dependence, the magnetic anisotropy constant is composition dependent [118].

2.3.5 Magnetic domain structure

The magnetic domain structure of martensite is of significance to the understanding of the mechanism of magnetic shape memory effect and it is also a prerequisite for modeling the magneto-mechanical behavior in Ni-Mn-Ga alloys [119]. The first observation of magnetic domain structure was made by magnetic force microscopy [11], which reveals a hierarchical domain structure with a herring-bone pattern. Similar patterns were also observed by Lorentz microscopy, but with a different domain width [120]. The evolution of this kind of pattern under applied magnetic fields is studied by Pan *et al.* [121]. It was found that the application of a weak field evolves this pattern to a fir-tree pattern meeting at the twin boundaries and the application of a mediate field causes the magnetization vector of the neighboring twin variants to rotate a little, while the application of a strong field rotates the magnetization vector to the field direction and eliminates the domain structure within one variant [121].

In a surface with a magnetization vector out of plane a labyrinth pattern [122] or a patch-like pattern [121] can be observed. In addition, a fine ripple domain pattern superimposed with twin variants under a weak field was observed by means of Interference-Contrast-Colloid technique [123]. The magnetic domain structure in thin foil samples has also been widely studied. Park *et al.* [124] studied the evolution of magnetic domain structure with temperature by Lorentz microscopy. In the parent phase, large plate-like domains exceeding $1\mu\text{m}$ at the edge and distinctive stripe domains in the inside area were reported. The stripe domains develop further upon cooling, and bend into a maze domain pattern before martensitic transformation. On further cooling the stripe domains disappear with the formation of martensite and finer magnetic domains within the twin variants emerge [124].

Ge *et al.* [119, 125-127] further studied the magnetic domain structure and its evolution under magnetic fields in great detail by means of optical microscopy and Type I and Type II magnetic contrasts in scanning electron microscope (SEM). It was reported that in 5M martensite the magnetization vectors are parallel and anti-parallel to the c_C axis separated by a 180° domain wall within one variant and the magnetization vectors continue to follow the c_C axis in the adjacent variant when crossing a twin boundary [125]. Their direct observation of the magnetic domains by optical microscopy indicates a large magnetic domain associated surface relief, which is believed to arise from different straining of the surface and the bulk material [126]. In addition, the investigation on the evolution of magnetic domain patterns, by alternately applying magnetic fields in two perpendicular directions for several times, shows that each time the magnetic domain and martensitic twin nucleation take a unique path determined by the local imperfections [127].

Despite a large amount of investigations on the magnetic properties of Ni-Mn-Ga alloys, there are still many fundamental aspects remaining unclear. For instance, the influence of heat treatments on the magnetic properties has not been widely reported. The magnetoelastic coupling and magnetocaloric effect have not been well understood. Furthermore, the correlation between the magnetic domain structure and magnetic shape memory effect still remains mysterious. Research into these issues will help to reveal the underlying mechanism

of the thermo-magneto-mechanical behavior of the FSMAs.

2.4 Magnetic shape memory effect in Ni-Mn-Ga alloys

2.4.1 Prerequisite

The magnetic shape memory effect (MSME) in Ni-Mn-Ga alloys, which manifest itself in terms of magnetic-field-induced strain (MFIS), originates from the rearrangement of the martensitic variants under applied magnetic fields. The prerequisite for the MSME in Ni-Mn-Ga alloys is listed as follows:

(i) The alloys must have the ferromagnetic twinned martensitic microstructure in the working temperature range. This means that the MSME is possible only at temperatures below the Curie temperature T_C and below the reverse transformation start temperature A_s .

(ii) The magnetic-field-induced stress must exceed the twinning stress of these alloys. In this context, the twinning stress σ_{tw} is the stress needed for the rearrangement of the twin variants. It can be determined from the stress-strain curve of single crystals. Since the magnetic-field-induced stress σ_{mag} cannot exceed the saturation value given by the ratio of the magnetic anisotropy (K_U) and the theoretical maximum MFIS (ε_0), i.e. $\frac{K_U}{\varepsilon_0}$ [32, 128],

where the value for the strain ε_0 can also be evaluated from the stress-strain curve of single crystals with a single variant as the maximum strain of the detwinning, the above-mentioned prerequisite can be formulated as

$$\sigma_{mag} = \frac{K_U}{\varepsilon_0} > \sigma_{tw} \quad (1-6)$$

It is worth noting that both σ_{mag} and σ_{tw} strongly depend on the type of martensite. It was reported that the twinning stress σ_{tw} in compression varies from less than 2 MPa for the 5M and 7M martensites to 18-20 MPa for the NM martensite [32].

2.4.2 Mechanism

In Ni-Mn-Ga FSMAs, the formation of twin boundaries accommodates the stress

generated by the diffusionless martensitic transformation from the high-temperature, high-symmetry austenite to the low-temperature, low-symmetry martensite. The magnetic moment in martensite is aligned to the easy axis of magnetization by the high magnetic anisotropy and the preferred direction of magnetization changes across the twin boundary, as illustrated in Fig. 1-4. When a magnetic field is applied parallel to the easy axis of magnetization of one of the variants, the energy of the variant with the easy axis parallel to the field will be different from that of others. This energy difference exerts a stress σ_{mag} on the twin boundary and provides the driving force for the twin boundary motion. If this magnetic-field-induced stress σ_{mag} is larger than the twinning stress σ_{tw} needed for the rearrangement of the twin variants, the twin boundary will move and the variant with easy axis of magnetization parallel to the field direction will grow at the expense of the other variants, leading to the macroscopic shape change of the sample, namely MFIS. Ideally, with the magnetic field increasing to a certain critical value, all martensitic variants align themselves along the magnetic field direction and the MFIS reaches its maximum value. The schematic illustration of the rearrangement of martensitic variants under a magnetic field is shown in Fig. 1-4. In fact, the rearrangement of the martensitic variants under an applied magnetic field has already been directly observed by optical observations [123]. It should be noted that the macroscopic shape change remains even after the magnetic field is removed. Thus, alternating magnetic field direction or simultaneous application of external stress and magnetic fields is needed to obtain reversible MFIS in such FSMAs [32, 85].

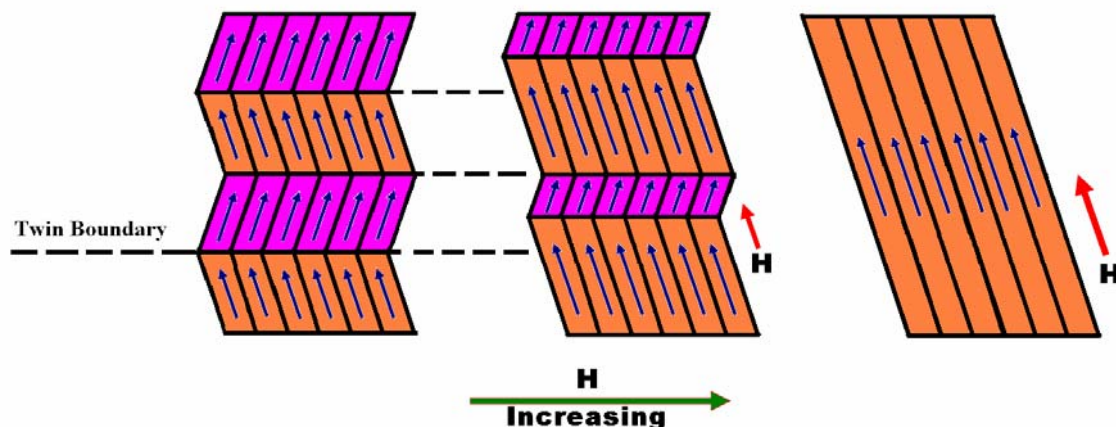


Fig. 1-4 Schematic illustration of the rearrangement of martensitic variants under a magnetic field in ferromagnetic shape memory alloys (FSMAs).

2.4.3 Theoretical and observed values of MFIS

The theoretical maximum MFIS in Ni-Mn-Ga FSMA corresponds to the macroscopic shape change during the reorientation from one single variant to another whose easy axis of magnetization is orthogonal to the easy axis of the initial variant. Thus, it can be given as a function of lattice parameters as follows:

$$\varepsilon_0 = \left| \frac{a_C - c_C}{a_C} \right| = \left| 1 - \frac{c_C}{a_C} \right| \quad (1-7)$$

where a_C and c_C are the lattice parameters of the martensite expressed with respect to the cubic coordinate system of the parent phase. In the modulated structures, the theoretical maximum strains for 5M and 7M martensites are ~6% and ~10%, respectively, while the theoretical maximum MFIS for NM martensite is as large as 20%. As the lattice parameters in Eq. (1-7) vary with temperature and chemical composition of Ni-Mn-Ga alloys, the maximum MFIS is also temperature dependent and composition dependent.

Table 1-1 Observed strain (ε_{obs}), together with magnetic-field-induced stress (σ_{mag}), twinning stress (σ_{tw}) and theoretical maximum strain (ε_0), in Ni-Mn-Ga alloys.

Alloy (type of martensite)	ε_{obs} (%)	σ_{mag} (MPa)	σ_{tw} (MPa)	ε_0 (%)	Reference
Ni _{50.7} Mn _{28.4} Ga _{20.9} (5M)	>6	2.8	1-4	6.2	[41]
Ni ₄₈ Mn ₃₀ Ga ₂₂ (5M)	5	2.25	2.12	5.8	[129]
Ni _{49.2} Mn _{29.6} Ga _{21.2} (5M)	4.78	2.14	2	5.7	[42]
	5.8	2.1	1	5.8	[43]
Ni _{50.5} Mn _{29.4} Ga _{20.1} (7M)	0.47	1.6	3-5	10.7	[41]
	9.4	1.9	1.1	10.66	[43]
Ni _{48.8} Mn _{29.7} Ga _{21.5} (7M)	9.5	1.5	<1.5	10.66	[5, 130]
	~9.2	1.5	1.2	10.6	[131]
Ni _{52.1} Mn _{27.3} Ga _{20.6} (NM)	<0.02	1.1	15	20.5	[42, 43]
Ni _{50.5} Mn _{30.4} Ga _{19.1} (NM)	0	0.7	17-25	21.0	[41]
Ni _{47.0} Mn _{33.1} Ga _{19.9} (NM)	<0.02	~1	>6	19.3	[132]

So far, the theoretical maximum strains of ~6% and ~10% in 5M and 7M martensites have already been experimentally achieved in single crystals with a single variant by Murray *et al.* [38] and Sozinov *et al.* [5], respectively. However, only negligible MFIS has been observed in NM martensite [42, 43], regardless of the large theoretical maximum MFIS in this

type of martensite. This is thought to be due to the fact that the magnetic-field-induced stress in the employed alloys is much lower than the twinning stress [42, 43]. The experimental data on the observed MFIS (ε_{obs}) in different types of martensites, together with the magnetic-field-induced stress (σ_{mag}), the twinning stress (σ_{tw}) and the theoretical maximum MFIS (ε_0) is summarized in Table 1-1.

Although large MFIS has not been observed in NM martensite up to now, the NM martensite has many advantages: (i) the theoretical maximum MFIS of the NM martensite is as large as 20%, so it has the great potential to exhibit very large MFIS; (ii) the NM martensite is the most stable one among the three types of martensites [42, 47-49]; (iii) the NM martensite can exist in a wide temperature range, both at high temperatures above Curie temperature as a first martensite transformed directly from parent phase and at very low temperatures as an intermartensitic transformation product [32]; (iv) the NM martensite possesses the best chemical properties, such as corrosion resistance, among the three types of martensites [45, 46]; (v) the ductility of the NM martensite is better compared with that of the 5M and 7M martensites. Therefore, how to achieve large MFIS in the NM martensite will undoubtedly be a hot topic in the future. In order to obtain large MFIS, the magnetic anisotropy and consequently the magnetic-field-induced stress should be increased, and/or the twinning stress should be decreased. Two possible ways to achieve these goals are (i) training the alloys by proper heat treatments, mechanical loading, or magnetization process and (ii) modifying the properties of the alloys by alloying with a fourth element. In addition to be FSMA, the NM martensite with high martensitic transformation temperatures can also be used as promising high-temperature shape memory alloys activated by a thermal field, because of its low cost and good thermal stability [26, 133, 134]. Hence, investigations on various properties of the NM martensite are quite necessary.

Furthermore, large MFIS is only observed in single crystals with a single variant. The observed MFIS in polycrystalline Ni-Mn-Ga samples is very small [135, 136]. However, from the application point of view, the polycrystals are more promising because of their easy fabrication process and low cost. Thus, the improvement of MFIS in Ni-Mn-Ga polycrystals

by exploring novel fabrication processes and proper heat treatments is of great significance to the practical application of these FSMAs.

2.5 Microstructure of Ni-Mn-Ga alloys

As is well known, the performances of the FSMAs, especially the MSME and mechanical behaviors, are strongly dependent on the microstructure of these alloys, so it is very important to have a good understanding of the detailed microstructural characteristics of these FSMAs. Nevertheless, there are only scattered investigations on the microstructure of Ni-Mn-Ga alloys up to now.

The microstructure of the martensitic phase is formed as a result of a temperature-induced martensitic transformation and consists of an aggregate of elastically self-accommodated martensitic variants [137] which account for the minimization of strain energy during martensitic transformation. The microstructure of the as-cast Ni-Mn-Ga alloys with different chemical compositions was studied with optical microscopy by Singh *et al.* [138]. It was found that the martensite in the as-cast alloys with relatively higher Mn content show dendritic morphology while that in the alloys with low Mn concentration shows equiaxed grains at room temperature. After annealing at 1273K for 3h, the lamellar twin structure becomes apparent in all the studied alloys [138]. The martensitic microstructure of the bulk Ni₂MnGa samples was also preliminary investigated by means of electron backscattered diffraction (EBSD) analysis and the twin band configuration was constructed from the orientation information of the martensitic variants [139].

The microstructure of melt-spun Ni-Mn-Ga ribbons was investigated with SEM by Rao *et al.* [140]. It was demonstrated that the microstructure of Ni₅₅Mn_{20.6}Ga_{24.4} (with a martensitic structure) and Ni₅₅Mn_{19.6}Ga_{25.4} (with an austenitic structure) ribbons consists of a well-developed cellular structure with the average grain size of ~2μm, much finer than that (~100μm) of the as-cast alloys. No martensitic twins were observed in Ni₅₅Mn_{20.6}Ga_{24.4} ribbon, although the X-ray diffraction (XRD) shows that it has a martensitic structure at room temperature. With the decrease of Ni concentration, the microstructure of the ribbons gradually changes from cellular to dendritic structure with the average grain size of ~20μm. The microstructure of Ni₅₃Mn_{20.4}Ga_{26.6} ribbon (with an austenitic structure) consists of

cellular as well as columnar grains, while that of $\text{Ni}_{49.5}\text{Mn}_{24.3}\text{Ga}_{26.2}$ ribbon (with an austenitic structure) are purely composed of dendritic grains [140]. The mechanism of the influence of composition on the microstructure of Ni-Mn-Ga ribbons is still not clear.

Solomon *et al.* [141] studied the microstructure of spark-eroded Ni-Mn-Ga alloy particles. They found that the spark-eroded Ni-Mn-Ga particles are predominantly micrometer-sized particles; those obtained in liquid argon are solid whereas those obtained in liquid nitrogen are primarily hollow. SEM and TEM investigations revealed the 5M twinned microstructure of annealed particles. The microstructure of the annealed Ni-Mn-Ga spark-eroded particles is found to be similar to that of single crystalline Ni-Mn-Ga with identical chemical composition [141].

The evolution of twin microstructure with increasing magnetic field in a Ni-Mn-Ga single crystal was investigated by James *et al.* [11, 142]. The volume fraction of one variant increases at the expense of that of the other as the magnetic field increases [11, 142], which confirms the mechanism that accounts for the MSME, namely the rearrangement of martensitic variants under external magnetic fields. Glavatska *et al.* [143] studied the time evolution of two martensitic variants in a single crystal under a static field of 0.3T, which is substantially smaller than the saturation field, during the time period of 0.37h and 17.37h. It was found that, as time prolongs, one variant slowly spreads through the experimental sample and its volume fraction increases at the expense of that of the other variant, due to the influence of the static magnetic field [143].

Kishi *et al.* [144] investigated the microstructural change associated with the martensitic transformation in a Pt-doped Ni-Mn-Ga bulk alloy during the cooling process by using polarized optical microscopy. Bennett *et al.* [145] performed the in situ TEM studies of the directionally solidified Ni-Mn-Ga alloys. It was found that in $\text{Ni}_{50.1}\text{Mn}_{28.2}\text{Ga}_{21.7}$ alloy the Heusler austenite phase exhibits characteristic “tweed” strain contrast at room temperature. On cooling, sharp satellite reflections associated with the formation of an intermediate phase appear at $\sim 200\text{K}$, prior to a martensitic transformation at $\sim 190\text{K}$ which generates a microstructure consisting of predominately 7M fine martensitic twins. In contrast, the microstructure of $\text{Ni}_{49.3}\text{Mn}_{28.8}\text{Ga}_{21.9}$ alloy consists of a fine scale intermixture of austenite with characteristic “tweed” contrast and martensite with fine microtwins at room temperature.

The regions of austenite transform to 5M martensite at $\sim 270\text{K}$ [145].

The effect of aging on microstructure of the parent austenite phase in a Fe-doped Ni-Mn-Ga alloy was studied with TEM by Chen *et al.* [146]. Tweed-like contrast was observed and no defects were found in the as-quenched sample. In contrast, the defects including stacking faults and dislocations are evident in the aged samples. The density of dislocations decreases firstly with increasing the aging temperature from 573K to 773K, and then increase when aging temperature is 873K [146]. The influence of pre-deformation on the martensitic microstructure of $\text{Ni}_{55}\text{Mn}_{20}\text{Ga}_{25}$ alloy was investigated by Gao *et al.* [147]. TEM observations showed a well-accommodated martensitic structure with straight and well-defined interfacial boundary in the undeformed sample. After deformation, the reorientation of martensitic variants occurs and the interfacial boundary changes from a sharp and straight morphology to a curved and irregular one. Meanwhile, some lattice defects are formed inside the variants even in slightly deformed samples, and with increasing deformation more lattice defects are generated inside the variants as well as at the interfacial boundaries between variants [147]. Pötschke *et al.* [148] studied the influence of different mold temperatures on the as-cast microstructure of $\text{Ni}_{48}\text{Mn}_{30}\text{Ga}_{22}$ by optical microscopy. It was found that the microstructure of the as-cast samples can be divided into four zones and the length of the zone of columnar grains depends on the casting parameters, especially the mold temperature. From the optical observations, it is evident that the area of elongated grains gets larger with increasing mold temperature [148].

In spite of the investigations reviewed above, the detailed information on the fine martensitic microstructure is still lacking. As a matter of fact, full information on microstructure, including variant selection, twin boundary characteristics, relative amounts of different twin variants and the thickness distribution of the martensitic twins is of vital importance to the microstructure control which will facilitate the improvement of the functional performances of the FSMAs. Thus, a systematic study on the microstructural characteristics and their correlation with the MSME in Ni-Mn-Ga alloys is greatly needed.

2.6 Crystallography of Ni-Mn-Ga alloys

2.6.1 Crystallographic texture

Compared with single crystals, the polycrystalline Ni-Mn-Ga alloys are more promising for practical applications because they are economic and easy to produce, but the MFIS in the polycrystalline alloys is relatively small. The improvement of the MSME in polycrystalline Ni-Mn-Ga alloys is very important. It is well known that the MSME in Ni-Mn-Ga alloys is attributed to the rearrangement of the martensitic variants through boundary motion under applied magnetic fields. Thus the MFIS in polycrystalline alloys is strongly dependent on the orientations of both the parent austenite and martensitic variants. The enhancement of preferred grain orientation (crystallographic texture) in the polycrystalline FSMAs undoubtedly benefits the improvement of their MSME. Shu *et al.* [149] and Thamburaja *et al.* [150] studied the influence of texture on the thermally controlled shape memory effect in polycrystalline shape memory alloys, which confirmed that the texture indeed plays an important role in improving the shape memory effect. Therefore it is of vital importance to explore some novel fabrication processes to enhance the crystallographic texture and systematically characterize the texture in the polycrystalline FSMAs. Unfortunately, the investigations on these aspects are very scarce; especially there is no systematic characterization on the texture in Ni-Mn-Ga FSMAs.

The crystallographic texture in polycrystalline Ni-Mn-Ga alloys can be obtained by directional solidification [148, 151], rapid solidification [140], or plastic deformation [152]. Preparation of melt textured $\text{Ni}_{48}\text{Mn}_{30}\text{Ga}_{22}$ alloy with an austenite structure at room temperature by means of directional solidification was reported by Pötschke *et al.* [148]. A texture of $[100]_C$ along the solidification direction, i.e. the direction of heat flow, was determined by EBSD technique [148]. The texture in directionally solidified $\text{Ni}_{50}\text{Mn}_{30}\text{Ga}_{20}$ alloy with a 7M martensitic structure at room temperature was studied by Gaitzsch *et al.* [151]. By using an X-ray diffraction texture device, a $[100]_C$ fiber texture along the solidification direction is detected. Nevertheless, as stated by the authors, the X-ray penetration depth is only some $100\mu\text{m}$ in the method they used, so complete volume information is not obtainable via XRD texture measurements [151]. Rao *et al.* [140] performed an investigation on the melt-spun Ni-Mn-Ga ribbons and they suggested that there exist some preferred orientations

in the ribbons, merely by comparing the XRD patterns. Despite the great brittleness of the bulk polycrystalline Ni-Mn-Ga alloys at room temperature, hot deformation on Ni-Mn-Ga polycrystalline ingots in special metallic cans was successfully conducted by Besseghini *et al.* [152]. However, no texture analysis was performed in their study [152]. In addition to the three techniques mentioned above, deposition has also been used to fabricate textured Ni-Mn-Ga thin films, but the texture in the thin films was only qualitatively studied by analyzing the XRD patterns of the films [153-155].

So far, no systematic investigation has been devoted to the characterization of the textures in Ni-Mn-Ga FSMAs. This is partly due to the difficulty of measuring the textures in the coarse-grained Ni-Mn-Ga alloys by the traditional XRD technique. Owing to the high penetration of neutron beam and the large difference in the neutron scattering factors for Ni, Mn and Ga atoms, neutron diffraction technique can be an ideal tool for characterizing the textures in this alloy system. For the sake of practical applications of the Ni-Mn-Ga FSMAs, the exploration of novel processes to develop textures in polycrystalline alloys, the systematic characterization of the textures by neutron diffraction technique and the investigation on the correlation between textures and MSME in FSMAs have become imperative.

2.6.2 Orientation relationships

Generally, during the solid state phase transformation, the high temperature parent phase transforms into the inherited product phase during cooling, with a specific orientation relationship between the two phases. The specific orientation relationship in Ni-Mn-Ga alloys will provide a great deal of information for a better understanding of the mechanism of martensitic transformation and thus be useful for the enhancement of MSME in these alloys. However, due to the fast and complete martensitic transformation in Ni-Mn-Ga alloys, it is difficult to obtain a mixed microstructure consisting of austenite and martensite, making it not possible to directly determine the orientation relationship between the two phases. Consequently, there is no report on the orientation relationship between the austenite and martensite in Ni-Mn-Ga alloys up to now. The investigation on the orientation relationship between the parent and product phases by using indirect methods is greatly needed.

On the other hand, clarification of the orientation relationship between the martensitic variants is quite helpful to understand the rearrangement of martensitic variants, which accounts for the MSME in the FSMAs. Nevertheless, there are only limited studies on the orientation relationship between the martensitic variants in Ni-Mn-Ga alloys. Han *et al.* [156, 157] investigated the orientation relationship between the martensitic variants in 5M and 7M martensites by TEM. It was found that there exists a twinning relationship between the variants in both 5M and 7M martensites. The twinning plane in the 5M martensite is $\{\bar{1}2\bar{5}\}$ [156], while that in the 7M martensite is $\{\bar{1}2\bar{7}\}$ [157] (it should be noted that these twinning planes are expressed with respect to the martensite coordinate system). The twinning relationship in the NM martensite is also reported and the twinning plane is found to be $\{110\}_C$ expressed in the cubic austenite coordinate system [158]. However, the twinning elements are not fully determined in those investigations [156-158]. Mogylnyy *et al.* [159] successfully determined the twinning mode in a Ni-Mn-Ga single crystal with 5M martensitic structure by X-ray diffraction methods, but one should keep in mind that X-ray diffraction analysis cannot be used for determining twinning relationship in polycrystalline alloys, as it is impossible to distinguish the diffraction data from the neighboring twins.

The information on the twinning relationship and the orientation relationship between austenite and martensite in Ni-Mn-Ga alloys is still lacking, partly because of the limitations of the conventional characterization techniques. Fortunately, recent development of the EBSD technique linked with high-resolution SEM equipped with a field emission gun provides a strong tool for local orientation analysis in polycrystalline materials. Actually, the systematic study on the martensitic transformation crystallography, especially the twinning relationship between martensitic variants and the orientation relationship between austenite and martensite, by using EBSD technique, is of fundamental importance to the development of high-performance FSMAs with optimal properties.

2.7 Mechanical properties of Ni-Mn-Ga alloys

Due to the brittleness of the Ni-Mn-Ga alloys, most of the investigations on mechanical

behaviors are focused on the compressive properties of these alloys. Among these investigations, many of them only studied the stress-strain behavior in the stress region needed for the twin boundary motion [32, 50, 131, 132], while only limited studies were devoted to the compressive properties in the whole stress region [133].

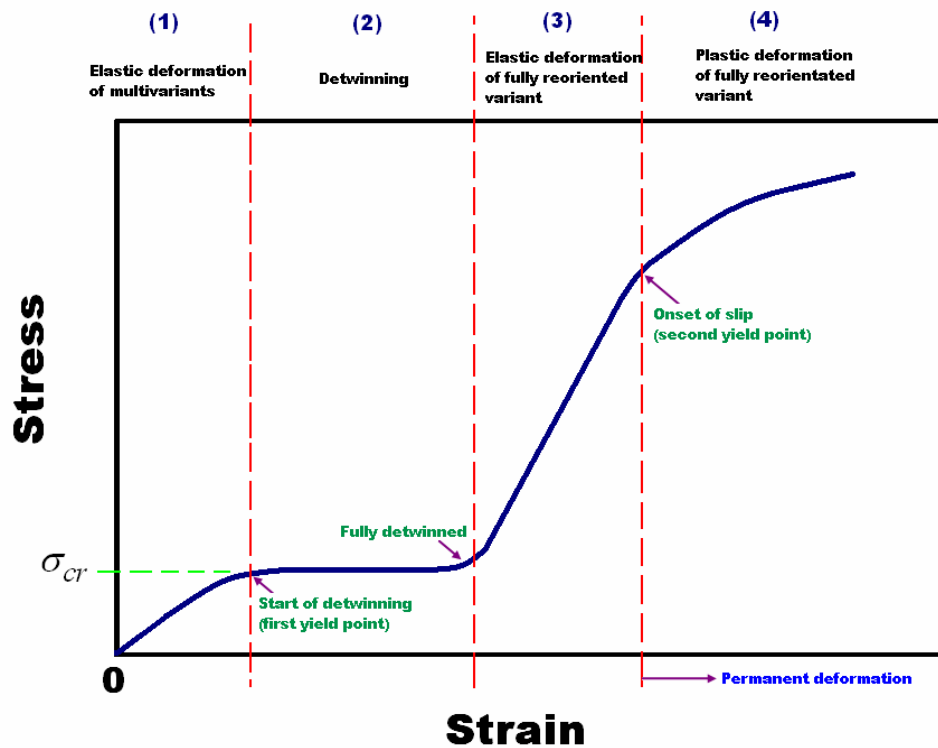


Fig. 1-5 Schematic illustration of the compressive stress-strain curve of Ni-Mn-Ga single crystals.

The schematic illustration of the compressive stress-strain curve of Ni-Mn-Ga single crystals is shown in Fig. 1-5. The Ni-Mn-Ga single crystal with the initial microstructure consisting of self-accommodated multivariants is compressed under an applied uniaxial stress. As the stress increases, there is a region of elastic deformation of the multivariants (region (1)) where the strain increases linearly with stress. At a critical stress level, σ_{cr} , the martensitic twin boundaries become mobile and the reorientation of martensitic variants (i.e. detwinning) starts. As these twin boundaries can be easily moved, the slope of this region (region (2)) is very small and generally there appears a characteristic stress plateau in the stress-strain curve. The material is undergoing an apparent plastic deformation in this region. However, this plastic deformation due to the twin boundary motion can be recovered by applying proper stress and/or magnetic fields, or by heating the sample to the temperature above its martensitic

transformation temperature (i.e by reverse transformation). After the completion of detwinning, the elastic deformation of the fully reoriented variant begins. The slope of the stress-strain curve in this region (region (3)) increases and becomes much larger than that in region (2). Eventually, when a limiting value of strain is reached, slip begins to occur and the material deforms plastically. The plastic strain in this region (region (4)) is permanent and cannot be recovered. Thus, there are two distinct yield points in the stress-strain curve. The first occurs just before twin boundary motion is activated and the second occurs at the onset of slip long after the material has been completely detwinned.

Xu *et al.* [133] investigated the room temperature compressive properties of the $\text{Ni}_{54}\text{Mn}_{25}\text{Ga}_{21}$ single crystal with $M_s \sim 533\text{K}$. The compressive strain is as large as 20.5% and the compressive strength reaches 845MPa. The four regions in the stress-strain curve of single crystals (Fig. 1-5) were clearly observed. A stress plateau at the critical stress level $\sigma_{cr} \sim 100\text{MPa}$ is apparent [133]. After a plastic deformation in the detwinning region with a strain less than 6%, the sample was heated to 673K followed by cooling and the complete recovery of the plastic strain was observed [133].

Different from the stress-strain curve of single crystals in Fig. 1-5, the four regions cannot be separated in the stress-strain curve of polycrystalline alloys. In addition, the compressive strength and strain of polycrystalline alloys are lower than those in single crystals. Tsuchiya *et al.* [160] found that the fracture strain in the polycrystalline $\text{Ni}_{49.6}\text{Mn}_{26.0}\text{Ga}_{24.4}$ alloy with a parent phase at room temperature is only about 2% and the compressive strength is around 200MPa. With the addition of a small amount of Nd, the fracture strain is raised to 6% [160]. Li *et al.* [161] and Xu *et al.* [162] reported that the compressive strain of the polycrystalline $\text{Ni}_{54}\text{Mn}_{25}\text{Ga}_{21}$ button sample with the NM martensite at room temperature is 10%. However, micro-cracks have already occurred when the strain exceeds 4% [161, 162]. Furthermore, the compressive strength of 440MPa [161, 162] is much lower than that in the single crystal with the same composition [133].

In addition to the compressive properties, the bending properties of Ni-Mn-Ga alloys are also studied in the literature. Three-point bending tests on $\text{Ni}_{50}\text{Mn}_{29}\text{Ga}_{21-x}\text{Gd}_x$ ($x=0, 0.5, 2$) polycrystalline alloys were performed at room temperature by Gao *et al.* [163]. The bending

strength of $\text{Ni}_{50}\text{Mn}_{29}\text{Ga}_{21}$ alloy with the parent phase at room temperature is 29MPa, while that of $\text{Ni}_{50}\text{Mn}_{29}\text{Ga}_{20.5}\text{Gd}_{0.5}$ alloy with the 7M martensite at room temperature is 220MPa. In contrast, the bending strength of $\text{Ni}_{50}\text{Mn}_{29}\text{Ga}_{19}\text{Gd}_2$ alloy with the 7M martensite at room temperature is 148MPa [163]. It is clear that the proper addition of Gd is efficient in increasing the bending strength of Ni-Mn-Ga alloys.

In spite of the great efforts that have been devoted to the investigations on the mechanical properties of Ni-Mn-Ga alloys, there are still many issues unresolved. For example, the fracture mechanism of the Ni-Mn-Ga alloys is not yet well understood. Moreover, the influence of fabrication process and heat treatment on the mechanical behavior is not clear. Further in-depth investigations on these aspects are quite necessary for the improvement of the mechanical properties of these alloys.

2.8 Alloying of Ni-Mn-Ga alloys

Although Ni-Mn-Ga FSMA have a lot of merits (as mentioned in Section 1), they also have some problems for practical applications. The Curie temperature of Ni-Mn-Ga alloys is around 370K, which is not high enough for some applications. The twinning stress of the alloys showing NM martensitic structure is too high and consequently large MFIS has not been observed in these alloys heretofore. On the other hand, the martensitic transformation temperatures of the alloys that show 5M and 7M martensitic structures and display large MFIS are generally too low for practical applications. Another problem, perhaps the most important, is the high brittleness of Ni-Mn-Ga alloys [164]. In recent years, great efforts have been devoted to the modification of the properties of these alloys and it is found that alloying can be an effective way to overcome some of these problems.

The effect of substitution of Fe for Ni or Mn on the martensitic transformation temperature, Curie temperature, MFIS and mechanical behaviors has been investigated by several groups [165-171]. Kikuchi *et al.* [165] found that by substituting a small amount of Mn with Fe, the martensitic transformation temperature decreases linearly with Fe content. This is due to the fact that Fe stabilizes the parent austenitic phase and makes transition to the martensitic state more unlikely. The Curie temperature increases with Fe content because

doping with Fe leads to a stronger exchange interaction between the electron spins [165]. After a systematic study on the alloys with Fe additions up to 11.6%, Koho *et al.* [166] found that the martensitic phases formed depend on the e/a ratio in the same way as in ternary Ni-Mn-Ga alloys. Liu *et al.* [167] found that when Fe substitutes Mn, the lattice parameter of the parent phase and the magnetic moment of martensite decrease, due to the smaller magnetic moment and atomic diameter of Fe, compared with Mn. Nevertheless, the reduction of magnetic moment does not impede the occurrence of large MFIS by variant rearrangement; in the $\text{Ni}_{49.9}\text{Mn}_{28.3}\text{Ga}_{20.1}\text{Fe}_{1.7}$ single crystal showing the 5M martensitic structure, Koho *et al.* [166] found a very good MFIS of 5.5%. Moreover, the doping with Fe is reported to enlarge the temperature interval where good MFIS takes place. A maximum strain of 1.15% is obtained at 290K in a $\text{Ni}_{52}\text{Mn}_{16}\text{Fe}_8\text{Ga}_{24}$ alloy and it is still 0.75% at 170K; for the corresponding ternary alloy, the MFIS has already dropped to 0.35% when the temperature lowers to 240K [167]. From the point of view of engineering applications, another positive effect of Fe doping is the improvement of ductility and toughness of the Ni-Mn-Ga alloys [168].

The alloying of Ni-Mn-Ga alloys with other elements has also been studied [103, 144, 160, 163, 171-180]. Tsuchiya *et al.* [160] investigated the addition of 4f rare earth elements (Nd, Sm and Tb), which are known to increase the magnetic anisotropy. It was found that these elements have a very low solubility in the alloys and have a high tendency to precipitate at the grain and subgrain boundaries. The martensitic transformation temperature and Curie temperature follow the same dependency on e/a ratio as the ternary alloys. The magnetization of the martensite in the alloys doped with Sm and Tb is similar to the corresponding ternary Ni-Mn-Ga alloys, while that of the alloys containing Nd has a higher value of magnetization at the high e/a range [160]. Gao *et al.* [163] studied the effect of Gd addition on martensitic transformation temperature and found that the martensitic transformation temperature increases remarkably with increasing Gd content. Glavatskyy *et al.* [172] found that the addition of Si and In drastically reduces the martensitic transformation temperature of Ni-Mn-Ga alloys. Söderberg *et al.* [173] found the same effect for Sn additions, while the influence of Pb, Zn and Bi on martensitic transformation temperature is much more moderate. The substitution of In for Ga and replacing Mn by V or Cu were reported to strongly decrease

the Curie temperature [174, 175]. The additions of Si and Ge were found to strongly decrease the martensitic transformation temperature, while C addition only causes a slight increase of this temperature [176]. The substitution of Ni by Pt was studied by Kishi *et al.* [144] with the purpose to increase the e/a ratio and consequently the martensitic transformation temperature. Indeed, the martensitic transformation temperature is greatly increased due to the increase of the e/a ratio; the $\text{Pt}_{10}\text{Ni}_{40}\text{Mn}_{25}\text{Ga}_{25}$ alloy shows a martensitic transformation temperature of $\sim 350\text{K}$ [144], much higher than that of the stoichiometric Ni_2MnGa . However, concluded from a large amount of investigations, the martensitic transformation temperature does not always depend on the change of e/a ratio, caused by the addition of a fourth element, in the expected way. According to Tsuchiya *et al.* [177], the dependence of the martensitic transformation temperature and Curie temperature on the e/a ratio in the alloys with Al, Cu, Ge or Sn seems to deviate from that in ternary Ni-Mn-Ga alloys.

Although achievements have been made on the modification of the properties of Ni-Mn-Ga alloys by alloying, the MFIS observed in the alloyed quaternary alloys is clearly lower than that in ternary Ni-Mn-Ga alloys. Overcoming the problems of Ni-Mn-Ga alloys without degrading their MSME is of great importance to the development of high-performance FSMAs with large MSME, high martensitic transformation temperature, high Curie temperature, and high ductility.

3. Significance and contents of the present work

During the past decade, extensive investigations have been devoted to various aspects of Ni-Mn-Ga alloys. However, as Ni-Mn-Ga FSMAs are a relatively new class of materials, many fundamental issues are still largely unexplored. The information on the crystal structure of these alloys is still lacking and some controversial results have been obtained arising from the limitations of the characterization techniques. Due to the complexity of transformation pathways and the interaction between the magnetic and structural transformations in these alloys, the intrinsic mechanism that governs the phase transformation in these alloys is still not clear. The microstructural characteristics and crystallographic features during phase transformation in these alloys are rarely investigated and the correlation between the

microstructure and crystallography of the martensitic variants still remains mysterious to the materials scientists. The development of novel fabrication processes for the enhancement of the MSME in polycrystalline FSMA has just started. The systematic characterization of crystallographic texture and the investigation on the correlation between texture and MSME in these alloys is still at the early beginning. These gaps in knowledge act as a great hindrance to the development of promising FSMA with optimal properties. Solving these fundamental issues has become quite imperative.

Based on this background, the present work has been orientated to the investigation on *the fundamental aspects, with emphasis on the microstructure, crystallography and phase transformation, of Ni-Mn-Ga ferromagnetic shape memory alloys*. The main contents of this work can be summarized as follows:

- (1) Precisely determine the crystal structures of the parent phase and different types of martensites in Ni-Mn-Ga alloys by means of high-resolution in situ neutron diffraction technique. Meanwhile, investigate the different phase transformation pathways in Ni-Mn-Ga alloys with different chemical composition.
- (2) Examine in detail the microstructural characteristics of the martensite and study the martensitic transformation crystallography in Ni-Mn-Ga alloys by using EBSD technique. Perform theoretical calculations by using crystallographic phenomenological theory to quantitatively explain the crystallographic features during martensitic transformation. Enrich the crystallographic data of these newly developed ferromagnetic shape memory alloys.
- (3) Develop fabrication processes to obtain textures in polycrystalline Ni-Mn-Ga alloys for possible enhancement of the magnetic shape memory effect in the polycrystalline alloys. Characterize the textures by neutron diffraction technique. Investigate the correlation between texture evolution and macroscopic shape memory effect in the Ni-Mn-Ga based alloys.
- (4) Study the effect of alloying with Co element on the materials properties of the Ni-Mn-Ga alloys, aiming at developing new promising ferromagnetic shape memory alloys with optimal properties.

The purpose of the present work is to reveal the fundamental issues of Ni-Mn-Ga alloys; enrich the existing data on crystal structure, crystallography and mechanical behaviors and discover new phenomena in this alloy system; lay a solid foundation for the improvement of the performances of the present Ni-Mn-Ga alloys and for the design of new promising ferromagnetic shape memory alloys.

References

1. K. Otsuka and C. M. Wayman, *Shape Memory Materials*, Cambridge University Press, Cambridge, 1998.
2. M. J. Hoffmann and H. Kungl: High strain lead-based perovskite ferroelectrics. *Current Opinion in Solid State and Materials Science* **8**, 51-57 (2004).
3. J. P. Teter, M. Wun-Fogle, A. E. Clark and K. Mahoney: Anisotropic perpendicular axis magnetostriction in twinned $Tb_xDy_{1-x}Fe_{1.95}$. *Journal of Applied Physics* **67**, 5004-5006 (1990).
4. K. Otsuka and X. Ren: Recent developments in the research of shape memory alloys. *Intermetallics* **7**, 511-528 (1999).
5. A. Sozinov, A. A. Likhachev, N. Lanska and K. Ullakko: Giant magnetic-field-induced strain in NiMnGa seven-layered martensitic phase. *Applied Physics Letters* **80**, 1746-1748 (2002).
6. R. N. Couch and I. Chopra: Experimental characterization of NiMnGa magnetic shape memory alloy rods under dynamic magnetic fields. *Proceedings of SPIE* **5053**, 169-180 (2003).
7. C. P. Henry, D. Bono, J. Feuchtwanger, S. M. Allen and R. C. O'Handley: ac field-induced actuation of single crystal Ni-Mn-Ga. *Journal of Applied Physics* **91**, 7810-7811 (2002).
8. K. Ullakko, J. K. Huang, C. Kantner, R. C. O'Handley and V. V. Kokorin: Large magnetic-field-induced strains in Ni_2MnGa single crystals. *Applied Physics Letters* **69**, 1966-1968 (1996).
9. S. J. Murray, M. A. Marioni, A. M. Kukla, J. Robinson, R. C. O'Handley and S. M. Allen:

- Large field induced strain in single crystalline Ni-Mn-Ga ferromagnetic shape memory alloy. *Journal of Applied Physics* **87**, 5774-5776 (2000).
10. A. N. Vasil'ev, A. D. Bozhko, V. V. Khovailo, I. E. Dikshtein, V. G. Shavrov V. D. Buchelnikov, M. Matsumoto, S. Suzuki, T. Takagi and J. Tani: Structural and magnetic phase transitions in shape-memory alloys $\text{Ni}_{2+x}\text{Mn}_{1-x}\text{Ga}$. *Physical Review B* **59**, 1113-1120 (1999).
 11. R. D. James, R. Tickle and M. Wuttig: Large field-induced strains in ferromagnetic shape memory materials. *Materials Science and Engineering A* **273-275**, 320-325 (1999).
 12. M. Wuttig, J. Li and C. Craciunescu: A new ferromagnetic shape memory alloy system. *Scripta Materialia* **44**, 2393-2397 (2001).
 13. H. Morito, A. Fujita, K. Fukamichi, R. Kainuma, K. Ishida and K. Oikawa: Magnetocrystalline anisotropy in single-crystal Co-Ni-Al ferromagnetic shape-memory alloy. *Applied Physics Letters* **81**, 1657-1659 (2002).
 14. K. Oikawa, L. Wulff, T. Iijima, G. Gejima, T. Ohmori, A. Fujita, K. Fukamichi, R. Kainuma and K. Ishida: Promising ferromagnetic Ni-Co-Al shape memory alloy system. *Applied Physics Letters* **79**, 3290-3292 (2001).
 15. Y. Murakami, D. Shindo, K. Oikawa, R. Kainuma and K. Ishida: Magnetic domain structure in a ferromagnetic shape memory alloy $\text{Ni}_{51}\text{Fe}_{22}\text{Ga}_{27}$ studied by electron holography and Lorentz microscopy. *Applied Physics Letters* **82**, 3695-3697 (2003).
 16. K. Oikawa, T. Ota, T. Ohmori, Y. Tanaka, H. Morito, A. Fujita, R. Kainuma, K. Fukamichi and K. Ishida: Magnetic and martensitic phase transitions in ferromagnetic Ni-Ga-Fe shape memory alloys. *Applied Physics Letters* **81**, 5201-5203 (2002).
 17. A. Fujita, K. Fukamichi, F. Gejima, R. Kainuma and K. Ishida: Magnetic properties and large magnetic-field-induced strains in off-stoichiometric Ni-Mn-Al Heusler alloys. *Applied Physics Letters* **77**, 3054-3056 (2000).
 18. R. D. James and M. Wuttig: Magnetostriction of martensite. *Philosophical Magazine A* **77**, 1273-1299 (1998).
 19. T. Kubota, T. Okazaki, Y. Furuya and T. Watanabe: Large magnetostriction in rapid-solidified ferromagnetic shape memory Fe-Pd alloy. *Journal of Magnetism and*

- Magnetic Materials* **239**, 551-553 (2002).
20. Y. Liang, T. Wada, H. Kato, T. Tagawa, M. Taya and T. Mori: Straining of a polycrystal of Fe-Pd with martensite structure by uniaxial loading. *Materials Science and Engineering A* **338**, 89-96 (2002).
 21. T. Takashita, T. Takeuchi, T. Fukuda, M. Tsujiguchi, T. Saburi, R. Oshima and S. Muto: Giant magnetostriction in an ordered Fe₃Pt single crystal exhibiting martensitic transformation. *Applied Physics Letters* **77**, 1502-1504 (2000).
 22. P. J. Webster, K. R. A. Ziebeck, S. L. Town and M. S. Peak: Magnetic order and phase transformation in Ni₂MnGa. *Philosophical Magazine B* **49**, 295-310 (1984).
 23. B. Wedel, M. Suzuki, Y. Murakami, C. Wedel, T. Suzuki, D. Shindo, K. Itagaki: Low temperature crystal structure of Ni-Mn-Ga alloys. *Journal of Alloys and Compounds* **290**, 137-143 (1999).
 24. W. H. Wang, G. H. Wu, J. L. Chen, C. H. Yu, S. X. Gao, W. S. Zhan, Z. Wang, Z. Y. Gao, Y. F. Zheng and L. C. Zhao: Stress-free two-way thermoelastic shape memory and field-enhanced strain in Ni₅₂Mn₂₄Ga₂₄ single crystals. *Applied Physics Letters* **77**, 3245-3247 (2000).
 25. W. H. Wang, Z. H. Liu, Z. W. Shan, J. L. Chen, G. H. Wu and W. S. Zhan: Effect of post-growth annealing and magnetic field on the two-way shape memory effect of Ni₅₂Mn₂₄Ga₂₄ single crystals. *Journal of Physics D: Applied Physics* **35**, 492-496 (2002).
 26. V. A. Chernenko, V. L'vov, J. Pons and E. Cesari: Superelasticity in high-temperature Ni-Mn-Ga alloys. *Journal of Applied Physics* **93**, 2394-2399 (2003).
 27. F. A. Hames: Ferromagnetic-alloy phases near the compositions Ni₂MnIn, Ni₂MnGa, Co₂MnGa, Pd₂MnSb, and PdMnSb. *Journal of Applied Physics* **31**, S370-S371 (1960).
 28. M. Elfazani, M. DeMarco, S. Jha, G. M. Julian and J. W. Blue: Hyperfine magnetic field at cadmium impurity in Heusler alloys Ni₂MnGa, Ni₂MnIn, Cu₂MnIn, and Au₂MnIn. *Journal of Applied Physics* **52**, 2043-2045 (1981).
 29. C. Mitros, S. Yehia, S. Kumar, S. Jha, M. DeMarco, D. Mitchell, G. M. Julian and R. A. Dunlap: Hyperfine magnetic field measurements in Heusler alloys Ni₂MnGa, Pd₂MnSn, and Ru₂FeSn. *Hyperfine Interactions* **34**, 419-422 (1987).
 30. T. Kanomata, K. Shirakawa and T. Kaneko: Effect of hydrostatic pressure on the Curie

- temperature of the Heusler alloys Ni_2MnZ ($Z = \text{Al, Ga, In, Sn}$ and Sb). *Journal of Magnetism and Magnetic Materials* **65**, 76-82 (1987).
31. S. Fujii, S. Ishida and S. Asano: Electronic structure and lattice transformation in Ni_2MnGa and Co_2NbSn . *Journal of the Physical Society of Japan* **58**, 3657-3665 (1989).
 32. O. Söderberg, *Novel Ni-Mn-Ga alloys and their magnetic shape memory behaviour*, Laboratory of Physical Metallurgy and Materials Science, Helsinki University of Technology, Doctoral Thesis TKK-ME-DT-2, 2004.
 33. J. Soltys: The magnetic properties of the Heusler alloy Ni_2MnGa . *Acta Physica Polonica A* **46**, 383-384 (1974).
 34. J. Soltys: The effect of heat treatment on the atomic arrangement and the magnetic properties in Ni_2MnGa . *Acta Physica Polonica A* **47**, 521-523 (1975).
 35. V. V. Kokorin and V. A. Chernenko: Martensitic transformation in a ferromagnetic Heusler alloy. *The Physics of Metals and Metallography* **68**, 111-115 (1989).
 36. V. A. Chernenko, V. V. Kokorin, A. N. Vasilev and Y. I. Savchenko: The behavior of the elastic-constants at the transformation between the modulated phases in Ni_2MnGa . *Phase Transitions* **43**, 187-191 (1993).
 37. R. C. O'Handley: Model for strain and magnetization in magnetic shape-memory alloys. *Journal of Applied Physics* **83**, 3263-3270 (1998).
 38. S. J. Murray, M. Marioni, S. M. Allen, R. C. O'Handley and T. A. Lograsso: 6% magnetic-field-induced strain by twin-boundary motion in ferromagnetic Ni-Mn-Ga. *Applied Physics Letters* **77**, 886-888 (2000).
 39. P. J. Brown, J. Crangle, T. Kanomata, M. Matsumoto, K. -U. Neumann, B. Ouladdiaf and K. R. A. Ziebeck: The crystal structure and phase transitions of the magnetic shape memory compound Ni_2MnGa . *Journal of Physics: Condensed Matter* **14**, 10159-10171 (2002).
 40. J. Pons, V. A. Chernenko, S. Santamarta and E. Cesari: Crystal structure of martensitic phases in Ni-Mn-Ga shape memory alloys. *Acta Materialia* **48**, 3027-3038 (2000).
 41. O. Heczko, L. Straka and K. Ullakko: Relation between structure, magnetization process and magnetic shape memory effect of various martensites occurring in Ni-Mn-Ga alloys. *Journal de Physique IV* **112**, 959-962 (2003).

42. A. Sozinov, A. A. Likhachev and K. Ullakko: Magnetic and magnetomechanical properties of Ni-Mn-Ga alloys with easy axis and easy plane of magnetization. *Proceedings of SPIE* **4333**, 189-196 (2001).
43. A. Sozinov, A. A. Likhachev and K. Ullakko: Crystal structures and magnetic anisotropy properties of Ni-Mn-Ga martensitic phases with giant magnetic-field-induced strain. *IEEE Transactions on Magnetics* **38**, 2814-2816 (2002).
44. K. Koho, J. Vimpari, L. Straka, N. Lanska, O. Söderberg, O. Heczko, K. Ullakko and V. K. Lindroos: Behaviour of Ni-Mn-Ga alloys under mechanical stress. *Journal de Physique IV* **112**, 943-946 (2003).
45. X.W. Liu, O. Söderberg, Y. Ge, A. Sozinov and V. K. Lindroos: Corrosion behavior of NiMnGa shape-memory alloy. *Materials Science Forum* **394-395**, 565-568 (2002).
46. X. W. Liu, O. Söderberg, Y. Ge, N. Lanska, K. Ullakko and V.K. Lindroos: On the corrosion of non-stoichiometric martensitic Ni-Mn-Ga alloys. *Journal de Physique IV* **112**, 935-938 (2003).
47. V. V. Martynov and V. V. Kokorin: The crystal structure of thermally- and stress-induced martensites in Ni₂MnGa single crystals. *Journal de Physique III* **2**, 739-749 (1992).
48. G. Feng, C. Jiang, T. Liang and H. Xu: Magnetic and structural transition of Ni_{50+x}Mn_{25-x/2}Ga_{25-x/2} (x=2-5) alloys. *Journal of Magnetism and Magnetic Materials* **248**, 312-317 (2002).
49. J. Enkovaara, *Atomistic simulations of magnetic shape memory alloys*, Laboratory of Physics, Helsinki University of Technology, Dissertation 119, 2003.
50. A. Sozinov, A. A. Likhachev, N. Lanska, O. Söderberg, K. Ullakko and V. K. Lindroos: Effect of crystal structure on magnetic-field-induced strain in Ni-Mn-Ga. *Proceedings of SPIE* **5053**, 586-594 (2003).
51. V. V. Khovailo, T. Takagi, J. Tani, R. Z. Levitin, A. A. Cherechukin, M. Matsumoto and R. Note: Magnetic properties of Ni_{2.18}Mn_{0.82}Ga Heusler alloys with a coupled magnetostructural transition. *Physical Review B* **65**, 092410 (2002).
52. C. Jiang, G. Feng and H. Xu: Co-occurrence of magnetic and structural transitions in the Heusler alloy Ni₅₃Mn₂₅Ga₂₂. *Applied Physics Letters* **80**, 1619-1621 (2002).
53. V. V. Martynov: X-ray diffraction study of thermally and stress-induced phase

- transformations in single crystalline Ni-Mn-Ga alloys. *Journal de Physique IV* **5 (C8)**, 91-99 (1995).
54. V. A. Chernenko, C. Segui, E. Cesari, J. Pons and V. V. Kokorin: Some aspects of structural behaviour of Ni-Mn-Ga alloys. *Journal de Physique IV* **7 (C5)**, 137-141 (1997).
 55. V. A. Chernenko, A. Amengual, E. Cesari, V. V. Kokorin and I. K. Zasimchuk: Thermal and magnetic properties of stress-induced martensites in Ni-Mn-Ga alloys. *Journal de Physique IV* **5 (C2)**, 95-98 (1995).
 56. G. Fritsch, V. V. Kokorin, V. A. Chernenko, A. Kempf, and I. K. Zasimchuk: Martensitic transformation in Ni-Mn-Ga alloys. *Phase Transitions* **57**, 233-240 (1996).
 57. L. Manosa, A. Planes, J. Zarestky, T. Lograsso, D. L. Schlagel and C. Stassis: Phonon softening in Ni-Mn-Ga alloys. *Physical Review B* **64**, 024305 (2001).
 58. N. Glavatska, G. Mogilniy, I. Glavatsky, S. Danilkin, D. Hohlwein, A. Beskrovnij, O. Söderberg and V. K. Lindroos: Temperature dependence of martensite structure and its effect on magnetic-field-induced strain in Ni₂MnGa magnetic shape memory alloys. *Journal de Physique IV* **112**, 963-967 (2003).
 59. Y. Ge, H. Jiang, A. Sozinov, O. Söderberg, N. Lanska, J. Keranen, E. I. Kauppinen, V. K. Lindroos and S. -P. Hannula: Crystal structure and macrotwin interface of five-layered martensite in Ni-Mn-Ga magnetic shape memory alloy. *Materials Science and Engineering A* **438-440**, 961-964 (2006).
 60. N. Lanska and K. Ullakko: Microstructure change in Ni-Mn-Ga seven-layered martensite connected with MSM effect. *Journal de Physique IV* **112**, 925-928 (2003).
 61. W. H. Wang, X. Ren and G. H. Wu: Martensitic microstructure and its damping behavior in Ni₅₂Mn₁₆Fe₈Ga₂₄ single crystals. *Physical Review B* **73**, 092101 (2006).
 62. A. Sozinov, A. A. Likhachev, N. Lanska, K. Ullakko and V. K. Lindroos: Crystal structure, magnetic anisotropy and mechanical properties of seven-layered martensite in Ni-Mn-Ga. *Proceedings of SPIE* **4699**, 195-205 (2002).
 63. V. A. Chernenko, C. Segui, E. Cesari, J. Pons and V. V. Kokorin: Sequence of martensitic transformations in Ni-Mn-Ga alloys. *Physical Review B* **57**, 2659-2662 (1998).
 64. V. A. Chernenko, E. Cesari, J. Pons and C. Segui: Phase transformations in rapidly

- quenched Ni-Mn-Ga alloys. *Journal of Materials Research* **15**, 1496-1504 (2000).
65. O. Söderberg, L. Straka, V. Novak, O. Heczko, S. -P. Hannula and V. K. Lindroos: Tensile/compressive behaviour of non-layered tetragonal Ni_{52.8}Mn_{25.7}Ga_{21.5} alloy. *Materials Science and Engineering A* **386**, 27-33 (2004).
66. X. W. Liu, O. Söderberg, K. Koho, N. Lanska, Y. Ge, A. Sozinov and V. K. Lindroos: Vibration cavitation behaviour of selected Ni-Mn-Ga alloys. *Wear* **258**, 1364-1371 (2005).
67. N. Lanska, O. Söderberg, A. Sozinov, Y. Ge, K. Ullakko and V. K. Lindroos: Composition and temperature dependence of the crystal structure of Ni-Mn-Ga alloys. *Journal of Applied Physics* **95**, 8074-8078 (2004).
68. L. Righi, F. Albertini, L. Pareti, A. Paoluzi and G. Calestani: Commensurate and incommensurate “5M” modulated crystal structures in Ni-Mn-Ga martensitic phases. *Acta Materialia* **55**, 5237-5245 (2007).
69. R. W. Overhosler, M. Wuttig and D. A. Neumann: Chemical ordering in Ni-Mn-Ga Heusler alloys. *Scripta Materialia* **40**, 1095-1102 (1999).
70. O. Söderberg, M. Friman, A. Sozinov, N. Lanska, Y. Ge, M. Hamalainen and V. K. Lindroos: Transformation behavior of two Ni-Mn-Ga alloys. *Zeitschrift für Metallkunde* **95**, 724-731 (2004).
71. V. V. Khovailo, T. Takagi, A. N. Vasilev, H. Miki, M. Matsumoto and R. Kainuma: On order-disorder (L2₁-B2') phase transition in Ni_{2+x}Mn_{1-x}Ga Heusler alloys. *Physica Status Solidi A* **183**, R1-R3 (2001).
72. A. Planes, E. Obrado, A. Gonzalez-Comas and L. Manosa: Premartensitic transition driven by magnetoelastic interaction in bcc ferromagnetic Ni₂MnGa. *Physical Review Letters* **79**, 3926-3929 (1997).
73. T. Castan, E. Vives and P. -A. Lindgard: Modeling premartensitic effects in Ni₂MnGa: a mean-field and Monte Carlo simulation study. *Physical Review B* **60**, 7071-7084 (1999).
74. A. Zheludev, S. M. Shapiro, P. Wochner and L. E. Tanner: Precursor effects and premartensitic transformation in Ni₂MnGa. *Physical Review B* **54**, 15045-15050 (1996).
75. P. Zhao, L. Dai, J. Cullen and M. Wuttig: Magnetic and elastic properties of Ni_{49.0}Mn_{23.5}Ga_{27.5} premartensite. *Metallurgical and Materials Transactions A* **38**,

- 745-751 (2007).
76. U. Stuhr, P. Vorderwisch, V. V. Kokorin and P. -A. Lindgard: Premartensitic phenomena in the ferro- and paramagnetic phases of Ni₂MnGa. *Physical Review B* **56**, 14360-14365 (1997).
 77. V. V. Khovailo, T. Takagi, A. D. Bozhko, M. Matsumoto, J. Tani and V. G. Shavrov: Premartensitic transition in Ni_{2+x}Mn_{1-x}Ga Heusler alloys. *Journal of Physics: Condensed Matter* **13**, 9655-9662 (2001).
 78. Y. Q. Fei and J. F. Wan: Magnetic susceptibility anomaly associated with premartensitic transition in Heusler alloy. *Physica B* **389**, 288-291 (2007).
 79. Y. T. Cui, J. L. Chen, G. D. Liu, G. H. Wu and W. L. Wang: Characteristics of the premartensitic transition strain in ferromagnetic shape memory Ni_{50.5}Mn_{24.5}Ga₂₅ single crystals. *Journal of Physics: Condensed Matter* **16**, 3061-3069 (2004).
 80. V. A. Chernenko, J. Pons, C. Segui and E. Cesari: Premartensitic phenomena and other phase transformations in Ni-Mn-Ga alloys studied by dynamical mechanical analysis and electron diffraction. *Acta Materialia* **50**, 53-60 (2002).
 81. F. J. Perez-Reche, E. Vives, L. Manosa, A. Planes: Calorimetric and acoustic emission study of the premartensitic and martensitic transitions in Ni-Mn-Ga. *Materials Science and Engineering A* **378**, 353-356 (2004).
 82. A. Gonzalez-Comas, E. Obrado, L. Manosa, A. Planes, V. A. Chernenko, B. J. Hantink and A. Labarta: Premartensitic and martensitic phase transitions in ferromagnetic Ni₂MnGa. *Physical Review B* **60**, 7085-7090 (1999).
 83. V. V. Kokorin, V. A. Chernenko, E. Cesari, J. Pons and C. Segui: Pre-martensitic state in Ni-Mn-Ga alloys. *Journal of Physics: Condensed Matter* **8**, 6457-6463 (1996).
 84. V. V. Kokorin, V. A. Chernenko, J. Pons, C. Segui and E. Cesari: Acoustic phonon mode condensation in Ni₂MnGa compound. *Solid State Communications* **101**, 7-9 (1997).
 85. A. N. Vasil'ev, V. D. Buchel'nikov, T. Takagi, V. V. Khovailo and E. I. Estrin: Shape memory ferromagnets. *Physics - Uspekhi* **46**, 559-588 (2003).
 86. V. A. Chernenko: Compositional instability of β -phase in Ni-Mn-Ga alloys. *Scripta Materialia* **40**, 523-527 (1999).

87. V. A. Chernenko, E. Cesari, V. V. Kokorin and I. N. Vitenko: The development of new ferromagnetic shape memory alloys in Ni-Mn-Ga system. *Scripta Metallurgica et Materialia* **33**, 1239-1244 (1995).
88. S. K. Wu and S. T. Yang: Effect of composition on transformation temperatures of Ni-Mn-Ga shape memory alloys. *Materials Letters* **57**, 4291-4296 (2003).
89. X. Jin, M. Marioni, D. Bono, S. M. Allen, R. C. O'Handley and T. Y. Hsu: Empirical mapping of Ni-Mn-Ga properties with composition and valence electron concentration. *Journal of Applied Physics* **91**, 8222-8224 (2002).
90. M. Kreissl, K. -U. Neumann, T. Stephens and K. R. A. Ziebeck: The influence of atomic order on the magnetic and structural properties of the ferromagnetic shape memory compound Ni₂MnGa. *Journal of Physics: Condensed Matter* **15**, 3831-3839 (2003).
91. K. Tsuchiya, D. Ohtoyo, M. Umemoto and H. Ohtsuka: Effect of isothermal aging on martensitic transformation in Ni-Mn-Ga alloys. *Transactions of the Materials Research Society of Japan* **25**, 521-523 (2000).
92. S. Besseghini, M. Pasquale, F. Passaretti, A. Sciacca and E. Villa: NiMnGa polycrystalline magnetically activated shape memory alloy: a calorimetric investigation. *Scripta Materialia* **44**, 2681-2687 (2001).
93. O. Heczko, N. Lanska, O. Soderberg and K. Ullakko: Temperature variation of structure and magnetic properties of Ni-Mn-Ga magnetic shape memory alloys. *Journal of Magnetism and Magnetic Materials* **242-245**, 1446-1449 (2002).
94. O. Söderberg, A. Sozinov, N. Lanska, Y. Ge, V. K. Lindroos and S. -P. Hannula: Effect of intermartensitic reaction on the co-occurrence of the magnetic and structural transition in Ni-Mn-Ga alloys. *Materials Science and Engineering A* **438-440**, 957-960 (2006).
95. C. Segui, V. A. Chernenko, J. Pons, E. Cesari, V. Khovailo and T. Takagi: Low temperature-induced intermartensitic phase transformations in Ni-Mn-Ga single crystal. *Acta Materialia* **53**, 111-120 (2005).
96. C. Segui, J. Pons and E. Cesari: Effect of atomic ordering on the phase transformation in Ni-Mn-Ga shape memory alloys. *Acta Materialia* **55**, 1649-1655 (2007).
97. L. Dai, J. Cullen and M. Wuttig: Intermartensitic transformation in a NiMnGa alloy. *Journal of Applied Physics* **95**, 6957-6959 (2004).

98. W. H. Wang, Z. H. Liu, J. Zhang, J. L. Chen, G. H. Wu, W. S. Zhan, T. S. Chin, G. H. Wen and X. X. Zhang: Thermoelastic intermartensitic transformation and its internal stress dependency in $\text{Ni}_{52}\text{Mn}_{24}\text{Ga}_{24}$ single crystals. *Physical Review B* **66**, 052411 (2002).
99. V. V. Kokorin, A. O. Perekos, A. A. Tshcherba, O. M. Babiy and T. V. Efimova: Intermartensitic phase transitions in Ni-Mn-Ga alloy, magnetic field effect. *Journal of Magnetism and Magnetic Materials* **302**, 34-39 (2006).
100. V. A. Chernenko, E. Cesari, V. Khovailo, J. Pons, C. Segui and T. Takagi: Intermartensitic phase transformations in Ni-Mn-Ga studied under magnetic field. *Journal of Magnetism and Magnetic Materials* **290-291**, 871-873 (2005).
101. V. V. Khovailo, K. Oikawa, C. Wedel, T. Takagi, T. Abe and K. Sugiyama: Influence of intermartensitic transitions on transport properties of $\text{Ni}_{2.16}\text{Mn}_{0.84}\text{Ga}$ alloy. *Journal of Physics: Condensed Matter* **16**, 1951-1961 (2004).
102. V. K. Srivastava, R. Chatterjee, A. K. Nigam and R. C. O'Handley: Electric and magnetic signatures of martensitic and intermartensitic transformations in Ni-Mn-Ga crystal. *Solid State Communications* **136**, 297-299 (2005).
103. M. Khan, S. Stadler and N. Ali: Intermartensitic transformations in $\text{Ni}_2\text{Mn}_{1-x}\text{Co}_x\text{Ga}$ Heusler alloys. *Journal of Applied Physics* **99**, 08M705 (2006).
104. W. H. Wang, G. H. Wu, J. L. Chen, S. X. Gao, W. S. Zhan, G. H. Wen and X. X. Zhang: Intermartensitic transformation and magnetic-field-induced strain in $\text{Ni}_{52}\text{Mn}_{24.5}\text{Ga}_{23.5}$ single crystals. *Applied Physics Letters* **79**, 1148-1150 (2001).
105. C. Segui, V. A. Chernenko, J. Pons and E. Cesari: Low-temperature-induced intermartensitic phase transformations in Ni-Mn-Ga single crystal. *Journal of Magnetism and Magnetic Materials* **290-291**, 811-815 (2005).
106. M. Pasquale, C. P. Sasso, L. H. Lewis, L. Giudici, T. Lograsso and D. Schlagel: Magnetostructural transition and magnetocaloric effect in $\text{Ni}_{55}\text{Mn}_{20}\text{Ga}_{25}$ single crystals. *Physical Review B* **72**, 094435 (2005).
107. P. J. Brown, A. Y. Bargawi, J. Crangle, K. -U. Neumann and K. R. A. Ziebeck: Direct observation of a band Jahn-Teller effect in the martensitic phase transition of Ni_2MnGa . *Journal of Physics: Condensed Matter* **11**, 4715-4722 (1999).

108. B. L. Ahuja, B. K. Sharma, S. Mathur, N. L. Heda, M. Itou, A. Andrejczuk, Y. Sakurai, A. Chakrabarti, S. Banik, A. M. Awasthi and S. R. Barman: Magnetic Compton scattering study of $\text{Ni}_{2+x}\text{Mn}_{1-x}\text{Ga}$ ferromagnetic shape-memory alloys. *Physical Review B* **75**, 134403 (2007).
109. A. Ayuela, J. Enkovaara and R. M. Nieminen: *Ab initio* study of tetragonal variants in Ni_2MnGa alloy. *Journal of Physics: Condensed Matter* **14**, 5325-5336 (2002).
110. O. Heczko and L. Straka: Compositional dependence of structure, magnetization and magnetic anisotropy in Ni-Mn-Ga magnetic shape memory alloys. *Journal of Magnetism and Magnetic Materials* **272-276**, 2045-2046 (2004).
111. J. Enkovaara, O. Heczko, A. Ayuela and R. M. Nieminen: Coexistence of ferromagnetic and antiferromagnetic order in Mn-doped Ni_2MnGa . *Physical Review B* **67**, 212405 (2003).
112. A. Aliev, A. Batdalov, S. Bosko, V. Buchelnikov, I. Dikshtein, V. Khovailo, V. Koledov, R. Levitin, V. Shavrov and T. Takagi: Magnetocaloric effect and magnetization in a Ni-Mn-Ga Heusler alloy in the vicinity of magnetostructural transition. *Journal of Magnetism and Magnetic Materials* **272-276**, 2040-2042 (2004).
113. A. B. Pakhomov, C. Y. Wong, X. X. Zhang, G. H. Wen and G. H. Wu: Magnetization and magnetocaloric effect in magnetic shape memory alloys Ni-Mn-Ga. *IEEE Transactions on Magnetics* **37**, 2718-2720 (2001).
114. J. Marcos, L. Manosa, A. Planes, F. Casanova, X. Batlle and A. Labarta: Multiscale origin of the magnetocaloric effect Ni-Mn-Ga shape-memory alloys. *Physical Review B* **68**, 094401 (2003).
115. R. Tickle and R. D. James: Magnetic and magnetomechanical properties of Ni_2MnGa . *Journal of Magnetism and Magnetic Materials* **195**, 627-638 (1999).
116. O. Heczko, L. Straka, N. Lanska, K. Ullakko and J. Enkovaara: Temperature dependence of magnetic anisotropy in Ni-Mn-Ga alloys exhibiting giant field-induced strain. *Journal of Applied Physics* **91**, 8228-8230 (2002).
117. L. Straka and O. Heczko: Magnetic anisotropy in Ni-Mn-Ga martensites. *Journal of Applied Physics* **93**, 8636-8638 (2003).
118. F. Albertini, L. Pareti, A. Paoluzi, L. Morellon, P. A. Algarabel, M. R. Ibarra and L. Righi:

- Composition and temperature dependence of the magnetocrystalline anisotropy in $\text{Ni}_{2+x}\text{Mn}_{1+y}\text{Ga}_{1+z}$ ($x+y+z=0$) Heusler alloys. *Applied Physics Letters* **81**, 4032-4034 (2002).
119. Y. Ge, *The crystal and magnetic microstructure of Ni-Mn-Ga alloys*, Laboratory of Materials Science, Helsinki University of Technology, Doctoral Thesis TKK-ME-DIS-6, 2007.
120. M. De Graef, Y. Kishi, Y. Zhu and M. Wuttig: Lorentz study of magnetic domains in Heusler-type ferromagnetic shape memory alloys. *Journal de Physique IV* **112**, 993-996 (2003).
121. Q. Pan and R. D. James: Micromagnetic study of Ni_2MnGa under applied field (invited). *Journal of Applied Physics* **87**, 4702-4706 (2000).
122. A. Sozinov, Y. Ezer, G. Kimmel, P. Yakovenko, D. Giller, Y. Wolfus, Y. Yeshurun, K. Ullakko and V. K. Lindroos: Large magnetic-field-induced strains in Ni-Mn-Ga alloys in rotating magnetic field. *Journal de Physique IV* **11 (Pr8)**, 311-316 (2001).
123. H. D. Chopra, C. Ji and V. V. Kokorin: Magnetic-field-induced twin boundary motion in magnetic shape-memory alloys. *Physical Review B* **61**, R14913 (2000).
124. H. S. Park, Y. Murakami, D. Shindo, V. A. Chernenko and T. Kanomata: Behavior of magnetic domains during structural transformations in Ni_2MnGa ferromagnetic shape memory alloy. *Applied Physics Letters* **83**, 3752-3754 (2003).
125. Y. Ge, O. Heczko, O. Söderberg and V. K. Lindroos: Various magnetic domain structures in a Ni-Mn-Ga martensite exhibiting magnetic shape memory effect. *Journal of Applied Physics* **96**, 2159-2163 (2004).
126. Y. Ge, O. Heczko, O. Söderberg and S. -P. Hannula: Direct optical observation of magnetic domains in Ni-Mn-Ga martensite. *Applied Physics Letters* **89**, 082502 (2006).
127. Y. Ge, O. Heczko, O. Söderberg and S. -P. Hannula: Magnetic domain evolution with applied field in a Ni-Mn-Ga magnetic shape memory alloy. *Scripta Materialia* **54**, 2155-2160 (2006).
128. L. Straka and O. Heczko: Superelastic response of Ni-Mn-Ga martensite in magnetic fields and a simple model. *IEEE Transactions on Magnetics* **39**, 3402-3404 (2003).
129. A. A. Likhav, A. Sozinov and K. Ullakko: Influence of external stress on the reversibility

- of magnetic-field-controlled shape memory effect in Ni-Mn-Ga. *Proceedings of SPIE* **4333**, 197-206 (2001).
130. A. Sozinov, A. A. Likhachev, N. Lanska, K. Ullakko and V. K. Lindroos: 10% magnetic-field-induced strain in Ni-Mn-Ga seven-layered martensite. *Journal de Physique IV* **112**, 955-958 (2003).
131. A. Sozinov, A. A. Likhachev, N. Lanska, O. Söderberg, K. Ullakko and V. K. Lindroos: Stress- and magnetic-field-induced variant rearrangement in Ni-Mn-Ga single crystals with seven-layered martensitic structure. *Materials Science and Engineering A* **378**, 399-402 (2004).
132. A. Sozinov, A. A. Likhachev, N. Lanska, O. Söderberg, K. Koho, K. Ullakko and V. K. Lindroos: Stress-induced variant rearrangement in Ni-Mn-Ga single crystals with nonlayered tetragonal martensitic structure. *Journal de Physique IV* **115**, 121-128 (2004).
133. H. Xu, Y. Ma and C. Jiang: A high-temperature shape-memory alloy Ni₅₄Mn₂₅Ga₂₁. *Applied Physics Letters* **82**, 3206-3208 (2003).
134. Y. Q. Ma, C. B. Jiang, G. Feng and H. B. Xu: Thermal stability of the Ni₅₄Mn₂₅Ga₂₁ Heusler alloy with high temperature transformation. *Scripta Materialia* **48**, 365-369 (2003).
135. M. Pasquale, C. Sasso, S. Besseghini, F. Passaretti, E. Villa and A. Sciacca: NiMnGa polycrystalline magnetically activated shape memory alloys. *IEEE Transactions on Magnetics* **36**, 3263-3265 (2000).
136. K. Ullakko, Y. Ezer, A. Sozinov, G. Kimmel, P. Yakovenko and V. K. Lindroos: Magnetic-field-induced strains in polycrystalline Ni-Mn-Ga at room temperature. *Scripta Materialia* **44**, 475-480 (2001).
137. P. Mullner, V. A. Chernenko and G. Kostorz: A microscopic approach to the magnetic-field-induced deformation of martensite (magnetoplasticity). *Journal of Magnetism and Magnetic Materials* **267**, 325-334 (2003).
138. R. K. Singh, M. Shamsuddin, R. Gopalan, R. P. Mathur and V. Chandrasekaran: Magnetic and structural transformation in off-stoichiometric NiMnGa alloys. *Materials Science and Engineering A* **476**, 195-200 (2008).
139. A. Koblishka-Veneva, C. Gachot, P. Leibenguth and F. Mucklich: Investigation of

- microstructure of bulk Ni₂MnGa alloy by means of electron backscatter diffraction analysis. *Journal of Magnetism and Magnetic Materials* **316**, e431-e434 (2007).
140. N. V. R. Rao, R. Gopalan, M. M. Raja, J. A. Chelvane, B. Majumdar and V. Chandrasekaran: Magneto-structural transformation studies in melt-spun Ni-Mn-Ga ribbons. *Scripta Materialia* **56**, 405-408 (2007).
141. V. C. Solomon, J. Hong, Y. Tang, A. E. Berkowitz and D. J. Smith: Electron microscopy investigation of spark-eroded Ni-Mn-Ga ferromagnetic shape-memory alloy particles. *Scripta Materialia* **56**, 593-596 (2007).
142. R. D. James and K. F. Hane: Martensitic transformation and shape memory materials. *Acta Materialia* **48**, 197-222 (2000).
143. N. Glavatska, V. A. L'vov and I. Glavatsky: Thermal phonons affecting the long-time evolution of Ni-Mn-Ga martensite under magnetic field. *Journal of Magnetism and Magnetic Materials* **309**, 244-250 (2007).
144. Y. Kishi, Z. Yajima, K. Shimizu and M. Wuttig: Transformation behavior and microstructures of PtNiMnGa ferromagnetic shape memory alloys. *Materials Science and Engineering A* **378**, 361-364 (2004).
145. J. C. Bennett, C. V. Hyatt, M. A. Gharghouri, S. Farrell, M. Robertson, J. Chen and G. Pirge: In situ transmission electron microscopy studies of directionally solidified Ni-Mn-Ga ferromagnetic shape memory alloys. *Materials Science and Engineering A* **378**, 409-414 (2004).
146. F. Chen, H. B. Wang, X. L. Meng, Z. Y. Gao, W. Cai and L. C. Zhao: Effect of aging on transformation temperatures and microstructure of an Fe-doped Ni-Mn-Ga ferromagnetic shape memory alloy. *Materials Science and Engineering A* **438-440**, 982-985 (2006).
147. Z. Y. Gao, F. Chen, W. Cai, L. C. Zhao, G. H. Wu, B. G. Shen and W. S. Zhan: Effect of pre-deformation on martensitic transformation behavior and the microstructure of a Ni-Mn-Ga alloy. *Materials Science and Engineering A* **438-440**, 974-977 (2006).
148. M. Pötschke, U. Gaitzsch, S. Roth, B. Rellinghaus and L. Schultz: Preparation of melt textured Ni-Mn-Ga. *Journal of Magnetism and Magnetic Materials* **316**, 383-385 (2007).
149. Y. C. Shu and K. Bhattacharya: The influence of texture on the shape-memory effect in polycrystals. *Acta Materialia* **46**, 5457-5473 (1998).

-
150. P. Thamburaja and L. Anand: Polycrystalline shape-memory materials: effect of crystallographic texture. *Journal of the Mechanics and Physics of Solids* **49**, 709-737 (2001).
151. U. Gaitzsch, M. Pötschke, S. Roth, B. Rellinghaus and L. Schultz: Mechanical training of polycrystalline 7M Ni₅₀Mn₃₀Ga₂₀ magnetic shape memory alloy. *Scripta Materialia* **57**, 493-495 (2007).
152. S. Besseghini, E. Villa, F. Passaretti, M. Pini and F. Bonfanti: Plastic deformation of NiMnGa polycrystals. *Materials Science and Engineering A* **378**, 415-418 (2004).
153. J. Ahn, N. Cheng, T. Lograsso and K. M. Krishnan: Magnetic properties, structure and shape-memory transitions in Ni-Mn-Ga thin films grown by ion-beam sputtering. *IEEE Transactions on Magnetism* **37**, 2141-2143 (2001).
154. V. Chernenko, M. Kohl, S. Doyle, P. Muller and M. Ohtsuka: Texture and transformation characteristics of Ni-Mn-Ga films deposited on alumina. *Scripta Materialia* **54**, 1287-1291 (2006).
155. A. Hakola, O. Heczko, A. Jaatinen, V. Kekkonen and T. Kajava: Substrate-free structures of iron-doped Ni-Mn-Ga thin films prepared by pulsed laser deposition. *Journal of Physics: Conference Series* **59**, 122-125 (2007).
156. M. Han, J. C. Bennett, M. A. Gharghoury, J. Chen and C. V. Hyatt: Understanding modulated twin transition at the atomic level. *Acta Materialia* **55**, 1731-1740 (2007).
157. M. Han and F. F. Kong: Twin boundary structure of the modulated variants in a Ni-Mn-Ga alloy. *Journal of Alloys and Compounds*, in press.
158. N. Creton and L. Hirsinger: Rearrangement surfaces under magnetic field and/or stress in Ni-Mn-Ga. *Journal of Magnetism and Magnetic Materials* **290-291**, 832-835 (2005).
159. G. Mogylnyy, I. Glavatsky, N. Glavatska, O. Söderberg, Y. Ge and V. K. Lindroos: Crystal structure and twinning in martensite of Ni_{1.96}Mn_{1.18}Ga_{0.86} magnetic shape memory alloy. *Scripta Materialia* **48**, 1427-1432 (2003).
160. K. Tsuchiya, A. Tsutsumi, H. Ohtsuka and M. Umemoto: Modification of Ni-Mn-Ga ferromagnetic shape memory alloy by addition of rare earth elements. *Materials Science and Engineering A* **378**, 370-376 (2004).
161. Y. Li, Y. Xin, C. Jiang and H. Xu: Shape memory effect of grain refined Ni₅₄Mn₂₅Ga₂₁

- alloy with high transformation temperature. *Scripta Materialia* **51**, 849-852 (2004).
162. H. B. Xu, Y. Li, C. B. Jiang: Ni-Mn-Ga high-temperature shape memory alloys. *Materials Science and Engineering A* **438-440**, 1065-1070 (2006).
163. L. Gao, W. Cai, A. L. Liu and L. C. Zhao: Martensitic transformation and mechanical properties of polycrystalline Ni₅₀Mn₂₉Ga_{21-x}Gd_x ferromagnetic shape memory alloys. *Journal of Alloys and Compounds* **425**, 314-317 (2006).
164. J. Pons, E. Cesari, C. Segui, F. Masdeu and R. Santamarta: Ferromagnetic shape memory alloys: Alternatives to Ni-Mn-Ga. *Materials Science and Engineering A* **481-482**, 57-65 (2008).
165. D. Kikuchi, T. Kanomata, Y. Yamaguchi, H. Nishihara, K. Koyama and K. Watanabe: Magnetic properties of ferromagnetic shape memory alloys Ni₂Mn_{1-x}Fe_xGa. *Journal of Alloys and Compounds* **383**, 184-188 (2004).
166. K. Koho, O. Söderberg, N. Lanska, Y. Ge, X. Liu, L. Straka, J. Vimpari, O. Heczko and V. K. Lindroos: Effect of the chemical composition to martensitic transformation in Ni-Mn-Ga-Fe alloys. *Materials Science and Engineering A* **378**, 384-388 (2004).
167. Z. H. Liu, M. Zhang, W. Q. Wang, W. H. Wang, J. L. Chen, G. H. Wu, F. B. Meng, H. Y. Liu, B. D. Liu, J. P. Qu and Y. X. Li: Magnetic properties and martensitic transformation in quaternary Heusler alloy of NiMnFeGa. *Journal of Applied Physics* **92**, 5006-5010 (2002).
168. A. A. Cherechukin, I. E. Dikshtein, D. I. Ermakov, A. V. Glebov, V. V. Koledov, D. A. Kosolapov, V. G. Shavrov, A. A. Tulaikova, E. P. Krasnoperov and T. Takagi: Shape memory effect due to magnetic field-induced thermoelastic martensitic transformation in polycrystalline Ni-Mn-Fe-Ga alloy. *Physics Letters A* **291**, 175-183 (2001).
169. G. H. Wu, W. H. Wang, J. L. Chen, L. Ao, Z. H. Liu, W. S. Zhan, T. Liang and H. B. Xu: Magnetic properties and shape memory of Fe-doped Ni₅₂Mn₂₄Ga₂₄ single crystals. *Applied Physics Letters* **80**, 634-636 (2002).
170. A. A. Cherechukin, V. V. Khovailo, R. V. Kopusov, E. P. Krasnoperov, T. Takagi and J. Tani: Training of the Ni-Mn-Fe-Ga ferromagnetic shape-memory alloys due cycling in high magnetic field. *Journal of Magnetism and Magnetic Materials* **258-259**, 523-525 (2003).

171. A. A. Cherechukin, T. Takagi, M. Miki, M. Matsumoto and M. Ohtsuka: Influence of three-dimensional transition elements on magnetic and structural phase transitions of Ni-Mn-Ga alloys. *Journal of Applied Physics* **95**, 1740-1742 (2004).
172. I. Glavatskyy, N. Glavatska, O. Söderberg, S. -P. Hannula and J. -U. Hoffmann: Transformation temperatures and magnetoplasticity of Ni-Mn-Ga alloyed with Si, In, Co or Fe. *Scripta Materialia* **54**, 1891-1895 (2006).
173. O. Söderberg, K. Koho, T. Sammi, X. W. Liu, A. Sozinov, N. Lansaka and V. K. Lindroos: Effect of the selected alloying on Ni-Mn-Ga alloys. *Materials Science and Engineering A* **378**, 389-393 (2004).
174. V. V. Khovailo, V. A. Chernenko, A. A. Cherechukin, T. Takagi and T. Abe: An efficient control of Curie temperature T_C in Ni-Mn-Ga alloys. *Journal of Magnetism and Magnetic Materials* **272-276**, 2067-2068 (2004).
175. M. Khan, I. Dubenko, S. Stadler and N. Ali: The structural and magnetic properties of $Ni_2Mn_{1-x}M_xGa$ ($M=Co, Cu$). *Journal of Applied Physics* **97**, 10M304 (2005).
176. X. Lu, X. Chen, L. Qiu and Z. Qin: Martensitic transformation of Ni-Mn-Ga (C, Si, Ge) Heusler alloys. *Journal de Physique IV* **112**, 917-920 (2003).
177. K. Tsuchiya, H. Nakamura, M. Umemoto and H. Ohtsuka: Effect of fourth elements on phase transformations in Ni-Mn-Ga alloys. *Transactions of the Materials Research Society of Japan* **25**, 517-519 (2000).
178. S. Stadler, M. Khan, J. Mitchell, N. Ali, A. M. Gomes, I. Dubenko, A. Y. Takeuchi and A. P. Guimaraes: Magnetocaloric properties of $Ni_2Mn_{1-x}Cu_xGa$. *Applied Physics Letters* **88**, 192511 (2006).
179. A. M. Gomes, M. Khan, S. Stadler, N. Ali, I. Dubenko, A. Y. Takeuchi and A. P. Guimaraes: Magnetocaloric properties of the $Ni_2Mn_{1-x}(Cu,Co)_xGa$ Heusler alloys. *Journal of Applied Physics* **99**, 08Q106 (2006).
180. I. Glavatskyy, N. Glavatska, A. Dobrinsky, J. -U. Hoffmann, O. Söderberg and S. -P. Hannula: Crystal structure and high-temperature magnetoplasticity in the new Ni-Mn-Ga-Cu magnetic shape memory alloys. *Scripta Materialia* **56**, 565-568 (2007).

Chapter 1 Investigation on crystal structure and phase transformation in Ni-Mn-Ga alloys by in situ neutron diffraction technique

Introduction

As a kind of newly developed materials, Ni-Mn-Ga FSMA have many fundamental issues remaining unclear. This has significantly impeded the improvement of the functional performances of these alloys. Full information on crystal structure of these alloys serves as the foundation for further crystallographic analysis and is of great fundamental importance to the design of high-performance FSMA with optimal properties. However, the detailed information on crystal structure of these alloys, such as space group and atomic positions, is still lacking. Precise determination of the crystal structure of parent phase and martensite in Ni-Mn-Ga alloys with different chemical composition is greatly needed. On the other hand, the phase transformation of Ni-Mn-Ga alloys, which is closely related to their MSME, is still not well understood up to now. In situ neutron diffraction study on the phase transformation process in these alloys is quite necessary.

In this chapter, the crystal structures as a function of temperature in two Ni-Mn-Ga alloys (i.e. $\text{Ni}_{53}\text{Mn}_{25}\text{Ga}_{22}$ and $\text{Ni}_{48}\text{Mn}_{30}\text{Ga}_{22}$) with different martensitic structure are precisely determined by means of in situ neutron powder diffraction technique that proves highly advantageous in determining the crystal structure of those alloy systems consisting of nearby constituent elements in the periodic table. Meanwhile, the phase transformation behaviors of the $\text{Ni}_{53}\text{Mn}_{25}\text{Ga}_{22}$ and $\text{Ni}_{48}\text{Mn}_{30}\text{Ga}_{22}$ alloys are directly investigated from the structural change, lattice parameter variation and unit-cell volume change, as revealed by in situ neutron diffraction experiments. The magnetic structure evolution in $\text{Ni}_{53}\text{Mn}_{25}\text{Ga}_{22}$ as temperature increases from 20K to 473K is tentatively investigated. The possible mechanism for the different sequences of phase transformation in Ni-Mn-Ga alloys with different martensitic transformation temperature is discussed.

Crystal structure and phase transformation in Ni₅₃Mn₂₅Ga₂₂ shape memory alloy from 20 K to 473 K

D. Y. Cong

Key Laboratory of Electromagnetic Processing of Materials (Ministry of Education), Northeastern University, Shenyang 110004, China

P. Zetterström

The Studsvik Neutron Research Laboratory (NFL), Uppsala University, S-61182 Nyköping, Sweden

Y. D. Wang

Department of Materials Science Engineering, Northeastern University, Shenyang 110004, China

R. Delaplane

The Studsvik Neutron Research Laboratory (NFL), Uppsala University, S-61182 Nyköping, Sweden

R. Lin Peng

Department of Mechanical Engineering, Linköping University, S-58183 Linköping, Sweden

X. Zhao and L. Zuo

Key Laboratory of Electromagnetic Processing of Materials (Ministry of Education), Northeastern University, Shenyang 110004, China

Abstract

The crystal structures, magnetic structures, and phase transformation of the off-stoichiometric Ni₅₃Mn₂₅Ga₂₂ were studied by neutron powder diffraction at different temperatures. It is shown that Ni₅₃Mn₂₅Ga₂₂ has a tetragonal I4/mmm structure from 20 K to 403 K. An abrupt jump in unit-cell volume around room temperature, corresponding to an endothermic peak in the differential scanning calorimetry curve, was observed. This indicates a pretransformation in the martensitic phase of Ni₅₃Mn₂₅Ga₂₂, which is completely different from the phase transformation in the stoichiometric Ni₂MnGa. The sequence of structural transformation in Ni₅₃Mn₂₅Ga₂₂ is closely related to its intrinsic temperature-dependent magnetic structure.

Key words: ferromagnetic shape memory alloy, crystal structure, phase transformation, neutron diffraction

The ferromagnetic shape-memory alloys (FSMAs) with the chemical composition close to the stoichiometric compound Ni_2MnGa have received great interest during the past several years due to the shape memory effect driven by magnetic fields. The magnetic shape memory effect is caused by the rearrangements of some martensitic variants or the movements of favorably orientated variants in applied magnetic fields.^{1,2} Although many studies have been carried out on microstructures and on the strain response to various applied magnetic fields in these Ni_2MnGa alloys,¹⁻⁵ many fundamental issues still remain to be answered, including the space group and magnetic structure of the low-temperature phase. Some controversial results have been resolved from earlier investigations by the x-ray diffraction due to the similar x-ray scattering factors for Ni, Mn, and Ga atoms.^{3,6,7}

Webster *et al.*⁸ reported the crystal structure and lattice parameters of the stoichiometric Ni_2MnGa investigated by the neutron scattering technique, however, the space group of the martensitic phase was not determined as it is influenced by many martensitic variants in the single crystal. Brown *et al.*⁹ systematically studied the crystal structures of the stoichiometric Ni_2MnGa alloy with the Curie temperature, T_c , higher than the martensitic transformation temperature, M_s , at different temperatures ranging from 20 to 400 K, but not for some off-stoichiometric Ni-Mn-Ga alloys. Some different crystal structures of (modulated and nonmodulated) martensite have already been found in the Ni-Mn-Ga alloy system, highly sensitive to the chemical compositions or the martensitic transformation temperature.¹⁰ It was also known that the sequence of structural transformation in the FSMAs is closely related to the phonon soft mode during phase transformation, intermediated by the interaction between the temperature-dependent magnetic order and the chemical- or mechanical-force-induced multiscaled structural defects. Thus, investigations of the phase transformation by neutron scattering technique in the off-stoichiometric Ni_2MnGa with T_c lower than or close to M_s could show some different transformation behaviors due to a change of magnetic structure in martensite and will answer the critical issue as to whether there exists a pretransformation phenomenon. In the present letter, we report the crystal structures, lattice parameters, and magnetic structures as a function of various temperatures from 20 K to 473 K in the $\text{Ni}_{53}\text{Mn}_{25}\text{Ga}_{22}$ alloy. We found that the phase transformation process in a $\text{Ni}_{53}\text{Mn}_{25}\text{Ga}_{22}$ alloy

is completely different from previous investigations on the stoichiometric Ni₂MnGa alloy.⁹ The present results will provide a direct experimental input for some theoretical models to elucidate the different sequence of structural transformation and different crystal structure of martensite in the Ni–Mn–Ga alloy system, still mysterious in solid-state physics and materials science.

A 100 g button ingot of Ni₅₃Mn₂₅Ga₂₂ (at. %) was prepared by repeated melting of the constituent elements, Ni, Mn, and Ga, of 3N high purity in an arc furnace protected under an argon atmosphere. The ingot was then crushed into powder with a particle size of about 200 μm, which was used for determining phase transformation temperatures and crystal structures. The Curie temperature T_c for this alloy is 380 K, which was determined by a vibrating sample magnetometer. The phase transformation temperatures were determined by differential scanning calorimetry (DSC) in the temperature range of 208 K–573 K, with a heating and cooling rate of 10 K/min. The DSC measurement demonstrates that the martensitic transformation start temperature M_s , the martensitic transformation finish temperature M_f , the austenitic transformation start temperature A_s , and the austenitic transformation finish temperature A_f are 386 K, 368 K, 408 K, and 424 K, respectively.

The crystal structure of Ni₅₃Mn₂₅Ga₂₂ as a function of temperature was determined by neutron powder diffractometry. The neutron scattering experiments were performed on SLAD (Ref. 11) at the Studsvik Neutron Research Laboratory in Sweden. The neutron wavelength used in the experiments was 1.116 Å and the diffraction pattern was collected for 2θ in the range of 3°–134°. The scattering data were then corrected for absorption, extinction, and multiple scattering in a standard way. The diffraction experiments were carried out at 20 K, 100 K, 150 K, 200 K, 250 K, 273 K, 293 K, 403 K, 423 K, and 473 K, respectively, with a CCR/furnace attached on SLAD. Both crystal structure and magnetic structure were refined from the whole diffraction profiles by the Fullprof Rietveld method.^{12,13}

The observed and calculated neutron diffraction patterns of Ni₅₃Mn₂₅Ga₂₂ at room temperature are illustrated in Fig. 1. The profile refinement of the diffracted intensities suggests a tetragonal I4/mmm-symmetric structure with $a=3.865$ Å and $c=6.596$ Å. Ni atoms occupy $4d$ (0,0.5,0.25) positions, while Mn and Ga atoms occupy $2b$ (0,0,0.5) and $2a$ (0,0,0) positions, respectively. Wedel *et al.*³ reported the same structure in their work, but they

determined the structure from only a few peaks in the x-ray diffraction pattern, which only provides limited information.

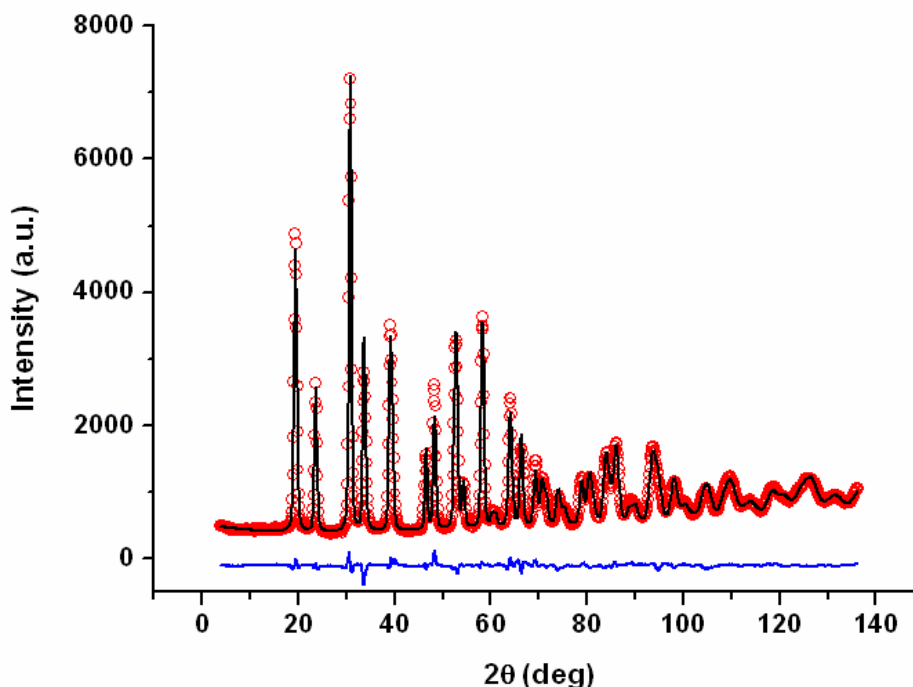
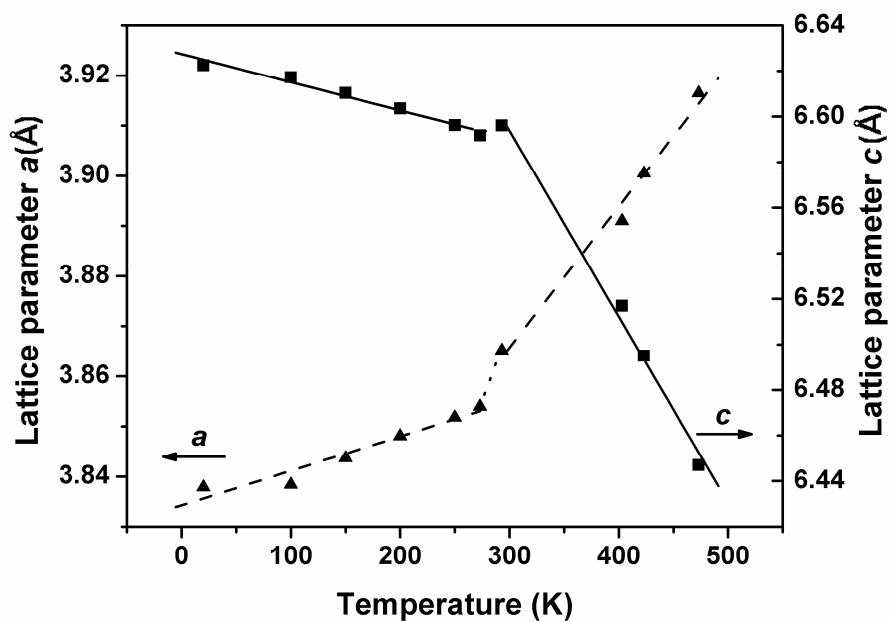
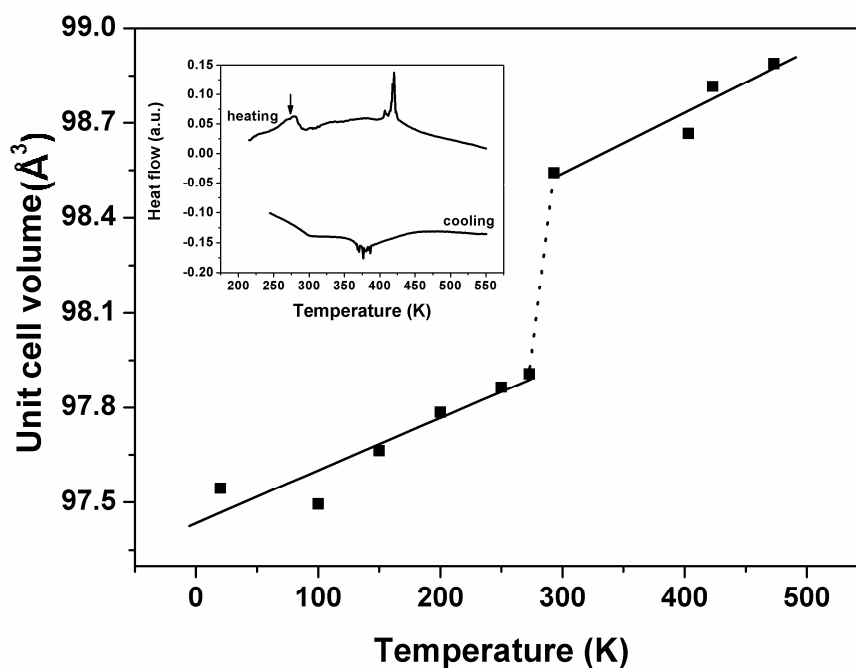


FIG. 1. The observed (circle symbol) and calculated (solid line) neutron diffraction pattern of $\text{Ni}_{53}\text{Mn}_{25}\text{Ga}_{22}$ at room temperature, together with the difference pattern at the bottom.

The neutron diffraction patterns at 20 K, 100 K, 150 K, 200 K, 250 K, 273 K, and 403 K also suggest the tetragonal $I4/mmm$ martensitic structure with some parameter variations as temperature changes. No indication of a modulated structure is observed because there are no small side peaks around the main Bragg peaks in all the diffraction patterns, which is different from the structure of the stoichiometric Ni_2MnGa alloy.⁹ The neutron diffraction patterns at 423 K and 473 K show that there are two mixed phases in the $\text{Ni}_{53}\text{Mn}_{25}\text{Ga}_{22}$ alloy, one tetragonal martensitic phase and one austenitic parent phase, suggesting the starting of the austenitic transformation. However, there is still a pretransformation occurring before the austenitic transformation, as discussed below.



(a)



(b)

FIG. 2. Temperature dependence of lattice parameters a (triangle symbol) and c (square symbol) (a) and the unit-cell volume (b) of $\text{Ni}_{53}\text{Mn}_{25}\text{Ga}_{22}$. All the data are linearly fitted in two different temperature regions: 20 K–273 K and 293 K–473 K. The inset shows the DSC curve of $\text{Ni}_{53}\text{Mn}_{25}\text{Ga}_{22}$, in which the arrow indicates the endothermic peak corresponding to the unit-cell volume jump around room temperature.

The temperature dependence of lattice parameters and the unit-cell volume are shown in Fig. 2. The lattice parameter a increases with increasing temperature, while lattice parameter c has a tendency to decrease as temperature increases, as illustrated in Fig. 2(a). The unit-cell volume expands as the temperature increases, as illustrated in Fig. 2(b). It is worth noting that there is an abrupt jump in unit-cell volume between 273 K–293 K. Aside from this, the temperature dependencies of lattice parameters (a and c) and unit-cell volumes are well linearly fitted in the two different temperature regions, i.e., 20 K–273 K and 293 K–403 K, respectively, showing obvious changes of slopes in these two regions. It is also noteworthy that the temperature range of 273 K–293 K corresponds well to the endothermic peak around room temperature (marked by the arrow) in the DSC curve during heating, as illustrated in the inset of Fig. 2(b).

The unit-cell volume jump and the corresponding endothermic peak observed around room temperature indicate that there is a pretransformation between 273 K–293 K during the heating process of $\text{Ni}_{53}\text{Mn}_{25}\text{Ga}_{22}$. The low-temperature martensitic phase first transforms into the intermartensitic phase around room temperature and then into the austenitic phase at higher temperature. This transformation process is completely different from the transformation behavior in the stoichiometric Ni_2MnGa reported previously.⁹ This is attributed to the fact that the phonon softening and soft mode condensation—in a premartensitic phase prior to the martensitic transformation—occur in stoichiometric Ni_2MnGa with M_s about 200 K, but the softening process is inhibited by the martensitic transformation occurring before in the Ni–Mn–Ga alloys with a higher M_s temperature.^{10,14} Therefore, the $\text{Ni}_{53}\text{Mn}_{25}\text{Ga}_{22}$ alloy does not undergo any premartensitic transformation with modulated structure, but experiences an intermartensitic transformation instead.

One unique feature with neutron scattering is that it reveals the magnetic structure, which cannot be studied by x-ray diffraction. For comparison, the data were refined both with and without magnetic structure. The magnetic structure at 20 K, obtained as the difference between the calculated patterns with and without magnetic structure, is shown in Fig. 3. The influence of magnetic structure on the first two low-angle Bragg peaks was clearly observed. The magnetic structures at 100 K, 150 K, 200 K, 250 K, 273 K, and 293 K were also obtained,

as illustrated in the inset of Fig. 3. The results show that magnetic structure of $\text{Ni}_{53}\text{Mn}_{25}\text{Ga}_{22}$ becomes weaker as the temperature increases, which is due to the decreasing magnetic order. We also tried to refine the data collected at 403 K with magnetic structure, but it shows that the influence of magnetic structure is negligible, attributed to the magnetic disorder (paramagnetic structure) at this temperature, in agreement with the magnetic measurement. It should be noted that the decreasing magnitude of the Mn moment with increasing temperature was also observed in the refinements, confirming that the magnetic structure weakens with increasing temperature.

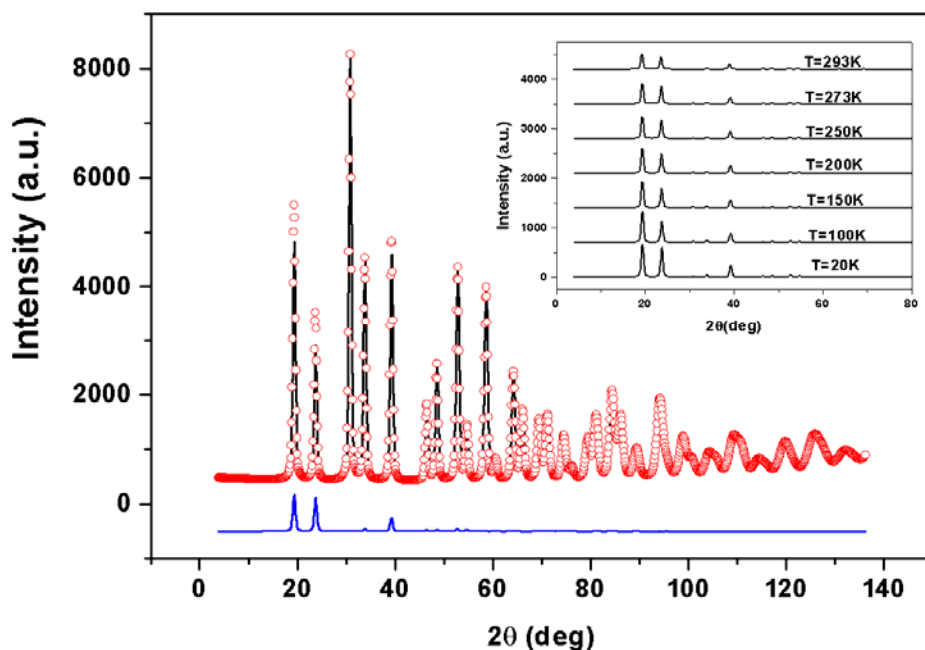


FIG. 3. The calculated neutron diffraction pattern with (circle symbol) and without (solid line) magnetic structure at 20 K. The bottom curve shows the magnetic structure of $\text{Ni}_{53}\text{Mn}_{25}\text{Ga}_{22}$ at 20 K. The inset shows the magnetic structure evolution as temperature increases.

Our above tentative experimental investigation of magnetic structure as a function of temperature provides unambiguous evidence that the changes of magnetic structure are closely related to the intermartensitic transformation for $\text{Ni}_{53}\text{Mn}_{25}\text{Ga}_{22}$. The present authors believed that the difference in the sequences of structural transformation for Ni_2MnGa and $\text{Ni}_{53}\text{Mn}_{25}\text{Ga}_{22}$ is due to the difference between T_c and M_s , rather than just M_s .¹⁰ While T_c is

higher than M_s , pretransformation may occur in the austenite, as observed for the stoichiometric Ni₂MnGa reported previously.⁹ While T_c is lower than or close to M_s , pretransformation occurs in martensite, as observed for the present composition. Finally, we hope that this finding will provide some fundamental experimental data for the prediction of the detailed nonmodulated or modulated crystal structure in martensite and for establishing theory on the kinetics and dynamics of martensitic transformation in the Ni–Mn–Ga FSMAs.

In summary, the martensitic structure of the polycrystalline sample Ni₅₃Mn₂₅Ga₂₂ investigated by neutron scattering technique shows that it has a tetragonal I4/mmm structure from 20 K to 403 K. No modulation appears at low temperature, which differs from earlier investigations of the stoichiometric Ni₂MnGa alloy.⁹ The temperature dependence of lattice parameters and unit-cell volume of Ni₅₃Mn₂₅Ga₂₂ shows that there is an abrupt jump in unit-cell volume between 273 K and 293 K, which corresponds to an endothermic peak observed in the measured DSC curve. The above observation indicates the existence of a pretransformation in martensite around room temperature in the Ni₅₃Mn₂₅Ga₂₂ alloy, which is closely related to its intrinsic temperature-dependent magnetic structure.

The authors are grateful to the National Ministry of Education of China (with the New-Century Outstanding Scholars Fund), the National Natural Science Foundation of China (Grant No. 50471026), and the Swedish Research Council in the frame of the SIDA project (Grant No. 348-2004-3475) for their financial support.

References

- ¹A. Sozinov, A. A. Likhachev, N. Lanska, and K. Ullakko, *Appl. Phys. Lett.* **80**, 1746 (2002).
- ²S. J. Murray, M. A. Marioni, A. M. Kukla, J. Robinson, R. C. O’Handley, and S. M. Allen, *J. Appl. Phys.* **87**, 5774 (2000).
- ³B. Wedel, M. Suzuki, Y. Murakami, C. Wedel, T. Suzuki, D. Shindo, and K. Itagaki, *J. Alloys Compd.* **290**, 137 (1999).
- ⁴J. Pons, V. A. Chernenko, R. Santamarta, and E. Cesari, *Acta Mater.* **48**, 3027 (2000).
- ⁵K. Ullakko, Y. Ezer, A. Sozinov, G. Kimmel, P. Yakovenko, and V. K. Lindroos, *Scr. Mater.* **44**, 475 (2001).

- ⁶G. Mogylnyy, I. Glavatsky, N. Glavatska, O. Söderberg, Y. Ge, and V. A. Lindroos, *Scr. Mater.* **48**, 1427 (2003).
- ⁷C. Jiang, Y. Muhammad, L. Deng, W. Wu, and H. Xu, *Acta Mater.* **52**, 2779 (2004).
- ⁸P. J. Webster, K. R. A. Ziebeck, S. L. Town, and M. S. Peak, *Philos. Mag. B* **49**, 295 (1984).
- ⁹P. J. Brown, J. Crangle, T. Kanomata, M. Matsumoto, K.-U. Neumann, B. Ouladdiaf, and K. R. A. Ziebeck, *J. Phys.: Condens. Matter* **14**, 10159 (2002).
- ¹⁰V. A. Chernenko, J. Pons, C. Segui, and E. Cesari, *Acta Mater.* **50**, 53 (2002).
- ¹¹A. Wannberg, A. Møllergård, P. Zetterström, R. Delaplane, M. Grönros, L.-E. Karlsson, and R. L. McGreevy, *J. Neutron Res.* **8**, 133 (1999).
- ¹²R. A. Young and D. B. Wiles, *J. Appl. Crystallogr.* **15**, 430 (1982).
- ¹³L. B. McCusker, R. B. Von Dreele, D. E. Cox, D. Louer, and P. Scardi, *J. Appl. Crystallogr.* **32**, 36 (1999).
- ¹⁴V. A. Chernenko, C. Segui, E. Cesari, J. Pons, and V. V. Kokorin, *Phys. Rev. B* **57**, 2659 (1998).

Neutron diffraction study on crystal structure and phase transformation in Ni-Mn-Ga ferromagnetic shape memory alloys

D. Y. Cong, Y. D. Wang, J. Z. Xu, and L. Zuo

Key Laboratory for Anisotropy and Texture of Materials (MOE), Northeastern University, Shenyang, 110004, China

P. Zetterström

Department of Structural Chemistry, Stockholm University, S-10691 Stockholm, Sweden

R. Delaplane

The Studsvik Neutron Research Laboratory (NFL), Uppsala University, S-61182 Nyköping, Sweden

Abstract

Crystal structure and phase transformation behaviors in two Ni-Mn-Ga ferromagnetic shape memory alloys (FSMAs) with compositions of $\text{Ni}_{48}\text{Mn}_{30}\text{Ga}_{22}$ and $\text{Ni}_{53}\text{Mn}_{25}\text{Ga}_{22}$ (at. %) as a function of temperature were investigated by *in situ* neutron diffraction experiments. Neutron diffraction technique proves to be highly efficient in characterizing structural transformation in Ni-Mn-Ga FSMAs, which consist of nearby elements in the periodic table. Our neutron results show that $\text{Ni}_{48}\text{Mn}_{30}\text{Ga}_{22}$ has a cubic, $L2_1$ Heusler structure from 373 to 293 K. Its crystal structure changes into a seven-layered orthorhombic martensitic structure when cooled to 243 K, and no further transformation is observed upon cooling to 19 K. Neutron diffraction results also show that $\text{Ni}_{53}\text{Mn}_{25}\text{Ga}_{22}$ has a tetragonal $I4/mmm$ martensitic structure from 20 to 403 K. A pre-transformation around room temperature is observed from an abrupt jump in unit-cell volume of $\text{Ni}_{53}\text{Mn}_{25}\text{Ga}_{22}$, which corresponds to an endothermic peak detected in a heated DSC curve.

Key words: neutron powder diffraction, ferromagnetic shape memory alloy, crystal structure, martensitic transformation, Ni-Mn-Ga alloy

I. INTRODUCTION

Ni-Mn-Ga ferromagnetic shape memory alloys (FSMAs) with a chemical composition close to stoichiometric Ni_2MnGa compound prove to be promising materials as potential candidates for magnetic-field-driven actuators and sensors (Sozinov *et al.*, 2002; Murray *et al.*, 2000). Although intensive studies have been carried out on many aspects in the Ni-Mn-Ga alloy system (Sozinov *et al.*, 2002; Murray *et al.*, 2000; Wedel *et al.*, 1999; Pons *et al.*, 2000; Wang *et al.*, 2006), there remain many important fundamental issues, such as crystal structures of both parent phase and low-temperature martensite and phase transformation behavior. Previous reports focus mostly on crystal structures of Ni-Mn-Ga alloys characterized by X-ray diffraction technique (Wedel *et al.*, 1999; Pons *et al.*, 2000). Since the atomic numbers of Ni, Mn, and Ga are close, X-ray scattering factors of these elements are quite similar, which makes it very difficult to accurately determine crystal structures of Ni-Mn-Ga alloys (Wedel *et al.*, 1999; Pons *et al.*, 2000).

One of the unique features in neutron diffraction is that neutron scattering factors of elements show irregular changes with atomic numbers, and this provides an acute discernment of adjacent or nearby elements in the periodic table. Therefore, the neutron diffraction technique is an ideal tool for studying crystal structures of the Ni-Mn-Ga FSMAs. In addition, *in situ* neutron diffraction experiments at different temperatures also enable a study of phase transformation behavior, which is closely related to the shape memory effects of those alloys. In the present study, the crystal structure and phase transformation behaviors of $\text{Ni}_{48}\text{Mn}_{30}\text{Ga}_{22}$ and $\text{Ni}_{53}\text{Mn}_{25}\text{Ga}_{22}$ alloys are studied by the neutron diffraction technique. For comparison, some X-ray diffraction results are also included. It will be demonstrated that neutron diffraction is highly efficient in determining the crystal structures of those alloy systems consisting of nearby constituent elements in the periodic table, including the newly developed Ni-Mn-Ga FSMAs.

II. EXPERIMENTAL

Two Ni-Mn-Ga button ingots with chemical compositions of $\text{Ni}_{48}\text{Mn}_{30}\text{Ga}_{22}$ and $\text{Ni}_{53}\text{Mn}_{25}\text{Ga}_{22}$ (at. %) were prepared by repeated melting of high-purity constituent elements

of Ni, Mn, and Ga under Ar atmosphere. The ingots were then crushed into powders for determining phase transformation temperatures and crystal structures. Differential scanning calorimetry (DSC) measurements were used and show that martensitic transformation starting temperatures M_s of $\text{Ni}_{48}\text{Mn}_{30}\text{Ga}_{22}$ and $\text{Ni}_{53}\text{Mn}_{25}\text{Ga}_{22}$ are 269 and 386 K, respectively. Thus, $\text{Ni}_{48}\text{Mn}_{30}\text{Ga}_{22}$ has an austenitic structure while $\text{Ni}_{53}\text{Mn}_{25}\text{Ga}_{22}$ has a martensitic structure at room temperature. Crystal structures at different temperatures were determined by neutron diffraction experiments on beam line R2D2 with an attached CCR/furnace at the Studsvik Neutron Research Laboratory in Sweden. Neutron wavelength used in the experiments was 1.5515 Å, and neutron diffraction patterns were collected for a 2θ range of 5 to 114 deg. Crystal structures were refined from whole diffraction profiles by the Fullprof Rietveld method (McCusker *et al.*, 1999).

III. RESULTS AND DISCUSSION

Figure 1 (a) shows an X-ray diffraction pattern of $\text{Ni}_{48}\text{Mn}_{30}\text{Ga}_{22}$ alloy at room temperature, in which only one strong Bragg peak together with three relatively weaker peaks can be detected. It is difficult to determine crystal structure from such limited numbers of X-ray diffraction peaks. In contrast, 14 distinct Bragg peaks can be clearly observed from a neutron diffraction pattern, as illustrated in Figure 1(b), and this enables an accurate determination of its crystal structure. Rietveld refinement of all peaks in the neutron diffraction pattern shows that $\text{Ni}_{48}\text{Mn}_{30}\text{Ga}_{22}$ has a cubic, $L2_1$ Heusler austenitic structure with lattice parameters $a=b=c=5.8398$ Å at room temperature. The space group for this structure is $Fm\bar{3}m$, No. 225. Ni atoms occupy $8c$ (0.25,0.25,0.25) sites, while Mn and Ga atoms occupy $4b$ (0.5,0.5,0.5) and $4a$ (0,0,0) sites, respectively (Cong *et al.*, 2005a).

In order to study phase transformation behavior of $\text{Ni}_{48}\text{Mn}_{30}\text{Ga}_{22}$, the alloy was cooled continuously from 373 to 19 K, and neutron diffraction measurements were performed at 373, 323, 293, 243, 203, 183, 140, and 19 K. Figure 2 illustrates observed and calculated neutron diffraction patterns at 203 K, and it can be seen that some Bragg peaks split because of a lower symmetry in the martensitic structure. All peaks in the neutron diffraction pattern can be indexed according to an orthorhombic structure with lattice parameters $a=4.2334$ Å,

$b=29.4093 \text{ \AA}$, and $c=5.5588 \text{ \AA}$. Rietveld refinement indicates that the space group of this structure is $Pnmm$ (No. 58). Parameters of this structure are summarized in Table I. Rietveld refinement results also show that $\text{Ni}_{48}\text{Mn}_{30}\text{Ga}_{22}$ has a seven-layered martensitic structure with a small orthorhombic distortion, i.e., $(a-b/7) = 0.0321 \text{ \AA}$.

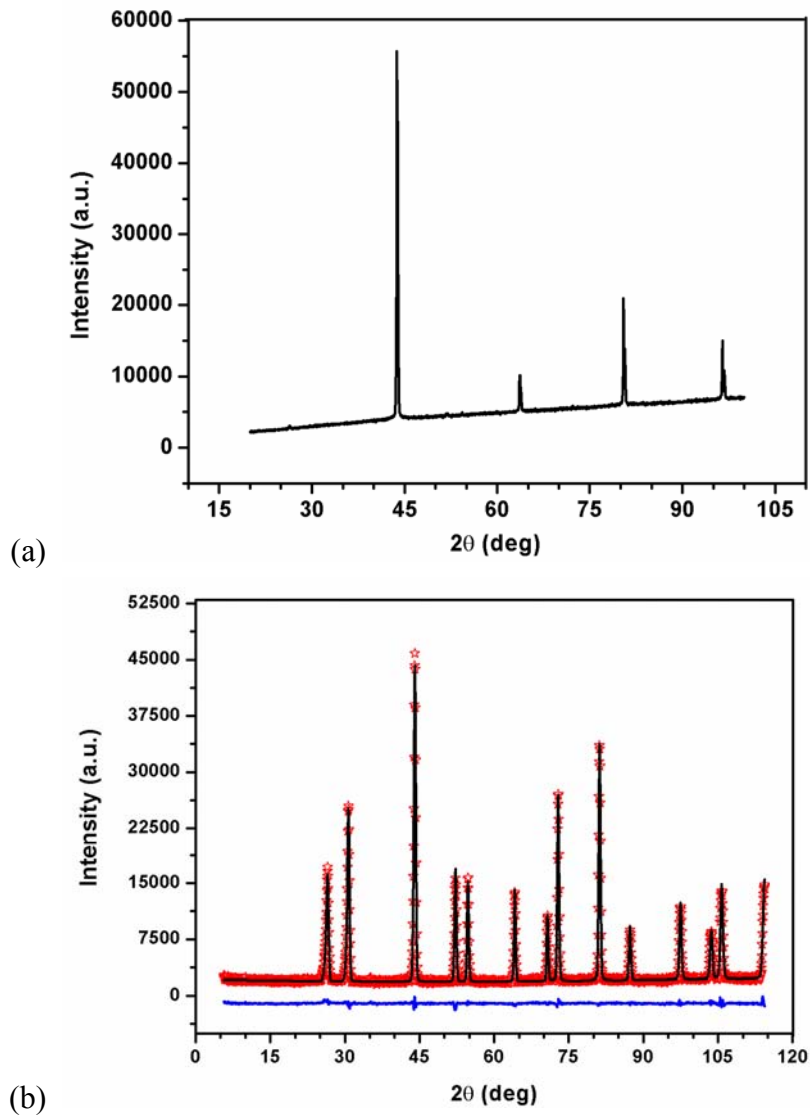


Figure 1. (a) X-ray diffraction pattern. (b) Observed (open star) and calculated (solid curve) neutron diffraction patterns, together with the difference pattern at the bottom, of $\text{Ni}_{48}\text{Mn}_{30}\text{Ga}_{22}$ at room temperature.

Crystalline phases, lattice parameters, and unit-cell volumes of $\text{Ni}_{48}\text{Mn}_{30}\text{Ga}_{22}$ at different temperatures from 373 to 19 K are listed in Table II. For ease of comparison, lattice parameter and unit-cell volume variations as a function of temperature are plotted in Figure 3. From

Table II and Figure 3, it can be clearly seen that the alloy has an austenitic structure in a temperature range between 373 and 293 K. Its lattice parameter a decreases and the unit-cell volume shrinks with temperature decreasing. When cooled to 243 K, the alloy transforms to martensite. Upon further cooling, lattice parameters a and b increase gradually, while c decreases rapidly. As a consequence, unit-cell volume shrinks as temperature decreases. No substantial changes can be observed in the neutron diffraction patterns at temperatures cooling from 243 down to 19 K. This indicates that there is no intermartensitic transformation, which is different from the transformation process found in other Ni-Mn-Ga alloys with high martensitic transformation temperatures (Wang *et al.*, 2001).

Lattice parameters and their temperature dependencies can be used to understand martensitic transformation and the related phenomena in the FSMAs. Also, the lattice parameters for the austenite and martensite can also be used to determine theoretical maximum output of magnetic shape memory effect. Our results on crystal structure and its change as a function of temperature may offer useful information for verifying theories and establishing numerical models to elucidate functional behaviors in the Ni-Mn-Ga FSMAs.

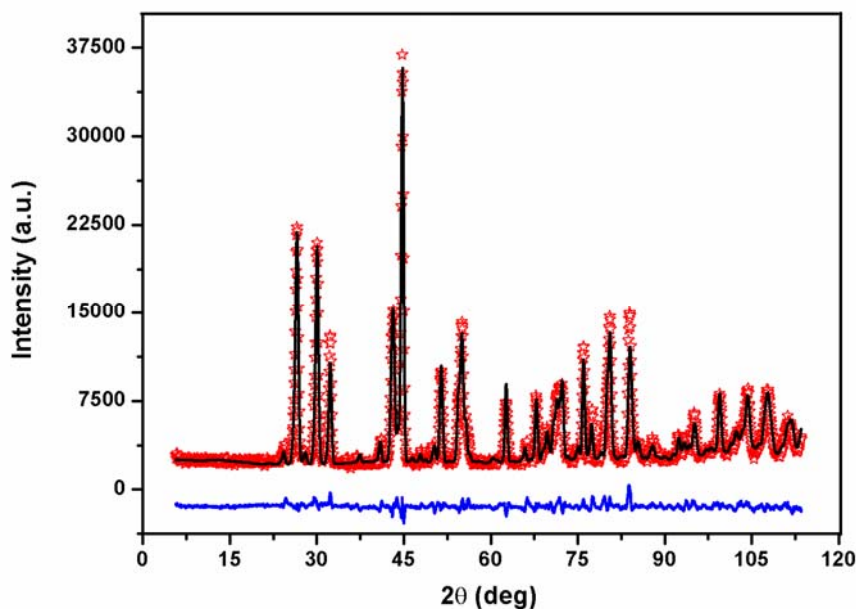


Figure 2. Observed (open star) and calculated (solid curve) neutron diffraction patterns, together with the difference pattern at the bottom, of $\text{Ni}_{48}\text{Mn}_{30}\text{Ga}_{22}$ at 203 K.

TABLE I. Parameters of the crystal structure for Ni₄₈Mn₃₀Ga₂₂ at 203 K, with space group *Pnnm* (No. 58). Lattice parameters $a=4.2334 \text{ \AA}$, $b=29.4093 \text{ \AA}$, and $c=5.5588 \text{ \AA}$.

Atom	Wyckoff position	x	y	z
Ni1	4 <i>f</i>	1/2	0	1/4
Ni2	8 <i>h</i>	0.4463	1/7	1/4
Ni3	8 <i>h</i>	0.5197	2/7	1/4
Ni4	8 <i>h</i>	0.4228	3/7	1/4
Mn1	2 <i>a</i>	0	0	0
Mn2	4 <i>g</i>	-0.0451	1/7	0
Mn3	4 <i>g</i>	0.1064	2/7	0
Mn4	4 <i>g</i>	0.0030	3/7	0
Ga1	2 <i>b</i>	0	0	1/2
Ga2	4 <i>g</i>	-0.0116	1/7	1/2
Ga3	4 <i>g</i>	0.0855	2/7	1/2
Ga4	4 <i>g</i>	-0.0342	3/7	1/2

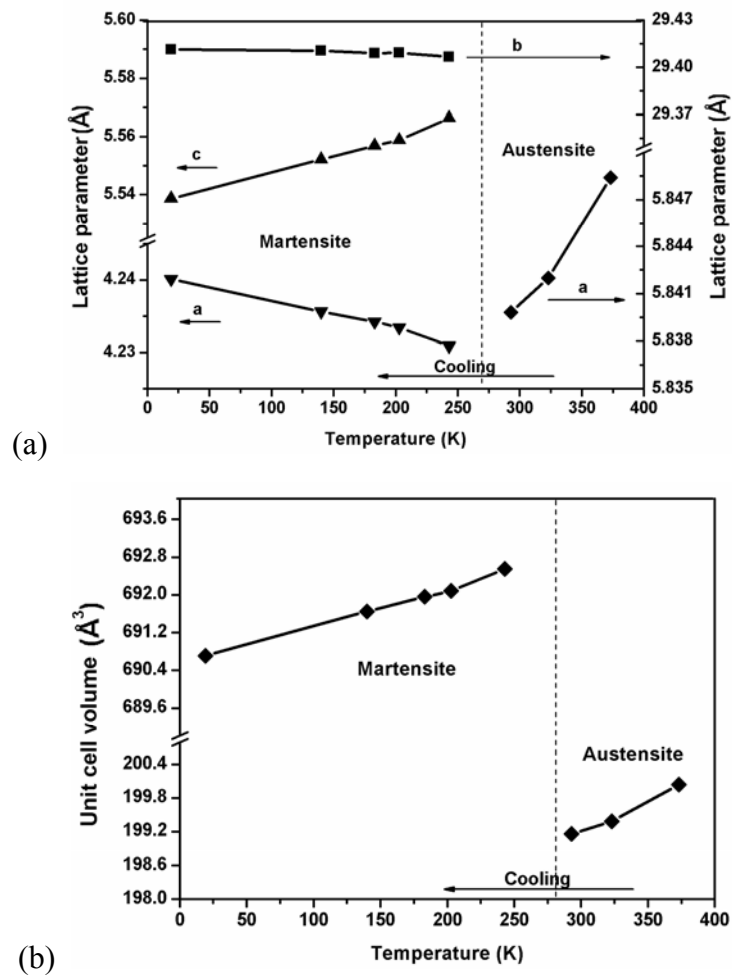
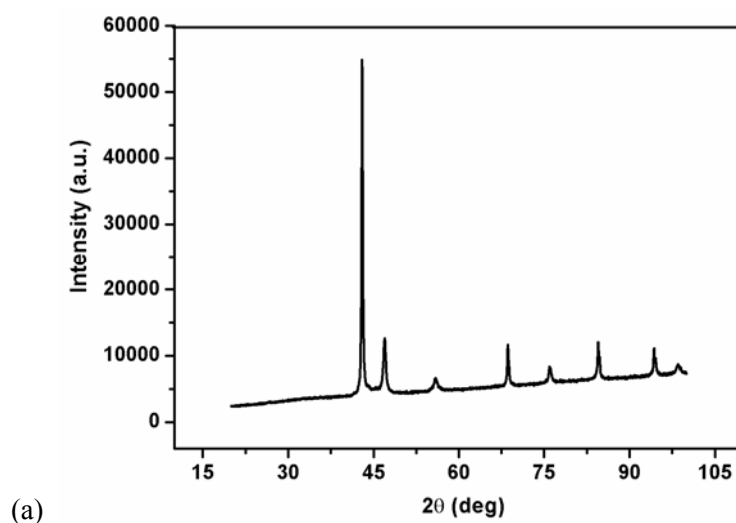


Figure 3. (a) Lattice parameters. (b) Variation in unit-cell volume as a function of temperature in Ni₄₈Mn₃₀Ga₂₂ alloy.

TABLE II. Lattice parameters and unit-cell volumes for Ni₄₈Mn₃₀Ga₂₂ alloy at different temperatures.

Temperature (K)	Phase	<i>a</i> (Å)	<i>b</i> (Å)	<i>c</i> (Å)	Unit-cell volume (Å ³)
373	Austenite	5.8484			200.04
323	Austenite	5.8420			199.38
293	Austenite	5.8398			199.16
243	Martensite	4.2309	29.4066	5.5664	692.55
203	Martensite	4.2334	29.4093	5.5588	692.08
183	Martensite	4.2342	29.4089	5.5569	691.96
140	Martensite	4.2356	29.4107	5.5522	691.65
19	Martensite	4.2401	29.4113	5.5387	690.71

Figure 4 shows X-ray and neutron diffraction patterns of Ni₅₃Mn₂₅Ga₂₂ at room temperature. Only one strong Bragg peak and several relatively weaker peaks can be observed in the X-ray diffraction pattern [Figure 4(a)], and this precludes an accurate crystal-determination of a martensite with a low symmetry for this alloy. Fortunately, a large number of Bragg peaks appear in its neutron diffraction pattern [Figure 4 (b)], making it feasible to determine its crystal structure. Rietveld refinement of all peaks in the neutron diffraction pattern suggests a tetragonal martensitic structure with $a=b=3.865$ Å and $c=6.596$ Å. The space group of this structure is $I4/mmm$, No. 139. Ni atoms occupy $4d$ (0,0.5,0.25) sites, while Mn and Ga atoms occupy $2b$ (0,0,0.5) and $2a$ (0,0,0) sites, respectively (Cong *et al.*, 2005b).



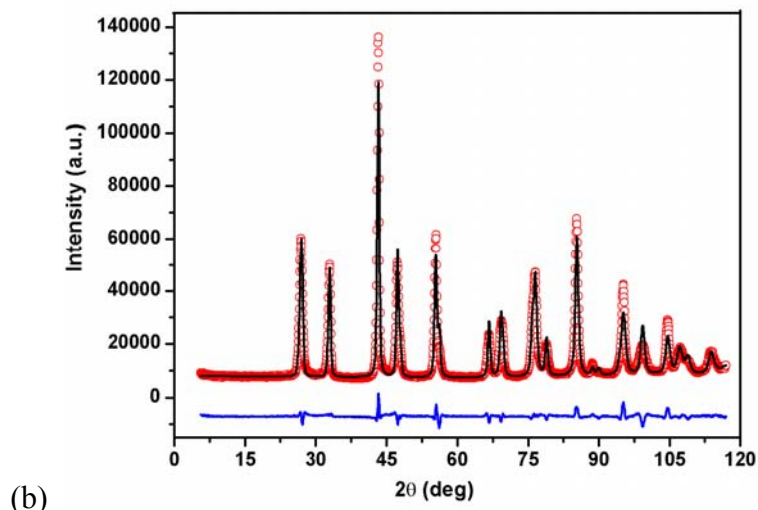


Figure 4. (a) X-ray diffraction pattern. (b) Observed (open circle) and calculated (solid curve) neutron diffraction patterns, together with the difference pattern at the bottom, of $\text{Ni}_{53}\text{Mn}_{25}\text{Ga}_{22}$ at room temperature.

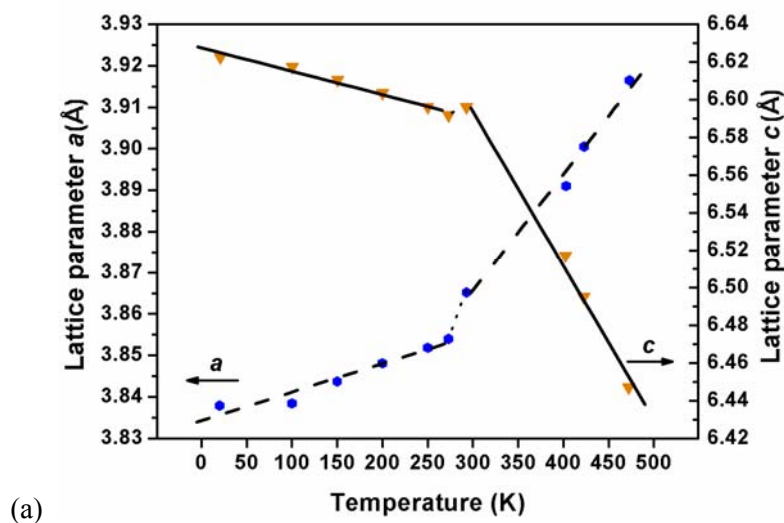
In order to study phase transformation behavior of $\text{Ni}_{53}\text{Mn}_{25}\text{Ga}_{22}$, neutron diffraction experiments were also performed from 20 to 473 K. A study of the neutron diffraction patterns at 20, 100, 150, 200, 250, 273, and 403 K also suggests the tetragonal $I4/mmm$ martensitic structure with lattice parameters varying with temperature. The diffraction patterns at 423 and 473 K indicate two mixed phases in this alloy: the tetragonal martensitic phase and a minor cubic austenitic phase. Lattice parameters a and c , c/a ratios, and unit-cell volumes of the martensitic phase at different temperatures are summarized in Table III. Variations of lattice parameters a and c , c/a ratio, and unit-cell volume as a function of temperature are shown in Figure 5. Lattice parameter a increases, while c decreases as temperature increases [see Figure 5(a)], resulting in a decrease of the c/a ratio with increasing temperature [see Figure 5(b)]. Unit-cell volume expands with increasing temperature, as shown in Figure 5(c). It is worth noting that there is an abrupt jump in unit-cell volume between 273 and 293 K. In addition, temperature dependencies of lattice parameters, c/a ratio, and unit-cell volume each are found to vary linearly with two very different slopes in two different temperature regions of 20 to 273 K and 293 to 473 K. Moreover, it is also noteworthy that the temperature range of 273 K to 293 K corresponds well with an endothermic peak appearing around room temperature in a heated DSC curve shown in Figure

5(d.) A jump in the unit-cell volume together with the observed endothermic peak observed around room temperature indicates that there is a pre-transformation between 273 and 293 K prior to the austenitic transformation at a higher temperature. The low-temperature martensitic phase first transforms into intermartensitic phase around room temperature and then into the austenitic phase at higher temperature. This transformation process in $\text{Ni}_{53}\text{Mn}_{25}\text{Ga}_{22}$ is completely different from that in stoichiometric Ni_2MnGa reported previously (Zheludev *et al.*, 1996).

TABLE III. Lattice parameters a , c , c/a ratios, and unit-cell volumes for $\text{Ni}_{53}\text{Mn}_{25}\text{Ga}_{22}$ martensites at different temperatures.

Temperature (K)	a (Å)	c (Å)	c/a	Unit-cell volume (Å ³)
20	3.8379	6.6225	1.7256	97.544
100	3.8384	6.6172	1.7240	97.494
150	3.8437	6.6104	1.7198	97.664
200	3.8481	6.6035	1.7160	97.784
250	3.8518	6.5962	1.7125	97.865
273	3.8540	6.5918	1.7104	97.907
293	3.8652	6.5962	1.7066	98.542
403	3.8910	6.5170	1.6749	98.667
423 ^a	3.9005	6.4950	1.6652	98.816
473 ^a	3.9165	6.4470	1.6461	98.888

^aThere are two phases at these temperatures, but only the parameters of martensite are listed.



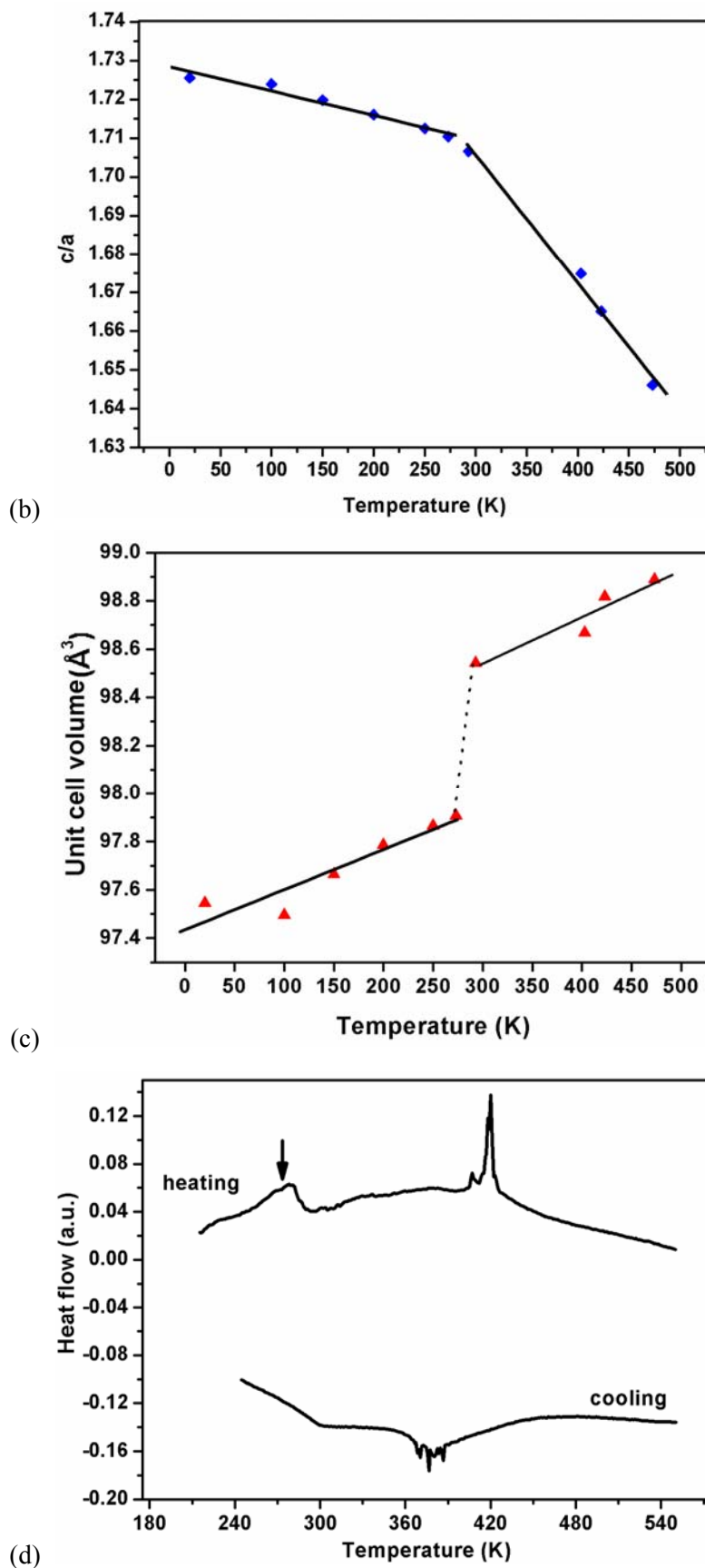


Figure 5. (a) Lattice parameters. (b) c/a ratio. (c) Variation in unit-cell volume as a function of temperature in $\text{Ni}_{53}\text{Mn}_{25}\text{Ga}_{22}$ alloy. (d) DSC curves for $\text{Ni}_{53}\text{Mn}_{25}\text{Ga}_{22}$ alloy.

IV. SUMMARY

Neutron diffraction technique proves to be highly efficient in studying the crystal structure and phase transformation behavior for Ni-Mn-Ga FSMAs, whereas this is very difficult, if not impossible, by X-ray diffraction technique. Our neutron diffraction experiments show that $\text{Ni}_{48}\text{Mn}_{30}\text{Ga}_{22}$ has a cubic $L2_1$ Heusler structure from 373 to 293 K. The crystal structure changes into a seven-layered orthorhombic martensitic structure when cooled to 243 K, and no new transformation is found upon further cooling to 19 K. Neutron diffraction results also show that $\text{Ni}_{53}\text{Mn}_{25}\text{Ga}_{22}$ has a tetragonal $I4/mmm$ martensitic structure from 20 to 403 K. A pre-transformation around room temperature is observed in $\text{Ni}_{53}\text{Mn}_{25}\text{Ga}_{22}$ from an abrupt jump in unit-cell volume, which corresponds to an endothermic peak in the heated DSC curve.

ACKNOWLEDGMENTS

This work is supported by the National Natural Science Foundation of China (Grant No. 50531020), the Ministry of Education of China with the Specialized Research Fund for a Doctoral Program of High Education, and the Swedish Research Council in the frame of the SIDA project (Grant No.348-2004-3475). One of the authors (D. Y. Cong) acknowledges the financial support from the project PRA MX04-02 and a Ph.D. fund from Northeastern University.

REFERENCES

- Cong, D. Y., Wang, Y. D., Zetterström, P., Peng, R. L., Delaplane, R., Zhao, X., and Zuo, L. (2005a). “Crystal structures and textures of hot forged $\text{Ni}_{48}\text{Mn}_{30}\text{Ga}_{22}$ alloy investigated by neutron diffraction technique,” *Mat. Sci. Technol.* **21**, 1412–1416.
- Cong, D. Y., Zetterström, P., Wang, Y. D., Delaplane, R., Peng, R. L., Zhao, X., and Zuo, L. (2005b). “Crystal structure and phase transformation in $\text{Ni}_{53}\text{Mn}_{25}\text{Ga}_{22}$ shape memory alloy from 20 K to 473 K,” *Appl. Phys. Lett.* **87**, 111906.
- McCusker, L. B., Von Dreele, R. B., Cox, D. E., Louër, D., and Scardi, P. (1999). “Rietveld refinement guidelines,” *J. Appl. Crystallogr.* **32**, 36–50.

- Murray, S. J., Marioni, M. A., Kukla, A. M., Robinson, J., O'Handley, R. C., and Allen, S. M. (2000). "Large field induced strain in single crystalline Ni-Mn-Ga ferromagnetic shape memory alloy," *J. Appl. Phys.* **87**, 5774–5776.
- Pons, J., Chernenko, V. A., Santamarta, R., and Cesari, E. (2000). "Crystal structure of martensitic phases in Ni-Mn-Ga shape memory alloys," *Acta Mater.* **48**, 3027–3038.
- Sozinov, A., Likhachev, A. A., Lanska, N., and Ullakko, K. (2002). "Giant magnetic-field-induced strain in NiMnGa seven-layered martensitic phase," *Appl. Phys. Lett.* **80**, 1746–1748.
- Wang, W. H., Wu, G. H., Chen, J. L., Gao, S. X., Zhan, W. S., Wen, G. H., and Zhang, X. X. (2001). "Intermartensitic transformation and magnetic-field-induced strain in $\text{Ni}_{52}\text{Mn}_{24.5}\text{Ga}_{23.5}$ single crystals," *Appl. Phys. Lett.* **79**, 1148–1150.
- Wang, Y. D., Cong, D. Y., Peng, R. L., Zetterström, P., Zhang, Z. F., Zhao, X., and Zuo, L. (2006). "Textures and compressive properties of ferromagnetic shape-memory alloy $\text{Ni}_{48}\text{Mn}_{25}\text{Ga}_{22}\text{Co}_5$ prepared by isothermal forging process," *J. Mater. Res.* **21**, 691–697.
- Wedel, B., Suzuki, M., Murakami, Y., Wedel, C., Suzuki, T., Shindo, D., and Itagaki, K. (1999). "Low temperature crystal structure of Ni-Mn-Ga alloys," *J. Alloys Compd.* **290**, 137–143.
- Zheludev, A., Shapiro, S. M., Wochner, P., and Tanner, L. E. (1996). "Precursor effects and premartensitic transformation in Ni_2MnGa ," *Phys. Rev. B* **54**, 15045–15050.

Chapter 2 Microstructure and martensitic transformation crystallography of Ni-Mn-Ga alloys

Introduction

As is well known, the microstructure and crystallography of the FSMAs plays an important role in determining the performances of these materials. A thorough understanding of the detailed microstructural characteristics of the martensitic variants in FSMAs is of great significance to the microstructure control and thus the property optimization of these materials. Nevertheless, no systematic investigation has been devoted to these aspects heretofore. Furthermore, the crystallographic information on this new kind of materials is still insufficient. The orientation relationship between martensitic variants and the orientation relationship between austenite and martensite during phase transformation have rarely been studied. As a matter of fact, insight into the correlation between the microstructural and crystallographic features of the Ni-Mn-Ga alloys is of both theoretical significance and practical interest to the development of the promising FSMAs with optimal properties.

Based on the crystal structure information obtained in Chapter 1, EBSD technique in a high-resolution SEM equipped with a field emission gun is utilized to investigate the crystallographic and microstructural features of the martensitic variants in $\text{Ni}_{53}\text{Mn}_{25}\text{Ga}_{22}$ FSMAs treated under different procedures in this chapter. Misorientation calculations are conducted to determine the orientation relationship between the neighboring martensitic variants. Two-surface trace analysis is performed to determine the twin interface plane. An indirect method is used to determine the orientation relationship between austenite and martensite from the measured orientations of martensite. The crystallographic phenomenological theory proposed by Wechsler, Lieberman and Read (WLR theory) is employed to quantitatively explain the crystallographic features during the martensitic transformation.

Determination of microstructure and twinning relationship between martensitic variants in 53 at.%Ni–25 at.%Mn–22 at.%Ga ferromagnetic shape memory alloy

D. Y. Cong,^{a,b} Y. D. Zhang,^{a,b} Y. D. Wang,^a C. Esling,^b X. Zhao^a and L. Zuo^a

^aKey Laboratory of Anisotropy and Texture of Materials (MOE), Northeastern University, Shenyang 110004, People's Republic of China

^bLETAM, CNRS-UMR 7078, University of Metz, Ile du Saulcy, 57045 Metz, France.

Abstract

A recent study by high-resolution neutron powder diffraction provided accurate crystallographic information for the newly developed ferromagnetic shape memory alloy 53 at.%Ni–25 at.%Mn–22 at.%Ga. This made it possible to study by high-resolution electron backscatter diffraction the local microstructures and the twinning relationships between martensitic variants. The twin interfaces were also investigated and they are found to be coherent on the {112} planes.

Key words: electron backscattering diffraction; twinning; misorientation; ferromagnetic shape memory alloy; martensitic phase transformation.

1. Introduction

Ferromagnetic shape memory alloys (FSMAs) display a shape memory effect actuated by an applied magnetic field, rather than the slow shape change induced by a thermal field as in the case of conventional shape memory alloys such as NiTi, Fe–Mn–Si and Cu–Al–Mn, thereby combining the advantages of both large output strain and short reaction time. Among such FSMAs, Ni–Mn–Ga alloys have attracted great attention during the past few years due to their relatively large magnetic shape memory effect (MSME) (Murray *et al.*, 2000; Sozinov *et al.*, 2002). Intensive studies have been carried out on various aspects of these alloys, including the composition dependence of phase transformations (Takeuchi *et al.*, 2003), magnetic properties (Khovailo *et al.*, 2004), magnetocaloric effects (Tang *et al.*, 2005) and martensite stabilization (Segui *et al.*, 2005). However, the crystallographic data of this alloy system are still insufficient, which greatly hinders attempts to enhance the MSME.

It is well known that the MSME in Ni–Mn–Ga alloys with compositions close to that of the stoichiometric compound Ni₂MnGa is intimately related to the reorientation of the martensitic variants and the movement of the twin boundaries (Murray *et al.*, 2000; Sozinov *et al.*, 2002), so it is of great importance to study the twin boundary characteristics and twinning crystallography in these alloys. Mogyl'nyy *et al.* (2003) studied the twinning mode in a five-layered Ni–Mn–Ga single crystal using X-ray texture analysis. However, the twinning relationship in the non-modulated Ni–Mn–Ga alloys has not been reported. Moreover, polycrystalline X-ray diffraction analysis cannot be used for determining twinning crystallography in polycrystalline alloys, as it is impossible to distinguish the diffraction data from neighbouring twins. So far, the electron backscatter diffraction (EBSD) technique linked with high-resolution scanning electron microscopy (field emission gun, FE-SEM) has been well developed for local orientation analysis in polycrystalline materials. Our recent study on the crystal structure of these Ni–Mn–Ga alloys by means of high-resolution neutron powder diffraction (Cong, Wang *et al.*, 2005; Cong, Zetterström *et al.*, 2005; Wang *et al.*, 2006) provided the accurate crystallographic information that makes the related orientation measurements possible. Based on this, the crystallographic orientation relationship between martensitic variants of a polycrystalline 53 at.%Ni–25 at.%Mn–22 at.%Ga alloy with non-modulated structure was investigated by high-resolution EBSD and the twinning crystallography was unambiguously determined. The results offer new crystallographic information on the martensitic phase that will facilitate related studies of these materials.

2. Experimental

The polycrystalline 53 at.%Ni–25 at.%Mn–22 at.%Ga ingot was prepared by repeated melting of the high-purity constituent elements of Ni, Mn and Ga in an arc furnace, protected under an argon atmosphere. The phase transformation temperatures and the crystal structure were determined by differential scanning calorimetry (DSC) and neutron powder diffraction, respectively. The sample for the EBSD measurement was firstly mechanically polished and then electrolytically polished. The orientation analysis was performed with a Jeol JSM 6500 F scanning electron microscope equipped with *Channel 5* software (HKL Technology, Denmark). The 'beam controlled' mode was applied with a step size of 50 nm.

3. Results and discussion

DSC measurements demonstrate that the martensitic transformation start temperature, M_s , and finish temperature, M_f , are 386 and 368 K, respectively, and the austenitic transformation start temperature, A_s , and finish temperature, A_f , are 408 and 424 K, respectively. They also indicate that the martensitic transformation process in 53 at.%Ni–25 at.%Mn–22 at.%Ga is different from the two-stage transformation observed in other shape memory alloys (Otsuka & Ren, 2005; Sitepu *et al.*, 2002, 2005). Neutron powder diffraction at room temperature reveals a non-modulated tetragonal structure of the alloy with $a = 3.865 \text{ \AA}$, $c = 6.596 \text{ \AA}$ and $c/a = 1.707$. The space group is $I4/mmm$ (No. 139), with Ni atoms occupying $4d$ $(0, \frac{1}{2}, \frac{1}{4})$ Wyckoff positions, while Mn and Ga atoms occupy $2b$ $(0, 0, \frac{1}{2})$ and $2a$ $(0, 0, 0)$ positions, respectively, which was discussed in detail in an earlier study (Cong, Wang *et al.*, 2005; Cong, Zetterström *et al.*, 2005). The precise determination of the crystal structure is crucial for the EBSD measurements, as X-ray diffraction cannot give detailed information on the crystal structure of Ni–Mn–Ga alloys because of the similar X-ray scattering factors for Ni, Mn and Ga atoms.

The self-accommodated martensitic microstructure of 53 at.%Ni–25 at.%Mn–22 at.%Ga alloy is shown in Fig. 1. Typical fine lamellar structure, with straight boundaries between lamellae, is located in certain colonies that represent the initial austenite grains. An orientation map, taken in the same area as shown in Fig. 1, is illustrated in Fig. 2, in which the lamellae are coloured according to their orientations. From the colour pattern presented in each colony, one can see that there are mainly two martensitic variants distributed alternately in each initial austenite grain. The bending of some variants, presented by a colour change from dark pink to red in Fig. 2, gives a misorientation of around 5° . This may result from the high local transformation stress. Misorientation calculation (see Appendix A) shows that each pair of neighbouring lamellae have the same equivalent misorientation angles and axes. The misorientations between the two variants in the square of Fig. 2, with Euler angles (in Bunge's convention) of $(284.8^\circ, 146.4^\circ, 325.1^\circ)$ and $(9.1^\circ, 77.4^\circ, 193.5^\circ)$ as an example, are given in Table 1. It is seen that there are eight sets of equivalent misorientations, each set

being defined by a misorientation angle ω , and the eight corresponding rotation axes, equivalent through the rotation point symmetry group. In fact, the minimum misorientation angle of each pair of lamellae is 82–85° (with a mean value of 83°) around $\langle 110 \rangle$ axes. The variation of the misorientation angle by several degrees can be attributed to the inhomogeneous stress in the arc-melted sample.

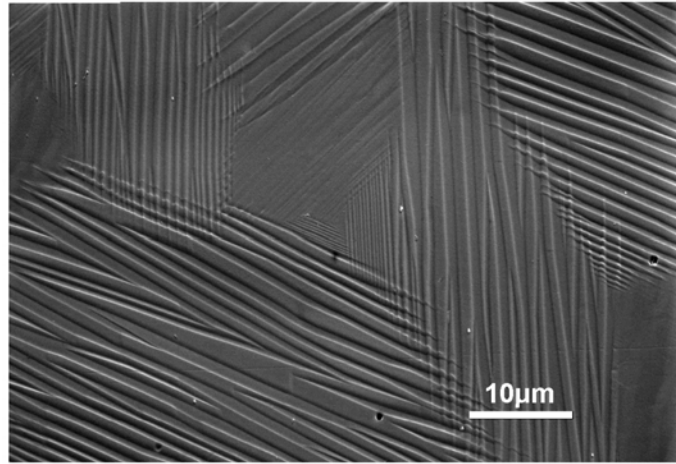


Figure 1 SEM secondary electron micrograph of 53 at.%Ni–25 at.%Mn–22 at.%Ga alloy at room temperature.

Table 1 The misorientation angles and rotation axes between the two variants in the square of Fig. 2, with Euler angles of (284.8°, 146.4°, 325.1°) and (9.1°, 77.4°, 193.5°), respectively.

For each misorientation angle ω , there is a family of eight equivalent rotations with eight equivalent axes \mathbf{d} which transform according to the tetragonal rotation symmetry group.

Misorientation angles, ω (°)	Coordinates of rotation axes, \mathbf{d}		
	d_1	d_2	d_3
179.5	45.10	48.23	75.10
177.5	53.40	52.84	66.01
126.4	0.45	84.14	54.04
122.3	85.73	0.45	51.48
116.2	77.72	2.61	62.87
115.5	2.62	78.04	62.47
97.4	70.30	71.05	2.95
82.6	73.04	68.30	0.60

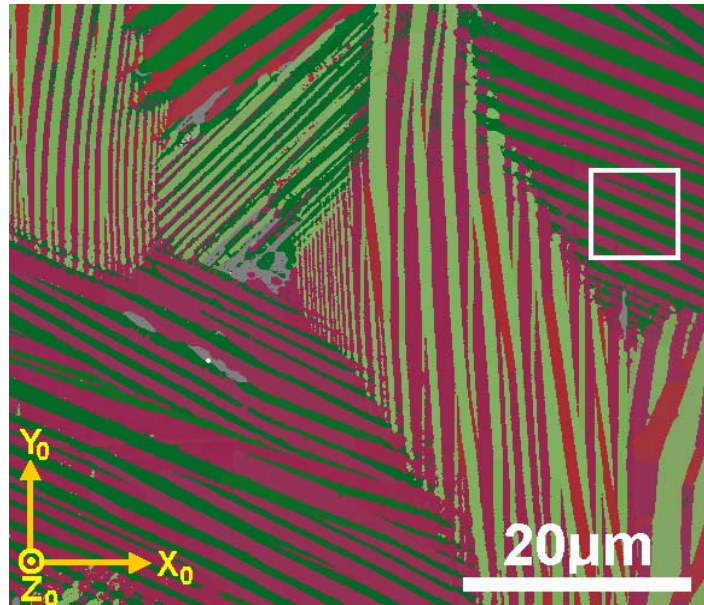


Figure 2 Orientation map of 53 at.%Ni–25 at.%Mn–22 at.%Ga alloy taken from the same area in Fig. 1, and the corresponding sample coordinates. The orientation data in the square are taken as an example for misorientation calculation (Table 1) and pole-figure construction (Figs. 3 and 4).

Clarification of the special orientation relationship, or twinning relationship, between two neighbouring lamellae offers useful information to obtain a better understanding of the martensitic transformation behaviour and variant selection rule for this new shape memory alloy. From the eight sets of equivalent misorientations given in Table 1, there are two sets of nearly 180° rotations around two families of equivalent axes (the deviation of misorientation angle by several degrees from 180° can be attributed to the internal stress in the sample). The Miller indices in the tetragonal system for the two 180° rotation axes are $\langle 45.10\ 48.23\ 43.99 \rangle$ and $\langle 53.40\ 52.84\ 38.67 \rangle$, which are 2.1° away from $\langle 111 \rangle$ and 2.5° away from $\langle 332 \rangle$, respectively. The two axes $[111]$ and $[33\bar{2}]$ are almost perpendicular to each other. The planes normal to $\langle 111 \rangle$ and $\langle 332 \rangle$ are close to $\{113\}$ (with 0.8° deviation) and $\{112\}$ (with 0.8° deviation). According to the classical definition of twinning (Christian & Mahajan, 1995; Kelly & Groves, 1970), if there are two 180° rotations around two rational axes and the planes normal to the rotation axes are also rational, the two crystals have a twin relationship and the twin is a compound twin, with one rotation axis being the twinning direction η_1 and the other being the normal of the twinning plane \mathbf{K}_1 . Hence there are two possibilities: (i) $\mathbf{K}_1 = \{112\}$,

$\eta_1 = \langle 11\bar{1} \rangle$; and (ii) $\mathbf{K}_1 = \{113\}$, $\eta_1 = \langle 33\bar{2} \rangle$. Since metallic materials tend to twin on the close-packed plane and in the close-packed direction (Kelly & Groves, 1970), the second possibility is excluded. The exclusion of the second possibility is further confirmed to be reasonable by the calculation of the amount of shear and the analysis of the twin interface, as discussed later. The $\{112\}$ pole figure, illustrated in Fig. 3(a), shows that one of the $\{112\}$ planes is common between the twin-related variants. The common plane is determined to be (112). Similarly, one common $\langle 111 \rangle$ direction can be clearly seen from the pole figure of $\langle 111 \rangle$ directions, as shown in Fig. 3(b), and the common direction is $[11\bar{1}]$. These observations confirm that the twinning plane and twinning direction are (112) and $[11\bar{1}]$, respectively.

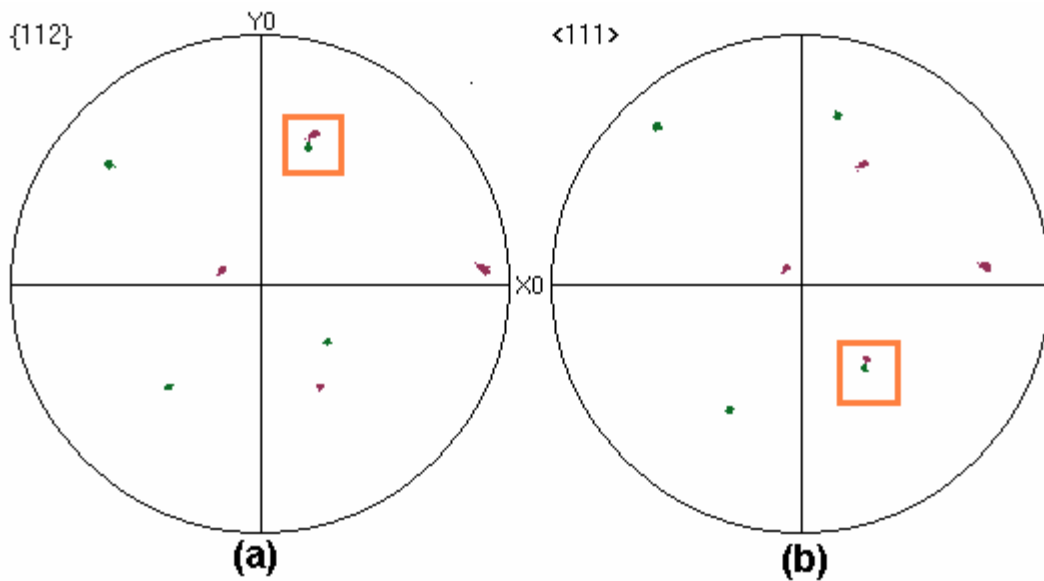


Figure 3 Pole figures of $\{112\}$ planes (a) and $\langle 111 \rangle$ directions (b), obtained from the twin variants enclosed in the square of Fig. 2. The sample coordinate $X_0Y_0Z_0$ is shown in Fig. 2. The square in this figure shows the overlapping poles of the two variants in the sample coordinate system.

In compound twins, all four twinning elements, \mathbf{K}_1 , \mathbf{K}_2 (the conjugate twinning plane), η_1 and η_2 (the conjugate twinning direction) should be rational (Christian & Mahajan, 1995). According to the methods of analyzing twinning elements used by Kishida *et al.* (2004, 2005),

the normal of \mathbf{K}_2 must be close to η_1 for the twinning shear to be realistically small and have low and rational indices (Cahn, 1953). The most reasonable choice of \mathbf{K}_2 is then found to be $(11\bar{2})$, the normal of which is 10.7° away from η_1 . The plane of shear \mathbf{P} containing η_1 and the normals of \mathbf{K}_1 and \mathbf{K}_2 , can thus be determined to be $(1\bar{1}0)$, and η_2 , the intersection of \mathbf{K}_2 and \mathbf{P} , is $[111]$. The magnitude of shear, s , can then be calculated as follows:

$$s = \frac{2}{\tan \theta} = 2 \cot \theta, \quad (1)$$

where θ is the acute angle between \mathbf{K}_1 and \mathbf{K}_2 . In the case of the present study, the magnitude of shear, s , is calculated to be 0.379. It is worth noting that, if $\{113\}$ is chosen as \mathbf{K}_1 , the amount of shear obtained from similar calculations would be larger than of the present value (*i.e.* 0.438). This gives another reason to exclude the second possibility mentioned above. The twinning elements in the observed twin variants are finally summarized as

$$\mathbf{K}_1 = \{112\}, \mathbf{K}_2 = \{11\bar{2}\}, \eta_1 = \langle 11\bar{1} \rangle, \eta_2 = \langle 111 \rangle, \mathbf{P} = \{1\bar{1}0\}, s = 0.379.$$

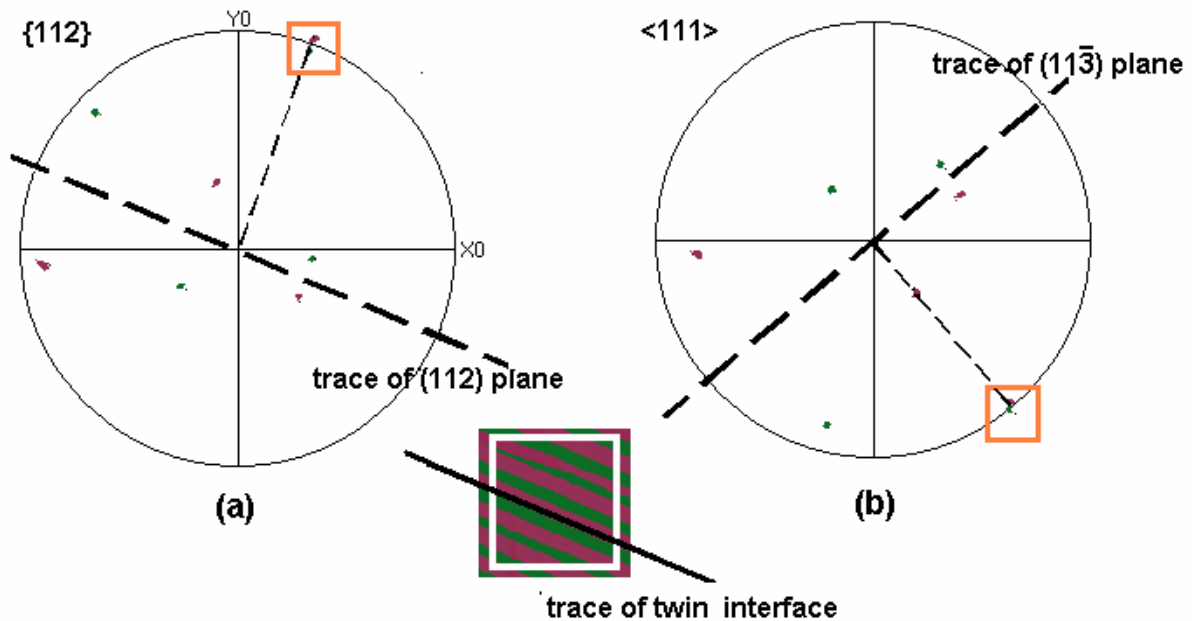


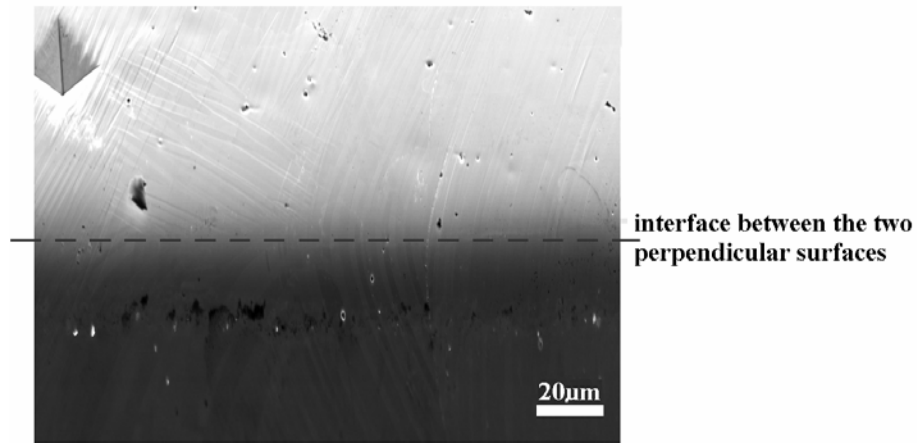
Figure 4 Rotated pole figures of $\{112\}$ planes (a) and $\langle 111 \rangle$ directions (b), corresponding to the original pole figures shown in Fig. 3. The traces of the twin interface and the overlapping planes are also illustrated.

By a simple rotation of the $\{112\}$ pole figure in Fig. 3(a), it is possible to bring the common (112) poles shared by the two martensitic variants to the outer circle. This is obtained by a rotation of the common (112) poles along the radius running through these common poles, so that the final orientation of the common (112) planes is vertical, as seen in Fig. 4(a). As $\langle 111 \rangle$ is nearly normal to $\{113\}$, by a similar rotation of the common $[11\bar{1}]$ poles in Fig. 3(b), it is possible to obtain the final orientation of the common $(11\bar{3})$ planes as vertical too, as shown in Fig. 4(b). The mirror relationship between the two variants is clearly seen in Figs. 4(a) and 4(b). However, in Fig. 4(a), the trace of the twin interface and the trace of the overlapping (112) planes are parallel to each other, suggesting that the twin interface may be $\{112\}$, while in Fig. 4(b), the trace of the overlapping (113) planes is not parallel to the trace of the twin interface. This gives further confirmation that $\{113\}$ cannot be \mathbf{K}_1 .

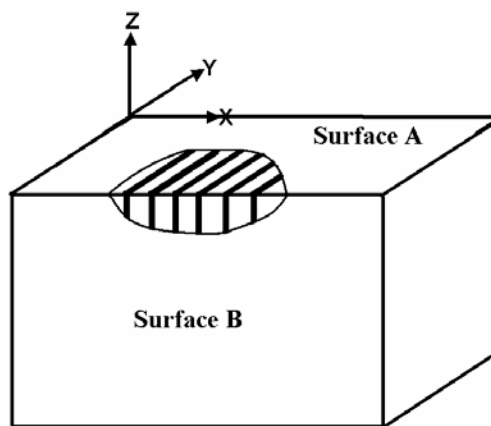
The twin interfaces were further determined by means of double-surface trace analysis (Lieberman *et al.*, 1955; Zimmermann & Humbert, 2002). Two perpendicular surfaces of the sample and the schematic illustration of these two surfaces in the corresponding macroscopic coordinate system are shown in Figs. 5(a) and 5(b). The directions of the twin lamellae in surfaces A and B were determined. The normalized vector product of the unit vectors in the measured directions represents the normal of the twin interface expressed in the macroscopic coordinate system. With the grain orientations determined by EBSD, the twin interface normal and the interface plane were calculated in the crystal coordinate system of each considered grain. The interface normal is $\langle 332 \rangle$ with 2.1° deviation and the interface plane is $\{112\}$ with 2.6° deviation. This gives a strong indication that the twin interfaces are coherent on the twinning plane $\{112\}$, which can be attributed to the minimization of interfacial energy. In order to study the intrinsic nature of the twin interfaces in great detail, direct observations by transmission electron microscopy (TEM) are still needed.

The crystallographic information on this new kind of material is insufficient. The present study enriches the crystallographic data of the Ni–Mn–Ga alloy system and may provide direct input for orientation determinations related to the phase transformations. Moreover, the individual grain orientations from EBSD measurements can be helpful for texture simulations using advanced techniques (Blendell *et al.*, 1999). These fundamental aspects will be of great

importance for understanding the MSME in Ni-Mn-Ga FSMA and may further be useful for the enhancement of this effect.



(a)



(b)

Figure 5 (a) Micrographs of the twins on two perpendicular sample surfaces showing twin traces and (b) schematic illustration of the two perpendicular sample surfaces with twin traces in the macroscopic coordinate system.

4. Conclusions

The microstructure and twinning relationship of the non-modulated 53 at.%Ni–25 at.%Mn–22 at.%Ga shape memory alloy were characterized by FE-SEM/EBSD, with the help of accurate crystal structure data from neutron powder diffraction. The results can be summarized as follows.

(i) In 53 at.%Ni–25 at.%Mn–22 at.%Ga alloy, there are only two martensitic variants with twin relationships existing in each initial austenite grain. All observed martensitic twins are found to be compound twins and the twinning elements are determined as: $\mathbf{K}_1 = \{112\}$, $\mathbf{K}_2 = \{11\bar{2}\}$, $\eta_1 = \langle 11\bar{1} \rangle$, $\eta_2 = \langle 111 \rangle$, $\mathbf{P} = \{1\bar{1}0\}$ and $s = 0.379$.

The neighbouring twin variants have a minimum misorientation angle of $\sim 83^\circ$ around the $\langle 110 \rangle$ axis.

(ii) The twin interfaces between the neighbouring variants are coherent on the $\{112\}$ planes, which can be attributed to the minimization of interfacial energy.

APPENDIX A

Misorientation calculation

The misorientation between two crystals is defined by sets of rotations from one of the symmetrically equivalent coordinate systems of one crystal to another equivalent coordinate system of the other crystal.

The orientation \mathbf{g} of a crystal with Euler angles $(\varphi_1, \Phi, \varphi_2)$ in Bunge's convention can be described by a rotation matrix (Bunge, 1993) which transforms the sample coordinate system into the crystal coordinate system. Owing to the crystal symmetry, one orientation \mathbf{g}_I has eight equivalent orientations in the tetragonal system, expressed by $\mathbf{S}_i \mathbf{g}_I$, where \mathbf{S}_i is the generic element of the tetragonal rotation symmetry group. For convenience, the eight rotation elements of tetragonal symmetry are listed in Table 2, which can be of great importance for orientation calculations.

The misorientation between two variants is expressed by $\Delta \mathbf{g}$:

$$\Delta \mathbf{g} \mathbf{S}_i \mathbf{g}_I = \mathbf{S}_j \mathbf{g}_2, \text{ or } \Delta \mathbf{g} = \mathbf{S}_j \mathbf{g}_2 \mathbf{g}_I^{-1} \mathbf{S}_i^{-1}. \quad (2)$$

If we denote

$$\Delta \mathbf{g} = \begin{pmatrix} a_{11} & a_{12} & a_{13} \\ a_{21} & a_{22} & a_{23} \\ a_{31} & a_{32} & a_{33} \end{pmatrix}, \quad (3)$$

then, according to analytical methods (Bunge, 1993; Humbert *et al.*, 1995; Mao, 2002), the misorientation angle ω and rotation axis \mathbf{d} can be derived from

$$\cos \omega = \frac{a_{11} + a_{22} + a_{33} - 1}{2} \quad (4)$$

and

$$\mathbf{d} = (d_1, d_2, d_3) = \left(\frac{a_{23} - a_{32}}{2 \sin \omega}, \frac{a_{31} - a_{13}}{2 \sin \omega}, \frac{a_{12} - a_{21}}{2 \sin \omega} \right) \quad (5)$$

where d_1 , d_2 and d_3 are the coordinates of the rotation axis in the orthonormal crystal coordinate system.

According to the definition mentioned above and considering the equivalent orientations by symmetry, there are 64 possible misorientations between two variants in the tetragonal crystals, which are finally reduced into eight sets of misorientation angles and axes. In each set, there is one misorientation angle with a family of eight equivalent rotation axes. An example is given in Table 1. Conventionally, the minimum misorientation angle with its rotation axes is used to represent the misorientation between two crystals.

Table 2 The eight rotation elements of the tetragonal point symmetry group.

Element	Rotation	Euler angles of rotation	Matrix of change of reference frame	Element	Rotation	Euler angles of rotation	Matrix of change of reference frame
1	xyz	$0, 0, 0$	$\begin{pmatrix} 1 & 0 & 0 \\ 0 & 1 & 0 \\ 0 & 0 & 1 \end{pmatrix}$	$4^+ 0, 0, z$	$\bar{y}xz$	$\frac{\pi}{2}, 0, 0$	$\begin{pmatrix} 0 & -1 & 0 \\ 1 & 0 & 0 \\ 0 & 0 & 1 \end{pmatrix}$
$2 x, 0, 0$	$\bar{\bar{x}}y\bar{z}$	$0, \pi, 0$	$\begin{pmatrix} 1 & 0 & 0 \\ 0 & -1 & 0 \\ 0 & 0 & -1 \end{pmatrix}$	$4^- 0, 0, z$	$\bar{y}x\bar{z}$	$\frac{3\pi}{2}, 0, 0$	$\begin{pmatrix} 0 & 1 & 0 \\ -1 & 0 & 0 \\ 0 & 0 & 1 \end{pmatrix}$
$2 0, y, 0$	$\bar{\bar{x}}y\bar{z}$	$\pi, \pi, 0$	$\begin{pmatrix} -1 & 0 & 0 \\ 0 & 1 & 0 \\ 0 & 0 & -1 \end{pmatrix}$	$2 x, x, 0$	$yx\bar{z}$	$\frac{\pi}{2}, \pi, 0$	$\begin{pmatrix} 0 & 1 & 0 \\ 1 & 0 & 0 \\ 0 & 0 & -1 \end{pmatrix}$
$2 0, 0, z$	$\bar{\bar{x}}y\bar{z}$	$\pi, 0, 0$	$\begin{pmatrix} -1 & 0 & 0 \\ 0 & -1 & 0 \\ 0 & 0 & 1 \end{pmatrix}$	$2 x, \bar{x}, 0$	$\bar{\bar{y}}x\bar{z}$	$\frac{3\pi}{2}, \pi, 0$	$\begin{pmatrix} 0 & -1 & 0 \\ -1 & 0 & 0 \\ 0 & 0 & -1 \end{pmatrix}$

Acknowledgements

The authors are grateful to the National Natural Science Foundation of China (Grant Nos. 50325102, 50531020 and 50528102) and the National Ministry of Education of China, with NCET-04-0282. Financial support from project PRA MX04-02 is greatly acknowledged. One of the authors (DYC) is grateful for support from the PhD fund of Northeastern University. The authors also gratefully acknowledge Professor M. Humbert and Dr S. Dey for fruitful discussions, and Dr J.-J. Fundenberger for writing the misorientation calculation program.

References

- Blendell, J. E., Vaudin, M. D. & Fuller, E. R. (1999). *J. Am. Ceram. Soc.* **82**, 3217–3220.
- Bunge, H. J. (1993). *Texture Analysis in Materials Science – Mathematical Methods*. Göttingen: Cuvillier Press.
- Cahn, R. W. (1953). *Acta Metall.* **1**, 49–52.
- Christian, J. W. & Mahajan, S. (1995). *Prog. Mater. Sci.* **39**, 1–157.
- Cong, D. Y., Wang, Y. D., Zetterström, P., Peng, R. L., Delaplane, R., Zhao, X. & Zuo, L. (2005). *Mater. Sci. Tech.* **21**, 1412–1416.
- Cong, D. Y., Zetterström, P., Wang, Y. D., Delaplane, R., Peng, R. L., Zhao, X. & Zuo, L. (2005). *Appl. Phys. Lett.* **87**, 111906.
- Humbert, M., Wagner, F., Moustahfid, H. & Esling, C. (1995). *J. Appl. Cryst.* **28**, 571–576.
- Kelly, A. & Groves, G. W. (1970). *Crystallography and Crystal Defects*. London: Longman Press.
- Khovailo, V. V., Novosad, V., Takagi, T., Filippov, D. A., Levitin, R. Z. & Vasil'ev, A. N. (2004). *Phys. Rev. B*, **70**, 174413.
- Kishida, K., Takahama, Y. & Inui, H. (2004). *Acta Mater.* **52**, 4941–4952.
- Kishida, K., Takahama, Y. & Inui, H. (2005). *Mater. Sci. Eng. A*, **400**, 339–344.
- Lieberman, D. S., Wechsler, M. S. & Read, T. A. (1955). *J. Appl. Phys.* **26**, 473–484.
- Mao, W. (2002). *Crystallographic Textures and Anisotropy in Metal Materials*. Beijing: Science Press.
- Mogylnyy, G., Glavatsky, I., Glavatska, N., Söderberg, O., Ge, Y. & Lindroos, V. K. (2003). *Scr. Mater.* **48**, 1427–1432.

- Murray, S. J., Marioni, M. A., Kukla, A. M., Robinson, J., O'Handley, R. C. & Allen, S. M. (2000). *J. Appl. Phys.* **87**, 5774–5776.
- Otsuka, K. & Ren, X. (2005). *Prog. Mater. Sci.* **50**, 511–678.
- Segui, C., Cesari, E., Font, J., Muntasell, J. & Chernenko, V. A. (2005). *Scr. Mater.* **53**, 315–318.
- Sitepu, H., Schmahl, W. W., Allafi, J. K., Eggeler, G., Dlouhy, A., Toebbens, D. M. & Tovar, M. (2002). *Scr. Mater.* **46**, 543–548.
- Sitepu, H., Wright, J. P., Hansen, T., Chateigner, D., Brokmeier, H.-G., Ritter, C. & Ohba, T. (2005). *Mater. Sci. Forum*, **495–497**, 255–260.
- Sozinov, A., Likhachev, A. A., Lanska, N. & Ullakko, K. (2002). *Appl. Phys. Lett.* **80**, 1746–1748.
- Takeuchi, I., Famodu, O. O., Read, J. C., Aronova, M. A., Chang, K.-S., Craciunescu, C., Lofland, S. E., Wuttig, M., Wellstood, F. C., Knauss, L. & Orozco, A. (2003). *Nature Mater.* **2**, 180–184.
- Tang, Y. J., Solomon, V. C., Smith, D. J., Harper, H. & Berkowitz, A. E. (2005). *J. Appl. Phys.* **97**, 10M309.
- Wang, Y. D., Cong, D. Y., Peng, R. L., Zetterström, P., Zhang, Z. F., Zhao X. & Zuo, L. (2006). *J. Mater. Res.* **21**, 691–697.
- Zimmermann, F. & Humbert, M. (2002). *Acta Mater.* **50**, 1735–1740.

Experiment and theoretical prediction of martensitic transformation crystallography in a Ni–Mn–Ga ferromagnetic shape memory alloy

D.Y. Cong ^{a,b}, Y.D. Zhang ^{a,b}, Y.D. Wang ^a, M. Humbert ^b, X. Zhao ^a, T. Watanabe ^a, L. Zuo ^a, C. Esling ^b

^aKey Laboratory for Anisotropy and Texture of Materials (MOE), Northeastern University, Shenyang 110004, China

^bLETAM, CNRS-UMR 7078, University of Metz, Ile du Saulcy, 57045 Metz, France

Abstract

A detailed study of martensitic transformation crystallography and microstructural characteristics in the Ni₅₃Mn₂₅Ga₂₂ ferromagnetic shape memory alloy (FSMA) was performed by both experimental observation and theoretical calculation. It is revealed that there are two microscopically twin-related martensitic variants with a misorientation of ~82° around the <110>_M axis in each initial austenite grain. The twin interface plane was determined to be {0.399 0.383 0.833}_M (1.79° away from {112}_M). The ratio of the amounts of the two variants inherited from one single austenite grain is about 1.70. The prevalent orientation relationship between austenite and martensite was found to be Kurdjumov–Sachs (K–S) relationship with (111)_A//(101)_M, [$\bar{1}\bar{1}0$]_A//[$\bar{1}\bar{1}\bar{1}$]_M. A successful explanation of the crystallographic features during martensitic transformation will shed light on the development of FSMAs with optimal performance.

Keywords: Shape memory alloys (SMAs); Martensitic phase transformation; Twin variant selection; Electron backscattered diffraction (EBSD); Microstructure

1. Introduction

Conventional shape memory alloys (SMAs) can generate large displacements or forces via thermoelastic martensitic transformation for intelligent micro-electro-mechanical systems (MEMS), such as sensors and actuators. However, these SMAs have a slow dynamic response because their actuation is induced by a thermal field. Ferromagnetic SMAs (FSMAs) display

a shape memory effect (SME) actuated by an applied magnetic field [1–6], combining the advantages of both large output strain and short reaction time, and thus show promise for practical applications. Among such FSMA, Ni–Mn–Ga alloys with a composition close to the stoichiometric compound Ni_2MnGa have attracted much attention because of their high performance which can provide magnetic-field-induced strain that is an order of magnitude higher than that found for magnetostrictive materials [2,7,8]. In recent years, extensive studies have been performed on many aspects of the Ni–Mn–Ga alloys, such as crystal structure [9,10], phase transformation [11,12], magnetic-field-induced strain [2,7,8], magnetic properties [13], mechanical behavior [14,15] and the effects of magnetic fields on martensitic transformation [16,17]. Nevertheless, many fundamental issues concerning these newly developed materials still remain unclear, and these gaps in knowledge are a great hindrance to developing alloys with much larger SMEs. We have previously investigated the twinning relationship in a cast Ni–Mn–Ga alloy and unambiguously determined the twinning elements [18]. However, the orientation relationship (OR) between the austenite and martensite has not been reported up to now. Moreover, detailed information on the microstructure, such as twin variant selection, relative amount of differently oriented twins and twin thickness distribution, is still not available. Insight into these aspects is of both theoretical significance and practical interest. In fact, full understanding of the correlation between the microstructure and crystallography of martensitic variants and the OR between parent austenite and product martensite that governs the martensitic transformation is fundamental to the development of high-performance FSMA with large SMEs, high ductility and good stability during cyclic treatments. This is the motivation of our work.

In the present study, the crystallographic and microstructural characteristics of martensitic variants in $\text{Ni}_{53}\text{Mn}_{25}\text{Ga}_{22}$ alloy were investigated by means of electron backscattered diffraction (EBSD) in a high-resolution scanning electron microscope equipped with a field emission gun (FE-SEM). The twin interface plane and the OR between austenite and martensite were unambiguously determined. Crystallographic phenomenological theory was employed to quantitatively explain the crystallographic features during the martensitic transformation. This study should enrich the crystallographic information of the martensitic transformation process in FSMA and facilitate further investigations to improve the SME in

these alloys.

2. Experimental procedure

2.1. Material preparation

A 100 g button ingot of Ni₅₃Mn₂₅Ga₂₂ (at.%) was prepared by repeated melting of the high-purity constituent elements under an argon atmosphere in an arc furnace. Parts of the ingot were then crushed into fine powder to determine the phase transformation temperatures and crystal structure. The phase transformation temperatures and crystal structure were determined by differential scanning calorimetry (DSC) and neutron powder diffraction [9]. DSC measurements demonstrate that the martensitic transformation start temperature (M_s) and finish temperature (M_f) are 386 K and 368 K, respectively, and the austenitic transformation start temperature (A_s) and finish temperature (A_f) are 408 K and 424 K, respectively.

Samples of $10 \times 2 \times 2 \text{ mm}^3$ were cut out from the ingot for subsequent heat treatment. They were first annealed at 1073 K for 4 h to homogenize the microstructure in the austenite state, and then cooled to 473 K (above M_s) at $\sim 4 \text{ K min}^{-1}$ and isothermally held for 30 min to further reduce the thermal stress introduced by cooling. After the second stage annealing, the samples were cooled at $\sim 10 \text{ K min}^{-1}$ to room temperature to allow austenite to transform into martensite.

2.2. Crystal structure information of austenite and martensite

Recent high-resolution neutron powder diffraction measurements on the Ni₅₃Mn₂₅Ga₂₂ alloy [9] showed that it has a non-modulated tetragonal martensitic structure at room temperature, with $a = 3.865 \text{ \AA}$, $c = 6.596 \text{ \AA}$ and $c/a = 1.707$. The space group for this structure is $I4/mmm$ (No. 139), with Ni atoms occupying 4d (0,0.5,0.25) Wyckoff sites while Mn and Ga atoms occupying 2b (0,0,0.5) and 2a (0,0,0) sites, respectively (Fig. 1a). Indeed, the precise determination of the crystal structure by neutron diffraction is crucial for the EBSD measurements, as X-ray diffraction cannot give detailed information on the crystal structure of Ni–Mn–Ga alloys due to the similar X-ray scattering factors for Ni, Mn and Ga atoms. The high temperature austenite phase in the Ni₂MnGa-based alloys was confirmed by neutron

diffraction to have a cubic $L2_1$ Heusler structure (space group $Fm\bar{3}m$), with lattice parameter $a_0 = 5.840\text{\AA}$ [19,20], as shown in Fig. 1b. Ni atoms occupy 8c (0.25,0.25,0.25) Wyckoff sites, while Mn and Ga atoms occupy 4b (0.5,0.5,0.5) and 4a (0,0,0) sites, respectively.

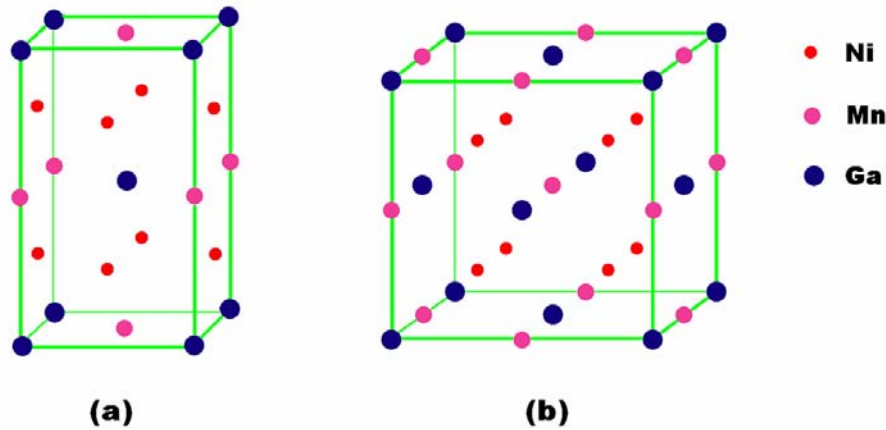


Fig. 1. Crystal structures of martensite (a) and austenite (b) in the $\text{Ni}_{53}\text{Mn}_{25}\text{Ga}_{22}$ alloy. Ni, Mn and Ga atoms occupy, respectively, 4d (0, 0.5, 0.25), 2b (0, 0, 0.5) and 2a (0, 0, 0) Wyckoff sites in martensite, and 8c (0.25, 0.25, 0.25), 4b (0.5, 0.5, 0.5) and 4a (0, 0, 0) Wyckoff sites in austenite.

2.3. EBSD measurement

The microstructure and crystallographic orientation of transformed martensite were analyzed by EBSD. Before EBSD measurements, the samples were first mechanically and then electrolytically polished. The orientation analysis was performed on a JEOL JSM 6500F FE-SEM (angular resolution 0.5°), equipped with Channel 5 software (HKL Technology, Denmark) based on the above-mentioned crystal structure information. The ‘beam-controlled’ mode was applied with a step size of 30 nm for a fine scan in a small area, and with a step size of 200 nm for a quick scan to cover a large area.

3. Experimental and calculated results

3.1. Microstructure

The orientation map obtained from a fine scan of EBSD within an initial austenite grain is shown in Fig. 2a, in which the martensitic variants are colored according to their orientation. It can be seen that there are only two martensitic variants, V_A and V_B , in this grain. The

indexed Kikuchi patterns of the two variants V_A and V_B in Fig. 2a are illustrated in Fig. 2b and 2c. It is notable that the patterns are well indexed according to the above-mentioned tetragonal structure, which confirms the reliability of the crystal structure information determined by high-resolution neutron powder diffraction [9].

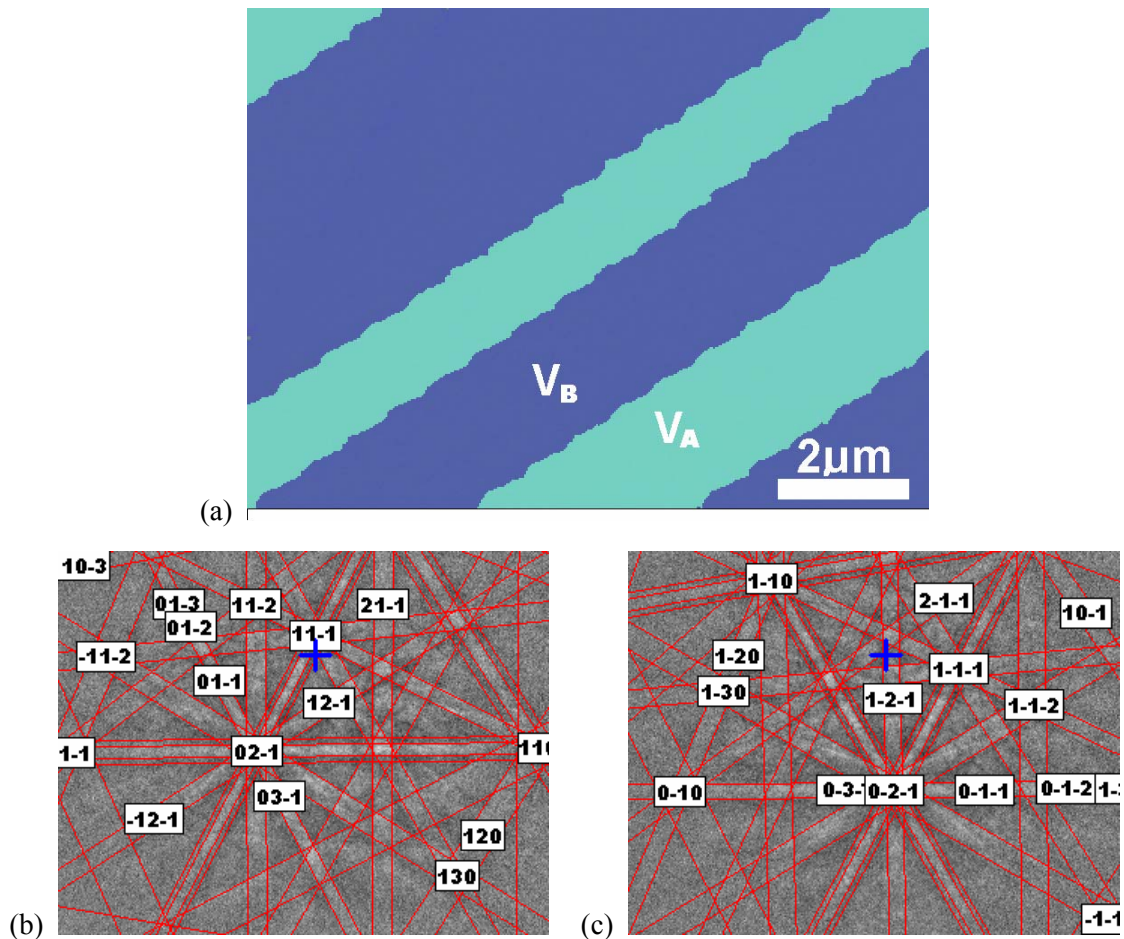


Fig. 2. (a) Orientation map of $\text{Ni}_{53}\text{Mn}_{25}\text{Ga}_{22}$ within an initial austenite grain. (b, c) Indexed Kikuchi patterns of variant V_A and V_B in (a).

In order to represent the global microstructure, we took an orientation map covering a large area (Fig. 3a). A typical lamellar martensitic microstructure can be clearly seen in each colony that represents the initial austenite grain. From the patterns colored according to the orientations of the variants, it can be confirmed that there are indeed only two martensitic variants distributed alternately in each initial austenite grain. The lamellar martensite appears in two kinds of morphologies: one with straight lamellae running through the whole austenite

grain, and the other with bent or bifurcated lamellae (grain 4 in Fig. 3a). A misorientation of $4\text{--}7^\circ$ can be found in the curved lamellae. This may be related to the presence in the large lamellae of small variants that are undetectable at the measurement resolution with the 200 nm step size. The straight martensitic lamellae might form at the beginning of the martensitic transformation and therefore could grow freely with low volume constraints; while the bent lamellae may form at a relatively late stage and thus their growth was confined by the surrounding hard martensite.

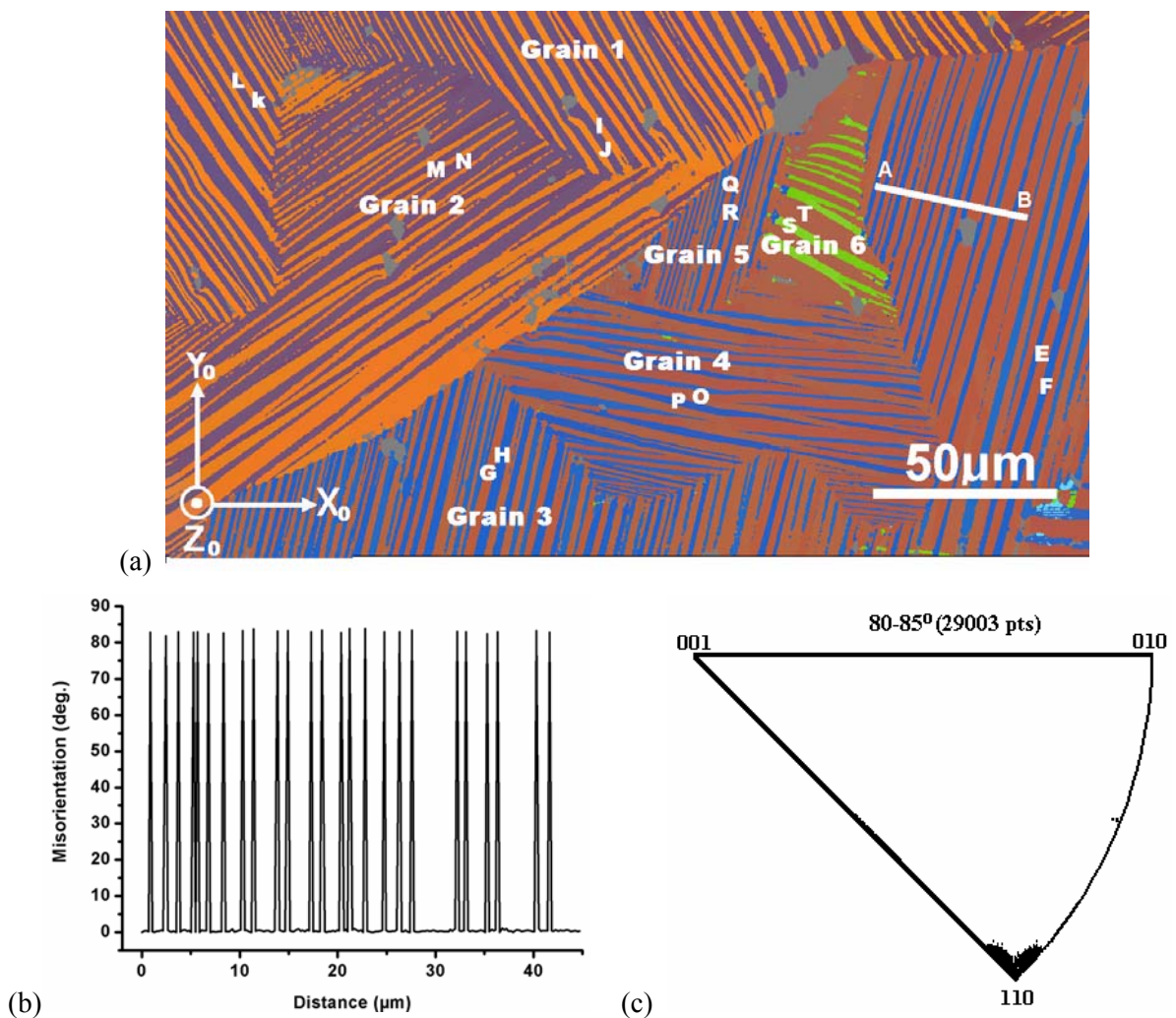


Fig. 3. (a) Orientation map of $\text{Ni}_{53}\text{Mn}_{25}\text{Ga}_{22}$ covering a large area. $X_0Y_0Z_0$ shows the macroscopic sample coordinate system. (b) Correlated misorientation profile, along line AB in (a). (c) Distribution of the rotation axes corresponding to $80\text{--}85^\circ$ misorientation angles between each neighboring variants in (a) in the tetragonal crystal coordinate system.

3.2. OR between martensitic variants

The correlated misorientation angle distribution along the line AB drawn over the twin cluster in Fig. 3a is shown in Fig. 3b. It is evident that the orientations within one twin variant are almost homogeneous and the misorientation angle between the two neighboring twins is about 82° . Fig. 3c shows the distribution of the rotation axes in the crystal coordinate system, corresponding to the misorientation angles $80\text{--}85^\circ$. It can clearly be seen that the rotation axes are around $\langle 110 \rangle_M$ (hereafter the subscripts M and A in the indices of the crystallographic planes and directions denote that the planes and directions are expressed in the tetragonal crystal coordinate system of martensite and the cubic crystal coordinate system of austenite, respectively). Therefore, the misorientations between the neighboring twins in $\text{Ni}_{53}\text{Mn}_{25}\text{Ga}_{22}$ alloy are 82° around the $\langle 110 \rangle_M$ axis. Further calculations [18] were carried out to determine the OR between the martensitic variants. Results show that the two variants have a twinning relationship. They are compound twins with the twinning elements $\mathbf{K}_1 = \{112\}$, $\mathbf{K}_2 = \{11\bar{2}\}$, $\boldsymbol{\eta}_1 = \langle 11\bar{1} \rangle$, $\boldsymbol{\eta}_2 = \langle 111 \rangle$, $\mathbf{P} = \{1\bar{1}0\}$ and $s = 0.379$. These results are in good agreement with those found for the cast $\text{Ni}_{53}\text{Mn}_{25}\text{Ga}_{22}$ alloy [18].

3.3. Twin interface plane and relative amount of twins

The twin interface plane was determined by means of two-surface trace analysis [21,22]. Two perpendicular surfaces of the sample, in the macroscopic coordinate system, were employed. For each grain on the two perpendicular surfaces, the directions of the twin interface traces on both surfaces were determined. The normalized vector product of the unit vectors in the measured directions represents the normal of the twin interface plane expressed in the macroscopic coordinate system. With the twin orientations determined from EBSD measurements, the twin interface normal and thus the interface plane were calculated in the crystal coordinate system of each considered twin. Table 1 lists the coordinates of the twin interface normal in the microscopic crystal coordinate system determined from 16 different initial austenite grains. It can be seen that the coordinates of the twin interface normal disperse around a mean value (0.541, 0.519, 0.662), which was calculated using the formula

$\bar{\mathbf{n}} = \frac{\sum \mathbf{n}_i}{\|\sum \mathbf{n}_i\|}$. The deviation of the individual twin interface normal from the mean value is also

shown in Table 1 from which one can see that the twin interface normal determined from most grains has only a slight deviation from the mean value. In the $\text{Ni}_{53}\text{Mn}_{25}\text{Ga}_{22}$ alloy with $c/a=1.707$, the plane corresponding to the mean value of the twin interface normal is $\{0.399 \ 0.383 \ 0.833\}_M$, when expressed in the tetragonal crystal coordinate system of martensite. Thus the mean twin interface plane is determined to be $\{0.399 \ 0.383 \ 0.833\}_M$, which is 1.79° away from $\{112\}_M$ plane in martensite.

Table 1 Coordinates of the twin interface normal \mathbf{n} in the microscopic crystal coordinate system determined from different austenite grains, and the deviation ω of the individual twin interface normal from the mean value

Grain no.	Coordinates of the twin interface normal \mathbf{n}			ω ($^\circ$)
	n_1	n_2	n_3	
1	0.503	0.534	0.680	1.94
2	0.536	0.489	0.688	2.26
3	0.554	0.537	0.636	1.90
4	0.523	0.535	0.663	1.79
5	0.520	0.589	0.619	4.59
6	0.571	0.504	0.648	1.88
7	0.630	0.478	0.612	6.25
8	0.573	0.518	0.635	2.28
9	0.511	0.588	0.627	4.66
10	0.468	0.514	0.719	5.17
11	0.578	0.488	0.654	2.67
12	0.524	0.479	0.704	3.50
13	0.529	0.485	0.696	2.97
14	0.549	0.438	0.712	5.33
15	0.513	0.579	0.634	3.85
16	0.559	0.517	0.648	1.36
Mean twin interface normal	0.541	0.519	0.662	

Statistical analyses have also been performed on the thickness distribution and relative amount of martensitic twins in the studied $\text{Ni}_{53}\text{Mn}_{25}\text{Ga}_{22}$ alloy. The thickness of each martensitic twin from the initial austenite grains 1–6 in Fig. 3a is calculated according to the relative angle of the twin interface with respect to the sample surface that is determined from

the positions of their poles in pole figures. As illustrated in Fig. 4a, the thickness of twins shows a wide distribution, ranging from 0.2 to 4.6 μm , with a peak value of 1.1 μm . However, most of the twins have a thickness of 0.2–2.6 μm and the average value is about 1.3 μm . In addition to the thickness distribution of martensitic twins, the relative amount of the two twin variants in each individual initial austenite grain is also important and may provide useful information as to how to improve the SME in FSMAs. If we denote the total amount of one martensitic variant in one initial austenite grain as $(1 - x)$ and that of the other variant as x (where x is related to the thinner variant), the ratio of the amounts of the two variants can be expressed as $\frac{1-x}{x}$. The calculated values obtained from the initial austenite grains 1–6 shown in Fig. 3a are illustrated in Fig. 4b. It is clear that the ratios in all the studied grains are almost the same and have a value around 1.70 (namely the percentages of the two variants in each initial austenite grain are 63% and 37%, respectively).

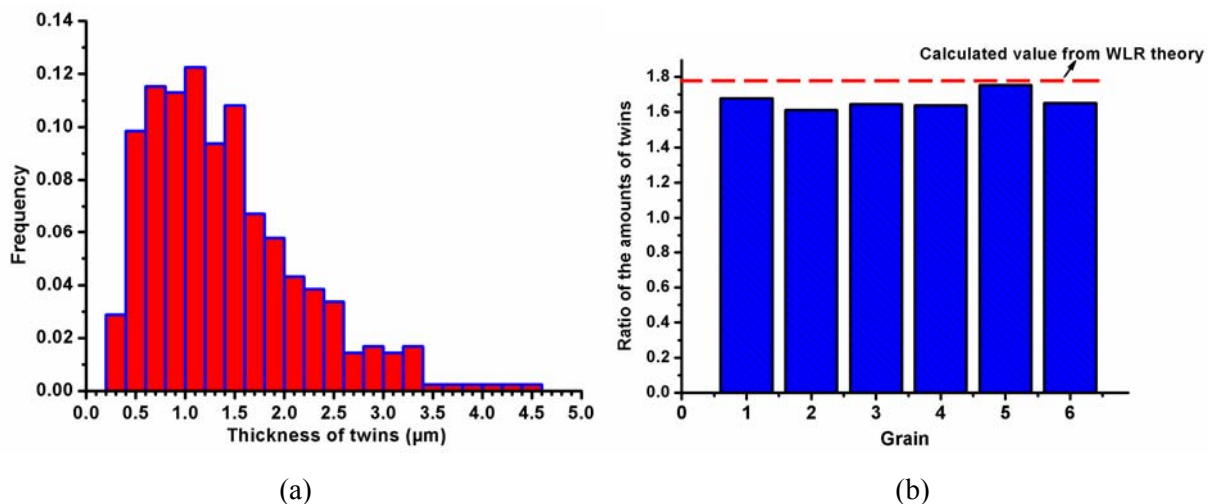


Fig. 4. (a) Thickness distribution of twins from the initial austenite grains 1–6 in Fig. 3a. (b) Ratio of the amounts of two differently orientated twins in each initial austenite grain. The dashed line shows the calculated value from the WLR crystallographic phenomenological theory.

3.4. OR between austenite and martensite determined from measured orientations of martensite

During martensitic transformation, one initial austenite grain transforms into several

differently orientated martensitic variants, and there generally exists a specific OR between the two phases. If the OR between austenite and martensite is assumed to be expressed by the matrix \mathbf{T} , it is possible to construct the orientation of the austenite grain from the measured orientations of the martensitic variants [23,24]. In the case of the $\text{Ni}_{53}\text{Mn}_{25}\text{Ga}_{22}$ alloy used in this study, only two martensitic variants with tetragonal structure are obtained after transformation from an initial austenite grain with cubic structure. Here, we denote the rotations characterizing the orientations of the austenite grain and one of the martensitic variants as \mathbf{g}^{A} and \mathbf{g}_1^{M} , and Bunge's convention is used to describe the symmetry operations and the rotations [25]. The following equation can be obtained:

$$\mathbf{S}_i^{\text{A}} \mathbf{g}^{\text{A}} = \mathbf{T} \mathbf{S}_j^{\text{M}} \mathbf{g}_1^{\text{M}} \quad (1)$$

or

$$\mathbf{g}^{\text{A}} = (\mathbf{S}_i^{\text{A}})^{-1} \mathbf{T} \mathbf{S}_j^{\text{M}} \mathbf{g}_1^{\text{M}} \quad (2)$$

where \mathbf{S}_i^{A} and \mathbf{S}_j^{M} represent the symmetry elements of cubic and tetragonal symmetry groups. As there are, in total, 24 symmetry elements in the cubic symmetry group and eight symmetry elements in the tetragonal symmetry group, 192 possible orientations of the austenite grain can be calculated according to Eq. (2). However, there are only several (say, N) distinct orientations among the 192 possibilities and any of the others is equivalent to one of the N distinct orientations. Hence, we may represent the N distinct orientations calculated from \mathbf{g}_1^{M} by $\mathbf{g}_{1n}^{\text{A}}$ ($n = 1, 2, \dots, N$). Similarly, from the orientation of the other variant, represented by \mathbf{g}_2^{M} , another N distinct orientations of the austenite grain, represented by $\mathbf{g}_{2n}^{\text{A}}$ ($n = 1, 2, \dots, N$), can be determined. As the two variants are transformed from the same initial austenite grain, if the distinct austenite orientations calculated from the two variants, represented by $\mathbf{g}_{1n}^{\text{A}}$ and $\mathbf{g}_{2n}^{\text{A}}$, have at least one orientation in common, it can be deduced that the assumed OR indeed exists and the common orientation is the orientation of the austenite grain. The schematic illustration of the determination of the OR between austenite and martensite is shown in Fig. 5.

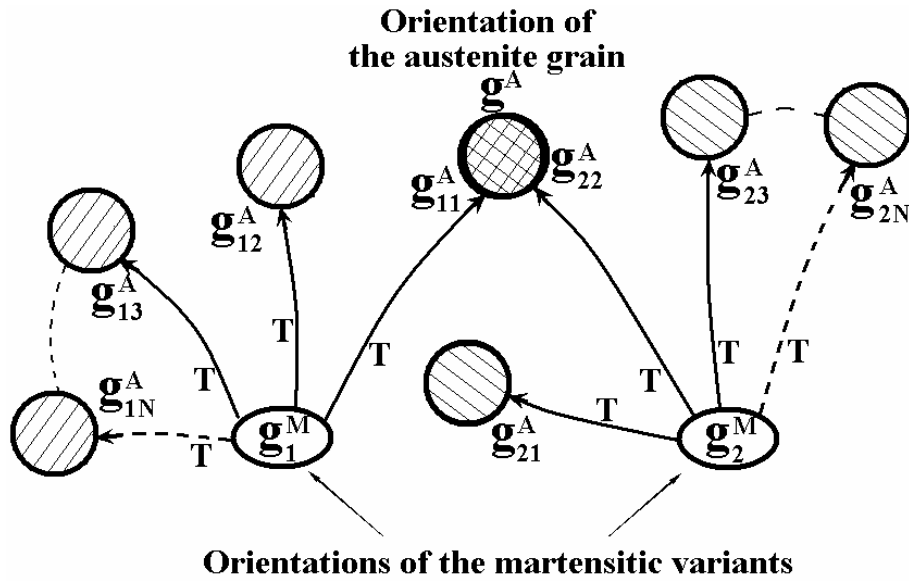


Fig. 5. Schematic illustration of the determination of OR between austenite and martensite. g_{1n}^A and g_{2n}^A ($n=1,2,\dots,N$) represent possible distinct orientations of the austenite grain calculated from g_1^M and g_2^M , respectively. The common orientation denoted as g^A is the true orientation of the austenite grain and T is the orientation relationship existing between austenite and martensite.

Considering the crystal structures and atomic arrangements of both austenite and martensite in $\text{Ni}_{53}\text{Mn}_{25}\text{Ga}_{22}$ (see Fig. 1) and consulting the published ORs in the literature, the possible ORs between austenite and martensite are listed as follows:

Bain relationship [26]: $(001)_A // (001)_M$, $[100]_A // [1\bar{1}0]_M$.

Kurdjumov–Sachs (K–S) relationship [27]: $(111)_A // (101)_M$, $[1\bar{1}0]_A // [11\bar{1}]_M$.

Nishiyama–Wassermann (N–W) relationship [28,29]: $(111)_A // (101)_M$, $[\bar{2}11]_A // [10\bar{1}]_M$.

Pitsch relationship [30]: $(110)_A // (1\bar{1}\bar{2})_M$, $[1\bar{1}0]_A // [\bar{1}1\bar{1}]_M$

Using the method described above, the orientations of the initial austenite grain were calculated from the orientations of the two martensitic variants existing in the same grain, by assuming that the ORs between the austenite and martensite are the ORs listed above. For statistical analysis, we selected eight pairs of orientations of martensitic variants from

different martensite colonies shown in Fig. 3a. The locations of the selected pairs are indicated by uppercase letters E F, G H, ..., S T in the figure. The calculated orientations of the austenite grain are plotted on the standard $\{001\}$ projection of austenite. The representative $\{001\}$ projections of the orientations of the austenite grain calculated from the points E and F under the above-mentioned ORs (Bain, K–S, N–W and Pitsch) are shown in Fig. 6 as an example. In all the projections in Fig. 6, the black solid squares represent the distinct orientations of the austenite grain calculated from one martensitic variant, and the red solid squares represent those calculated from the other variant. As one austenite orientation corresponds to three poles in its standard $\{001\}$ projection, only if all the three poles of one orientation coincide with those of the other orientation, can we say that the two orientations are the same. From Fig. 6, it can clearly be seen that the number of distinct austenite orientations is different under different ORs. There is one distinct austenite orientation under Bain, eight under K–S, four under N–W and four under Pitsch ORs. Moreover, the misfit levels of the calculated austenite orientations from the two different martensitic variants in Fig.6 are also quite different from one OR to another. The minimum misorientation angle between the orientations of the austenite grain calculated from different pairs of variants, according to Bain, K–S, N–W and Pitsch relationships, respectively, have been calculated and are shown in Table 2. One can see that under the K–S and N–W ORs, the calculated austenite orientations have the smallest minimum misorientation angles (the pairs of common orientations calculated from variants E F under these two ORs are enclosed in the open squares in Fig. 6 for easy visualization), suggesting that the OR between austenite and martensite in the studied material could be K–S or N–W, or both. It should be noted that for the pairs of martensitic variants E F, G H, I J, K L, M N, Q R and S T that have straight boundaries between them, the minimum misorientation angle between the orientations of the austenite grain calculated according to K–S and N–W relationships are the same, with a value of $0.80\text{--}2.44^\circ$. However, for the martensitic variants O P with bent boundaries the minimum misorientation angle between the orientations calculated according to the K–S OR is slightly larger than that calculated according to N–W OR. The detailed distinction of the K–S and N–W ORs in terms of energy condition will be discussed in Section 5.

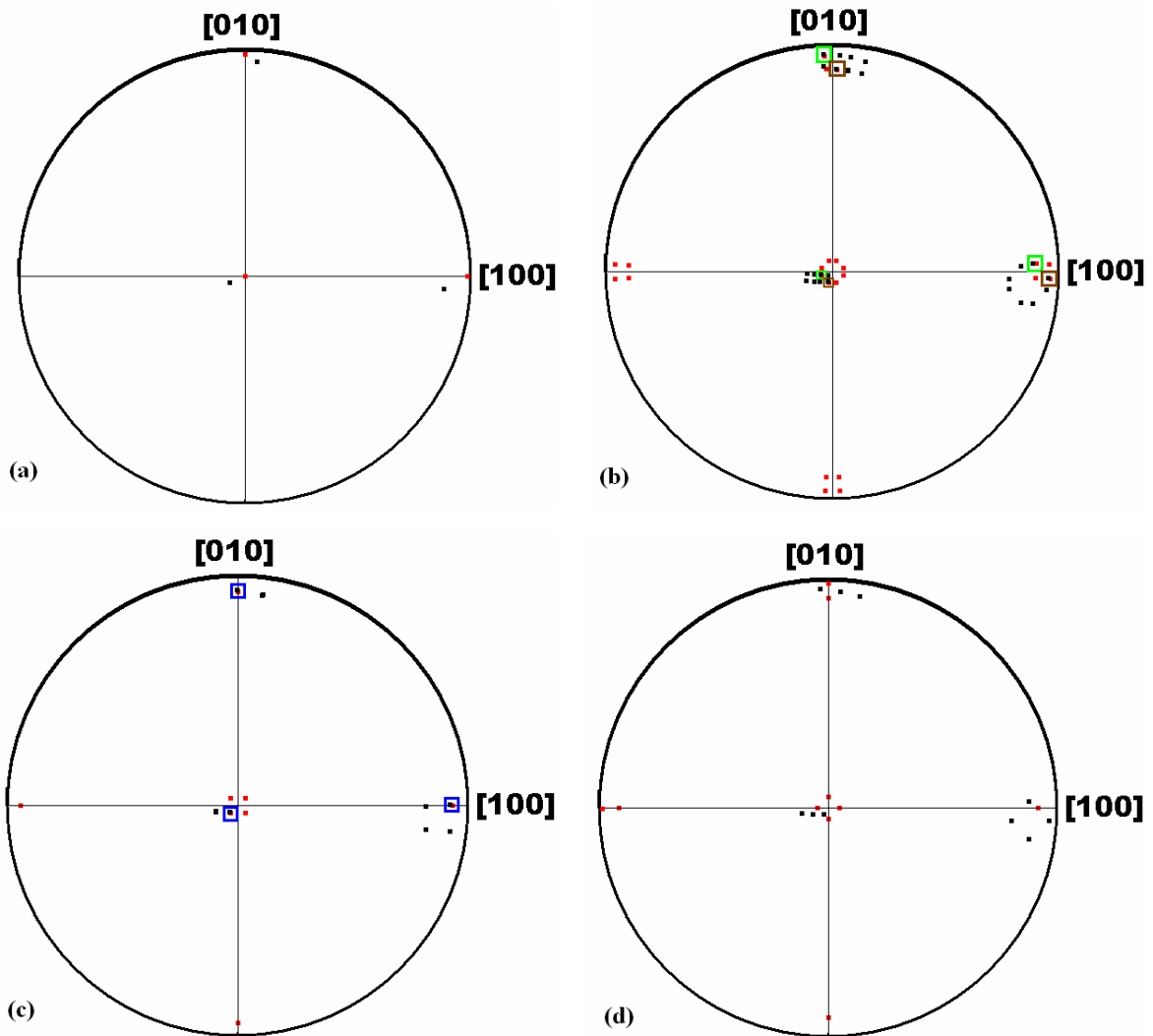


Fig. 6. $\{001\}$ standard projections for the orientations of the austenite grain calculated from the variant pair E F in Fig. 3a according to (a) Bain, (b) K - S, (c) N - W and (d) Pitsch relationships, respectively. The common austenite orientations are enclosed in the open squares.

4. Theoretical prediction of martensitic transformation crystallography by crystallographic phenomenological theory and comparison with experimental results

During the past few decades, the crystallographic phenomenological theory has been applied to the martensitic transformations in many alloy systems [21,31–34]. The phenomenological theory proposed by Wechsler, Lieberman and Read (WLR theory) [21,35] is in particular applicable to the martensitic transformation from face-centered cubic (fcc) structure to body-centered tetragonal (bct) structure, with a product microstructure consisting

of two twinned lamellar variants that have a fixed thickness ratio, which is the case of the present work. Moreover, it requires only the crystal structure and lattice parameters of the austenite and martensite as an input to obtain crystallographic information relating to the transformation process. According to the WLR theory, the total distortion that occurs during complete martensitic transformation can be treated as a pure Bain distortion to obtain the lattice change and a rigid body rotation to achieve an invariant plane (which is finally done by adjusting the amount of martensitic twins). The two twins are formed in the way that different cube axes of the austenite structure become the principal distortion axes along which extension occurs [35]. It should be noted that the reference system for all the following calculations is the cubic crystal coordinate system of the as-yet untransformed austenite.

Table 2 The minimum misorientation angle between the orientations of the austenite grain calculated from different pairs of martensitic variants labeled in Fig. 3a, according to the Bain, K - S, N - W and Pitsch relationships, respectively

Variant pairs	Bain (°)	K-S (°)	N-W (°)	Pitsch (°)
E	8.91	0.84	0.84	4.29
F				
G	8.31	1.61	1.61	4.19
H				
I	8.62	1.41	1.41	4.14
J				
K	8.80	0.80	0.80	4.14
L				
M	7.70	2.44	2.44	4.25
N				
O	9.19	2.55	1.39	4.75
P				
Q	9.00	2.11	2.11	4.28
R				
S	8.86	2.40	2.40	4.02
T				

Assume that the relative amounts of twins V_1 produced by extension along the y axis of austenite and V_2 produced by extension along the x axis of austenite are $(1 - x)$ and x , respectively. The total distortion \mathbf{E} can be expressed as

$$\mathbf{E} = (1-x)\Phi_1\mathbf{T}_1 + x\Phi_2\mathbf{T}_2, \quad (3)$$

where \mathbf{T}_1 and \mathbf{T}_2 are the Bain distortions, and Φ_1 and Φ_2 are the rotations for V_1 and V_2 in order to achieve an invariant plane. In the present case,

$$\mathbf{T}_1 = \begin{pmatrix} \eta_1 & 0 & 0 \\ 0 & \eta_2 & 0 \\ 0 & 0 & \eta_1 \end{pmatrix} \text{ and } \mathbf{T}_2 = \begin{pmatrix} \eta_2 & 0 & 0 \\ 0 & \eta_1 & 0 \\ 0 & 0 & \eta_1 \end{pmatrix}, \quad (4)$$

$$\text{where } \eta_1 = \frac{\sqrt{2}a}{a_0}, \quad \eta_2 = \frac{c}{a_0}.$$

If the relative amount of each twin reaches a certain critical value, there exists a plane in the austenite such that no line in this plane changes in length when averaged over many lamellae of twins. Since this plane forms an interface between the austenite and martensite, the property that this plane does not rotate allows the determination of the total distortion [35]. Subsequently, the habit plane normal, the relative amount of twins, the magnitude and direction of macroscopic shear, the twinning plane and the OR between austenite and martensite can be determined. The concept that the interface between the two phases be one of zero average distortion serves as the foundation upon which this analysis is based [35].

The calculated habit plane, relative amount of twins, macroscopic shear magnitude, shear direction and shear angle, twinning plane and the misorientation angle and axis between the two variants are shown in Table 3. It should be noted that all the crystallographic planes and directions without specific subscript are expressed with respect to the cubic crystal coordinate system of the as-yet untransformed austenite. From Table 3, the theoretical ratio of the amounts of twins within one initial austenite grain, $\frac{1-x}{x}$, is calculated to be 1.786. This theoretical value is plotted in Fig. 4b (dashed line) for easier comparison with the experimental values. One can see that the theoretical ratio of the amounts of twins is in reasonable agreement with the experimental values obtained from individual grains. In coherent twins, the twin interface plane is also the twinning plane. The mean twin interface plane was determined in Section 3.3 to be $\{0.399 \ 0.383 \ 0.833\}_M$. In order to compare with the theoretical value, it is further expressed with respect to the cubic crystal coordinate of the untransformed austenite. For the twin V_1 , $\{0.399 \ 0.383 \ 0.833\}_M$ has the indices $\{0.665 \ 0.747$

$-0.018\}$ when expressed in the austenite coordinate system, which has a discrepancy of 1.13° from the theoretical value $\{0.687\ 0.726\ -0.035\}$ shown in Table 3. For V_2 , $\{0.399\ 0.383\ 0.833\}_{M2}$ has the indices $\{-0.710\ -0.703\ 0.021\}$ (equivalent to $\{0.710\ 0.703\ -0.021\}$) when expressed in the austenite coordinate system, which is 2.03° away from the theoretical value. This suggests that the twinning plane calculated from the WLR theory is in good agreement with that determined by means of two-surface trace analysis. The good agreements of the theoretical predictions in the relative amounts of twins and the twinning plane with the experimental results suggest that the crystallographic information concerning the martensitic transformation (e.g. habit plane and transformation shear given in Table 3) that cannot be readily obtained from experimental determination is reliable.

Table 3 Crystallographic features of martensitic transformation calculated according to the WLR crystallographic phenomenological theory

Crystallographic feature	Result
Habit plane	$\{0.690\ -0.102\ 0.716\}$
Ratio of the amounts of the two variants (1-x)/x	1.786 (1-x=0.641; x=0.359)
Magnitude of macroscopic shear	0.121
Direction of macroscopic shear	$\langle -0.709\ 0.105\ 0.698 \rangle$
Shear angle	6.88°
Twinning plane	$\{0.687\ 0.726\ -0.035\}$
Misorientation between V_1 and V_2	79.31° around $\langle 0.707\ 0.707\ 0.001 \rangle_{M}$ axis ^a

^a The subscript M in the indices of the crystallographic directions denotes that the directions are expressed with respect to the tetragonal crystal coordinate system of martensite.

Based on the above calculated results, the OR between the initial austenite and the two martensitic variants expressed in matrices are obtained as follows:

$$\mathbf{r}_A = \begin{pmatrix} 0.7432 & 0.6584 & -0.1192 \\ 0.0784 & 0.0910 & 0.9927 \\ 0.6645 & -0.7472 & 0.0158 \end{pmatrix} \cdot \mathbf{r}_{M1}$$

for austenite and twin V_1 , (5)

and

$$\mathbf{r}_A = \begin{pmatrix} -0.0897 & -0.0050 & -0.9960 \\ -0.6992 & -0.7108 & 0.0668 \\ -0.7091 & 0.7025 & 0.0604 \end{pmatrix} \cdot \mathbf{r}_{M2}$$

for austenite and twin V_2 , (6)

where \mathbf{r}_{Mi} ($i=1,2$) is the vector expressed with respect to the tetragonal crystal coordinate system of martensite, and \mathbf{r}_A is the same vector when expressed with respect to the cubic crystal coordinate system of the as-yet untransformed austenite. According to the calculated OR matrices in Eqs. (5) and (6), the misorientation between the two martensitic variants, expressed with a rotation angle and a rotation axis, is 79.31° around the $\langle 0.707 \ 0.707 \ 0.001 \rangle_M$ axis (shown in Table 3), which also agrees well with the experimental results.

The OR between austenite and the respective two martensitic variants are further expressed in terms of parallel planes and directions for easy comparison with the K–S and N–W relationships obtained in Section 3.4:

$$\begin{aligned} (111)_A \ 0.54^\circ \text{ from } (101)_{M1}, \quad [\bar{1}\bar{1}0]_A \ 3.19^\circ \text{ from } [1\bar{1}\bar{1}]_{M1} \\ (\bar{1}\bar{1}\bar{1})_A \ 0.54^\circ \text{ from } (101)_{M2}, \quad [\bar{1}\bar{1}0]_A \ 3.20^\circ \text{ from } [1\bar{1}\bar{1}]_{M2} \end{aligned} \quad (7)$$

$$\begin{aligned} (111)_A \ 0.54^\circ \text{ from } (101)_{M1}, \quad [1\bar{2}\bar{1}]_A \ 6.32^\circ \text{ from } [10\bar{1}]_{M1} \\ (\bar{1}\bar{1}\bar{1})_A \ 0.54^\circ \text{ from } (101)_{M2}, \quad [2\bar{1}\bar{1}]_A \ 1.25^\circ \text{ from } [10\bar{1}]_{M2} \end{aligned} \quad (8)$$

It can easily be seen that the above-predicted ORs are quite close to K–S and N–W, confirming that these two ORs are possible ORs governing the martensitic transformation in this material.

5. Discussion

The method used for calculating the OR between austenite and martensite from the measured orientations of martensite in Section 3.4, as well as the WLR theory in Section 4, is built purely on geometrical consideration of the martensitic transformation process. It is difficult to decide the preference between the K–S and N–W ORs. Therefore, the transformation strain that gives rise to the transformation strain energy associated with different ORs could be a criterion to discern the possible OR(s) that governs the martensitic transformation.

For a diffusionless martensitic transformation that changes the crystal structure of the

parent phase into that of the product phase through collective atomic movements, the formation of the new phase tends to select the smallest atomic movement in order to minimize the transformation strain and consequently the transformation strain energy. To realize this, a specific OR between the parent and the product phases is achieved according to the crystallographic compatibility between the two phases. In the case of the Ni₅₃Mn₂₅Ga₂₂ alloy, the (111)_A//(101)_M plane parallelism (in K–S or N–W ORs) offers an ideal three-dimensional atomic matching between austenite and martensite, as the stacking sequences of different constituent elements on (111)_A and (101)_M are the same, i.e. Ga–Ni–Mn–Ni–Ga, as shown in Fig.7, and moreover, the interplanar spacing of (111)_A (3.37 Å) is very close to that of (101)_M (3.34 Å). On (111)_A, there are two distinct atom rows $[1\bar{1}0]_A$ (atomic spacing 4.13Å) and $[\bar{2}11]_A$ (atomic spacing 7.15 Å) with an acute intersecting angle of 30°. Coincidentally, there are also two atom rows on (101)_M having quite close atomic spacing, $[11\bar{1}]_M$ (4.28 Å) and $[10\bar{1}]_M$ (7.64 Å) with an intersecting angle of 26.8°, as shown in Fig. 8. The former direction parallelism $[1\bar{1}0]_A//[11\bar{1}]_M$ results in the K–S OR, while the latter $[\bar{2}11]_A//[10\bar{1}]_M$ leads to the N–W OR. Although the two ORs are very close to each other (only deviating by 3.2°), the atom movements under the two ORs during the transformation are somewhat different, which requires different amounts of transformation energy. The less energy consuming one should be the prevalent one. As seen in Fig. 8, the transformation under the K–S OR requires an expansion of 3.63% of the austenite lattice in $[1\bar{1}0]_A$ direction and a shrinkage of 3.63% in its perpendicular direction $[11\bar{2}]_A$. Transformation under the N–W OR, however, demands the austenite lattice to expand 6.85% in the $[\bar{2}11]_A$ direction and shrink 6.31% in its perpendicular direction $[01\bar{1}]_A$. Obviously, the transformation following K–S OR is less energy consuming than that following the N–W OR. Therefore, in the present study, the martensitic transformation under the K–S OR between the parent austenite and martensite is energetically favorable. However, the N–W OR should not be totally excluded. Under certain local stresses and strains accumulated during the transformation process, this OR could be prevalent over the K–S OR. It could be a sort of accommodation of the main K–S OR, as

shown by grain 4 in Fig. 3a.

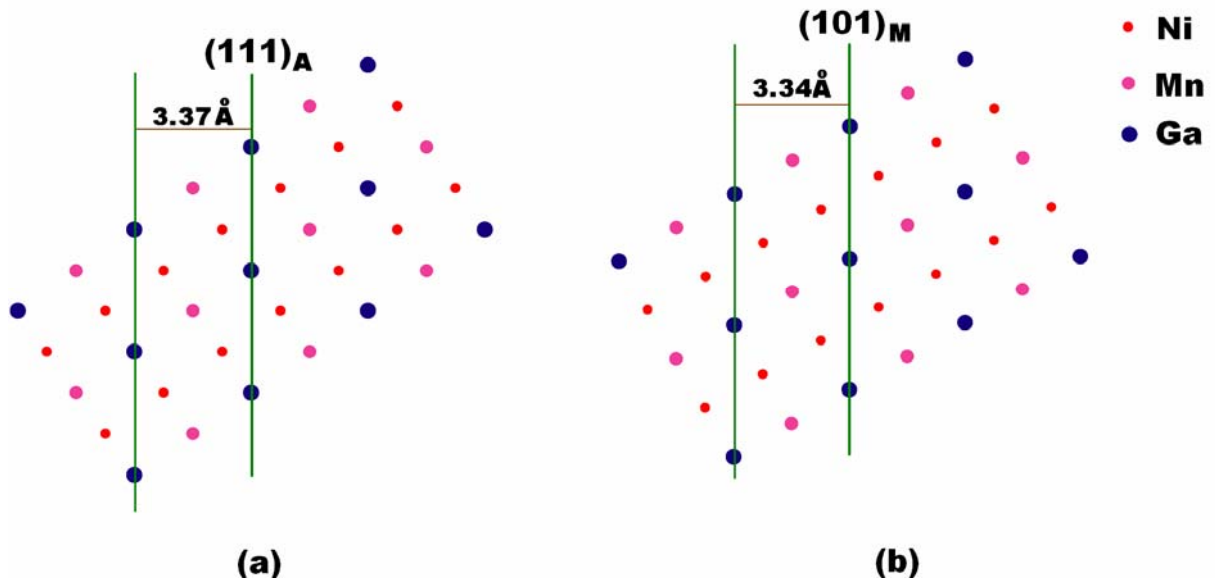
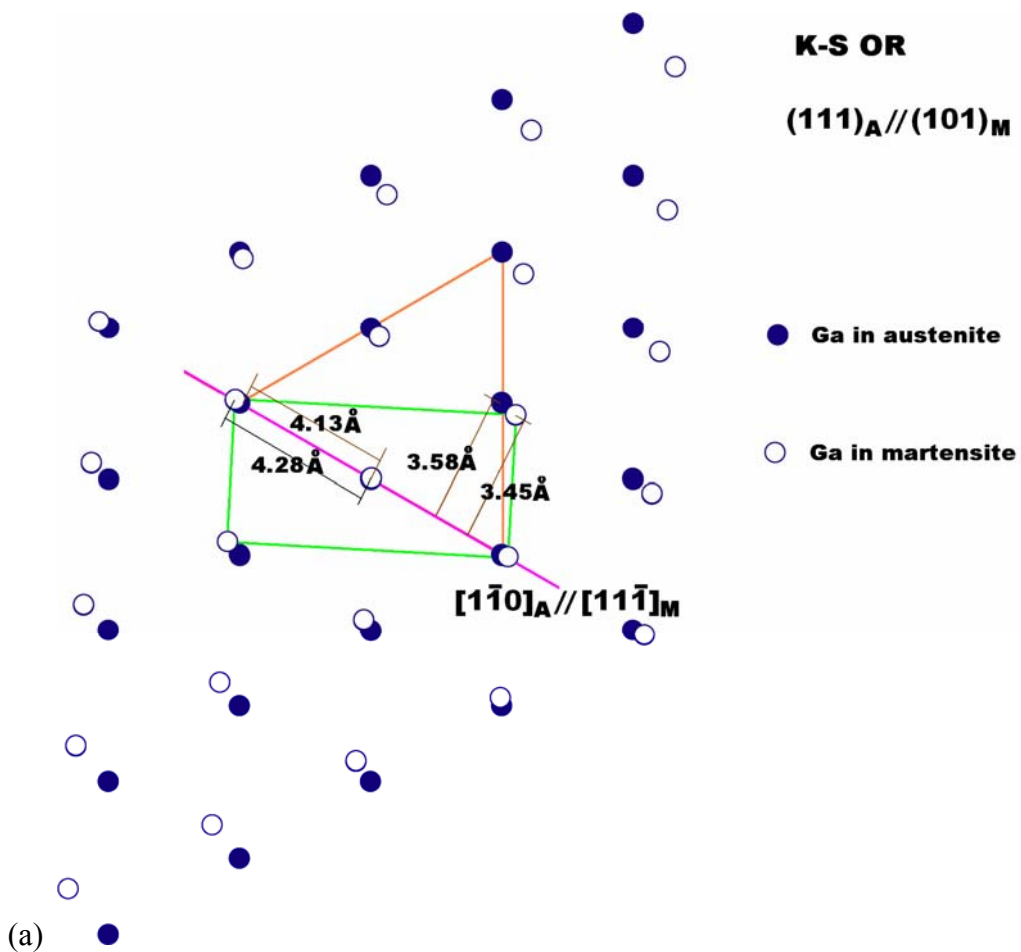


Fig. 7. The stacking sequence and interplanar spacing of (a) (111)_A and (b) (101)_M planes in austenite and martensite, respectively.



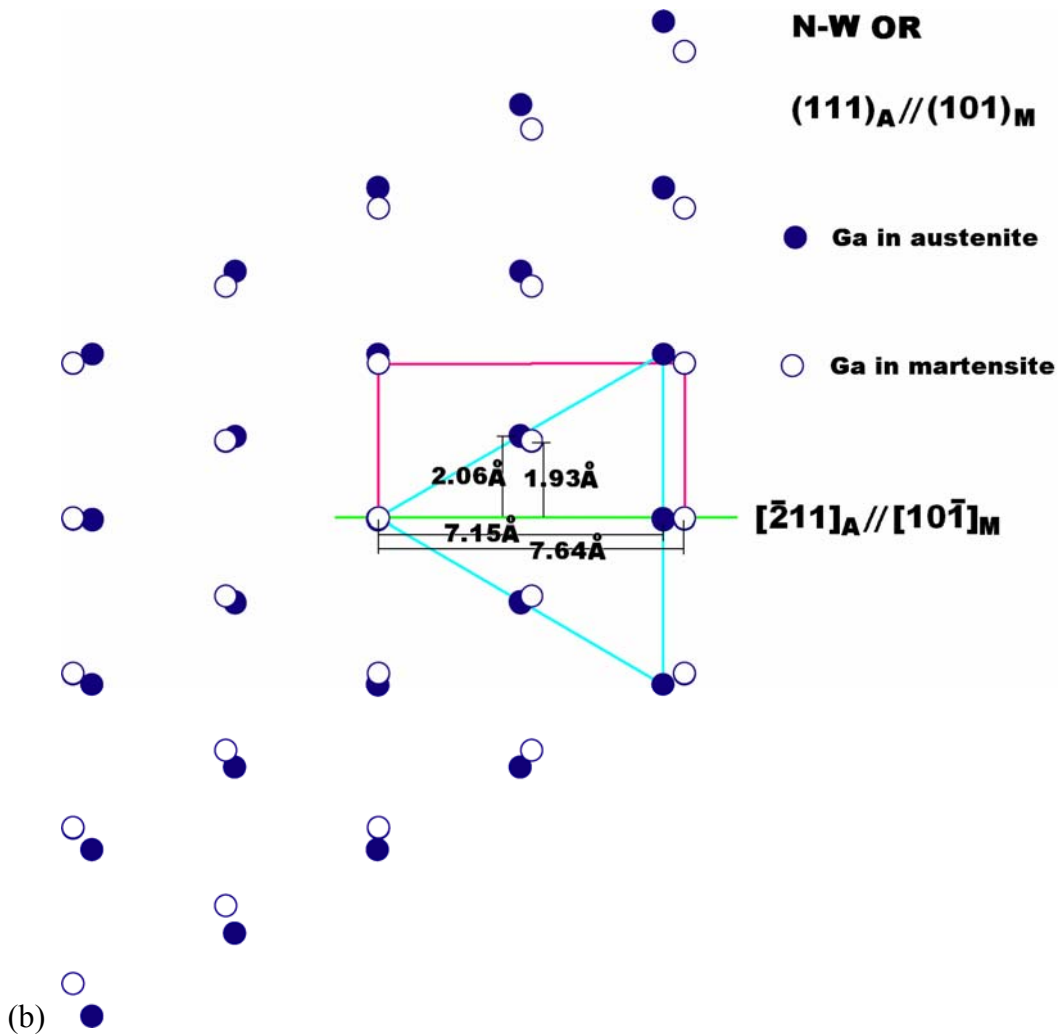


Fig. 8. Correspondence of atomic positions and crystallographic directions on $(111)_A$ and $(101)_M$ planes for (a) K - S and (b) N - W relationships. K-S relationship: $(111)_A // (101)_M$, $[\bar{1}\bar{1}0]_A // [1\bar{1}\bar{1}]_M$; N-W relationship: $(111)_A // (101)_M$, $[\bar{2}\bar{1}1]_A // [10\bar{1}]_M$.

6. Summary and conclusions

Martensitic transformation crystallography and microstructure of the $\text{Ni}_{53}\text{Mn}_{25}\text{Ga}_{22}$ FSMA were studied in detail by means of experimental observation and theoretical calculations. The twinning relationship between the martensitic variants and the OR between austenite and martensite during transformation were unambiguously determined. The following conclusions can be drawn:

1. There are two microscopically twin-related martensitic variants distributed alternately in each initial austenite grain. The misorientation between the neighboring twin variants is $\sim 82^\circ$

around the $\langle 110 \rangle_M$ axis.

2. The twin interface plane is $\{0.399\ 0.383\ 0.833\}_M$ expressed in the tetragonal crystal coordinate system of martensite, which is 1.79° from $\{112\}_M$ plane. Most of the twins have a thickness of $0.2\text{--}2.6\ \mu\text{m}$ with an average value of $\sim 1.3\ \mu\text{m}$. The ratio of the relative amounts of twins within the same initial austenite grain is ~ 1.70 .

3. The main OR between austenite and martensite is determined to be the Kurdjumov–Sachs (K–S) relationship with $(111)_A // (101)_M$, $[1\bar{1}0]_A // [11\bar{1}]_M$.

4. The habit plane calculated from the WLR theory is $\{0.690\ -0.102\ 0.716\}_A$, and the magnitude, direction and shear angle of the macroscopic transformation shear are 0.121 , $\langle -0.709\ 0.105\ 0.698 \rangle_A$ and 6.88° , respectively.

Acknowledgements

The authors are grateful to the National Natural Science Foundation of China (Grant Nos. 50325102, 50531020 and 50528102) and the Ministry of Education of China with the NCET-04-0282. Financial support from the 111 Project (B07015) and the PRA Project (MX04-02) is greatly acknowledged. One of the authors (D.Y. Cong) is grateful to the financial support from the PhD fund of Northeastern University, China. Thanks are due to the anonymous reviewer who has suggested the reasonable interpretation of the curvature of some variants offered in Section 3.1 Microstructure.

References

- [1] Wuttig M, Liu L, Tsuchiya K, James RD. *J Appl Phys* 2000;87:4707.
- [2] Müllner P, Chernenko VA, Kosterz G. *J Appl Phys* 2004;95:1531.
- [3] James RD, Wuttig M. *Philos Mag A* 1998;77:1273.
- [4] Kosterz G, Müllner P. *Z Metallkd* 2005;96:703.
- [5] Morito M, Oikawa K, Fujita A, Fukamichi K, Kainuma R, Ishida K. *Scripta Mater* 2005;53:1237.
- [6] Imano Y, Omori T, Oikawa K, Sutou Y, Kainuma R, Ishida K. *Mater Sci Eng A* 2006;438–440:970.

- [7] Sozinov A, Likhachev AA, Lanska N, Ullakko K. *Appl Phys Lett* 2002;80:1746.
- [8] Ullakko K, Huang JK, Kantner C, O'Handley RC, Kokorin VV. *Appl Phys Lett* 1996;69:1966.
- [9] Cong DY, Zetterström P, Wang YD, Delaplane R, Peng RL, Zhao X, et al. *Appl Phys Lett* 2005;87:111906.
- [10] Pons J, Chernenko VA, Santamarta R, Cesari E. *Acta Mater* 2000;48:3027.
- [11] Khovaylo VV, Buchelnikov VD, Kainuma R, Koledov VV, Ohtsuka M, Shavrov VG, et al. *Phys Rev B* 2005;72:224408.
- [12] Chernenko VA, Pons J, Segui C, Cesari E. *Acta Mater* 2002;50:53.
- [13] Khovailo VV, Takagi T, Tani J, Levitin RZ, Cherechukin AA, Matsumoto M, et al. *Phys Rev B* 2002;65:092410.
- [14] Wang YD, Cong DY, Peng RL, Zetterström P, Zhang ZF, Zhao X, et al. *J Mater Res* 2006;21:691.
- [15] Xiong F, Liu Y, Pagounis E. *J Magn Magn Mater* 2005;285:410.
- [16] Kakeshita T, Fukuda T, Takeuchi T. *Mater Sci Eng A* 2006;438–440:12.
- [17] Kim JH, Inaba F, Fukuda T, Kakeshita T. *Acta Mater* 2006;54:493.
- [18] Cong DY, Zhang YD, Wang YD, Esling C, Zhao X, Zuo L. *J Appl Crystallogr* 2006;39:723.
- [19] Cong DY, Wang YD, Zetterström P, Peng RL, Delaplane R, Zhao X, et al. *Mater Sci Technol* 2005;21:1412.
- [20] Webster PJ, Ziebeck KRA, Town SL, Peak MS. *Philos Mag B* 1984;49:295.
- [21] Lieberman DS, Wechsler MS, Read TA. *J Appl Phys* 1955;26:473.
- [22] Zimmermann F, Humbert M. *Acta Mater* 2002;50:1735.
- [23] Humbert M, Wagner F, Moustahfid H, Esling C. *J Appl Cryst* 1995;28:571.
- [24] Humbert M, Dey SR, Bouzy E, Hazotte A. *Mater Sci Forum* 2005;495–497:1219.
- [25] Bunge HJ, Esling C, Muller J. *Acta Crystallogr A* 1981;37:889.
- [26] Bain EC. *Trans AIME* 1924;70:25.
- [27] Kurdjumov G, Sachs G. *Z Phys* 1930;64:325.
- [28] Nishiyama Z. *Sci Rep Tohoku Imp Univ* 1934;23:637.
- [29] Wassermann G. *Mitt K-Wilh-Inst Eisenforsch* 1935;17:149.

- [30] Pitsch W. *Acta Metall* 1962;10:897.
- [31] Ueda M, Yasuda HY, Umakoshi Y. *Acta Mater* 2003;51:1007.
- [32] Burkart MW, Read TA. *Trans AIME* 1953;197:1516.
- [33] Pond RC, Celotto S. *Int Mater Rev* 2003;48:225.
- [34] Pond RC, Ma X, Hirth JP. *Mater Sci Eng A* 2006;438–440:109.
- [35] Wechsler MS, Lieberman DS, Read TA. *Trans AIME* 1953;197:1503.

Multipley twinned nanostructure in novel ferromagnetic shape-memory alloys

D. Y. CONG^{1,2}, Y. D. ZHANG^{1,2}, C. ESLING², Y. D. WANG¹, J. S. LECOMTE², X. ZHAO¹
and L. ZUO¹

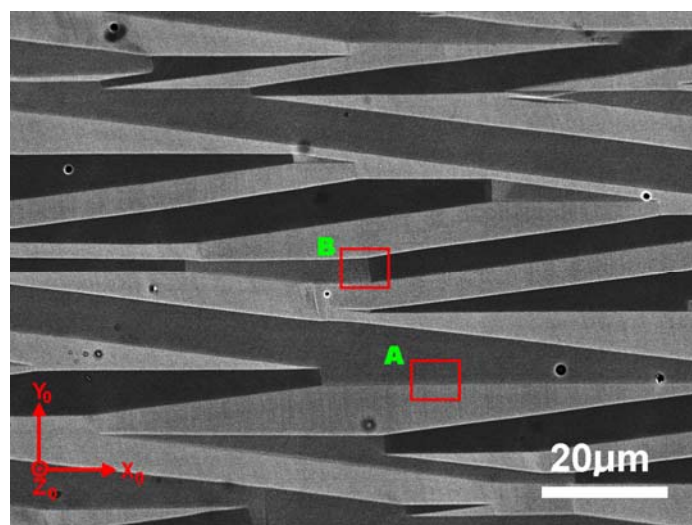
¹Key Laboratory for Anisotropy and Texture of Materials (MOE), Northeastern University, Shenyang 110004, China

²LETAM, CNRS-UMR 7078, University of Metz, Ile du Saulcy, 57045 Metz, France

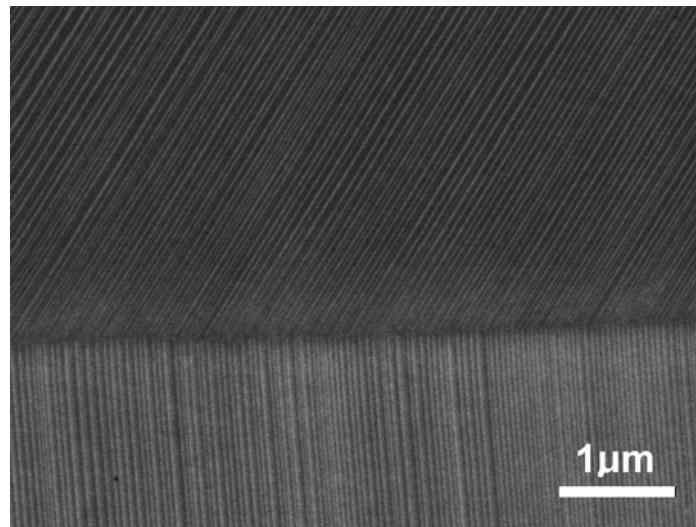
Shape-memory alloys (SMAs) are attractive smart materials that have an intrinsic ability to recover their initial configurations upon the application of thermal or magnetic fields¹. During the past few decades, great efforts have been made to investigate various aspects of the SMAs²⁻⁶ due to their wide applications in medical, aerospace and marine industries^{1,7}. The newly developed ferromagnetic SMAs (FSMAs)⁸⁻¹² can integrate the advantages of both conventional thermally controlled SMAs and magnetostrictive materials, and show giant output strain and fast dynamic response^{13,14}, which make them extremely promising for use in sensors and actuators. It is well recognized that twins in the martensitic phase play an important role in the shape-memory effect of both thermally and magnetically controlled SMAs^{13,14}. Up to now, nanoscale twins in the SMAs have been observed in several studies¹⁵⁻¹⁹. However, the intrinsic nature of the nanotwins and the twin interfaces is far from being understood. Particularly, the orientation relationships between the nanotwins have never been demonstrated. The lack of fundamental crystallographic information has greatly hindered further attempts to develop high-performance SMAs with large shape-memory effect, excellent mechanical properties and high stability during cyclic treatments. A full understanding of the correlation between the microstructure and crystallography of the nanotwins is thus of great significance. Here, we report for the first time the orientation relationships between the nanotwins and the intrinsic nature of different kinds of twin interfaces in the FSMAs.

A Ni-Mn-Ga FSMA with composition of Ni₅₃Mn₂₅Ga₂₂ (at.%) (see the Methods section for detailed information) was used in this study. Scanning electron microscopy (SEM) observations indicate that this alloy has a typical lamellar martensitic microstructure at room temperature (Fig. 1(a)). The martensitic lamellae, with a thickness of several micrometers, are

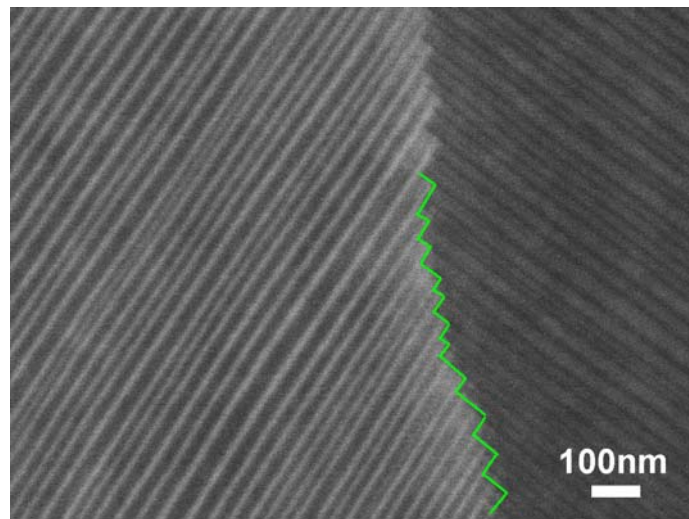
well self-accommodated and separated from each other by straight inter-lamellar boundaries at the micrometer scale. However, the lamellae often bifurcate or bend through reorientation. The intra-lamellar reorientation can be readily seen through the contrast change of the backscattered electron (BSE) image, as the contrast of the SEM-BSE image originates from the crystal orientation in the case of single phase with a homogeneous composition in the $\text{Ni}_{53}\text{Mn}_{25}\text{Ga}_{22}$ alloy. High magnification observations demonstrate that the martensitic lamellae are composed of a vast amount of fine internal plates having two contrasts distributed alternately, as shown in Fig. 1(b) (the zoom image of Frame A in Fig. 1(a)). The two distinct contrasts indicate that the internal plates in each lamella have only two orientations, suggesting that they might be twin-related (their orientation relationship and interface plane will be determined later). The thickness of the internal plates ranges from several nanometers to several tens of nanometers. The nanoplates are paired, and clearly the two nanoplates in each pair have quite different thickness. One is thicker (Major) and the other is thinner (Minor). The interfaces between the nanoplates are straight, sweeping the whole lamella. High magnification SEM observations also reveal that the intra-lamellar interface that borders the straight lamella with its bent part is non-straight and has a “step” configuration that consists of well-defined fine steps, as shown in Fig. 1(c) (the zoom image view of Frame B in Fig. 1(a)). In the “step” configuration, one bundle of nanoplates from a lamella ends at the intra-lamellar interface and this forms one step.



(a)



(b)



(c)

Figure 1. (a) Backscattered electron image of $\text{Ni}_{53}\text{Mn}_{25}\text{Ga}_{22}$ alloy showing a self-accommodated lamellar microstructure, and the sample coordinate system $X_0Y_0Z_0$ for pole figure construction (Figs. 2(b) and 3(b)). Frames A and B display the inter-lamellar and intra-lamellar interface, respectively. (b) Zoom image of Frame A in (a), showing the nanoplates in two neighboring lamellae. (c) Zoom image of Frame B in (a), demonstrating the “step” configuration of the intra-lamellar interface. Solid lines are drawn to underline the stepped interface.

In order to determine the orientation correlation between the adjacent nanoplates, we calculated their misorientations expressed with the misorientation angle and the rotation axis. According to the definition of twinning^{20, 21}, if there are two 180° rotations around two

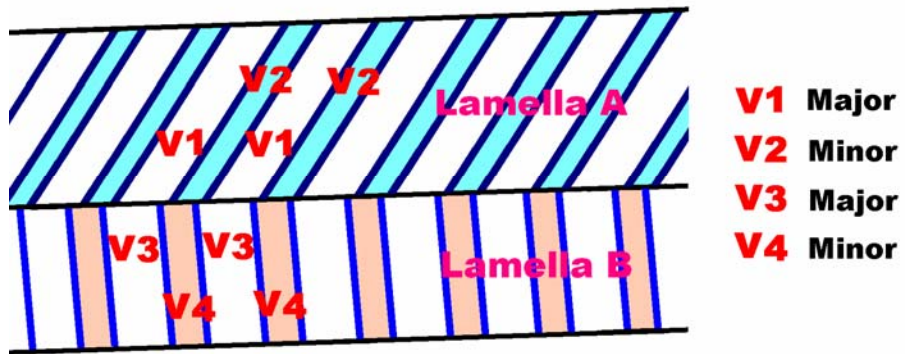
rational axes and the planes normal to the rotation axes are also rational, the two crystals have a twinning relationship and the twin is a compound twin, with one rotation axis being the twinning direction $\boldsymbol{\eta}_1$ and the other being the normal of the twinning plane \mathbf{K}_1 . By taking into account the criterion of minimum twinning shear, all the twinning elements (\mathbf{K}_1 , $\boldsymbol{\eta}_1$, the conjugate twinning plane \mathbf{K}_2 , the conjugate twinning direction $\boldsymbol{\eta}_2$ and the magnitude of shear s) can be determined²². With the misorientation calculation²³, the internal nanoplates within each lamella are specified as compound twins with the twinning elements $\mathbf{K}_1=\{112\}$, $\mathbf{K}_2=\{11\bar{2}\}$, $\boldsymbol{\eta}_1=\langle 11\bar{1}\rangle$, $\boldsymbol{\eta}_2=\langle 111\rangle$, $\mathbf{P}=\{1\bar{1}0\}$ and $s=0.379$. These internal nanotwins are related to each other by a rotation of $\sim 79^\circ$ around one $\langle 110\rangle$ axis. With the direction vectors of the trace of the twin interface and the individual orientations of the twins, it is possible to determine the twin interface plane by the indirect two-trace method²⁴. The calculated results show that the twin interface plane between the internal nanotwins is $\{0.4084\ 0.4086\ 0.8163\}$ when expressed in the tetragonal crystal coordinate system²⁵, which is actually a $\{112\}$ plane (with 0.03° deviation) within the experimental accuracy. The fact that the interface plane coincides with the twinning plane gives an indication that the twin interfaces between the nanotwins are coherent on the $\{112\}$ twinning plane, which ensures the minimization of the interfacial energy. Obviously, the alternate formation of the internal nanotwins is the requirement of the invariant lamellar interface, that is, the total accumulated strain resulting from the martensitic transformation at the lamellar interface is zero, which can be achieved by adjusting the thickness of the nanotwins²⁶.

The adjacencies of the nanotwins at the straight inter-lamellar interfaces (Fig. 1(b)) and the stepped intra-lamellar interfaces (Fig. 1(c)) represent two kinds of crystallographic connections. These connections result in different orientation relationships between those neighboring pairs of nanotwins across the interfaces. So far, such orientation relationships have not been reported and the determination of them undoubtedly provides new insights into the crystallography of the newly developed FSMAs. For a clear presentation, the two kinds of configurations are analyzed separately as follows.

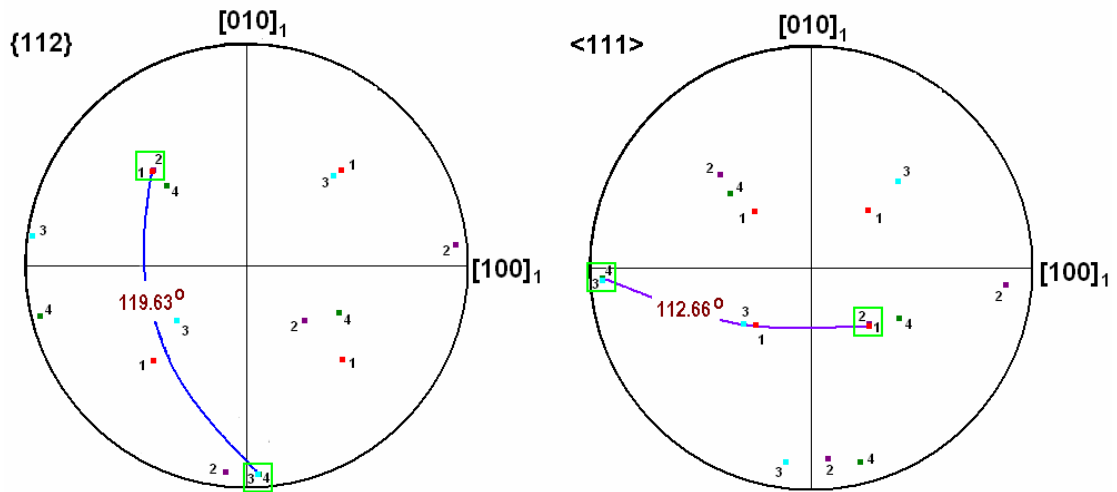
For the inter-lamellar connection, Fig. 2(a) illustrates the nanotwins (V1 and V2 in Lamella A and V3 and V4 in Lamella B) connected by the inter-lamellar interfaces and Fig.

2(b) displays the $\{112\}$ and $\langle 111 \rangle$ standard stereographic projections (in the crystal coordinate system of V1) of the four nanotwin variants. As shown in Fig. 2(b), the intersecting angles between the twinning planes and between the twinning directions of the nanotwins in Lamella A and Lamella B are 119.63° and 112.66° , respectively. This geometrical configuration offers four possible adjacencies (V1 and V3, V1 and V4, V2 and V3, V2 and V4) between the respective nanotwins in Lamella A and Lamella B. Table 1(a) displays the misorientation calculation results of the minimum misorientation angle and two near- 180° misorientation angles, with their corresponding rotation axes, between those adjacent nanotwins. As a reference, the same misorientation information from the internal nanotwin pairs (V1 and V2, V3 and V4) is also given in the table. The twinning planes and twinning directions are summarized in Table 1(b). It is revealed that when the major nanotwin variants V1 and V3 meet, these two variants are still twin-related, with the twinning elements of the same family as those of the internal nanotwins (V1 and V2, V3 and V4), i.e. $\mathbf{K}_1 = \{112\}$, $\mathbf{K}_2 = \{11\bar{2}\}$, $\boldsymbol{\eta}_1 = \langle 11\bar{1} \rangle$, $\boldsymbol{\eta}_2 = \langle 111 \rangle$, $\mathbf{P} = \{1\bar{1}0\}$ and $s = 0.379$. Indirect two-trace method calculation also shows that the inter-lamellar interface plane is in general agreement with the $\{112\}$ twinning plane. However, the corresponding $\{112\}$ planes of the variants V1 and V3 have a deviation of 3.55° and the corresponding $\langle 111 \rangle$ directions have a deviation of 5.50° . This suggests that the twinning relationship between V1 and V3 is not perfect. The imperfectness of the twinning relationship results in that the two variants (V1 and V3) are related to each other by a rotation of 83.00° around $\langle 110 \rangle$ axis, rather than a rotation of $\sim 79^\circ$ between the internal nanotwins (e.g. V1 and V2). When the major and minor variants (V1 and V4, V2 and V3) meet, the $\{112\}$ twinning relationship suffers an enlarged imperfectness (Table 1(b)). The corresponding $\{112\}$ planes and corresponding $\langle 111 \rangle$ directions (in V1 and V4) deviate by 8.18° and 13.66° , respectively. The major and minor variants are related to each other by a rotation of $\sim 88^\circ$ around roughly the $\langle 110 \rangle$ axis. Notably, when the minor variants V2 and V4 meet, the twinning relationship is totally lost. They are only related to each other by a rotation of 13.36° around the $\langle 0.9630 \ 0.0614 \ 0.2623 \rangle$ axis of the tetragonal structure. The above results show that the twinning relationship between the internal twins are perfect and of the first order; while that between the lamellae are imperfect and of lower order.

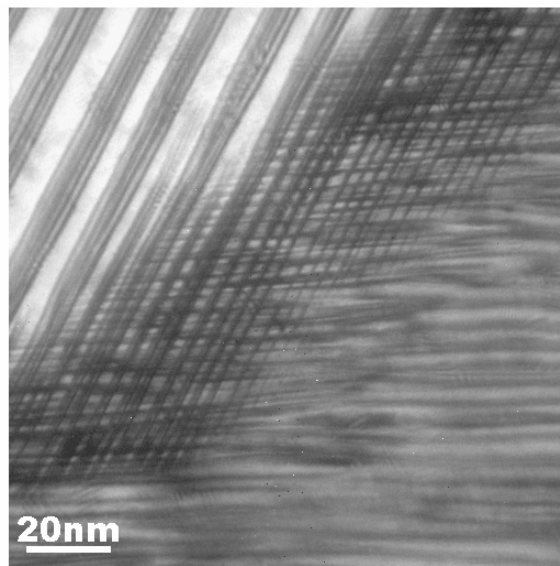
This means the perfect twinning relationships between the internal nanotwins and between the lamellae cannot be satisfied at the same time and the internal twins have the higher priority.



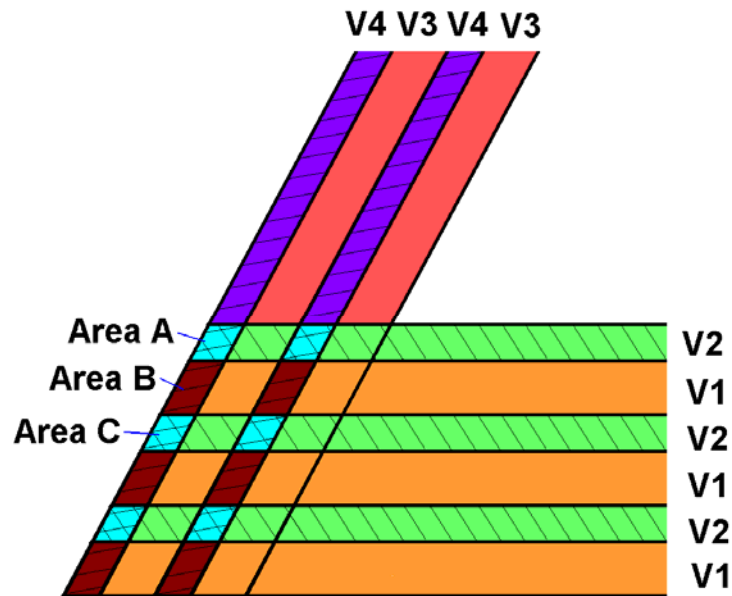
(a)



(b)



(c)



(d)

Figure 2. (a) Schematic illustration of the nanotwins connected by the inter-lamellar interface shown in Fig. 1(b). (b) $\{112\}$ and $\langle 111 \rangle$ standard stereographic projections, in the crystal coordinate system of V1, of the individual orientations of the nanotwins in (a). The number i ($i=1, 2, 3, 4$) in the projections corresponds to the orientation of each variant V_i of a nanotwin. The common $\{112\}$ planes (twinning planes) and $\langle 111 \rangle$ directions (twinning directions) of the internal nanotwins are enclosed in the squares. (c) TEM image showing the detailed microstructure at an interpenetrated inter-lamellar interface. (d) Schematic illustration of the formation mechanism of the interpenetrated inter-lamellar interface shown in (c).

The detailed fine microstructure at the inter-lamellar interface is shown in Fig. 2(c). It is interesting to see that the inter-lamellar interface that is straight at the micrometer scale (Fig. 1(a)) shows a kind of grid structure in the TEM image, which means that the nanotwins in the two neighboring lamellae penetrate, to some extent, into each other. As the volumes of the interpenetrated parts are relatively small, it is difficult to determine the orientation relationships between the neighboring penetrated and non-penetrated parts using selected area electron diffraction (SAED) due to the insufficient diffraction. Calculation would be a potential alternative to determine the orientation relationship and to explain the formation mechanism of the interpenetrated inter-lamellar interface.

Table 1. (a) The minimum misorientation angle and the two near-180° misorientation angles, with their corresponding rotation axes, between the nanotwins connected by an inter-lamellar interface as illustrated in Fig. 2(a). For each misorientation angle ω , there is a family of 8 equivalent rotations with 8 corresponding equivalent axes \mathbf{d} which transform into each other according to the tetragonal rotation symmetry group. (b) Orientation relationships between the nanotwins connected by the inter-lamellar interface. (c, d) Planes and directions in nanotwin variants V1 (c) and V2 (d) before and after the shear introduced by the penetration of V4 at the interpenetrated inter-lamellar interface as illustrated in Fig. 2(d). The subscripts 1 and 2 in the indices denote that these indices are expressed with respect to the crystal coordinate systems of V1 and V2, respectively.

(a)

Pair of nanotwins	Misorientation angle, ω (°)	Rotation axis, \mathbf{d}			
		d_1	d_2	d_3	
V1/V2	79.38	0.7030	0.7111	0.0114	0.73° from <110> direction
	179.16	0.4541	0.4490	0.7695	0.21° from <111> direction
	179.58	0.5390	0.5493	0.6386	0.42° from the normal of {112} plane
V3/V4	79.24	0.7062	0.7080	0.0003	0.08° from <110> direction
	179.91	0.5448	0.5445	0.6377	0.03° from the normal of {112} plane
	179.98	0.4515	0.4504	0.7703	0.06° from <111> direction
V1/V3	83.00	0.6688	0.7434	0.0049	3.04° from <110> direction
	175.99	0.5276	0.5322	0.6621	1.82° from the normal of {112} plane
	179.63	0.4926	0.4432	0.7490	2.70° from <111> direction
V2/V4	13.36	0.9053	0.0577	0.4209	
	174.39	0.0067	0.1054	0.9944	6.06° from <001> direction
	179.23	0.0490	0.9932	0.1053	6.67° from the normal of {010} plane
V1/V4	88.03	0.6034	0.7974	0.0078	7.90° from <110> direction
	169.06	0.5147	0.5070	0.6914	4.11° from the normal of {112} plane
	179.38	0.5541	0.4193	0.7191	6.83° from <111> direction
V2/V3	88.80	0.7884	0.6151	0.0098	7.06° from <110> direction
	170.17	0.5120	0.5022	0.6969	4.55° from the normal of {112} plane
	179.21	0.4304	0.5516	0.7145	6.68° from <111> direction

Note: The rotation axes in Table 1 (a) are expressed in coordinates; the c/a ratio should be taken into account when transforming the coordinates into the Miller indices.

(b)

Pair of nanotwins	Orientation relationship	
V1/V2	$(\bar{1} \ 1 \ 2)_1 // (\bar{1} \ \bar{1} \ 2)_2$	$[1 \ \bar{1} \ 1]_1 // [1 \ \bar{1} \ \bar{1}]_2$
V3/V4	$(1 \ \bar{1} \ 2)_3 // (\bar{1} \ \bar{1} \ 2)_4$	$[\bar{1} \ 1 \ 1]_3 // [\bar{1} \ \bar{1} \ \bar{1}]_4$
V1/V3	$(1 \ 1 \ 2)_1$ 3.55° from $(\bar{1} \ \bar{1} \ 2)_3$	$[\bar{1} \ \bar{1} \ 1]_1$ 5.50° from $[1 \ 1 \ 1]_3$
V1/V4	$(1 \ \bar{1} \ \bar{2})_1$ 8.18° from $(1 \ \bar{1} \ 2)_4$	$[1 \ \bar{1} \ 1]_1$ 13.66° from $[\bar{1} \ 1 \ 1]_4$
V2/V3	$(1 \ 1 \ 2)_2$ 9.06° from $(\bar{1} \ 1 \ \bar{2})_3$	$[1 \ 1 \ \bar{1}]_2$ 13.37° from $[1 \ \bar{1} \ \bar{1}]_3$

(c)

Plane before shear	Plane after shear	Direction before shear	Direction after shear
$(1 \ 1 \ 2)_1$	$(0.9810 \ 1.3661 \ 1.9235)_1$ 9.46° from $(1 \ 1 \ 2)_1$	$[\bar{1} \ \bar{1} \ 1]_1$	$[\overline{0.5665} \ \overline{0.9805} \ \overline{0.9853}]_1$ 10.59° from $[\bar{1} \ \bar{1} \ 1]_1$
$(\bar{1} \ 1 \ 2)_1$	$(\overline{0.9801} \ 0.6167 \ 2.0801)_1$ 11.56° from $(\bar{1} \ 1 \ 2)_1$	$[1 \ \bar{1} \ 1]_1$	$[1.4725 \ \overline{0.9788} \ 0.9840]_1$ 10.33° from $[1 \ \bar{1} \ 1]_1$
$(\bar{1} \ \bar{1} \ 2)_1$	$(\overline{0.9783} \ \overline{1.4169} \ 2.0872)_1$ 9.26° from $(\bar{1} \ \bar{1} \ 2)_1$	$[1 \ 1 \ 1]_1$	$[0.7231 \ 0.9876 \ 1.0094]_1$ 6.83° from $[1 \ 1 \ 1]_1$
$(1 \ \bar{1} \ 2)_1$	$(0.9827 \ \overline{0.6676} \ 1.9305)_1$ 8.98° from $(1 \ \bar{1} \ 2)_1$	$[\bar{1} \ 1 \ 1]_1$	$[\overline{1.3159} \ 0.9858 \ 1.0107]_1$ 6.72° from $[\bar{1} \ 1 \ 1]_1$

(d)

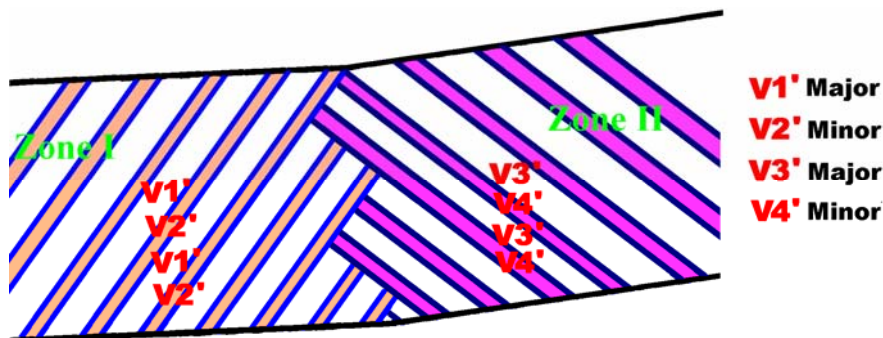
Plane before shear	Plane after shear	Direction before shear	Direction after shear
$(1\ 1\ 2)_2$	$(1.0534\ 1.0492\ 2.1403)_2$ 0.51° from $(1\ 1\ 2)_2$	$[\bar{1}\ \bar{1}\ 1]_2$	$[\overline{1.0528}\ \overline{1.0840}\ 1.0496]_2$ 0.74° from $[\bar{1}\ \bar{1}\ 1]_2$
$(\bar{1}\ 1\ 2)_2$	$(\overline{1.0961}\ 0.9115\ 1.7475)_2$ 5.74° from $(\bar{1}\ 1\ 2)_2$	$[1\ \bar{1}\ 1]_2$	$[0.7977\ \overline{1.3218}\ 1.1898]_2$ 8.95° from $[1\ \bar{1}\ 1]_2$
$(\bar{1}\ \bar{1}\ 2)_2$	$(\overline{1.3339}\ \overline{1.3076}\ 1.1227)_2$ 20.25° from $(\bar{1}\ \bar{1}\ 2)_2$	$[1\ 1\ 1]_2$	$[0.6600\ 0.4592\ 1.3190]_2$ 20.55° from $[1\ 1\ 1]_2$
$(1\ \bar{1}\ 2)_2$	$(0.8156\ \overline{1.1698}\ 1.5155)_2$ 11.26° from $(1\ \bar{1}\ 2)_2$	$[\bar{1}\ 1\ 1]_2$	$[\overline{1.1905}\ 0.6970\ 1.1787]_2$ 10.22° from $[\bar{1}\ 1\ 1]_2$

As the twinning deformation is relative between the twinned part and the undeformed matrix, we assume that the minor variants V2 and V4 are the “twinned” parts with respect to the “undeformed” matrix, the major variants V1 and V3, respectively. Thus the crystal deformation of V4 can be described by a matrix \mathbf{F} expressed in the crystal coordinate of V3. We further assume that V4 penetrates into V1 and V2, i. e. V1 and V2 will suffer the twinning deformation of V4. This deformation will displace a vector \mathbf{u} that lies in a plane whose normal is initially \mathbf{h} in V_i ($i=1, 2$) to a new vector \mathbf{v} within a plane whose normal is \mathbf{k} in the same coordinate system:

$$\begin{aligned} \mathbf{v} &= \mathbf{F}_i \mathbf{u} \\ \mathbf{k} &= (\mathbf{F}_i^{-1})^T \mathbf{h} \end{aligned} \quad \mathbf{i} = 1, 2 \quad (1)$$

where the superscripts -1 and T denote the inverse and the transpose of a matrix, respectively. $\mathbf{F}_i = \mathbf{Q}_i \mathbf{F} \mathbf{Q}_i^T$, where \mathbf{Q}_i is the coordinate transformation matrix transforming the tetragonal crystal coordinate system of V3 into that of V_i ($i=1, 2$). If the “penetrated” part of V_i ($i=1, 2$) assumes a twinning relationship with the “non-penetrated” part, the twinning plane and the twinning direction should be kept invariant. Calculations show that there exist one $\{112\}$

plane and one in-plane $\langle 11\bar{1} \rangle$ direction remaining more or less invariant. The $\{112\}$ planes and $\langle 11\bar{1} \rangle$ directions in variants V1 and V2 before and after the deformation introduced by the penetration of V4 are listed in Table 1 (c) and (d), respectively. It is seen from Table 1 (d) that when V4 penetrates into V2 (illustrated as Area A in Fig. 2 (d)) at the inter-lamellar interface, the penetrated part in V2 possesses an invariant plane and an in-plane direction ($(112)_2$ and $[\bar{1}\bar{1}1]_2$), indicating that the “penetrated” and the “non-penetrated” parts in V2 are also twin-related. This shows the possibility for the penetration. Using the new shear elements (plane and direction) to further penetrate V1 (Area B in Fig. 2 (d)), although there are no invariant exact $\{112\}$ plane and in-plane $\langle 11\bar{1} \rangle$ direction kept, there is one pair quite close to $(11\bar{2})_1$ (with 5.84° deviation) and $[111]_1$ (with 7.91° deviation). This suggests that the penetrated part and the non-penetrated part in V1 possess a deteriorated $\{112\}$ twinning relationship. If V4 continues to penetrate into V2 (Area C in Fig. 2 (d)) with the new shear plane $(11\bar{2})_1$ and shear direction $[111]_1$, it is interesting to see the repetition of the $(112)_2$ (with 6.91° deviation) and $[\bar{1}\bar{1}1]_2$ (with 6.94° deviation) as a kind of invariant plane and direction. This repetition offers the possibility of a continuous penetration and the deterioration of the twinning relationship imposes a kind of hindrance to the penetration. Finally the penetration loses its power and stops after a certain number of repetitions, as seen in Fig. 2 (c). The occurrence of this interpenetration may be due to the high symmetry of the tetragonal structure. The high multiplicity of $\{112\}$ plane and $\langle 11\bar{1} \rangle$ direction offers high chances for multiple twinning.



(a)

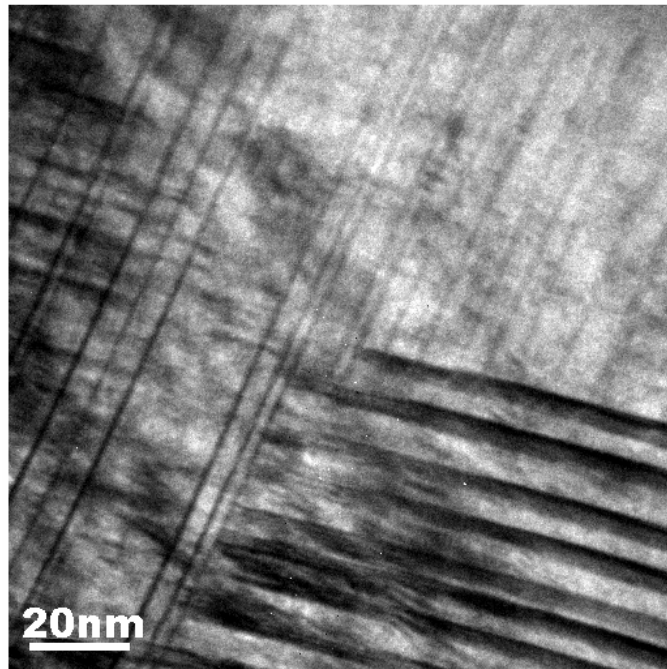
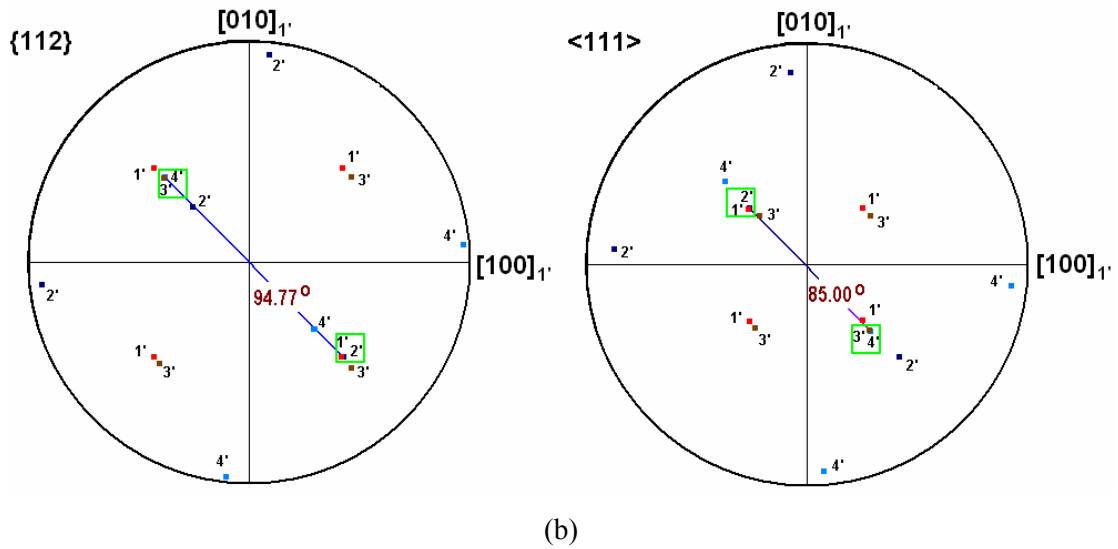


Figure 3. (a) Schematic illustration of the nanotwins connected by the intra-lamellar interface shown in Fig. 1(c). (b) $\{112\}$ and $\langle 111 \rangle$ standard stereographic projections, in the crystal coordinate system of $V1'$, of the individual orientations of the nanotwins in (a). The number i' ($i'=1', 2', 3', 4'$) in the projections corresponds to the orientation of each variant $V_{i'}$ of a nanotwin. The common $\{112\}$ planes (twinning planes) and $\langle 111 \rangle$ directions (twinning directions) of the internal nanotwins are enclosed in the squares. (c) TEM image showing the detailed microstructure at a stepped intra-lamellar interface.

Table 2. (a) The minimum misorientation angle and the two near-180° misorientation angles, with their corresponding rotation axes, between the nanotwins connected by an intra-lamellar interface as illustrated in Fig. 3(a). For each misorientation angle ω , there is a family of 8 equivalent rotations with 8 corresponding equivalent axes \mathbf{d} which transform into each other according to the tetragonal rotation symmetry group. (b) Orientation relationships between the nanotwins connected by the intra-lamellar interface. (c, d) Planes and directions in nanotwin variants V1' (c) and V2' (d) before and after the shear introduced by the assumed penetration of V4' at the stepped intra-lamellar interface. The subscripts 1' and 2' in the indices denote that these indices are expressed with respect to the crystal coordinate systems of V1' and V2', respectively.

(a)

Pair of nanotwins	Misorientation angle, ω (°)	Rotation axis, \mathbf{d}			
		d_1	d_2	d_3	
V1' and V2'	79.24	0.7061	0.7082	0.0006	0.09° from <110> direction
	179.89	0.5449	0.5444	0.6377	0.04° from the normal of {112} plane
	179.96	0.4516	0.4503	0.7703	0.06° from <111> direction
V3' and V4'	79.21	0.7053	0.7089	0.0018	0.18° from <110> direction
	179.82	0.5456	0.5440	0.6375	0.08° from the normal of {112} plane
	179.87	0.4519	0.4496	0.7705	0.10° from <111> direction
V1' and V3'	5.88	0.7257	0.6672	0.1680	9.96° from <110> direction
	179.01	0.0342	0.0372	0.9987	2.90° from the normal of {001} plane
	179.76	0.7001	0.7123	0.0505	2.94° from <110> direction
V2' and V4'	15.78	0.7453	0.6667	0.0093	3.23° from <110> direction
	179.13	0.6995	0.7013	0.1371	7.88° from the normal of {110} plane
	179.85	0.0915	0.1023	0.9905	7.89° from <001> direction
V1' and V4'	85.00	0.7129	0.7012	0.0060	0.58° from <110> direction
	179.36	0.5185	0.5242	0.6756	2.86° from the normal of {112} plane
	179.53	0.4737	0.4817	0.7373	2.87° from <111> direction
V2' and V3'	85.04	0.7020	0.7120	0.0125	0.82° from <110> direction
	179.03	0.4745	0.4813	0.7371	2.88° from <111> direction
	179.45	0.5152	0.5271	0.6758	2.91° from the normal of {112} plane

Note: The rotation axes in Table 2 (a) are expressed in coordinates; the c/a ratio should be taken into account when transforming the coordinates into the Miller indices.

(b)

Pair of nanotwins	Orientation relationship	
V1'/V2'	$(1 \bar{1} 2)_1 // (\bar{1} \bar{1} 2)_2$	$[\bar{1} 1 1]_1 // [\bar{1} \bar{1} \bar{1}]_2$
V3'/V4'	$(\bar{1} 1 2)_3 // (\bar{1} \bar{1} \bar{2})_4$	$[1 \bar{1} 1]_3 // [\bar{1} \bar{1} 1]_4$
V1'/V3'	$(1 \bar{1} 2)_1$, 5.87° from $(1 \bar{1} 2)_3$	$[\bar{1} 1 1]_1$, 5.81° from $[\bar{1} 1 1]_3$
V1'/V4'	$(1 \bar{1} \bar{2})_1$, 5.72° from $(1 1 2)_4$	$[\bar{1} 1 \bar{1}]_1$, 5.74° from $[1 1 \bar{1}]_4$
V2'/V3'	$(\bar{1} \bar{1} 2)_2$, 5.82° from $(1 \bar{1} 2)_3$	$[1 1 1]_2$, 5.77° from $[1 \bar{1} \bar{1}]_3$

(c)

Plane before shear	Plane after shear	Direction before shear	Direction after shear
$(\bar{1} 1 2)_1$	$(\overline{0.9657} \overline{0.9647} \overline{1.9146})_1$ 0.23° from $(\bar{1} 1 2)_1$	$[1 \bar{1} 1]_1$	$[0.9581 \overline{0.9564} \overline{0.9651}]_1$ 0.23° from $[1 \bar{1} 1]_1$
$(\bar{1} \bar{1} 2)_1$	$(\overline{1.1563} \overline{0.8393} \overline{2.3886})_1$ 8.22° from $(\bar{1} \bar{1} 2)_1$	$[1 1 1]_1$	$[0.7701 \overline{1.2397} \overline{0.8084}]_1$ 11.34° from $[1 1 1]_1$
$(1 \bar{1} 2)_1$	$(\overline{0.6608} \overline{0.6512} \overline{2.8433})_1$ 21.24° from $(1 \bar{1} 2)_1$	$[\bar{1} 1 1]_1$	$[\overline{1.4128} \overline{1.4303} \overline{0.6559}]_1$ 21.25° from $[\bar{1} 1 1]_1$
$(1 1 2)_1$	$(\overline{0.8515} \overline{1.1528} \overline{2.3693})_1$ 7.76° from $(1 1 2)_1$	$[\bar{1} \bar{1} 1]_1$	$[\overline{1.2248} \overline{0.7657} \overline{0.8127}]_1$ 10.96° from $[\bar{1} \bar{1} 1]_1$

(d)

Plane before shear	Plane after shear	Direction before shear	Direction after shear
$(\bar{1} \ 1 \ 2)_2$	$(\overline{1.1005} \ 0.9029 \ 1.6563)_2$ 7.00° from $(\bar{1} \ 1 \ 2)_2$	$[1 \ \bar{1} \ 1]_2$	$[0.6937 \ \overline{1.3175} \ 1.1792]_2$ 11.05° from $[1 \ \bar{1} \ 1]_2$
$(\bar{1} \ \bar{1} \ 2)_2$	$(\overline{1.2843} \ \overline{1.2746} \ 1.0275)_2$ 21.24° from $(\bar{1} \ \bar{1} \ 2)_2$	$[1 \ 1 \ 1]_2$	$[0.5225 \ 0.5050 \ 1.2794]_2$ 21.24° from $[1 \ 1 \ 1]_2$
$(1 \ \bar{1} \ 2)_2$	$(0.8930 \ \overline{1.1033} \ 1.6341)_2$ 7.41° from $(1 \ \bar{1} \ 2)_2$	$[\bar{1} \ 1 \ 1]_2$	$[\overline{1.3003} \ 0.6887 \ 1.1757]_2$ 11.01° from $[\bar{1} \ 1 \ 1]_2$
$(1 \ 1 \ 2)_2$	$(1.0768 \ 1.0742 \ 2.2628)_2$ 1.43° from $(1 \ 1 \ 2)_2$	$[\bar{1} \ \bar{1} \ 1]_2$	$[\overline{1.1290} \ \overline{1.1337} \ 1.0755]_2$ 1.43° from $[\bar{1} \ \bar{1} \ 1]_2$

For the intra-lamellar connection, Fig. 3 (a) illustrates the nanotwins (V1' and V2' in Zone I and V3' and V4' in Zone II) connected by the intra-lamellar interface and Fig. 3 (b) displays the $\{112\}$ and $\langle 111 \rangle$ standard stereographic projections (in the crystal coordinate system of V1') of the four twin variants. It can be seen that the intersecting angle between the twinning planes of the nanotwins in Zone I and Zone II is 94.77° and that between the twinning directions is 85.00° , different from the case at the inter-lamellar interface. The intra-lamellar interface configuration also offers four possible adjacencies (V1' and V3', V2' and V4', V1' and V4', V2' and V3') between the nanotwins in the two zones. When the major variants (V1' and V3') meet, although there are two 180° rotations between them (See the misorientation calculation results displayed in Table 2 (a)), the plane $\{001\}$ and direction $\langle 110 \rangle$ corresponding to the rotation axes of the two 180° rotations are intrinsic symmetry elements of the tetragonal structure in this alloy. So these two variants are not twin-related²⁷ but only related to each other by a rotation of 5.88° around roughly $\langle 110 \rangle$ axis. This slight crystallographic reorientation of the nanotwins gives rise to the change of the direction of the inter-lamellar interface. Similarly, when the two minor variants (V2' and V4') meet, the orientation relationship between them is achieved by the same kind of rotation but with a

larger angle (15.78° around $\langle 110 \rangle$ axis). These two small rotations between the major variants (V1' and V3') and the minor variants (V2' and V4') render the major variant in one zone and the minor variant in the other zone (V1' and V4', V2' and V3') to be twin-related and possess the twinning elements of the same family as those of the internal nanotwins, as shown in Table 2 (b). Nevertheless, this twinning relationship also suffers some crystallographic imperfectness (the corresponding $\{112\}$ planes and corresponding $\langle 111 \rangle$ directions in V1' and V4' deviate by 5.72° and 5.74° , respectively). Obviously, the combination of these orientation relationships between the nanotwin variants provides the reorientation of the martensitic lamellae to achieve the self-accommodation of the lamellar structure.

The detailed microstructure at the intra-lamellar interface is shown in Fig. 3 (c). It is revealed that the intra-lamellar interface that is stepped in the SEM-BSE image (Fig. 1 (c)) still possesses the “step” configuration in the TEM image and no interpenetration is observed. This is quite different from the microstructure at the inter-lamellar interface. In fact, the calculation results from equation (1), demonstrated in Table 2 (b), (c) and (d), show that the nanotwins encountered at the intra-lamellar interface also provides the possibility for penetration. Nevertheless, no penetration occurs as observed by TEM (Fig. 3 (c)). This suggests that the formation mechanism of the stepped intra-lamellar interface is different. It is quite possible that V1'/V2' pair and V3'/V4' pair do not form simultaneously but one after the other. Suppose that V1'/V2' forms before V3'/V4'. Constrained by the neighboring lamellae, the deformation strain due to the formation of V1'/V2' accumulates at the inter-lamellar interface area and creates a resisting force in the opposite direction. Driven by this resisting force, the formation of V3'/V4' may become energetically favorable. In this way, V3'/V4' pair forms, leading to the reorientation of the martensitic lamellae and consequently no interpenetration occurs at the intra-lamellar interface area.

It is known that the magnetic shape-memory effect in the FSMAs is achieved by the reorientation of the martensitic twins through boundary motion under an actuating magnetic field, thus the thorough and accurate microstructural information of the materials is instructive for further microstructure modification and property optimization. Our present study thoroughly reveals the crystallographic orientation relationships between martensitic variants and the intrinsic nature of the interfaces. Obviously the twin relation and the coherent twin

interface between the internal twins would be ideal for the reorientation of nanotwins, while the interpenetrated inter-lamellar interface imposes very strong constraint for the reorientation of the nanotwins. Therefore, such a microstructure should be avoided for the FSMAs. As the orientation relationship between the penetrated and the non-penetrated parts is still close to the {112} twinning relationship due to high symmetry of the tetragonal structure, to obtain low symmetry martensite, such as the modulated 5M and 7M martensites, would eliminate the possibility for penetrating. The present study opens new perspectives for property optimization of the FSMAs.

Methods

A 70g button ingot of Ni-Mn-Ga alloy with chemical composition of Ni₅₃Mn₂₅Ga₂₂ (at.%) was prepared by repeated melting of the high-purity constituent elements Ni, Mn and Ga in an arc furnace protected under an argon atmosphere. The phase transformation temperatures and crystal structure of the alloy were determined by differential scanning calorimetry (DSC) and neutron powder diffraction, respectively. DSC measurements show that the martensitic transformation start temperature, M_s , and finish temperature, M_f , are 386 K and 368 K, respectively and the reverse transformation start temperature, A_s , and finish temperature, A_f , are 408 K and 424 K, respectively. High-resolution neutron powder diffraction reveals that this alloy has a tetragonal martensitic structure at room temperature, with $a=0.3865$ nm, $c=0.6596$ nm and $c/a=1.707$. The space group for this structure is $I4/mmm$ (No.139), with Ni atoms occupying 4d (0, 0.5, 0.25) Wyckoff sites while Mn and Ga atoms occupying 2b (0, 0, 0.5) and 2a (0, 0, 0) sites, respectively. The detailed description of this structure is given in the literature²⁵.

A prism sample with the dimension of 3 mm × 6 mm × 12 mm was cut from the ingot. The sample was further annealed at 1173 K for 4 hr, followed by furnace cooling in order to allow the martensitic transformation to happen under a low thermal stress condition. The transformed microstructure was observed with a JEOL JSM 6500F SEM equipped with a field emission gun in BSE imaging mode, and the detailed microstructures at the inter-lamellar and intra-lamellar interfaces were examined with a Philips CM 200 LaB₆ cathode TEM. The orientations of the microstructural constituents were determined by indexing the electron

backscattered diffraction (EBSD) Kikuchi patterns acquired with the SEM equipped with the HKL's Channel 5 software. The orientation relationships between the microstructural constituents and the interface planes were determined by the misorientation calculation²³ and indirect two-trace method²⁴, respectively.

References

1. Otsuka, K. & Wayman, C. M. *Shape Memory Materials* (Cambridge University Press, Cambridge, 1998).
2. Ren, X. & Otsuka, K. Origin of rubber-like behaviour in metal alloys. *Nature* **389**, 579-582 (1997).
3. Zhang, J. M. & Guo, G. Y. Microscopic theory of the shape memory effect in TiNi. *Phys. Rev. Lett.* **78**, 4789-4792 (1997).
4. Huang, X., Ackland, G. J. & Rabe, K. M. Crystal structures and shape-memory behaviour of NiTi. *Nature Mater.* **2**, 307-311 (2003).
5. Bhattacharya, K., Conti, S., Zanzotto, G. & Zimmer, J. Crystal symmetry and the reversibility of martensitic transformations. *Nature* **428**, 55-59 (2004).
6. Cai, J. M., Langford, S. C., Wu, M., Huang, W., Xiong, G., Droubay, T. C., Joly, A. G., Beck, K. M., Hess, W. P. & Dickinson, J. T. Study of martensitic phase transformation in a NiTiCu thin-film shape memory alloy using photoelectron emission microscopy. *Adv. Funct. Mater.* **17**, 161-167 (2007).
7. Langer, R. & Tirrell, D. A. Designing materials for biology and medicine. *Nature* **428**, 487-492 (2004).
8. Ullakko, K., Huang, J. K., Kantner, C., O'Handley, R. C. & Kokorin, V. V. Large magnetic-field-induced strains in Ni₂MnGa single crystals. *Appl. Phys. Lett.* **69**, 1966-1968 (1996).
9. James, R. D. & Wuttig, M. Magnetostriction of martensite. *Philos. Mag. A* **77**, 1273-1299 (1998).
10. Takeuchi, I., Famodu, O. O., Read, J. C., Aronova, M. A., Chang, K.-S., Craciunescu, C., Lofland, S. E., Wuttig, M., Wellstood, F. C., Knauss, L. & Orozco, A. Identification of novel compositions of ferromagnetic shape-memory alloys using composition spreads.

- Nature Mater.* **2**, 180-184 (2003).
11. Wang, Y. D., Ren, Y., Li, H., Choo, H., Benson, M. L., Brown, D. W., Liaw, P. K., Zuo, L., Wang, G., Brown, D. E. & Alp, E. E. Tracing memory in polycrystalline ferromagnetic shape-memory alloys. *Adv. Mater.* **18**, 2392-2396 (2006).
 12. Kainuma, R., Imano, Y., Ito, W., Sutou, Y., Morito, H., Okamoto, S., Kitakami, O., Oikawa, K., Fujita, A., Kanomata, T. and Ishida, K. Magnetic-field-induced shape recovery by reverse phase transformation. *Nature* **439**, 957-960 (2006).
 13. Sozinov, A., Likhachev, A. A., Lanska, N. & Ullakko, K. Giant magnetic-field-induced strain in NiMnGa seven-layered martensitic phase. *Appl. Phys. Lett.* **80**, 1746-1748 (2002).
 14. Murray, S. J., Marioni, M. A., Kukla, A. M., Robinson, J., O'Handley, R. C. & Allen, S. M. Large field induced strain in single crystalline Ni-Mn-Ga ferromagnetic shape memory alloy. *J. Appl. Phys.* **87**, 5774-5776 (2000).
 15. Ge, Y., Jiang, H., Sozinov, A., Soderberg, O., Lanska, N., Keranen, J., Kauppinen, E. I., Lindroos, V. K. & Hannula, S. P. Crystal structure and macro twin interface of five-layered martensite in Ni-Mn-Ga magnetic shape memory alloy. *Mater. Sci. Eng. A* **438-440**, 961-964 (2006).
 16. Müllner, P., Chernenko, V. A. & Kostorz, G. Stress-induced twin rearrangement resulting in change of magnetization in a Ni-Mn-Ga ferromagnetic martensite. *Scr. Mater.* **49**, 129-133 (2003).
 17. Waitz, T. The self-accommodated morphology of martensite in nanocrystalline NiTi shape memory alloys. *Acta Mater.* **53**, 2273-2283 (2005).
 18. Zhang, J. X., Zheng, Y. F. & Zhao, L. C. The structure and mobility of the intervariant boundaries in 18R martensite in a Cu-Zn-Al alloy. *Acta Mater.* **47**, 2125-2141 (1999).
 19. Han, M., Bennett, J. C., Gharghour, M. A., Chen, J. & Hyatt, C. V. Understanding modulated twin transition at the atomic level. *Acta Mater.* **55**, 1731-1740 (2007).
 20. Christian, J. W. & Mahajan, S. Deformation twinning. *Prog. Mater. Sci.* **39**, 1-157 (1995).
 21. Kelly, A. & Groves, G. W. *Crystallography and Crystal Defects*. (Longman Press, London, 1970).
 22. Kishida, K., Takahama, Y. & Inui, H. Deformation twinning in single crystals of a D0₁₉

- compound with an off-stoichiometric composition (Ti-36.5at.%Al). *Acta Mater.* **52**, 4941-4952 (2004).
23. Cong, D. Y., Zhang, Y. D., Wang, Y. D., Esling, C., Zhao, X. & Zuo, L. Determination of microstructure and twinning relationship between martensitic variants in 53at.%Ni-25at.%Mn-22at.%Ga ferromagnetic shape memory alloy. *J. Appl. Cryst.* **39**, 723-727 (2006).
24. Zhang, Y. D., Esling, C., Zhao, X., & Zuo, L. Indirect two-trace method to determine a faceted low-energy interface between two crystallographically correlated crystals. *J. Appl. Cryst.* **40**, 436-440 (2007).
25. Cong, D. Y., Zetterström, P., Wang, Y. D., Delaplane, R., Peng, R. Lin, Zhao, X. & Zuo, L. Crystal structure and phase transformation in Ni₅₃Mn₂₅Ga₂₂ shape memory alloy from 20 K to 473K. *Appl. Phys. Lett.* **87**, 111906 (2005).
26. Wechsler, M. S., Lieberman, D. S. & Read T. A. On the theory of the formation of martensite. *Trans. AIME* **197**, 1503-1515(1953).
27. Hahn, Th. & Klapper. H. Twinning of crystals. Section 3.3 in *International Tables for Crystallography, Vol. D: Physical Properties of Crystals*, edited by Authier, A. (Kluwer Academic Publishers, Dordrecht, 2003).

Chapter 3 Crystallographic texture in Ni-Mn-Ga alloys

Introduction

To date, the large magnetic shape memory effect is only observed in Ni-Mn-Ga single crystals. However, from the point of view of practical applications, the polycrystalline alloys are more promising because they are easy to be produced and the production cost is low. Thus how to improve the magnetic shape memory effect in polycrystalline Ni-Mn-Ga alloys has become a hot research topic. One practical way to achieve this is to produce highly textured polycrystalline alloys with coarse-grained microstructure, in order to have performances closest to those of the single crystals. Therefore, the development of some novel fabrication processes to produce desired texture components for possible enhancement of the magnetic shape memory effect in polycrystalline Ni-Mn-Ga alloys is of great importance. The systematic characterization of the textures and the investigation on the texture evolution during deformation and phase transformation are also quite essential.

In this chapter, the polycrystalline Ni-Mn-Ga(-Co) FSMAs with different phase at room temperature are successfully hot forged together with stainless steel jackets, in order to induce preferred orientation in these alloys. The textures in these hot-forged alloys are systematically characterized by neutron diffraction technique. Moreover, the texture evolution during room-temperature deformation and subsequent annealing is investigated and the correlation between texture evolution and thermally activated shape memory effect is revealed.

Crystal Structures and Textures in the Hot-Forged Ni-Mn-Ga Shape Memory Alloys

D.Y. CONG,¹ Y.D. WANG¹, R. LIN PENG², P. ZETTERSTRÖM³, X. ZHAO¹, P.K. LIAW⁴,
and L. ZUO¹

¹*School of Materials and Metallurgy, Northeastern University, Shenyang 110004, People's Republic of China.*

²*Department of Mechanical Engineering, Linköping University, S-58183 Linköping, Sweden.*

³*The Studsvik Neutron Research Laboratory (NFL), Uppsala University, S-61182 Nyköping, Sweden.*

⁴*Department of Materials Science and Engineering, The University of Tennessee, Knoxville, TN 37996, U.S.A.*

ABSTRACT

Three ferromagnetic shape-memory alloys with the chemical compositions of $\text{Ni}_{53}\text{Mn}_{25}\text{Ga}_{22}$, $\text{Ni}_{48}\text{Mn}_{30}\text{Ga}_{22}$, and $\text{Ni}_{48}\text{Mn}_{25}\text{Ga}_{22}\text{Co}_5$ were prepared by the induction-melting and hot-forging process. The crystal structures were investigated by the neutron powder diffraction technique, showing that $\text{Ni}_{53}\text{Mn}_{25}\text{Ga}_{22}$ and $\text{Ni}_{48}\text{Mn}_{25}\text{Ga}_{22}\text{Co}_5$ have a tetragonal, $I4/mmm$ martensitic structure at room temperature, while $\text{Ni}_{48}\text{Mn}_{30}\text{Ga}_{22}$ has a cubic, $L2_1$ austenitic structure at room temperature. The development of textures in the hot-forged samples shows the in-plane plastic flow anisotropy from the measured pole figures by means of the neutron diffraction technique. Significant texture changes were observed for the $\text{Ni}_{48}\text{Mn}_{25}\text{Ga}_{22}\text{Co}_5$ alloy after room temperature deformation, which is due to the deformation-induced rearrangements of martensitic variants. An excellent shape-memory effect (SME) with a recovery ratio of 74 pct was reported in this $\text{Ni}_{48}\text{Mn}_{25}\text{Ga}_{22}\text{Co}_5$ polycrystalline alloy after annealing above the martensitic transformation temperature, and the “shape-memory” influence also occurs in the distributions of grain orientations.

Key words: crystallographic texture, isothermal forging, martensitic structure, neutron diffraction, shape-memory alloy

I. INTRODUCTION

Ferromagnetic shape-memory alloys (FSMAs) have attracted great interest during the past several years due to their potential applications as sensors and actuators. Among those

FSMAs, Ni-Mn-Ga alloys with chemical compositions close to the stoichiometric intermetallic compound Ni_2MnGa have been studied extensively^[1-9] as they exhibit a giant shape-memory effect (SME) under applied magnetic fields. However, many fundamental issues remain unclear, such as crystal structures and crystallographic textures. Some controversial results^[7,8,9] on the crystal structure, which is highly sensitive to the chemical compositions of the alloys, have been obtained from some earlier investigations by X-ray diffraction due to similar X-ray scattering factors of Ni, Mn, and Ga atoms. The neutron diffraction technique provides accurate information on the crystal structures and shows advantages in texture measurements for the Ni-Mn-Ga alloys, attributed to the large difference in the neutron diffraction factors for the Ni, Mn, and Ga atoms.

The magnetic SME in Ni-Mn-Ga alloys is caused by the rearrangements of the martensitic variants and/or the growth of favorably oriented variants under applied magnetic fields.^[2,4,6] Meanwhile, the temperature- or stress-induced SME is also attributed to some preferential arrangements of martensitic variants during the phase transformation.^[10] The preferred orientation distribution (crystallographic texture) in the parent phase and the martensite clearly improves the SME in those alloys. Shu *et al.*^[11] and Thamburaja *et al.*^[12] studied the influence of texture on the SME in the polycrystalline shape memory alloys, which verified that the texture plays an important role in improving the SME. Therefore, it is of vital importance to explore some novel fabrication processes to enhance the crystallographic texture in the polycrystalline FSMAs. Despite the brittleness of Ni-Mn-Ga alloys at room temperature, the hot-forging process, a standard procedure for fabricating some structural intermetallic alloys, provides an effective way to modify textures in these alloys.

It is well known that a rearrangement of martensitic variants occurs during mechanical loading, which may change the textures in the Ni-Mn-Ga alloys. However, many earlier reports^[5,13,14] concentrated mainly on the deformation behavior during loading, and the stress plateau in the stress-strain curve was attributed to the rearrangements of martensitic variants. So far, there have been no reports on the texture evolution during deformation in the Ni-Mn-Ga alloys. In the current study, three Ni-Mn-Ga alloys— $\text{Ni}_{53}\text{Mn}_{25}\text{Ga}_{22}$, $\text{Ni}_{48}\text{Mn}_{30}\text{Ga}_{22}$, and $\text{Ni}_{48}\text{Mn}_{25}\text{Ga}_{22}\text{Co}_5$ —were prepared by induction melting and hot forging. The crystal structures and hot deformation textures in these alloys were characterized by the neutron

diffraction technique. The texture evolution in the $\text{Ni}_{48}\text{Mn}_{25}\text{Ga}_{22}\text{Co}_5$ alloy after room-temperature deformation and annealing above the martensitic transformation temperature was also studied, which was correlated with the SME to reveal the intrinsic micromechanisms.

II. EXPERIMENTS

Three 380-g button ingots with the chemical compositions of $\text{Ni}_{53}\text{Mn}_{25}\text{Ga}_{22}$, $\text{Ni}_{48}\text{Mn}_{30}\text{Ga}_{22}$, and $\text{Ni}_{48}\text{Mn}_{25}\text{Ga}_{22}\text{Co}_5$ (at. pct), were prepared by repeated melting of the high-purity constituent elements in an induction furnace protected under an argon atmosphere. To obtain homogeneity, the ingots were sealed into a vacuum quartz tube and annealed at 900 °C for 52 hours. A thin layer of yttria was wiped on the surface of the annealed ingots to prevent oxidation in the subsequent hot-forging process. The annealed ingots were then sealed into stainless steel jackets. Thereafter, fiberglass was filled into the empty sections of the stainless steel jacket. The sealed ingots were heated to 950 °C and held for 2 hours, then forged at 900 °C in the dies of the cast Ni_3Al alloy under a strain rate of about 10^{-2} s^{-1} . The $\text{Ni}_{53}\text{Mn}_{25}\text{Ga}_{22}$ alloy was deformed to a final strain of about 72 pct, whereas the $\text{Ni}_{48}\text{Mn}_{30}\text{Ga}_{22}$ and $\text{Ni}_{48}\text{Mn}_{25}\text{Ga}_{22}\text{Co}_5$ alloys were deformed to about 58 pct. Some small pieces from the hot-forged ingots were crushed into powders for the neutron powder diffraction experiment to determine the crystal structure. Cylindrical samples with the size of $16 \times \Phi 5$ mm were cut by an electrodischarge machine from the forged ingots, with the axial direction parallel to the uniaxial compression direction of hot forging, for texture measurements.

The room-temperature phase and its crystal structure were determined by the neutron powder diffraction performed on the beam line, R2D2, with the wavelength of 1.5515 Å and pole figure measurements were performed on REST (Residual Stress and Texture) with the wavelength of 1.7 Å, using the Eulerian cradle, at the Studsvik Neutron Research Laboratory, Sweden. The crystal structures were refined from the whole diffraction profiles by the Fullprof Rietveld method.^[15] The crystallographic orientation distribution and inverse pole figures were determined by popLA software^[16] from three measured pole figures.

Aside from the hot-forged samples, the textures were measured for the $\text{Ni}_{48}\text{Mn}_{25}\text{Ga}_{22}\text{Co}_5$ sample treated in the following three stages: (I) the initial hot-forged sample was heated to

250°C for 40 minutes, followed by quenching into water; (II) the quenched sample was deformed in compression at room temperature to a plastic strain of about 3.3 pct at a crosshead displacement speed of 0.08 mm/min; (III) the deformed sample was heated again at 250°C for 40 minutes, followed by quenching into water.

III. RESULTS AND DISCUSSION

A. Microstructures of the Ingots

The microstructure of the $\text{Ni}_{48}\text{Mn}_{25}\text{Ga}_{22}\text{Co}_5$ alloy after hot forging is illustrated in Figure 1(a), showing some equiaxed grains 300 to 600 μm in diameter. In addition, some fine grains 20 to 60 μm in diameter can be clearly seen along the grain boundaries of the coarse grains. It is believed that the appearance of the fine grains is caused by the dynamic recrystallization occurring in the hot-forging process. The microstructure of the $\text{Ni}_{53}\text{Mn}_{25}\text{Ga}_{22}$ alloy (Figure 1(b)), is similar to that of $\text{Ni}_{48}\text{Mn}_{25}\text{Ga}_{22}\text{Co}_5$, except that the volume fraction of fine grains is higher, indicating a higher degree of dynamic recrystallization. The different extent of the dynamic recrystallization in these two alloys is attributed to the various hot deformation strains during hot forging.

B. Crystal Structures of Ni-Mn-Ga Alloys

The neutron powder diffraction patterns of $\text{Ni}_{53}\text{Mn}_{25}\text{Ga}_{22}$, $\text{Ni}_{48}\text{Mn}_{30}\text{Ga}_{22}$, and $\text{Ni}_{48}\text{Mn}_{25}\text{Ga}_{22}\text{Co}_5$, taken at room temperature, are illustrated in Figure 2(a), (b), and (c), respectively. All the intensity peaks in Figure 2(a) can be indexed well according to a tetragonal structure with $a = 3.800 \text{ \AA}$, $c = 6.733 \text{ \AA}$, and $c/a = 1.77$. The space group of the structure of the $\text{Ni}_{53}\text{Mn}_{25}\text{Ga}_{22}$ alloy is $I4/mmm$ (No. 139). The neutron diffraction shown in Figure 2(c) suggests that $\text{Ni}_{48}\text{Mn}_{25}\text{Ga}_{22}\text{Co}_5$ also has a tetragonal, $I4/mmm$ -symmetry structure, with $a = 3.887 \text{ \AA}$, $c = 6.485 \text{ \AA}$, and $c/a = 1.67$. It can be concluded from the neutron diffraction patterns shown in Figures 2(a) and (c) that both $\text{Ni}_{53}\text{Mn}_{25}\text{Ga}_{22}$ and $\text{Ni}_{48}\text{Mn}_{25}\text{Ga}_{22}\text{Co}_5$ have the same martensitic structure at room temperature; the 5 pct substitution of Co for Ni atoms in $\text{Ni}_{53}\text{Mn}_{25}\text{Ga}_{22}$ does not alter its crystal structure, but the c/a ratio is dramatically reduced.

The neutron diffraction pattern of $\text{Ni}_{48}\text{Mn}_{30}\text{Ga}_{22}$ (Figure 2(b)) is completely different

from that in Figures 2(a) and (c). All 13 distinct Bragg peaks can be indexed well according to the cubic $L2_1$ structure with $a = 5.840 \text{ \AA}$, indicating that $\text{Ni}_{48}\text{Mn}_{30}\text{Ga}_{22}$ presents a Heusler austenitic phase at room temperature. This structure is in good agreement with the structure of the stoichiometric Ni_2MnGa at 300 K reported by Brown *et al.*,^[17] giving further proof that the off-stoichiometric Ni-Mn-Ga alloys also have a Heusler $L2_1$ structure in the austenitic state. It should be noted that the different phases in $\text{Ni}_{53}\text{Mn}_{25}\text{Ga}_{22}$ and $\text{Ni}_{48}\text{Mn}_{30}\text{Ga}_{22}$ at room temperature are due to the high sensitivity of the martensitic transformation temperature to the chemical composition of the Ni-Mn-Ga alloys, which was confirmed by many earlier reports.^[9,18,19]

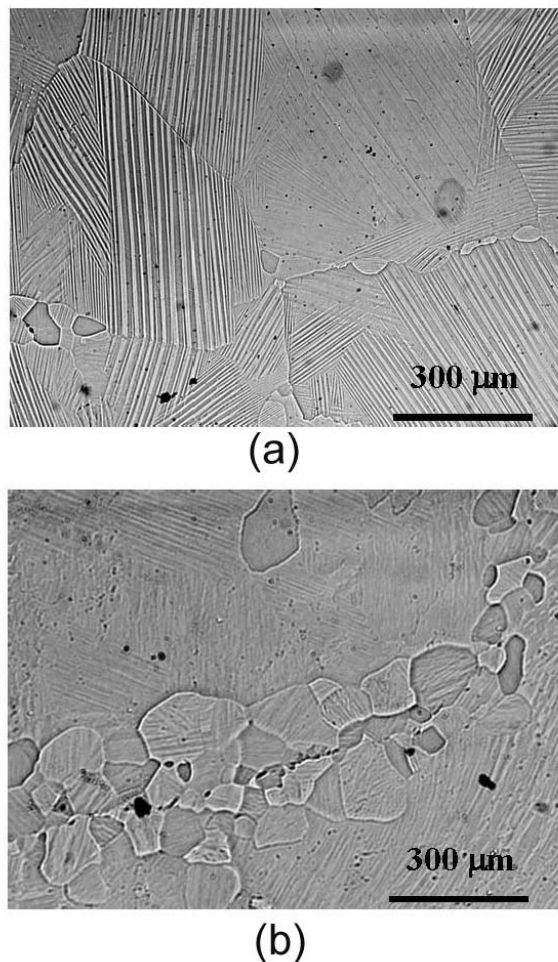


Fig. 1—Microstructures of the alloys $\text{Ni}_{48}\text{Mn}_{25}\text{Ga}_{22}\text{Co}_5$ (a) and $\text{Ni}_{53}\text{Mn}_{25}\text{Ga}_{22}$ (b) after hot forging.

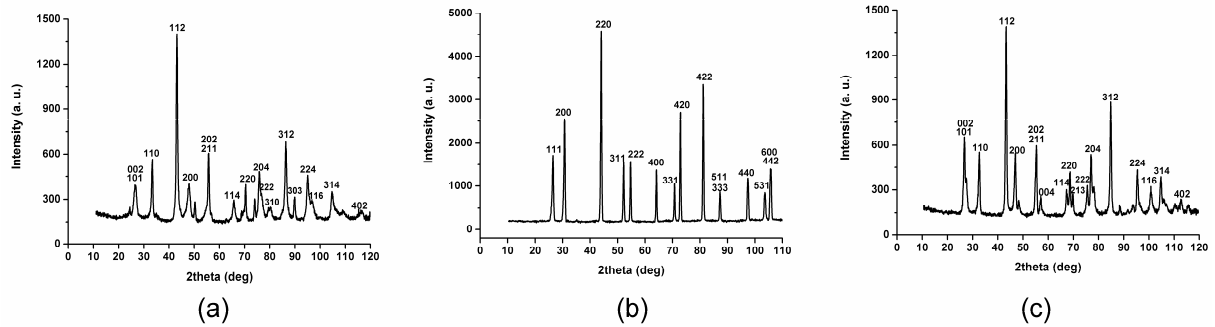


Fig. 2—Neutron diffraction patterns of the alloys $\text{Ni}_{53}\text{Mn}_{25}\text{Ga}_{22}$ (a), $\text{Ni}_{48}\text{Mn}_{30}\text{Ga}_{22}$ (b), and $\text{Ni}_{48}\text{Mn}_{25}\text{Ga}_{22}\text{Co}_5$ (c), taken at room temperature.

C. Textures in the Hot-Forged Ni-Mn-Ga Alloys

The texture in the hot-forged $\text{Ni}_{53}\text{Mn}_{25}\text{Ga}_{22}$ alloy with a tetragonal martensitic structure characterized by three measured (110)-, (112)-, and (312)-pole figures is shown in Figure 3(a). Strong textures developed in the hot-forging process, as clearly seen from the measured pole figures. Besides this, the lack of the axial symmetry observed in the pole figures demonstrates a large in-plane plastic flow anisotropy during hot forging. The inverse pole figures for the compression axis (CA) and the radial direction (RD) of the forged ingot, determined by the popLA software, are shown in Figure 3(b). It can be seen from the inverse pole figures that the main texture components are (110)[111]~[101] and (101)[111]~[101], in which the texture presentation, (hkl)[uvw], with a notation of the (hkl) plane perpendicular to the CA and the [uvw] direction parallel to the RD of the forged ingot is used. The corresponding OD sections with ψ constant (in Roe's notation), determined by texture analysis from the measured complete pole figures, are shown in Figure 3(c), which further confirms the texture components observed above.

Figure 4(a) shows the (200)-, (220)-, and (422)-pole figures of the hot-forged $\text{Ni}_{48}\text{Mn}_{30}\text{Ga}_{22}$ alloy with a cubic austenitic structure. Strong texture components and large plastic flow anisotropy can also be observed from the measured pole figures. The inverse pole figures for the CA and RD are illustrated in Figure 4(b), from which it can be seen that the main texture components may be approximately identified as [110]//RD, $\{100\} \perp \text{CA}$, and $\{111\} \perp \text{CA}$. The former texture component is in agreement with that found in the uniaxial tensile deformation, and the latter two components are in agreement with the uniaxial

compression textures in some bcc alloys.

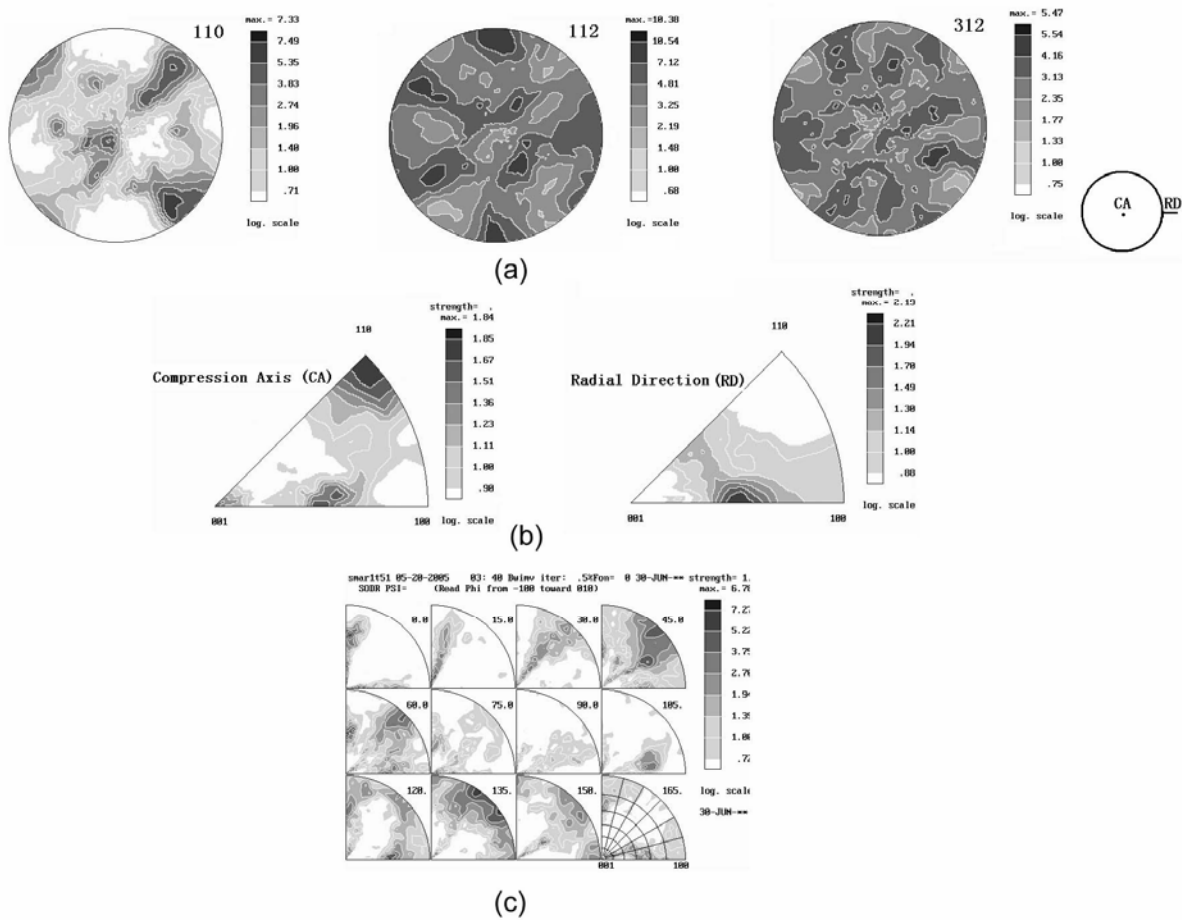


Fig. 3—The pole figures (a), inverse pole figures (b), and OD sections (c) in the hot-forged $\text{Ni}_{53}\text{Mn}_{25}\text{Ga}_{22}$ alloy.

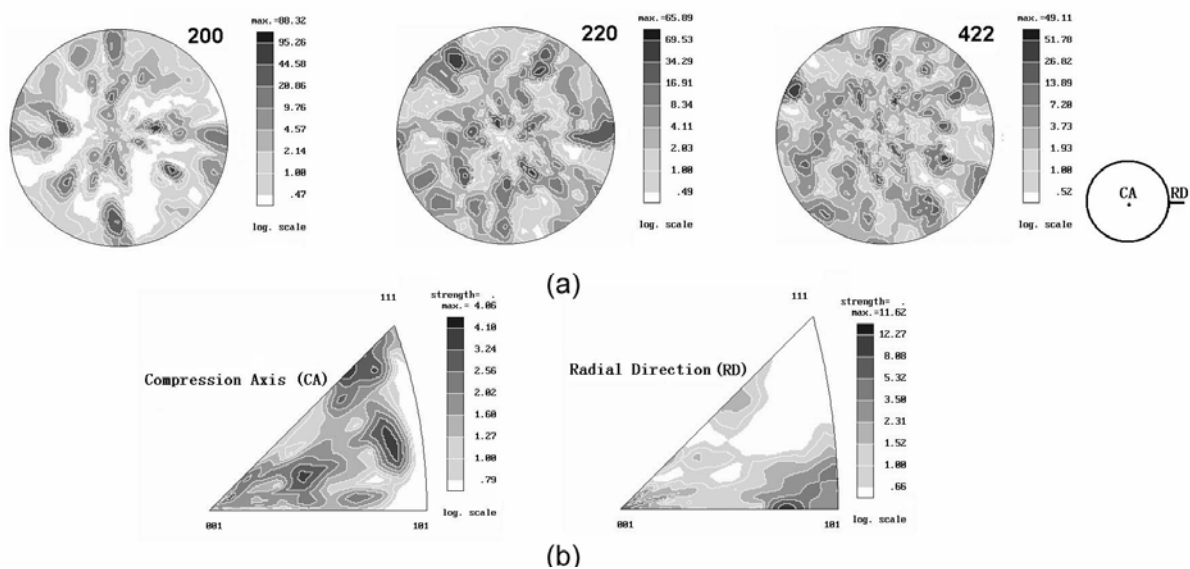


Fig. 4—The pole figures (a) and inverse pole figures (b) in the hot-forged $\text{Ni}_{48}\text{Mn}_{30}\text{Ga}_{22}$ alloy.

The measured (110)-, (112)-, and (312)-pole figures of the hot-forged $\text{Ni}_{48}\text{Mn}_{25}\text{Ga}_{22}\text{Co}_5$ with a tetragonal martensitic structure are shown in Figure 5(a). Once again, strong texture components and large plastic flow anisotropy are observed from the measured pole figures. The inverse pole figures for the CA and RD are shown in Figure 5(b), from which the main texture components (110)[1-12] and (001)[100] can be determined. The different texture components in the $\text{Ni}_{53}\text{Mn}_{25}\text{Ga}_{22}$ and $\text{Ni}_{48}\text{Mn}_{25}\text{Ga}_{22}\text{Co}_5$ alloys are attributed to the different deformation strains during hot forging.

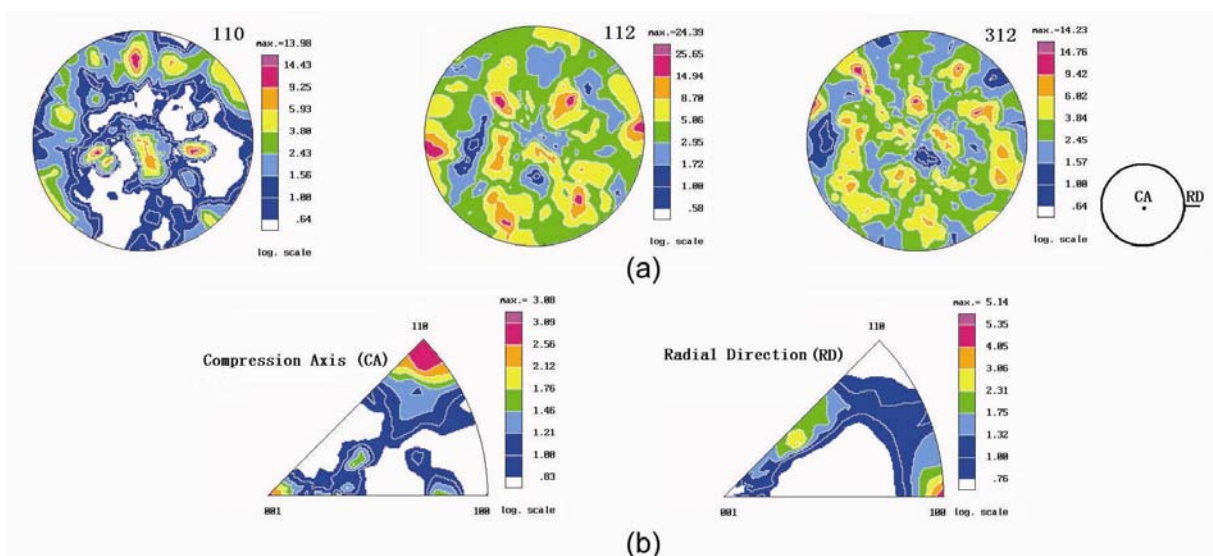


Fig. 5—The pole figures (a) and inverse pole figures (b) in the hot-forged $\text{Ni}_{48}\text{Mn}_{25}\text{Ga}_{22}\text{Co}_5$ alloy in the initial state.

D. Texture Evolution and Shape-Memory Effect

The influence of annealing treatments at 250 °C (above phase transformation), followed by water quenching, on changes of grain orientations for the hot-forged $\text{Ni}_{48}\text{Mn}_{25}\text{Ga}_{22}\text{Co}_5$ was further studied. The analysis of the pole figures and inverse pole figures of the quenched sample shows that the texture of the quenched sample is almost the same as that of the initial one, except for some slight changes of the intensities. This means that the heat treatment did not change the texture, as the annealing temperature was too low to cause atomic diffusions in the sample.

Figure 6 shows the pole figures and inverse pole figures of the room-temperature

deformed sample of the hot-forged $\text{Ni}_{48}\text{Mn}_{25}\text{Ga}_{22}\text{Co}_5$. It is interesting that the texture in the sample changed significantly after only a 3.3 pct plastic deformation. From the pole figures in Figure 6(a), one can see that some texture components (marked as B, D, D', and F) become much stronger, whereas others (marked as A, C, C', and E) almost disappear, compared with the corresponding texture components in the hot-forged sample (Figure 5(a)). It is also obvious from the inverse pole figures (Figure 6(b)) that the texture component (001)[100] (marked as P) completely disappears, whereas the texture component (110)[1-12] (marked as O) becomes much stronger. Meanwhile, a new texture component (marked as Q) develops after deformation. Such significant texture changes are attributed to the rearrangements of the martensitic variants induced by deformation. When the sample was mechanically loaded, some favorably oriented variants expanded under the applied stress, at the expense of the shrinkage of the unfavorably oriented variants,^[5,20] which consequently changed the preferred grain orientation (*i.e.*, crystallographic texture) in the sample.

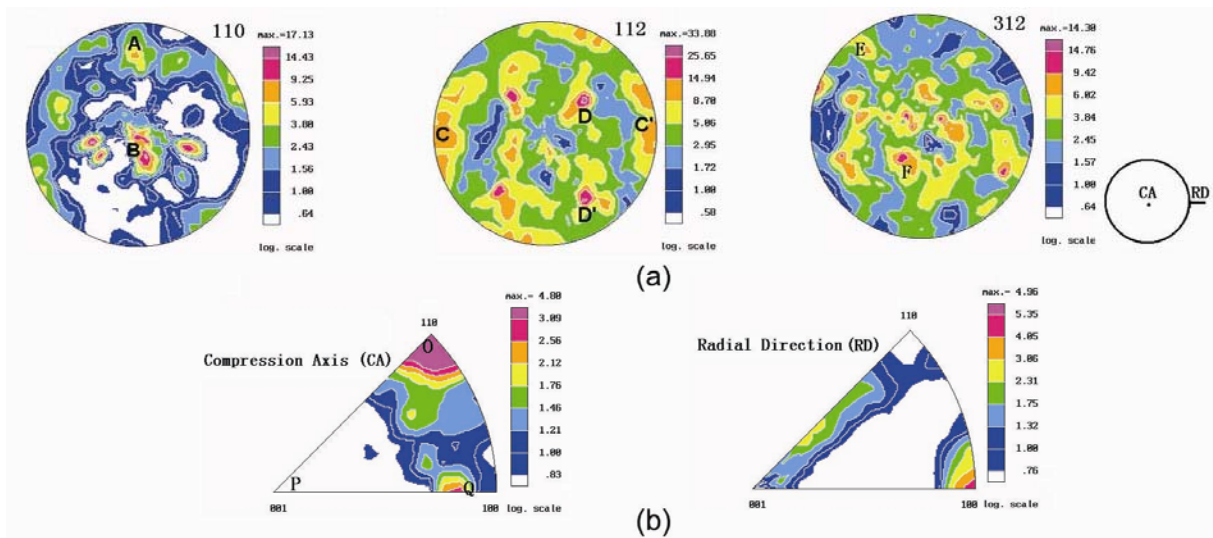


Fig. 6—The pole figures (a) and inverse pole figures (b) in the hot-forged $\text{Ni}_{48}\text{Mn}_{25}\text{Ga}_{22}\text{Co}_5$ alloy in the deformed state (stage II).

The pole figures and inverse pole figures of the annealed and quenched sample are shown in Figure 7. The texture in this sample is quite similar to that in the hot-forged sample (Figure 5), which indicates that the texture in this sample is recovered to its original state after heat treatment. This can be attributed to the fact that, after phase transformation, the martensitic

variants are rearranged to the initial orientations before room-temperature deformation (*i.e.*, the shape memory of textures). Thus, the macroscopic SME in this alloy is closely related to the shape memory of textures. Nevertheless, the texture was not completely recovered during heat treatment, as the intensities of some texture components (marked as A, B, C, D, and F in Figure 7(a)) lie between those of the corresponding components in the hot-forged (Figure 5(a)) and the deformed sample (Figure 6(a)).

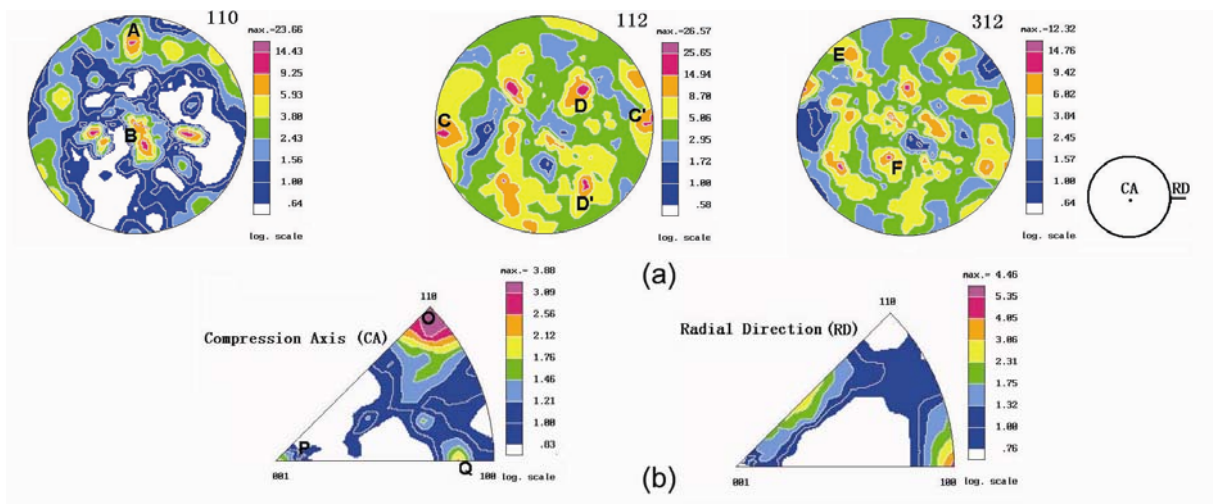


Fig. 7—The pole figures (a) and inverse pole figures (b) in the hot-forged $\text{Ni}_{48}\text{Mn}_{25}\text{Ga}_{22}\text{Co}_5$ alloy in the annealed and quenched state (stage III).

Table I. Sample Lengths of $\text{Ni}_{48}\text{Mn}_{25}\text{Ga}_{22}\text{Co}_5$ at Different Stages

Stage	Sample Length (mm)
Initial hot-forged	15.951
I (quenched)	15.948
II (deformed)	15.415
III (annealed and quenched)	15.809

The sample lengths of $\text{Ni}_{48}\text{Mn}_{25}\text{Ga}_{22}\text{Co}_5$ at different stages are summarized in Table I. It can be seen that in stage I, the sample length is almost the same as that in the initial hot-forged state, indicating that no SME is observed after quenching. As the sample was deformed at room temperature to a 3.3 pct plastic strain in stage II, it is interesting that a 2.4 pct reversible strain was recovered after the subsequent quenching in stage III. The recovery ratio is 74 pct, showing an excellent SME in the polycrystalline samples. However, there is

still a 26 pct plastic strain that remains irreversible after quenching. This irreversible plastic strain may be caused by dislocation slip and/or the constraints among the differently oriented grains in the polycrystalline sample.^[21]

IV. SUMMARY AND CONCLUSIONS

Three FSMAs with the chemical compositions of $\text{Ni}_{53}\text{Mn}_{25}\text{Ga}_{22}$, $\text{Ni}_{48}\text{Mn}_{30}\text{Ga}_{22}$, and $\text{Ni}_{48}\text{Mn}_{25}\text{Ga}_{22}\text{Co}_5$ were prepared by induction melting and hot forging. The crystal structures, textures, and texture evolution were investigated by means of the neutron diffraction technique. The following conclusions can be drawn:

1. The Ni-Mn-Ga ingots were successfully hot forged together with stainless steel jackets. Dynamic recrystallization occurred during the hot-forging process.

2. $\text{Ni}_{53}\text{Mn}_{25}\text{Ga}_{22}$ and $\text{Ni}_{48}\text{Mn}_{25}\text{Ga}_{22}\text{Co}_5$ have a tetragonal, $I4/mmm$ martensitic structure at room temperature. The substitution of Co for Ni atoms in $\text{Ni}_{53}\text{Mn}_{25}\text{Ga}_{22}$ does not alter its crystal structure but dramatically reduces the c/a ratio. $\text{Ni}_{48}\text{Mn}_{30}\text{Ga}_{22}$ has a cubic, $L2_1$ austenitic structure at room temperature, the same structure as in the stoichiometric compound Ni_2MnGa in the austenitic state.

3. Strong textures and a large in-plane plastic flow anisotropy developed during the hot-forging process. The different texture components in $\text{Ni}_{53}\text{Mn}_{25}\text{Ga}_{22}$ and $\text{Ni}_{48}\text{Mn}_{25}\text{Ga}_{22}\text{Co}_5$ are attributed to the different deformation strains.

4. Significant texture changes in $\text{Ni}_{48}\text{Mn}_{25}\text{Ga}_{22}\text{Co}_5$ during deformation were observed. Some texture components become much stronger while others disappear, which is attributed to the rearrangement of martensitic variants during mechanical deformation. The texture recovers to its original state after the subsequent heat treatment because the martensitic variants are rearranged to their initial orientation, which is closely related to the macroscopic SME in this alloy. An excellent SME with a recovery ratio of 74 pct was observed in the polycrystalline $\text{Ni}_{48}\text{Mn}_{25}\text{Ga}_{22}\text{Co}_5$ alloy.

ACKNOWLEDGMENTS

The authors are grateful to the National Natural Science Foundation of China (Grants No. 50531020 and 50528102), the National Ministry of Education of China in the frame of the

NCET project, and the Swedish Research Council in the frame of the SIDA project (Grant No. 348-2004-3475) for their financial support. This work is also supported by the National Science Foundation International Materials Institutes (IMI) Program, with Dr. C. Huber as the Program Director.

REFERENCES

1. V.A. Chernenko, V. L'vov, J. Pons, and E. Cesari: *J. Appl. Phys.*, 2003, vol. 93, pp. 2394-99.
2. A. Sozinov, A.A. Likhachev, N. Lanska, and K. Ullakko: *Appl. Phys. Lett.*, 2002, vol. 80, pp. 1746-48.
3. C.P. Henry, D. Bono, J. Feuchtwanger, S.M. Allen, and R.C. O'Handley: *J. Appl. Phys.*, 2002, vol. 91, pp. 7810-11.
4. K. Ullakko, Y. Ezer, A. Sozinov, G. Kimmel, P. Yakovenko, and V.K. Lindroos: *Scripta Mater.*, 2001, vol. 44, pp. 475-80.
5. P. Müllner, V.A. Chernenko, and G. Kostorz: *J. Appl. Phys.*, 2004, vol. 95, pp. 1531-35.
6. M.A. Marioni, R.C. O'Handley, and S.M. Allen: *Appl. Phys. Lett.*, 2003, vol. 83, pp. 3966-68.
7. B. Wedel, M. Suzuki, Y. Murakami, C. Wedel, T. Suzuki, D. Shindo, and K. Itagaki: *J. Alloys Comp.*, 1999, vol. 290, pp. 137-43.
8. G. Mogylnyy, I. Glavatsky, N. Glavatska, O. Söderberg, Y. Ge, and V.A. Lindroos: *Scripta Mater.*, 2003, vol. 48, pp. 1427-32.
9. C. Jiang, Y. Muhammad, L. Deng, W. Wu, and H. Xu: *Acta Mater.*, 2004, vol. 52, pp. 2779-85.
10. Z.H. Liu, M. Zhang, Y.T. Cui, Y.Q. Zhou, W.H. Wang, G.H. Wu, X.X. Zhang, and G. Xiao: *Appl. Phys. Lett.*, 2003, vol. 82, pp. 424-26.
11. Y.C. Shu and K. Bhattacharya: *Acta Mater.*, 1998, vol. 46, pp. 5457-73.
12. P. Thamburaja and L. Anand: *J. Mech. Phys. Solids*, 2001, vol. 49, pp. 709-37.
13. V.A. Chernenko, V.A. L'vov, E. Cesari, J. Pons, A.A. Rudenko, H. Date, M. Matsumoto, and T. Kanomata: *Mater. Sci. Eng.*, 2004, vol. A378, pp. 349-52.
14. A. Sozinov, A.A. Likhachev, N. Lanska, O. Söderberg, K. Ullakko, and V.K. Lindroos:

- Mater. Sci. Eng.*, 2004, vol. A378, pp. 399-402.
15. L.B. McCusker, R.B. Von Dreele, D.E. Cox, D. Louer, and P. Scardi: *J. Appl. Crystallogr.*, 1999, vol. 32, pp. 36-50.
 16. U.F. Kocks, J.S. Kallend, H.R. Wenk, A.D. Rollett, and S.I. Wright: *PopLA: Preferred Orientation Package*. Los Alamos, October 1995.
 17. P.J. Brown, J. Crangle, T. Kanomata, M. Matsumoto, K.-U. Neumann, B. Ouladdiaf, and K.R.A. Ziebeck: *J. Phys. Condens. Matter*, 2002, vol. 14, pp. 10159-71.
 18. N. Lanska, O. Söderberg, A. Sozinov, Y. Ge, K. Ullakko, and V.K. Lindroos: *J. Appl. Phys.*, 2004, vol. 95, pp. 8074-78.
 19. S.K. Wu and S.T. Yang: *Mater. Lett.*, 2003, vol. 57, pp. 4291-96.
 20. P. Müllner, V.A. Chernenko, and G. Kostorz: *Scripta Mater.*, 2003, vol. 49, pp. 129-33.
 21. Y. Li, Y. Xin, C. Jiang, and H. Xu: *Scripta Mater.*, 2004, vol. 51, pp. 849-52.

Chapter 4 Alloying of Ni-Mn-Ga alloys with Co element

Introduction

Although Ni-Mn-Ga FSMAs have demonstrated superior MSME, they also have some intrinsic problems for their use in industrial applications, such as brittleness and low Curie temperature. Addition of other elements is a classical way to modify the properties of a given alloy and it has been demonstrated that alloying with a fourth element is indeed efficient in improving certain properties of Ni-Mn-Ga alloys.

From the viewpoint of practical applications, the Ni-Mn-Ga FSMAs should have high martensitic transformation temperature and high Curie temperature. Due to the sensitivity of martensitic transformation temperature to the concentrations of Ni, Mn and Ga, high martensitic transformation temperature can be realized by composition design. Nevertheless, the Curie temperature of Ni-Mn-Ga alloys is not sensitive to their concentrations. Thus, the addition of a fourth element is needed to increase the Curie temperature of the Ni-Mn-Ga FSMAs.

This chapter aims to study the effect of substitution of Co for Ni in Ni-Mn-Ga alloys. The influence of Co addition on crystal structure, martensitic transformation, Curie temperature and mechanical behavior is systematically investigated. It will be demonstrated that when the Co content is less than 6 at.%, the Curie temperature is efficiently raised while the martensitic transformation temperature only decreases slightly; when Co content exceeds 6 at.%, the Curie temperature continues to increase, but the martensitic transformation temperature decreases abruptly. This finding is undoubtedly of great significance to the development of promising FSMAs with high martensitic transformation temperature and high Curie temperature.

Martensitic and magnetic transformation in Ni–Mn–Ga–Co ferromagnetic shape memory alloys

D. Y. Cong^{a,c}, S. Wang^a, Y. D. Wang^a, Y. Ren^b, L. Zuo^a, C. Esling^c

^aKey Laboratory of Anisotropy and Texture of Materials (MOE), Northeastern University, Shenyang 110004, China

^bX-ray Science Division, Argonne National Laboratory, Argonne, IL60439, USA

^cLETAM, CNRS-UMR 7078, University of Metz, Ile du Saulcy, 57045 Metz, France

Abstract

The effect of Co addition on crystal structure, martensitic transformation, Curie temperature and compressive properties of $\text{Ni}_{53-x}\text{Mn}_{25}\text{Ga}_{22}\text{Co}_x$ alloys with the Co content up to 14 at.% was investigated. An abrupt decrease of martensitic transformation temperature was observed when the Co content exceeded 6 at.%, which can be attributed to the atomic disorder resulting from the Co addition. Substitution of Co for Ni proved efficient in increasing the Curie temperature. Compression experiments showed that the substitution of 4 at.% Co for Ni did not change the fracture strain, but led to the increase in the compressive strength and the decrease in the yield stress. This study may offer experimental data for developing high performance ferromagnetic shape memory alloys.

Keywords: Ferromagnetic shape memory alloy; Martensitic transformation; Crystal structure; Curie temperature; Compressive properties; Ni–Mn–Ga–Co alloy

1. Introduction

Ni–Mn–Ga ferromagnetic shape alloys (FSMAs) with chemical composition close to the stoichiometric compound Ni_2MnGa have attracted great interest during the past decade, due to the large magnetic shape memory effect (MSME) that originates from the rearrangement of martensitic variants under the application of magnetic fields [1,2]. From the application point of view, high martensitic transformation temperature and Curie temperature are very important, because these FSMAs usually work in the ferromagnetic martensitic state. It was

found that a high martensitic transformation temperature in the Ni–Mn–Ga alloys could be achieved by composition adjustment [3–5], as the martensitic transformation temperature was very sensitive to their chemical compositions. In contrast, the Curie temperature (T_c) of these alloys is less composition dependent and has a value of around 370 K for a wide range of composition [3,6]. High T_c is required for developing FSMAs with a large magnetocrystalline anisotropy (MCA) at a high temperature. So far, great efforts have been devoted to alloying the ternary alloys with a fourth element to increase T_c . Recent investigations [7–10] show that the substitution of Co for Ni is an effective way to increase T_c , which leads to a slight decrease in the martensitic transformation temperature. However, those investigations [7–10] only focused on some limited addition of Co element (less than 5.8 at.%) to the ternary alloys, while alloys with higher Co content have not been studied. Actually, full information on the effect of Co on various physical and mechanical properties of Ni–Mn–Ga–Co alloys with a broad range of composition is greatly needed for materials design.

In the present study, Ni–Mn–Ga–Co alloys with Co content up to 14 at.% were prepared, and the effect of Co addition on crystal structure, martensitic transformation, Curie temperature and mechanical behavior was systematically investigated. An abrupt decrease in martensitic transformation temperature was observed when the Co content exceeds 6 at.%. This study will provide the fundamental experimental data for developing high temperature FSMAs in this alloy system.

2. Experimental

Polycrystalline $\text{Ni}_{53-x}\text{Mn}_{25}\text{Ga}_{22}\text{Co}_x$ (at.%, $x=0, 2, 4, \dots, 14$) alloys of about 70 g were prepared by repeated melting of the high-purity constituent elements in an arc furnace protected under an argon atmosphere. For convenience, hereafter the individual alloys will be notated as Co0, Co2, Co4, ... Co14, respectively, using the Co content. Parts of the alloys were then crushed into powders for determining crystal structure and martensitic transformation temperature. The powders and the bulk specimens were sealed into vacuum quartz tubes and further annealed at 1173K for 5h in order to get homogeneity in chemical composition, followed by water quenching.

The crystal structure at room temperature was identified by X-ray diffraction (XRD)

analysis with Cu K α radiation. The phase transformation temperature was determined by differential scanning calorimetry (DSC) in the temperature range of 188–573K, with a heating and cooling rate of 10K/min. The phase transformation behavior of the Co8 and Co10 alloys was further studied by in situ high-energy synchrotron XRD experiments performed at the 11-ID-C beamline, advanced photon source (APS), Argonne National Laboratory, from room temperature to 4K. The wavelength of the radiation was 0.1080 Å. T_c was determined by using a vibrating sample magnetometer (VSM). Room temperature compression tests with a strain rate of about $1.7 \times 10^{-4} \text{ s}^{-1}$ were performed on the samples with the size of 10mm \times Φ 8mm for investigating the compressive properties of the alloys.

3. Results and discussion

3.1. Microstructure

Microstructure observation of the Ni_{53-x}Mn₂₅Ga₂₂Co_x alloys shows that the alloys with $x \leq 6$ exhibit a martensitic microstructure while those with $x \geq 8$ have an austenitic microstructure at room temperature. This indicates that the alloys with $x \leq 6$ undergo a martensitic transformation above room temperature and no martensitic transformation occurs above room temperature in the alloys with $x \geq 8$. The representative microstructures of Co6 and Co8 alloys are shown in Fig.1 (a) and (b), respectively. Typical martensitic morphology with a well self-accommodated lamellar microstructure can be clearly seen from Fig. 1(a). In contrast, coarse equiaxed austenite grains with no fine submicrostructures were observed in Fig. 1(b).

3.2. Crystal structure

The XRD patterns of the Ni_{53-x}Mn₂₅Ga₂₂Co_x alloys at room temperature are illustrated in Fig. 2(a). Typical diffraction peaks from martensite can be clearly seen in the alloys with $x \leq 6$. The XRD patterns of these alloys can be well indexed according to a tetragonal structure with the space group of *I4/mmm* (no.139). For example, the lattice parameters of the Co2 alloy are $a=3.873 \text{ \AA}$, and $c=6.535 \text{ \AA}$, respectively. It is obvious that the substitution of Co for Ni with less than 6 at.% did not cause a change in the crystal structure. When Co content exceeded 8 at.%, the alloys displayed an austenite structure at room temperature. The Bragg peaks in the

XRD pattern can be well indexed as the Heusler $L2_1$ structure with the space group of $Fm\bar{3}m$ (no. 225). For example, the lattice parameter of the Co12 alloy is $a_0=5.798 \text{ \AA}$. The crystal structure information of the $\text{Ni}_{53-x}\text{Mn}_{25}\text{Ga}_{22}\text{Co}_x$ alloys is in good agreement with that reported in Ni–Mn–Ga alloys, which were investigated by neutron diffraction [11–13].

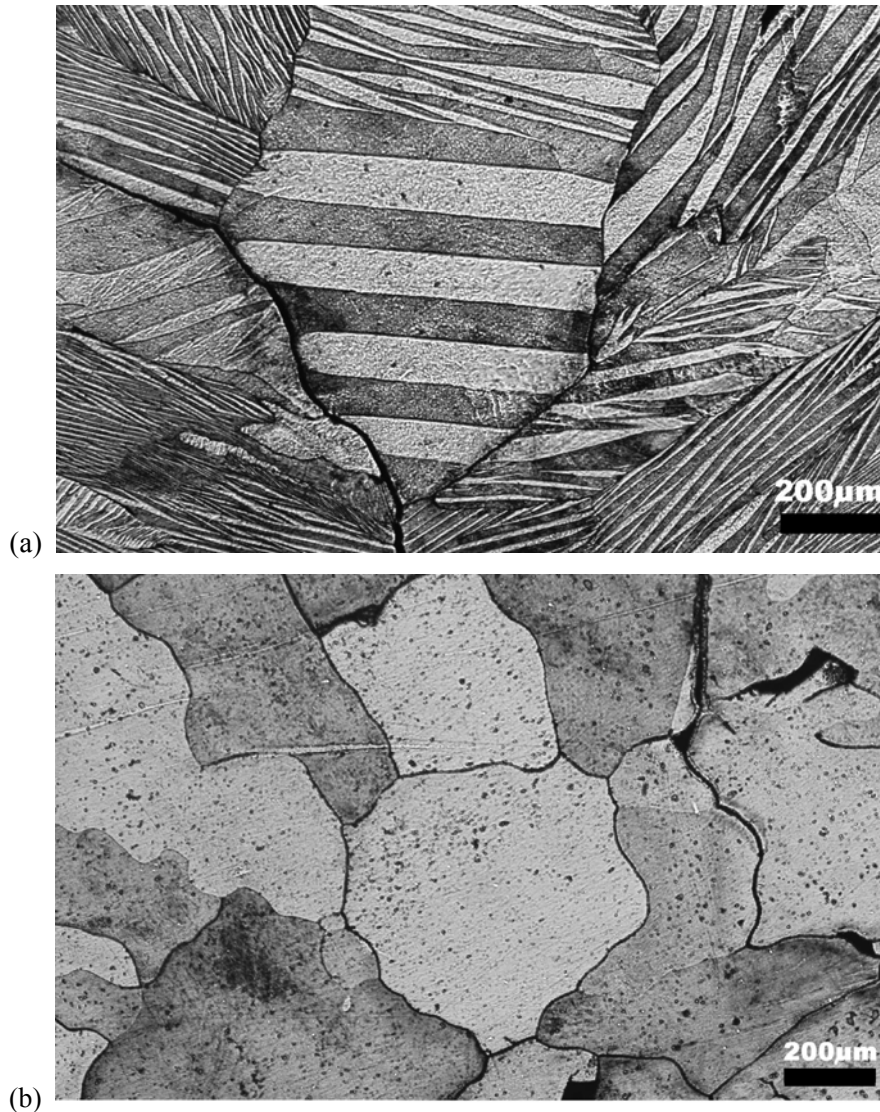
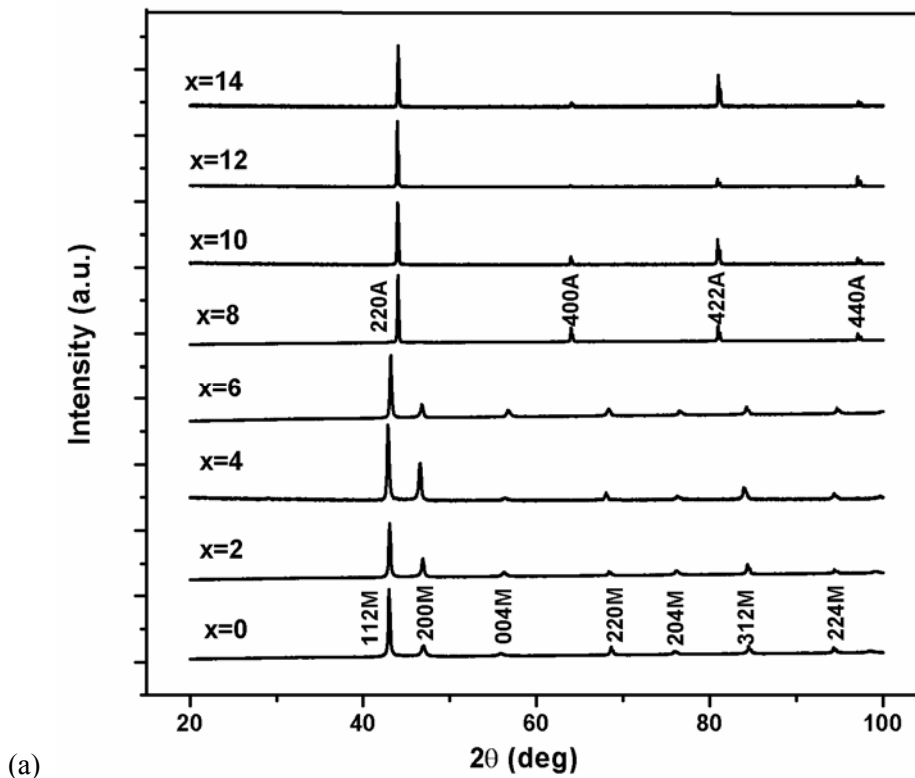


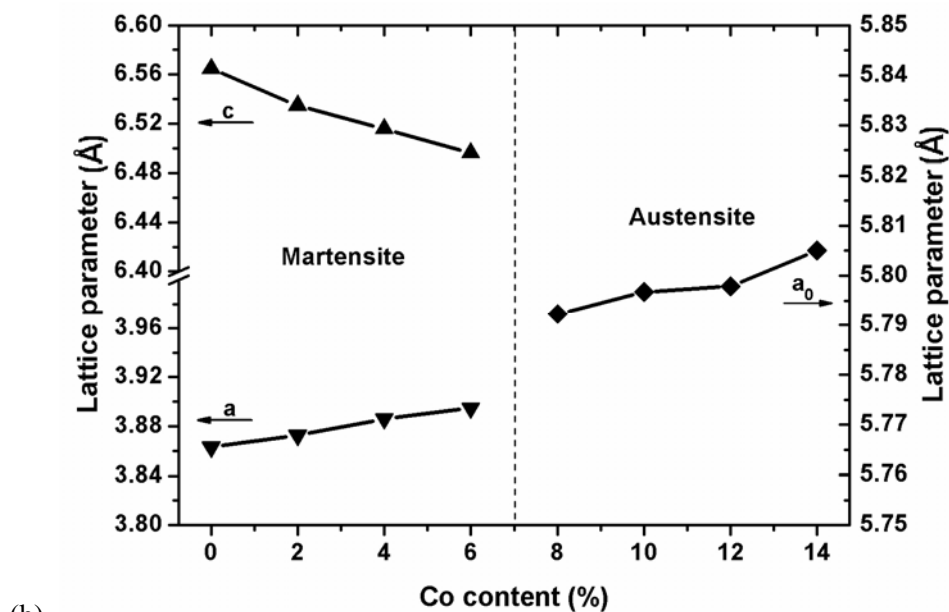
Fig. 1. Optical micrographs of (a) $\text{Ni}_{47}\text{Mn}_{25}\text{Ga}_{22}\text{Co}_6$ (Co6) and (b) $\text{Ni}_{45}\text{Mn}_{25}\text{Ga}_{22}\text{Co}_8$ (Co8) alloys at room temperature.

The lattice parameters of the $\text{Ni}_{53-x}\text{Mn}_{25}\text{Ga}_{22}\text{Co}_x$ as a function of Co content are shown in Fig. 2(b). It can be clearly seen that, for $x \leq 6$ (in martensite), the lattice parameter a increased and c decreased with increasing Co content. For $x \geq 8$ (in austenite), the lattice parameter a_0

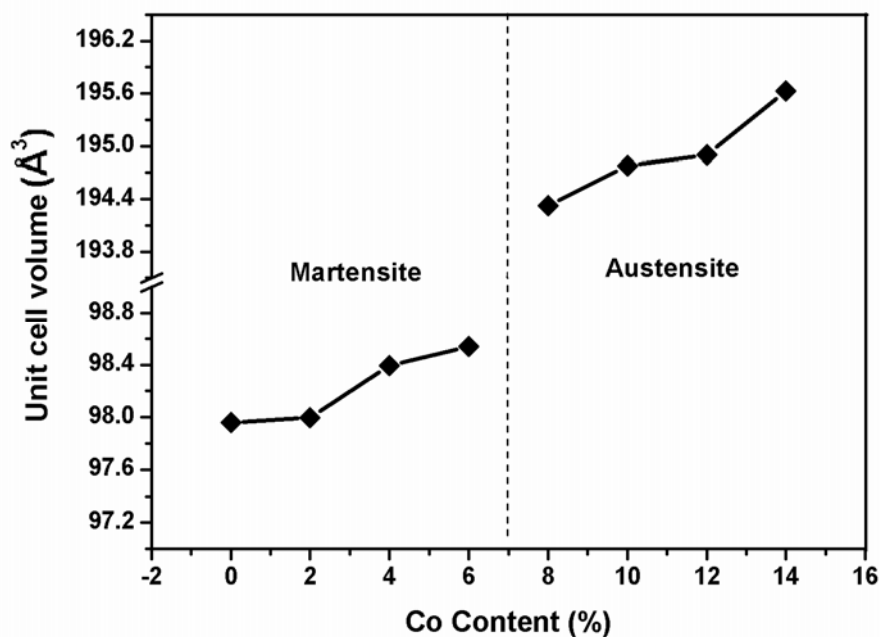
increased with increasing Co content. Fig. 2(c) shows the change in unit cell volume with increasing Co content. It can be seen from Fig. 2(c) that the unit cell volume increased monotonously, in the two regions of $x \leq 6$ and ≥ 8 , with increasing Co content. This trend is attributed to the fact that the atomic radius of Co is larger than that of Ni.

The crystal structure of the FSMAs is an important factor that affects both the magnetic anisotropy and mechanical properties. Moreover, the lattice parameters for the austenite and martensite determine the theoretical maximal MSME [6]. The above-mentioned experiments on crystal structure and the dependence of lattice parameters on the Co content indeed offer useful information for calculating the shape memory strain, predicting the crystallographic features from the crystallographic phenomenological theory and studying the electronic structure by the first-principle calculations in the FSMAs.





(b)



(c)

Fig. 2. (a) XRD patterns of $\text{Ni}_{53-x}\text{Mn}_{25}\text{Ga}_{22}\text{Co}_x$ alloys at room temperature, (b) lattice parameters and (c) unit cell volume as a function of Co content in $\text{Ni}_{53-x}\text{Mn}_{25}\text{Ga}_{22}\text{Co}_x$ alloys.

3.3. Martensitic transformation

DSC measurements were conducted in order to quantitatively study the martensitic transformation temperatures of the $\text{Ni}_{53-x}\text{Mn}_{25}\text{Ga}_{22}\text{Co}_x$ alloys. A typical DSC curve of the Co4 alloy is illustrated in Fig. 3(a). The exothermic peak corresponding to the martensitic transformation during cooling and the endothermic peak corresponding to the reverse

transformation during heating can be clearly seen. The martensitic transformation starting temperature M_s and finishing temperature M_f are 379 and 357K, respectively, and the reverse transformation starting temperature A_s and finishing temperature A_f are 373 and 396K, respectively. The martensitic transformation temperature, calculated as $T_m=(M_s + M_f + A_s + A_f)/4$, is 376K.

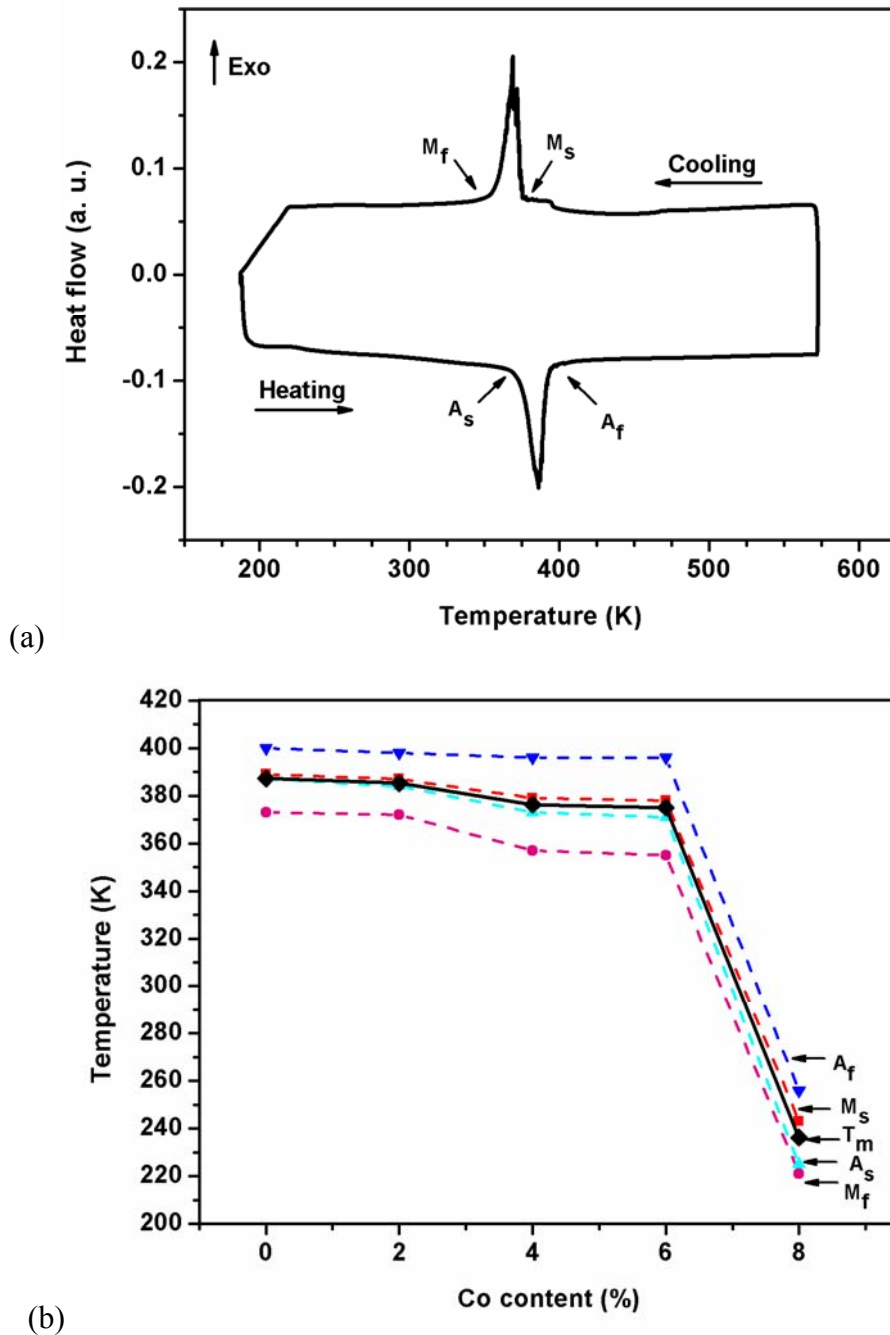


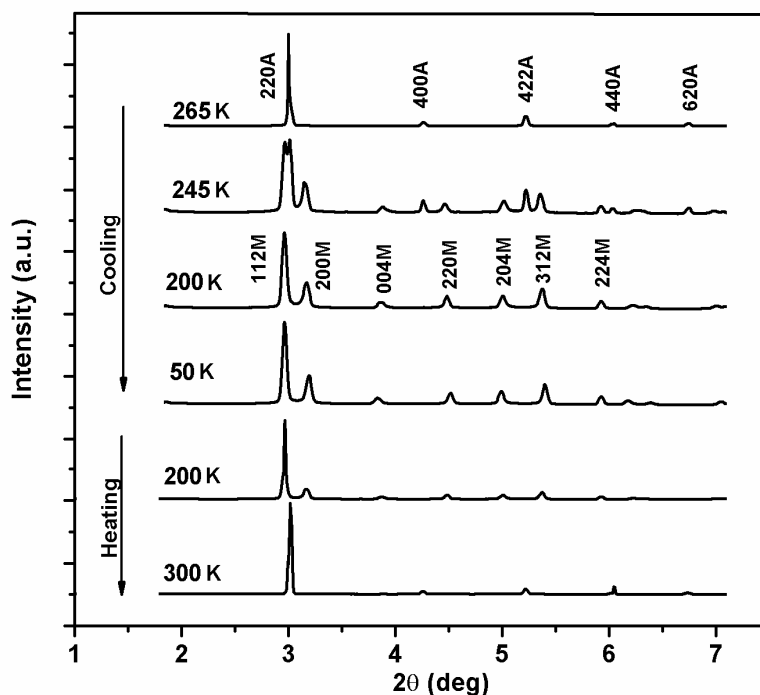
Fig. 3. (a) DSC curve of $\text{Ni}_{49}\text{Mn}_{25}\text{Ga}_{22}\text{Co}_4$ (Co4) alloy, with a heating and cooling rate of 10 K/min; (b) composition dependence of T_m , M_s , M_f , A_s and A_f in the $\text{Ni}_{53-x}\text{Mn}_{25}\text{Ga}_{22}\text{Co}_x$ alloys.

The composition dependence of T_m , M_s , M_f , A_s and A_f in the $\text{Ni}_{53-x}\text{Mn}_{25}\text{Ga}_{22}\text{Co}_x$ alloys is shown in Fig. 3(b). It can be seen that for $x \leq 6$ the martensitic transformation temperature only decreased slightly with increasing Co content ($T_m=387\text{K}$ for $x=0$ and $T_m=375\text{K}$ for $x=6$). However, when Co content exceeded 6 at.%, there was an abrupt decrease of the martensitic transformation temperature. T_m decreased drastically from 375K for $x=6$ to 236K for $x=8$. In the alloys with $x \geq 10$, no martensitic transformation was observed in the temperature range of 188–573K during the DSC measurement. As seen from the austenite microstructure observed at room temperature, it can be concluded that if there is a martensitic transformation in the alloys with $x \geq 10$, it must occur below 188K.

In situ synchrotron XRD experiments were performed for further investigation of the phase transformation in Co8 and Co10 alloys. The temperature dependence of the synchrotron XRD patterns of Co8 and Co10 alloys are shown in Fig. 4(a) and (b), respectively. From Fig. 4(a), it can be seen that Co8 alloy had a Heusler austenite structure at 265K. When cooled to 245K, the Bragg peaks of high temperature phase in the XRD pattern began to split into the patterns of lower symmetry phase due to the martensitic transformation. The XRD pattern at this temperature can be indexed as a mixed structure of austenite and martensite. When cooled to 200K, this alloy transformed fully to martensite and no new transformation occurred during further cooling to 50K. When heated to 300K, the alloy transformed back to a pure austenite state. This transformation behavior agrees well with that observed by the DSC measurement. In contrast, the Co10 alloy had an austenite structure in the experimental temperature region from 290K down to 4K and, then, up to 270K, as shown in Fig. 4(b). No phase transformation was observed in the whole temperature region, which indicates that the Heusler structure in Co10 alloy remained stable down to 4K.

The slight decrease in the martensitic transformation temperature with increasing Co content for $x \leq 6$ is attributed to decreasing of the electron concentration caused by the substitution of Co for Ni [7]. However, the description of the martensitic transformation temperature as a function of electron concentration can only be applied to the alloys with a limited Co addition. The abrupt decrease of martensitic transformation temperature for the alloys with the content of Co exceeding 6 at.% cannot be simply explained by the change in

the electron concentration. In fact, two other factors may influence the martensitic transformation temperature: (1) the atomic disorder caused by the Co addition and (2) the presence of the Co-rich precipitated phase. However, our chemical composition analyses by an energy dispersive spectrometer (EDS) attached to a scanning electron microscope (SEM) showed that there was no obvious composition change in both grain interiors and grain boundaries. The precipitation of the second phase was not observed at all. Hence, we attribute the abrupt decrease in martensitic transformation temperature to the atomic disorder caused by the addition of a large amount of Co. After the Co content reaches a critical value, the excess of Co atoms causes a disordered occupation of crystal lattice sites of Mn, Ga and/or Ni atoms. This trend suppresses the martensitic transformation in the alloys. Kreissl et al. [14,15] reported that the disorder existing between Mn and Ga atoms in Ni_2MnGa alloy substantially suppressed the structural phase transformation. The detailed determination of the long-range and short-range atomic disorder in the $\text{Ni}_{53-x}\text{Mn}_{25}\text{Ga}_{22}\text{Co}_x$ alloys still needs further investigations by high resolution neutron diffraction. To our knowledge, this is the first report on an abrupt decrease of martensitic transformation temperature in the Ni–Mn–Ga–Co alloys. These results are undoubtedly of great importance for designing high temperature Ni–Mn–Ga–Co FSMA.



(a)

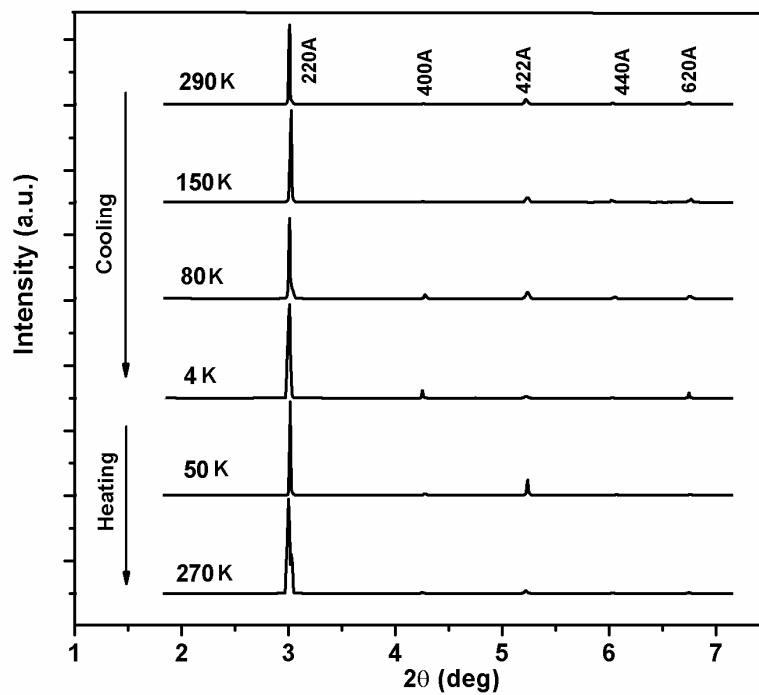


Fig. 4. Temperature dependence of the synchrotron XRD patterns of (a) $\text{Ni}_{45}\text{Mn}_{25}\text{Ga}_{22}\text{Co}_8$ (Co8) and (b) $\text{Ni}_{43}\text{Mn}_{25}\text{Ga}_{22}\text{Co}_{10}$ (Co10) alloy.

3.4. Curie temperature

The composition dependence of T_c in the $\text{Ni}_{53-x}\text{Mn}_{25}\text{Ga}_{22}\text{Co}_x$ alloys is shown in Fig.5. It can be seen that T_c increased monotonously in the broad composition region from $x=0$ to 14 ($T_c=377\text{K}$ for $x=0$ and $T_c=519\text{K}$ for $x=14$). The addition of Co was indeed effective in raising the Curie temperatures of Ni–Mn–Ga–Co alloys. It should be noted that T_c is more rapidly increased in the composition region for $x \geq 8$ than in the composition region for $x \leq 6$. It is proposed that the increase of T_c due to the substitution of Co for Ni is closely related to the magnetic properties in the Ni–Mn–Ga alloys. This is because that the small magnetic moment located on the Ni atom and its coupling with the magnetic moment of the Mn atom play a crucial role [7], although the magnetic moment in Ni–Mn–Ga alloys is mainly attributed to the Mn atoms [16]. Here we believe that the increase of T_c in the $\text{Ni}_{53-x}\text{Mn}_{25}\text{Ga}_{22}\text{Co}_x$ alloys is mainly due to a stronger Co–Mn exchange interaction as compared with that between the Ni–Mn pair [7]. The rapid increase of T_c for $x \geq 8$ may also be attributed to the atomic disorder in these alloys.

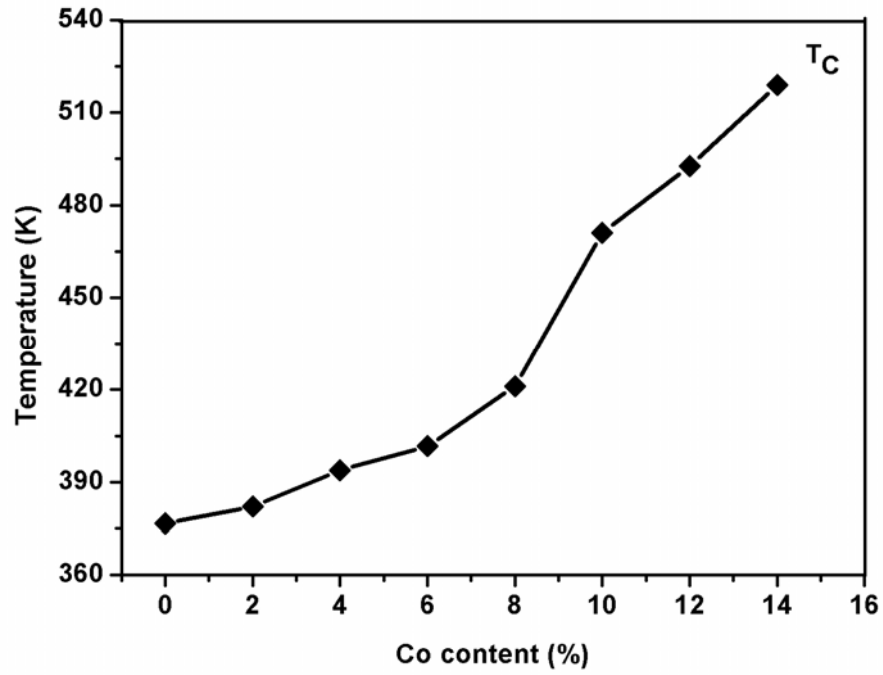
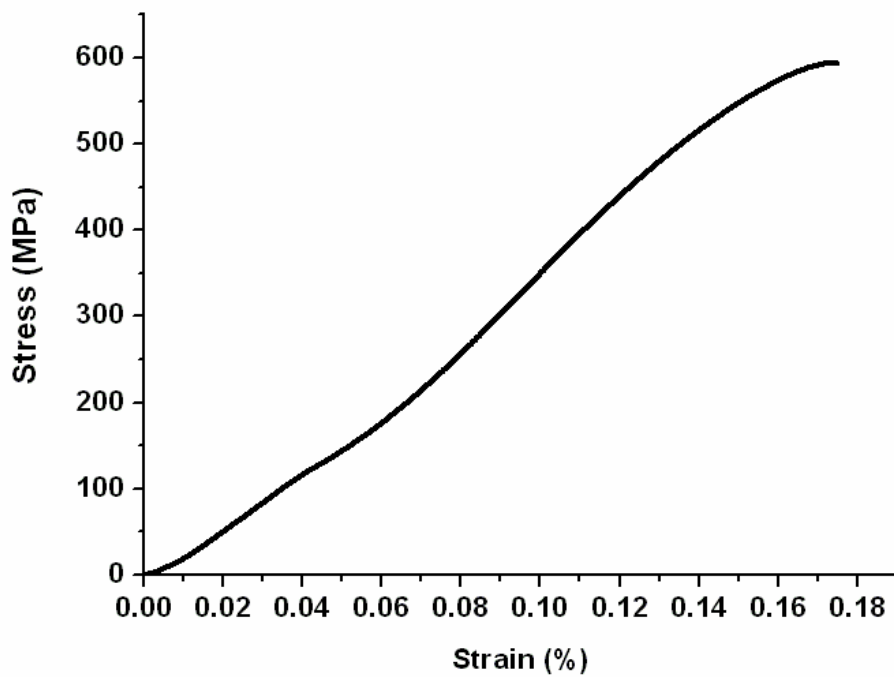
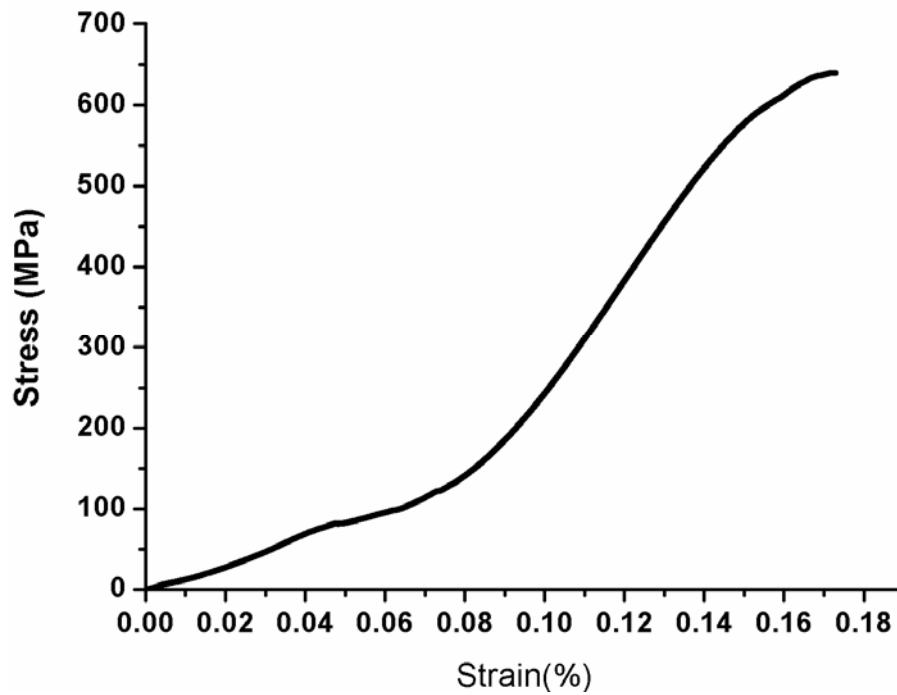


Fig. 5. Composition dependence of Curie temperature T_c in the $\text{Ni}_{53-x}\text{Mn}_{25}\text{Ga}_{22}\text{Co}_x$ alloys.



(a)



(b)

Fig. 6. Compressive stress vs. strain curves of (a) $\text{Ni}_{53}\text{Mn}_{25}\text{Ga}_{22}$ (Co0) and (b) $\text{Ni}_{49}\text{Mn}_{25}\text{Ga}_{22}\text{Co}_4$ (Co4) alloy.

3.5. Compressive properties

The compressive stress versus strain curves of the Co0 and Co4 alloys are illustrated in Fig. 6(a) and (b), respectively. It can be seen that there was a very high work hardening stage following the elastic deformation stage in both alloys. The yield stress, compressive strength and fracture strain for the Co0 alloy were 122MPa, 594MPa and 17.4%, respectively. For the Co4 alloy, the yield stress, compressive strength and fracture strain were 81MPa, 640MPa and 17.3%, respectively. The substitution of 4 at.% Co for Ni did not change the fracture strain, but increased the compressive strength by 46MPa and decreased the yield stress by 41MPa. The lower yield stress in the FSMAs indeed benefits the rearrangements of martensitic variants and movements of twin boundaries under stress and/or magnetic fields.

4. Conclusions

The effect of Co addition on microstructure, crystal structure, martensitic transformation, Curie temperature, and compressive properties of $\text{Ni}_{53-x}\text{Mn}_{25}\text{Ga}_{22}\text{Co}_x$ alloys was systematically investigated. Room temperature XRD experiments revealed that the alloys had

a tetragonal $I4/mmm$ symmetric martensitic structure for $x \leq 6$ and a Heusler $L2_1$ austenite structure for $x \geq 8$. An abrupt decrease in martensitic transformation temperature was observed for the alloys with the Co content exceeding 6 at.%. Substitution of Co for Ni proved efficient in increasing the Curie temperature. Compression experiments at room temperature showed that the substitution of 4 at.% Co for Ni does not change the fracture strain, but increases the compressive strength and decreases the yield stress.

Acknowledgements

The authors are grateful to the National Natural Science Foundation of China (grant no. 50531020) and the Ministry of Education of China with the Specialized Research Fund for the Doctoral Program of High Education and NCET-04-0282. One of the authors (D.Y. Cong) acknowledges the financial support from the project PRA MX04-02 and the PhD fund of Northeastern University. Use of the Advanced Photon Source was supported by the U.S. Department of Energy, Office of Science, Office of Basic Energy Science, under contract no. DE-AC02-CH11357.

References

- [1] A. Sozinov, A.A. Likhachev, N. Lanska, K. Ullakko, *Appl. Phys. Lett.* 80 (2002) 1746–1748.
- [2] S.J. Murray, M.A. Marioni, A.M. Kukla, J. Robinson, R.C. O’Handley, S.M. Allen, *J. Appl. Phys.* 87 (2000) 5774–5776.
- [3] V.A. Chernenko, E. Cesari, V.V. Kokorin, I.N. Vitenko, *Scripta Metall. Mater.* 33 (1995) 1239–1244.
- [4] S.K. Wu, S.T. Yang, *Mater. Lett.* 57 (2003) 4291–4296.
- [5] I. Takeuchi, O.O. Famodu, J.C. Read, M.A. Aronova, K.-S. Chang, C. Craciunescu, S.E. Lofland, M. Wuttig, F.C. Wellstood, L. Knauss, A. Orozco, *Nature Mater.* 2 (2003) 180–184.
- [6] N. Lanska, O. Söderberg, A. Sozinov, Y. Ge, K. Ullakko, V.K. Lindroos, *J. Appl. Phys.* 95 (2004) 8074–8078.
- [7] V.V. Khovailo, T. Abe, V.V. Koledov, M. Matsumoto, H. Nakamura, R. Note, M. Ohtsuka,

- V.G. Shavrov, T. Takagi, *Mater. Trans.* 44 (2003) 2509–2512.
- [8] S. Guo, Y. Zhang, B. Quan, J. Li, Y. Qi, X. Wang, *Smart Mater. Struct.* 14 (2005) S236–S238.
- [9] V.V. Khovailo, V.A. Chernenko, A.A. Cherechukin, T. Takagi, T. Abe, J. Magn. *Mater.* 272–276 (2004) 2067–2068.
- [10] I. Glavatskyy, N. Glavatska, O. Söderberg, S.-P. Hannula, J.-U. Hoffmann, *Scripta Mater.* 54 (2006) 1891–1895.
- [11] D.Y. Cong, P. Zetterström, Y.D. Wang, R. Delaplane, R.L. Peng, X. Zhao, L. Zuo, *Appl. Phys. Lett.* 87 (2005) 111906-1–111906-3.
- [12] Y.D. Wang, D.Y. Cong, R.L. Peng, P. Zetterström, Z.F. Zhang, X. Zhao, L. Zuo, *J. Mater. Res.* 21 (2006) 691–697.
- [13] D.Y. Cong, Y.D. Wang, P. Zetterström, R.L. Peng, R. Delaplane, X. Zhao, L. Zuo, *Mater. Sci. Technol.* 21 (2005) 1412–1416.
- [14] M. Kreissl, T. Kanomata, M. Matsumoto, K.-U. Neumann, B. Ouladdiaf, T. Stephens, K.R.A. Ziebeck, *J. Magn. Mater.* 272–276 (2004) 2033–2034.
- [15] M. Kreissl, K.-U. Neumann, T. Stephens, K.R.A. Ziebeck, *J. Phys.: Condens. Matter* 15 (2003) 3831–3839.
- [16] P.J. Webster, K.R.A. Ziebeck, S.L. Town, M.S. Peak, *Phil. Mag.* B49 (1984) 295–310.

Conclusions

Conclusions

From the above experimental and theoretical investigations, the following important conclusions can be drawn:

Investigation on crystal structure and phase transformation in Ni-Mn-Ga alloys by in situ neutron diffraction technique

The crystal structure and phase transformation behaviors in two Ni-Mn-Ga ferromagnetic shape memory alloys (FSMAs) with compositions of $\text{Ni}_{48}\text{Mn}_{30}\text{Ga}_{22}$ and $\text{Ni}_{53}\text{Mn}_{25}\text{Ga}_{22}$ as a function of temperature have been experimentally investigated by in situ neutron diffraction technique. It is confirmed that neutron diffraction technique is highly efficient in characterizing the crystal structure and structural transformation in Ni-Mn-Ga alloys that consist of nearby elements in the periodic table.

The results show that $\text{Ni}_{53}\text{Mn}_{25}\text{Ga}_{22}$ has a tetragonal $I4/mmm$ (space group No. 139) structure from 20K to 403K. An abrupt jump in unit-cell volume around room temperature, corresponding to an endothermic peak in the differential scanning calorimetry (DSC) curve, has been observed. This indicates a pretransformation in the martensitic phase of $\text{Ni}_{53}\text{Mn}_{25}\text{Ga}_{22}$, which is completely different from the phase transformation in the stoichiometric Ni_2MnGa . The sequence of structural transformation in $\text{Ni}_{53}\text{Mn}_{25}\text{Ga}_{22}$ is closely related to its temperature-dependent magnetic structure.

Neutron diffraction results also show that $\text{Ni}_{48}\text{Mn}_{30}\text{Ga}_{22}$ has a cubic, $L2_1$ Heusler structure (space group $Fm\bar{3}m$, No. 225) from 373K to 293 K. Its crystal structure changes into a seven-layered orthorhombic martensitic structure (space group $Pnmm$, No. 58) when cooled to 243K. No substantial change of the neutron diffraction pattern is observed upon further cooling to 19K, indicating that there is no intermartensitic transformation in this alloy.

The precise determination of the crystal structure of Ni-Mn-Ga alloys is of fundamental importance to the design of high-performance FSMAs and serves as the foundation for further

crystallographic analysis.

Microstructure and martensitic transformation crystallography of Ni-Mn-Ga alloys

Based on the accurate crystal structure information obtained from neutron powder diffraction, the microstructure and twinning relationship of the cast $\text{Ni}_{53}\text{Mn}_{25}\text{Ga}_{22}$ ferromagnetic alloy have been characterized by electron backscatter diffraction in a high-resolution scanning electron microscope equipped with a field emission gun (FE-SEM/EBSD). It is shown that there are only two martensitic variants with twin relationships existing in each initial austenite grain. The twins are found to be compound twins with the twinning elements: $\mathbf{K}_1 = \{112\}$, $\mathbf{K}_2 = \{11\bar{2}\}$, $\boldsymbol{\eta}_1 = \langle 11\bar{1} \rangle$, $\boldsymbol{\eta}_2 = \langle 111 \rangle$, $\mathbf{P} = \{1\bar{1}0\}$ and $s = 0.379$. The neighboring twin variants have a minimum misorientation angle of $\sim 83^\circ$ around the $\langle 110 \rangle$ axis.

The crystallographic and microstructural characteristic of martensitic variants in the $\text{Ni}_{53}\text{Mn}_{25}\text{Ga}_{22}$ alloy firstly annealed at 1073K for 4h followed by cooling to 473K at $\sim 4\text{K}/\text{min}$ and then isothermally held for 30min followed by cooling to room temperature at $\sim 10\text{K}/\text{min}$, have also been experimentally investigated by means of FE-SEM/EBSD. Crystallographic phenomenological theory has been employed to quantitatively explain the crystallographic features during the martensitic transformation. The experimental results show that the twin interface plane is $\{0.399\ 0.383\ 0.833\}$, which is actually $\{112\}$ plane within experimental error. The ratio of the relative amounts of twins within the same initial austenite grain is ~ 1.70 . The main orientation relationship between austenite (A) and martensite (M) is determined to be the Kurdjumov-Sachs (K-S) relationship with $(111)_A // (101)_M$, $[1\bar{1}0]_A // [11\bar{1}]_M$. The results calculated from the crystallographic phenomenological theory are in good agreement with the experimental values.

Nanoscale twins inside the martensitic lamellae on the micrometer scale are observed in the $\text{Ni}_{53}\text{Mn}_{25}\text{Ga}_{22}$ alloy annealed at 1173K for 4h followed by furnace cooling to room temperature. The orientation relationships between the nanotwins connected by different interface configurations have been determined. The intrinsic nature of the inter-lamellar and intra-lamellar interfaces has been revealed. The new insights into the correlation between

microstructure and crystallography of Ni-Mn-Ga alloys will shed light on the microstructure design to improve the novel performances of the FSMAs.

Crystallographic texture in Ni-Mn-Ga alloys

Three FSMAs with chemical compositions of $\text{Ni}_{53}\text{Mn}_{25}\text{Ga}_{22}$, $\text{Ni}_{48}\text{Mn}_{30}\text{Ga}_{22}$ and $\text{Ni}_{48}\text{Mn}_{25}\text{Ga}_{22}\text{Co}_5$, prepared by induction melting, are successfully hot forged together with the stainless steel jackets. Strong textures and a large in-plane plastic flow anisotropy are developed during the hot forging process.

Neutron diffraction measurements show that the main texture components in the hot forged $\text{Ni}_{48}\text{Mn}_{25}\text{Ga}_{22}\text{Co}_5$ alloy are $(110) [\bar{1}12]$ and $(001)[100]$, where the texture representation of $(hkl)[uvw]$ with a notation of the (hkl) plane perpendicular to the compression axis and the $[uvw]$ direction parallel to the radial direction of the forged ingot is used. The texture evolution in the $\text{Ni}_{48}\text{Mn}_{25}\text{Ga}_{22}\text{Co}_5$ alloy after room temperature deformation and subsequent annealing above the martensitic transformation temperature and its correlation with the thermally controlled shape memory effect are investigated. Significant texture changes during deformation have been observed. Some texture components become much stronger while others disappear, which is attributed to the rearrangements of martensitic variants during mechanical deformation. The texture recovers to its initial state after the subsequent annealing because the martensitic variants are rearranged to their original orientation, which is closely related to the macroscopic shape memory effect. An excellent shape memory effect with a recovery ratio of 74% is observed.

The concept that textures in Ni-Mn-Ga alloys can be developed and controlled by mechanical deformation can be of great significance to the improvement of the MSME of the polycrystalline FSMAs by texture control.

Alloying of Ni-Mn-Ga alloys with Co element

The effect of substitution of Co for Ni on crystal structure, martensitic transformation, Curie temperature and compressive properties of $\text{Ni}_{53-x}\text{Mn}_{25}\text{Ga}_{22}\text{Co}_x$ (at.%, $x=0, 2, 4, \dots, 14$) alloys has been systematically investigated. Room temperature X-ray diffraction experiments

show that the alloys have a tetragonal I4/mmm martensitic structure for $x \leq 6$ and a Heusler L2₁ austenite structure for $x \geq 8$. With the increase of Co content up to 6 at.%, the martensitic transformation temperature of the alloys only decreases slightly. In contrast, an abrupt decrease of martensitic transformation temperature is observed when the Co content exceeds 6 at.%, which can be attributed to the atomic disorder resulting from the Co addition. Substitution of Co for Ni proves very efficient in increasing the Curie temperature of the alloys. Compression experiments show that the substitution of 4 at.% Co for Ni does not change the fracture strain, but leads to the increase in the compressive strength and the decrease in the yield stress.

The finding that, when Co content is less than 6 at.%, the substitution of Co for Ni effectively increases the Curie temperature at the expense of only a slight decrease in the martensitic transformation temperature is of practical interest to the design of FSMA with high martensitic transformation temperature and high Curie temperature.

Perspectives

Up to now, the Ni-Mn-Ga FSMA have been investigated extensively on many aspects. Plenty of valuable information of both theoretical significance and practical interest has been obtained and many new phenomena have been revealed. As a kind of newly developed materials, Ni-Mn-Ga FSMA show promising prospects for future applications. However, we should be aware that there is still a long way to go before the large-scale practical applications of these materials. There are still several critical issues that need to be resolved. The key problems and future investigations on these problems can be summarized as follows:

- (1) Severe segregation in local composition frequently occurs during the slow growth of Ni-Mn-Ga single crystals, which significantly affects the crystal structure of different parts and consequently degrades the MFIS in the single crystals. Production of high-quality large single crystals with homogeneous composition by the standardization of crystal growth, thermal treatment, training procedures and quality assessment will be quite essential.
- (2) The blocking stress of the Ni-Mn-Ga FSMA is very low, only about a few MPa. Consequently, a tiny stress field may significantly reduce the MFIS, yielding a strong

degradation in the MSME. To try to increase the blocking stress of these materials by proper methods will be a research topic.

- (3) To date, the large MFIS is only observed in single crystalline 5M and 7M martensites and the MFIS observed in NM martensite is negligible. However, the NM martensite possesses many superior properties over 5M and 7M martensites and it has great potential to show the largest MFIS, as the theoretical maximum MFIS in NM martensite is as high as 20%. Thus, to increase the magnetic anisotropy energy and/or to decrease the twinning stress (namely, to increase the twin boundary mobility) by heat treatment, training under external fields and alloying in order to obtain large MFIS in NM martensite will be a good research direction.
- (4) The observed MFIS in polycrystalline Ni-Mn-Ga alloys is relatively small, but from the application point of view, polycrystalline alloys are more promising as they are easy and economic to produce. Highly textured polycrystals with coarse-grained microstructure have the closest performances to those of single crystals. In-depth study on the correlation between texture type and MSME and development of polycrystalline alloys with desired texture components to improve their MFIS are greatly needed.
- (5) The intrinsic brittleness of Ni-Mn-Ga alloys acts as a great hindrance to the practical applications of these alloys. To increase the ductility of these alloys by certain methods such as alloying and training is quite necessary.
- (6) To develop new promising ferromagnetic shape memory alloy systems with the help of the knowledge obtained in Ni-Mn-Ga alloy system will open new research areas.

Publication List

I. Refereed Publications in International Journals

1. **D. Y. Cong**, P. Zetterström, Y. D. Wang, R. Delaplane, R. Lin Peng, X. Zhao and L. Zuo: Crystal structure and phase transformation in Ni₅₃Mn₂₅Ga₂₂ shape memory alloy from 20K to 473K. *Applied Physics Letters* **87**(11), 111906 (2005).
2. **D. Y. Cong**, Y. D. Zhang, Y. D. Wang, C. Esling, X. Zhao and L. Zuo: Determination of microstructure and twinning relationship between martensitic variants in 53 at.%Ni-25 at.%Mn-22 at.%Ga ferromagnetic shape memory alloy. *Journal of Applied Crystallography* **39**(5), 723-727 (2006).
3. **D. Y. Cong**, Y. D. Zhang, Y. D. Wang, M. Humbert, X. Zhao, T. Watanabe, L. Zuo and C. Esling: Experiment and theoretical prediction of martensitic transformation crystallography in a Ni-Mn-Ga ferromagnetic shape memory alloy. *Acta Materialia* **55**(14), 4731-4740 (2007).
4. **D. Y. Cong**, Y. D. Wang, R. Lin Peng, P. Zetterström, X. Zhao, P. K. Liaw and L. Zuo: Crystal structures and textures in the hot-forged Ni-Mn-Ga alloys. *Metallurgical and Materials Transactions A* **37**(5), 1397-1403 (2006).
5. **D. Y. Cong**, S. Wang, Y. D. Wang, Y. Ren, L. Zuo and C. Esling: Martensitic and magnetic transformation in Ni-Mn-Ga-Co ferromagnetic shape memory alloys. *Materials Science and Engineering A* **473**(1-2), 213-218 (2008).
6. **D. Y. Cong**, Y. D. Wang, P. Zetterström, R. L. Peng, R. Delaplane, X. Zhao and L. Zuo: Crystal structures and textures of hot-forged Ni₄₈Mn₃₀Ga₂₂ alloy investigated by neutron diffraction technique. *Materials Science and Technology* **21**(12), 1412-1416 (2005).
7. **D. Y. Cong**, Y. D. Wang, J. Z. Xu, L. Zuo, P. Zetterström and R. Delaplane: Neutron diffraction study on crystal structure and phase transformation in Ni-Mn-Ga ferromagnetic shape memory alloys. *Powder Diffraction* **22**(4), 307-311 (2007).
8. Y. D. Wang, **D. Y. Cong**, R. Lin Peng, P. Zetterström, Z. F. Zhang, X. Zhao and L. Zuo: Textures and compressive properties of ferromagnetic shape-memory alloy Ni₄₈Mn₂₅Ga₂₂Co₅ prepared by isothermal forging process. *Journal of Materials Research* **21**(3), 691-697 (2006).
9. Y. D. Wang, D. W. Brown, H. Choo, P. K. Liaw, **D. Y. Cong**, M. L. Benson and L. Zuo: Experimental evidence of stress-field-induced selection of variants in Ni-Mn-Ga ferromagnetic shape-memory alloys. *Physical Review B* **75**(17), 174404 (2007).
10. Y. D. Zhang, C. Esling, **D. Y. Cong**, X. Zhao and L. Zuo: Orientation relationship, texture and microstructure in electromagnetic processed materials (EPM). *Archives of Metallurgy and Materials* **53** (1), 17-23 (2008).
11. **D. Y. Cong**, Y. D. Zhang, C. Esling, Y. D. Wang, J. S. Lecomte, X. Zhao and L. Zuo: Multiplex twinned nanostructure in novel ferromagnetic shape-memory alloys. *Submitted*.

II. Keynote and Invited Lectures at International Conferences

1. C. Esling, Y. D. Zhang, **D. Y. Cong**, X. Zhao and L. Zuo: Orientation relationship, texture and microstructure in Electromagnetic Processed Materials (EPM). 2nd Symposium on Texture and Microstructure Analysis, SOTAMA 2007, Cracow, Poland, September 26-28, 2007. [*Keynote Lecture*]
2. Y. D. Zhang, C. Esling, **D. Y. Cong**, X. Zhao and L. Zuo: Electromagnetic processing of materials (EPM) in solid state- A review. Japan-France Cooperative Science Program Seminar on Materials Processing under Magnetic Field, Nancy, France, May 20-23, 2007. [*Invited Lecture*]
3. Y. D. Zhang, **D. Y. Cong**, X. Zhao, L. Zuo and C. Esling: Overview on microstructure tailoring by electromagnetic processing of materials (EPM). International Joint Conference on Knowledge Management for Composite Materials, KMCM 2007, Dusseldorf, Germany, July 3-6, 2007. [*Invited Lecture*]
4. **D. Y. Cong**, Y. D. Zhang, C. Esling, Y. D. Wang, X. Zhao and L. Zuo: Crystal structure and martensitic transformation crystallography in Ni-Mn-Ga ferromagnetic shape memory alloys. To be presented at the 5th International Conference on Advanced Materials and Processing (ICAMP 5), Harbin, China, September 2-5, 2008. [*Invited Lecture*]

III. Contributions to International Conferences

1. **D. Y. Cong**, Y. D. Wang, J. Z. Xu, L. Zuo, P. Zetterström and R. Delaplane: Neutron diffraction study on crystal structure and phase transformation in Ni-Mn-Ga ferromagnetic shape memory alloys. **Proceedings** of 9th National Conference on X-ray Diffraction and ICDD Workshop, Hangzhou, China, October 14-21, 2006, pp58-62.
2. Y. D. Zhang, C. Esling, **D. Y. Cong**, X. Zhao and L. Zuo: Electromagnetic processing of materials (EPM) in solid state-A review. **Proceedings** of Japan-France Cooperative Science Program Seminar on Materials Processing under Magnetic Field, Nancy, France, May 20-23, 2007, pp95-99.
3. **D. Y. Cong**, P. Zetterström, Y. D. Wang, R. Lin Peng, X. Zhao and L. Zuo: Neutron diffraction studies on the crystal structures and textures of Ni-Mn-Ga alloys. The 2nd CCAST Workshop on Application of Spallation Neutron Sources, Beijing, China, July 27-29, 2005. [*Oral Presentation*]
4. Y. D. Wang, Y. Ren, H. Li, **D. Y. Cong**, H. Choo, P. K. Liaw, R. Lin Peng and L. Zuo: Measurement of textures and stresses in Ni₂MnGa ferromagnetic shape-memory alloys. The MECA SENS-III Conference, Santa Fe, New Mexico, USA, October 17-19, 2005. [*Oral Presentation*]
5. **D. Y. Cong**, Y. D. Wang, P. Zetterström, R. L. Peng, R. Delaplane, X. Zhao and L. Zuo: Investigation on crystal structures and textures of the hot-forged Ni₄₈Mn₃₀Ga₂₂ alloy by neutron diffraction technique. The 2nd Joint Danish-Chinese Symposium on Materials Science, Chengde, China, August 14-18, 2005. [*Poster*]

6. **D. Y. Cong**, Y. D. Wang, P. Zetterström, R. Lin Peng, R. Delaplane, X. Zhao and L. Zuo: Neutron diffraction study on crystal structure, phase transformation and texture evolution in Ni-Mn-Ga shape memory alloys. The 3rd CCAST Workshop on Application of Spallation Neutron Sources, Beijing, China, July 31-August 02, 2006. [**Poster**]
7. **D. Y. Cong**, Y. D. Zhang, C. Esling, Y. D. Wang, X. Zhao and L. Zuo: Crystal structure, microstructure and twinning relationship in a Ni-Mn-Ga ferromagnetic shape memory alloy. Séminaire de l'école doctorale EMMA 2007, Nancy, France, May 10, 2007. [**Poster**]
8. **D. Y. Cong**, Y. D. Zhang, C. Esling, Y. D. Wang, X. Zhao and L. Zuo: Crystallographic features during martensitic transformation in Ni-Mn-Ga ferromagnetic shape memory alloys. The 15th International Conference on Texture of Materials (ICOTOM 15), Pittsburgh, Pennsylvania, USA, June 1-6, 2008. [**Poster**]
9. Y. D. Wang, Y. Ren, H. Li, **D. Y. Cong**, H. Choo, P. K. Liaw, R. Lin Peng and L. Zuo: Global and local textures in Ni₂MnGa ferromagnetic shape-memory alloys. SNS-HFIR Users Meetings, Oak Ridge, Tennessee, USA, October 11-13, 2005. [**Poster**]
10. Z. H. Nie, Y. D. Wang, S. Wang, **D. Y. Cong**, H. Choo, Y. D. Liu, E. Maxy, J. W. Richardson, P. K. Liaw and L. Zuo: Transformation textures in the as-cast Ni-Mn-Ga ferromagnetic shape-memory alloys characterized by neutron diffraction technique. The 3rd CCAST Workshop on Application of Spallation Neutron Sources, Beijing, China, July 31-August 02, 2006. [**Poster**]